

NASA Contractor Report 181897

UHB Demonstrator Interior Noise Control Flight Tests and Analysis

**M.A. Simpson, P.M. Druez, A.J. Kimbrough,
M.P. Brock, P.L. Burgé, G.P. Mathur,
M.R. Cannon, and B.N. Tran**

**DOUGLAS AIRCRAFT COMPANY
MCDONNELL DOUGLAS CORPORATION
LONG BEACH, CA 90846**

**CONTRACT NAS1-18037
OCTOBER 1989**



National Aeronautics and
Space Administration

Langley Research Center
Hampton, Virginia 23665-5225

**(NASA-CR-181897) UHB DEMONSTRATOR INTERIOR
NOISE CONTROL FLIGHT TESTS AND ANALYSIS
Final Report (Douglas Aircraft Co.) 188 p**

CSCL 20A

N90-13198

**Unclas
0239479**

G3/71



NASA Contractor Report 181897

**UHB Demonstrator
Interior Noise Control
Flight Tests and Analysis**

**M.A. Simpson, P.M. Druez, A.J. Kimbrough,
M.P. Brock, P.L. Burgé, G.P. Mathur,
M.R. Cannon, and B.N. Tran**

**DOUGLAS AIRCRAFT COMPANY
MCDONNELL DOUGLAS CORPORATION
LONG BEACH, CA 90846**

**CONTRACT NAS1-18037
OCTOBER 1989**



National Aeronautics and
Space Administration

Langley Research Center
Hampton, Virginia 23665-5225

Preface

This report was prepared by McDonnell Douglas Corporation under Task Assignment 4 of Contract NAS1-18037 with NASA Langley Research Center. The NASA technical monitor was Dr. Kevin P. Shepherd.

Several individuals at Douglas Aircraft Company made significant contributions to this study. Craig van de Lune was responsible for acoustic and vibration data acquisition on the Demonstrator. Dr. Mark Lang planned and conducted the sound intensity survey, and Robert Boyd analyzed survey data. Dr. Daryl May designed the Quiet Cabin noise control treatment package, and Dr. Mahendra Joshi reviewed the report and offered many constructive comments throughout this program.

PRECEDING PAGE BLANK NOT FILMED

INTENTIONALLY BLANK

Contents

1	Introduction	1
1.1	Background	1
1.2	Objectives and Approach	3
1.3	Report Overview	4
2	Flight Test Program	6
2.1	Test Aircraft	6
2.2	Propulsion System	6
2.3	Interior Noise Test Points	7
3	Data Acquisition and Analysis	18
3.1	Acquisition System	18
3.2	Transducers	18
3.3	Data Processing and Analysis	19
3.4	Sound Intensity Measurements	19
4	Evaluation of Treatment Effectiveness	29
4.1	Description of Treatments	29
4.1.1	Torque Box (Structural Path)	29
4.1.2	Additional Frames (Structural Path)	30
4.1.3	Frame Damping (Structural Path)	30
4.1.4	Pressure Bulkhead Double Wall (Aft Section Path)	30
4.1.5	Sonic Fatigue Damping (Structural, Cabin Sidewall, and Aft Section Paths)	30
4.1.6	Cabin and Cargo Skin Damping (Structural and Cabin Sidewall Paths)	31
4.1.7	Floor Isolation (Structural Path)	31
4.1.8	Aft Section Absorption (Aft Section Path)	31
4.1.9	Torque Box Damping (Structural Path)	31
4.1.10	Engine Dynamic Absorbers (Structural Path)	31
4.1.11	Trim Panel Damping (Cabin Sidewall Path)	31
4.2	Selection of Test Points	32
4.3	Acoustic and Vibratory Loads	32
4.3.1	Exterior Noise Levels	32
4.3.2	Pylon Vibration Levels	33
4.4	Cabin Noise and Vibration Levels	33
5	Analysis of Quiet Cabin Noise Levels	57
5.1	Acoustic and Vibratory Loads	57
5.1.1	Exterior Noise Levels	57

5.1.2	Pylon Vibration Levels	57
5.2	Cabin Noise Levels	58
6	Comparison of 10x8 and 8x8 Data	73
6.1	Acoustic and Vibratory Loads	73
6.1.1	Exterior Noise Levels	73
6.1.2	Pylon and Fuselage Vibration Levels	74
6.2	Cabin Noise Levels	75
7	Comparison of Cruise and Non-Cruise Data	89
7.1	Acoustic and Vibratory Loads	89
7.1.1	Exterior Noise Levels	89
7.1.2	Pylon Vibration Levels	90
7.2	Cabin Noise Levels	90
8	Identification of Major Transmission Paths	109
8.1	Results of Sound Intensity Survey	109
8.2	Cabin Sidewall Path	110
8.3	Aft Section Path	111
8.4	Structural Path	113
8.5	Results of Partial Coherence Analyses	114
8.5.1	Partial Coherence Analysis Concepts	115
8.5.2	Analysis of 8x8 Data	116
8.5.3	Analysis of 10x8 Data	119
9	Summary and Conclusions	133
A	Estimation of The Turbulent Boundary Layer Pressure Wavenumber-Frequency Spectrum	136
A.1	Definition of Wavenumber-Frequency Spectra	136
A.2	Spectral Modeling of TBL Pressure Fluctuations	138
A.3	Estimation Procedure	139
A.4	Flight Test Results	142
A.5	References	144
B	Partial Coherence Techniques	171
B.1	Mathematical Formulation	171
B.2	Flight Test Applications	174

List of Tables

2-1. UDF Engine Characteristics	8
2-2. Test Point Summary	9
4-1. UHB Demonstrator Interior Treatment Configurations	35
4-2. Test Point Summary for Interior Treatment Evaluation	36
7-1. Test Point Summary for Non-Cruise Comparisons	93
8-1. Coherence Between Inputs and Outputs for BPF Tone (168 Hz), Test Point 19550A03	121
8-2. Reduction in BPF Tone Level at Interior Output Microphones Conditioned with Exterior Microphone and Accelerometer Inputs, Test Point 19550A03	122
8-3. Coherence Between Inputs and Outputs for BPF Tone (168 and 210 Hz), Test Point 19640B03	123
8-4. Reduction in BPF Tone Level at Interior Output Microphones Conditioned with Exterior Microphone and Accelerometer Inputs, Test Point 19640B03	124
A-1. Flight Test Conditions and Parameters	147

List of Figures

1-1. Demonstrator Noise Levels, Quiet Cabin Configuration	5
2-1. The MD-80 Aircraft	10
2-2. The UHB Engine and Pylon Installation	11
2-3. The Demonstrator in Flight	12
2-4. The Demonstrator on the Ground Showing Counter-Rotating Blades	13
2-5. View from Under the Demonstrator Showing Relative Positions of the JT8D and UDF Engines and Pylons	14
2-6. The Furnished Cabin Showing Selected Microphone Locations	15
2-7. UDF Propulsor Design Schematic	16
2-8. Close Up View of UDF 10x8 Engine on the Demonstrator	17
3-1. Exterior Microphone Locations on Fuselage and Pylon	21

3-2. Cabin Microphone Locations	22
3-3. Aft Section Microphone Locations	23
3-4. Location of Pylon and Fuselage Accelerometers	24
3-5. Location of Station 1271, Station 1322 and Aft Bulkhead Accelerometers	25
3-6. A Typical Interior Cabin Seat Microphone Spectrum	26
3-7. Sound Intensity Survey Areas	27
3-8. Location of Survey Grids	28
4-1. Predicted Noise Transmission Paths for the MD-UHB Demonstrator	37
4-2. Torque Box Design	38
4-3. Frame Modifications and Additions	39
4-4. Pressure Bulkhead Double Wall Design	40
4-5. Distribution of Sonic Fatigue Treatment Between Stations 1174 and 1510	41
4-6. Engine Dynamic Absorber Locations on Mount Beam	42
4-7. Exterior Acoustic Loads Distribution of the 8X8 Propeller Blade Passage Frequency for Each Test Point	43
4-8. Fuselage Acoustic Loads: A-Weighted Broadband Levels	44
4-9. Acceleration Levels at BPF, 2BPF and UN1 Measured at the Inboard Location of the Pylon Spar	45
4-10. Maximum A-Weighted Levels at Seated Positions of Row 6	46
4-11. Maximum A-Weighted Tone Levels at Seated Positions of Row 6	47
4-12a. A-Weighted Levels Measured at Microphone 6 in Row 6 (Window Seat, JT8D Side)	48
4-12b. A-Weighted Levels Measured at Microphone 4 in Row 6 (Aisle Seat, JT8D Side)	49
4-12c. A-Weighted Levels Measured at Microphone 2 in Row 6 (Aisle Seat, UDF Side)	50
4-12d. A-Weighted Levels Measured at Microphone 1 in Row 6 (Window Seat, UDF Side)	51
4-13. Measured Interior Noise Spectra in Row 6 for the Seat with the Maximum A-Level (Configurations 1, 2 and 3)	52
4-14. Measured Interior Noise Spectra in Row 6 for the Seat with the Maximum A-Level (Configurations 4, 5, 6 and 7)	53
4-15a. Frame Acceleration at BPF, 2BPF and UN1 at Fuselage Station 1271, Longeron 2	54
4-15b. Frame Acceleration at BPF, 2BPF and UN1 at Fuselage Station 1271, Longeron 5	55
4-15c. Frame Acceleration at BPF, 2BPF and UN1 at Fuselage Station 1271, Longeron 6	56

5-1. Variation of BPF Sound Pressure Level with Propeller Speed	60
5-2a. Aft Engine Mount Accelerations at BPF, 2BPF and UN1	61
5-2b. Inboard Pylon Spar Accelerations at BPF, 2BPF and UN1	62
5-3. A Weighted Interior Noise Levels at Row 4 (Configuration 4)	63
5-4. A-Weighted Interior Noise Levels at Row 6 (Configuration 4)	64
5-5. Maximum Measured Sound Pressure Levels at BPF, 2BPF, UN1 and JN1 Frequencies	65
5-6. Variation of the BPF A-Weighted Level in Row 4 and Row 6	66
5-7. Variation of the 2BPF A-Weighted Level in Row 4 and Row 6	67
5-8. Variation of the UN1 A-Weighted Level in Row 4 and Row 6	68
5-9. Variation of the JN1 A-Weighted Level in Row 4 and Row 6	69
5-10. Variation of the Tone Summations in Row 4 and Row 6	70
5-11. Variation of the Broadband Noise Levels in Row 4 and Row 6	71
5-12. Variation of the Overall A-Weighted Levels in Row 4 and Row 6	72
6-1. Comparison of 10x8 and 8x8 Spectra at Exterior Microphone 4	76
6-2a. Comparison of 10x8 and 8x8 BPF Tones on the Aft Fuselage	77
6-2b. Comparison of 10x8 and 8x8 BPF Tones on the Aft Fuselage	78
6-3a. Comparison of 10x8 and 8x8 Engine Mount Accelerations	79
6-3b. Comparison of 10x8 and 8x8 Pylon Accelerations	80
6-4. Comparison of 10x8 and 8x8 Fuselage Acceleration Levels	81
6-5a. Comparison of 10x8 and 8x8 Noise Levels at Row 6 Seat 1	82
6-5b. Comparison of 10x8 and 8x8 Noise Levels at Row 6 Seat 3	83
6-5c. Comparison of 10x8 and 8x8 Noise Levels at Row 6 Seat 4	84
6-5d. Comparison of 10x8 and 8x8 Noise Levels at Row 4 Seat 1	85
6-5e. Comparison of 10x8 and 8x8 Noise Levels at Row 4 Seat 3	86
6-6a. Comparison of 10x8 and 8x8 Spectra at Row 6 Seat 4	87
6-6b. Comparison of 10x8 and 8x8 Spectra at Row 4 Seat 3	88
7-1. Variation of 8x8 Exterior Sound Pressure Level at BPF	94
7-2. Variation of 10x8 Exterior Sound Pressure Level at BPF	95
7-3. Variation of 10x8 Longitudinal Pylon Acceleration	96
7-4. Variation of 10x8 Vertical Pylon Acceleration	97
7-5. Maximum Measured Sound Pressure Level in Row 6 at each BPF	98
7-6a. Variation of 8x8 Interior Noise Components with RPM at Row 6 Seat 1	99
7-6b. Variation of 8x8 Interior Noise Components with RPM at Row 6 Seat 3	100
7-6c. Variation of 8x8 Interior Noise Components with RPM at Row 6 Seat 4	101

7-6d. Variation of 8x8 Interior Noise Components with RPM at Row 6 Seat 5	102
7-6e. Variation of 8x8 Interior Noise Components with RPM at Row 6 Seat 6	103
7-7a. Variation of 10x8 Interior Noise Components with RPM at Row 6 Seat 1	104
7-7b. Variation of 10x8 Interior Noise Components with RPM at Row 6 Seat 3	105
7-7c. Variation of 10x8 Interior Noise Components with RPM at Row 6 Seat 4	106
7-7d. Variation of 10x8 Interior Noise Components with RPM at Row 5 Seat 1	107
7-7e. Variation of 10x8 Interior Noise Components with RPM at Row 5 Seat 6	108
8-1. Measured Sound Intensities for the 100, 160, 200 and 315 Hz One-Third Octave Bands, 8x8 Flight 2026	125
8-2. Measured Sound Power Levels for the 100, 160, 200 and 315 Hz One-Third Octave Bands, 8x8 Flight 2026	126
8-3a. Cabin Sidewall Transmission Path: Exterior Noise Spectra Measured on the Aircraft Fuselage, Test Point 19550A03	127
8-3b. Cabin Sidewall Path: Interior Noise Spectra, Test Point 19550A03	128
8-4. Aft Section Transmission Path: Unpressurized Section Noise Spectra, Test Point 19550A03	129
8-5. Aft Section Transmission Path: Comparison of Interior Noise Spectra at Row 6, Seat 1	130
8-6. Comparison of Noise and Vibration Data Acquired in the Aft Section of the Aircraft, Flight 1955	131
8-7. Transducers Used in the Partial Coherence Analysis of 8x8 Data	132
A-1. Sketch of the Wavenumber-Frequency Spectrum	148
A-2a. Sound Pressure Level Spectra for the Probe Microphones (Flight Condition 1)	149
A-2b. Sound Pressure Level Spectra for the Probe Microphones (Flight Condition 2)	150
A-2c. Sound Pressure Level Spectra for the Probe Microphones (Flight Condition 3)	151
A-2d. Sound Pressure Level Spectra for the Probe Microphones (Flight Condition 4)	152

A-2e. Sound Pressure Level Spectra for the Probe Microphones (Flight Condition 5)	153
A-3a. Estimated Wavenumber-Frequency Spectrum (Flight Condition 1)	154
A-3b. Estimated Wavenumber-Frequency Spectrum (Flight Condition 2)	155
A-3c. Estimated Wavenumber-Frequency Spectrum (Flight Condition 3)	156
A-3d. Estimated Wavenumber-Frequency Spectrum (Flight Condition 4)	157
A-3e. Estimated Wavenumber-Frequency Spectrum (Flight Condition 5)	158
A-4a. Wavenumber-Frequency Contour Plot for TBL Pressure Spectrum (Flt. Cond. 1)	159
A-4b. Wavenumber-Frequency Contour Plot for TBL Pressure Spectrum (Flt. Cond. 2)	160
A-4c. Wavenumber-Frequency Contour Plot for TBL Pressure Spectrum (Flt. Cond. 3)	161
A-4d. Wavenumber-Frequency Contour Plot for TBL Pressure Spectrum (Flt. Cond. 4)	162
A-4e. Wavenumber-Frequency Contour Plot for TBL Pressure Spectrum (Flt. Cond. 5)	163
A-5a. Wavenumber Variation of TBL Pressure Spectral Density (F=50 Hz)	164
A-5b. Wavenumber Variation of TBL Pressure Spectral Density (F=75 Hz)	165
A-5c. Wavenumber Variation of TBL Pressure Spectral Density (F=100 Hz)	166
A-5d. Wavenumber Variation of TBL Pressure Spectral Density (F=150 Hz)	167
A-6. Comparison of Flight Test TBL Pressure Data with Corcos' Model	168
A-7. Comparison of TBL Pressure Spectral Density with Laganelli's Model	169
A-8. Comparison of Flight Test TBL Pressure Data with Witting's Model	170
 B-1. Example of the Partial Coherence Conditioning Process for Output Microphone 5, 8x8 Test Point 19550A03	 175

1 Introduction

1.1 Background

Over the past fifteen years there has been a renewed interest in the use of fuel-efficient turboprop engines for aircraft powerplants, due to the concern over rising fuel costs and the accompanying desire for energy conservation. Advanced turboprop engines, which make use of recent developments in blade design and fabrication, have the potential for providing thrust that is comparable to today's turbofan engines with a significant reduction in fuel use.

McDonnell Douglas Corporation (MDC) is currently developing a new generation of commercial transport aircraft that would be powered by such advanced turboprop engines, designated as Ultra High Bypass (UHB) engines. MDC's plans are to develop a derivative of the MD-80 series aircraft, which would incorporate two aft-mounted UHB engines in place of the two turbofan engines now utilized.

One of the major concerns associated with UHB aircraft is the noise environment that may be experienced by passengers. The longest portion of a typical flight is spent at high altitude, high speed cruise. Under these conditions the UHB engine is expected to produce its highest noise levels since the tips of the propeller blades are moving at supersonic speeds. The resulting acoustic energy is generated in discrete tones, at frequencies corresponding to the blade passage frequency and its multiples for each propeller rotor. These blade passage frequencies lie typically between 100 and 250 Hz, where the transmission loss characteristics of standard aircraft sidewalls are not sufficient to reduce the high noise levels expected on the fuselage exterior to acceptably low interior levels.

In 1985, a UHB Technology Readiness Program was initiated at Douglas Aircraft Company to address the various technical issues associated with the development of UHB aircraft, including interior noise. A major element of this program was a series of demonstration flight tests using a modified MD-80 test aircraft with a prototype UHB engine in place of the left JT8D turbofan engine. One of the primary purposes of the flight tests of this MD-UHB Demonstrator aircraft was to prove that a "Quiet Cabin" could be achieved in a commercial transport aircraft powered by advanced turboprop engines. For these tests, a Quiet Cabin meant that the maximum noise level in the cabin during high altitude, high speed cruise conditions would not exceed 82 dBA.

In order to meet this interior noise goal for the MD-UHB Demonstrator, the approach adopted was to:

1. Estimate interior noise levels for an untreated aircraft, using projections of UHB exterior noise levels and vibration loads;

2. Propose candidate noise control treatments applicable to the various expected airborne and structureborne transmission paths which would reduce interior noise levels to meet the goal of 82 dBA;

3. Evaluate the effectiveness of the candidate treatments using fuselage ground tests; and

4. Progressively install and evaluate the most promising treatments on the Demonstrator aircraft.

This approach also provided noise and vibration data in flight for various treatment configurations, from which treatment effectiveness and noise transmission paths into the cabin could be studied.

Starting in October 1986, a series of interior noise control tests was conducted in a fuselage ground test facility to evaluate selected treatments planned for installation on the MD-UHB Demonstrator. Flight tests of the Demonstrator powered by one JT8D engine and one UHB engine began in June 1987, with a minimal noise control treatment package. The UHB engine used for these tests was a General Electric "Unducted Fan" (UDF) engine, which utilizes the exhaust from a small jet engine to drive two rows of highly swept, counter-rotating propeller blades. For the first several flight tests, the UDF engine configuration included eight blades on both the forward and aft rotors (an 8x8 configuration).

Additional noise control treatments were then added, aided by the ground test results. In July the installation of the full Quiet Cabin treatment package was completed, and the interior noise goal of 82 dBA was attained. In August, the 8x8 UDF engine configuration was replaced by a 10x8 configuration (10 blades on the forward rotor and 8 blades on the aft rotor), the 82 dBA interior noise goal was again achieved. Figure 1-1 illustrates the interior noise environment measured on the Demonstrator during one of the 10x8 flights. The measurements showed the noise levels throughout the aft cabin to be in a narrow range from 78 to 82 dBA; these levels are below the levels in the aft cabin of many current jet transports. Furthermore, observers on the aircraft (including representatives from the airlines and the press) noted that the propeller blade passage tones were not perceptible in flight, thus alleviating the early concern that these tones would render the cabin noise environment unacceptable.

In subsequent phases of the program the 8x8 configuration was reinstalled for additional testing, and in February 1988 selected treatments were removed to investigate the potential for reducing treatment weight while maintaining low cabin noise levels.

The entire MD-UHB Demonstrator flight test activity (including flights to study aerodynamic and structural dynamics issues and for marketing purposes) totaled 93 flights for 165.5 hours, over a 10-month period ending in March 1988. The flight tests

proved that UHB engine technology could successfully be applied to commercial transport aircraft. In particular, the achievement of a comfortable cabin noise environment on a UHB-powered aircraft, comparable to that on a turbofan-powered aircraft, was demonstrated to the technical community, the airlines, and the public.

As one element of NASA's Advanced Turboprop (ATP) technology program, the NASA/Industry flight demonstration program was started in 1987 to work with the aircraft industry in the study of passenger cabin noise in advanced turboprop aircraft. Under this program, a contract with MDC required detailed analysis of the interior noise measurement data acquired during the several ground and flight tests described above. This report describes the results of MD-UHB Demonstrator flight tests. (The results of the fuselage ground tests are documented in NASA CR 181819.)

1.2 Objectives and Approach

The objectives of the analyses described in this report are to investigate the interior noise characteristics of advanced turboprop aircraft with aft-mounted engines and to study the effectiveness of selected noise control treatments in reducing passenger cabin noise.

These objectives were accomplished by analyzing the noise and vibration data collected during numerous MD-UHB Demonstrator flight tests. The majority of the data were obtained at high altitude, high speed cruise conditions with the 8x8 engine configuration. Exterior and interior noise level distributions were determined from these data, for several noise treatment installations. Additional data were obtained under comparable cruise conditions with the 10x8 engine configuration, and for both configurations at lower speeds and altitudes. Differences in levels for these alternate conditions and configurations were determined relative to the 8x8 cruise data.

The relative strengths of airborne and structureborne transmission paths were defined using the results of a sound intensity survey, combined with measured cabin noise levels and exterior noise and vibration data measured on the fuselage and pylon. Partial coherence analysis techniques were also used to provide further insight into the noise transmission paths.

Since broadband noise due to the turbulent boundary layer was found to be a significant contributor to the total interior noise level, a supplementary study of this noise source was undertaken. Estimates of the turbulent boundary layer pressure wavenumber-frequency spectrum were made with a new spectral analysis technique using noise levels measured on the fuselage surface, and compared with theoretical models and empirical models based on wind tunnel data.

1.3 Report Overview

This report documents the measurement and analysis procedures for MD-UHB Demonstrator noise and vibration flight test data related to passenger cabin noise, and describes the test results. The next two sections of this report discuss the flight test program and data acquisition and analysis, respectively. In Section 4, the various noise control treatments installed on the Demonstrator are defined and their effectiveness is evaluated. Section 5 presents the results of measurements in the fully treated "Quiet Cabin", for high speed, high altitude cruise conditions with the 8x8 engine configuration. Sections 6 and 7 compare measurement results for the 10x8 engine configuration and for non-cruise conditions, respectively, with the Section 5 results. The following section identifies the major transmission paths (airborne and structureborne) into the cabin. The final section summarizes the conclusions of this study. In Appendix A, results of the wavenumber-frequency analysis of turbulent boundary layer noise are presented. Appendix B provides the mathematical background for the partial coherence analysis used in Section 8. Tables, figures, and references are located at the end of each section or Appendix.

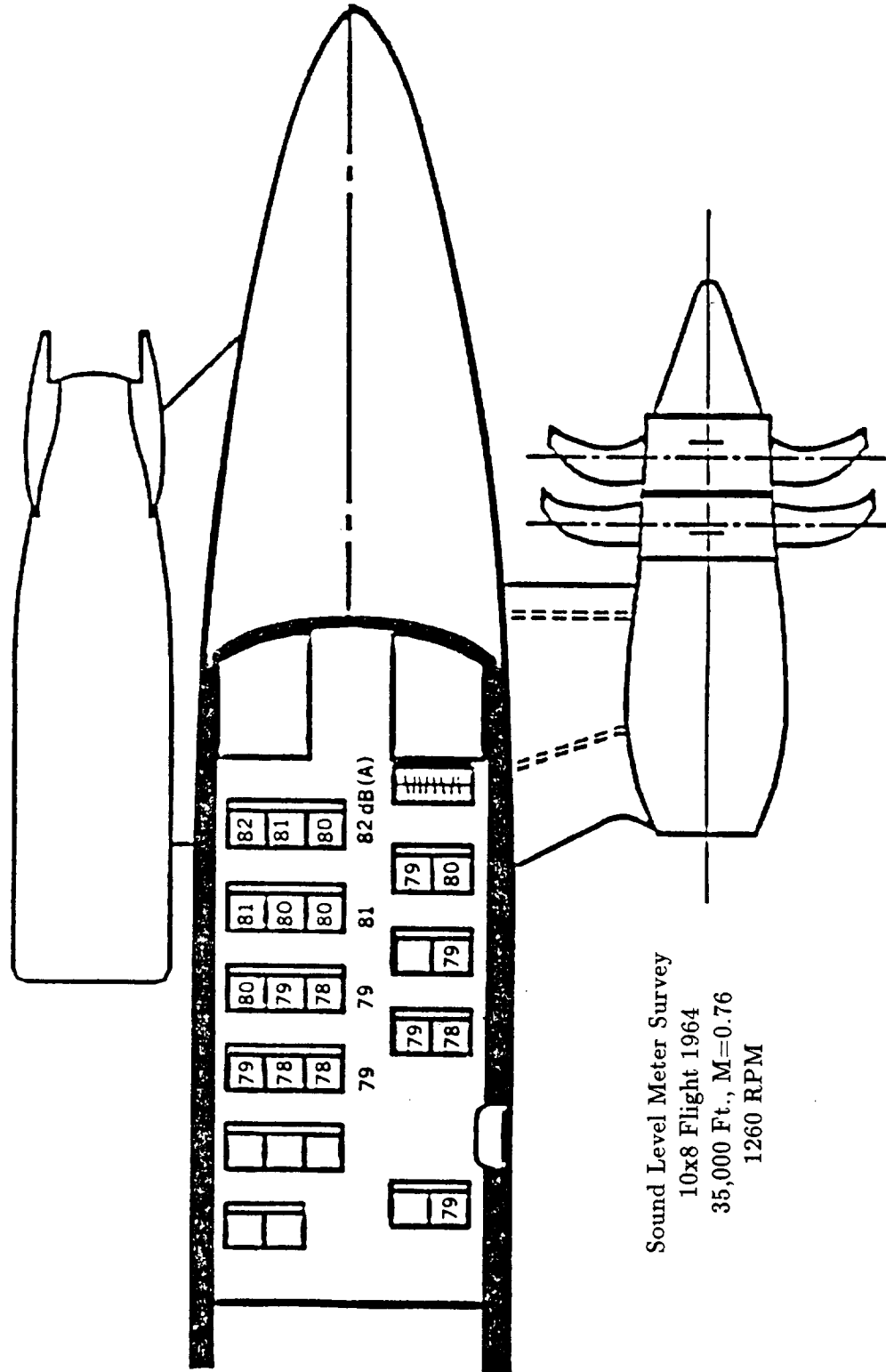


FIGURE 1-1. Demonstrator Noise Levels, Quiet Cabin Configuration

2 Flight Test Program

2.1 Test Aircraft

The Demonstrator aircraft is a modified MD-80 series aircraft. The MD-80 (see Figure 2-1), characterized by an overall length of 147.8 ft and a wingspan of 107.8 ft, is designed to carry 155 passengers on short-to-medium range routes. The aircraft is normally powered by two Pratt & Whitney JT8D-209 engines. The JT8D-209 is a dual-rotor, fully ducted turbofan with a low bypass ratio of 1.8.

The Douglas Aircraft-owned MD-80 (ship 909) was modified by replacing the left engine with a General Electric proof-of-concept Unducted Fan (UDF). Although the nacelles of the JT8D-209 and the UDF are of comparable diameter, the large diameter of the propellers required that the thrust axis be moved outboard and higher than that of the JT8D-209 to provide sufficient blade tip-to-fuselage and tip-to-ground clearance. Accordingly a new pylon was installed with an approximate 5 ft span to replace the 9 inch stub pylon used with the JT8D engine, and stonger fuselage frames were installed at the forward and aft pylon spar locations to support the new structure. The relative positioning of the JT8D and of the UDF is illustrated in Figure 2-2. Figures 2-3, 2-4, and 2-5 are photographs showing different views of the Demonstrator aircraft.

The last 20 ft of the cabin was configured with a current generation MD-80 interior, including seats, baggage racks, interior lighting and trim, and a functional lavatory. This was done to provide the most realistic environment for noise measurements and to provide an attractive and comfortable interior environment for demonstration flights. Flight test instrumentation was located forward of this cabin area. Figure 2-6 shows the furnished aft cabin, with microphones mounted at selected seat and aisle locations.

2.2 Propulsion System

The UDF engine consists of an F404 low bypass ratio turbofan thermodynamically coupled to the aft mounted propellers. Figure 2-7 illustrates how the core engine exhausts are driven through a set of counter-rotating turbines at the base of the two counter-rotating propellers. Figure 2-8 is a close-up view of the engine mounted on the Demonstrator.

During the flight test program, two propeller configurations were used: eight-bladed propellers on both the forward and aft rotors (designated as an 8x8 configuration), and a combination ten-bladed propeller on the forward rotor and eight-bladed propeller on the aft rotor (designated as a 10x8 configuration). The pertinent characteristics of the UDF engine with both rotor configurations are summarized in Table 2-1.

2.3 Interior Noise Test Points

Of the 93 flights in the test program, several were primarily oriented to interior noise measurement purposes. Interior noise data were also acquired on several flights that were oriented to other purposes. Table 2-2 lists all the flights and test points in which interior data were collected. As this table shows, data were obtained for both engine configurations, for seven interior configurations (defined in Table 4-1 and described in detail in Section 4), and several altitude, Mach No., and engine speed combinations.

Table 2-1 UDF Engine Characteristics

10x8 Configuration

Forward Fan Diameter:	3.556m(11.67 ft.)
Aft Fan Diameter:	3.353m(11.00 ft.)
Forward Fan:	CCW looking forward
Aft Fan Rotation:	CW looking forward
Number of Blades:	10 fwd, 8 aft

8x8 Configuration

Forward Fan Diameter:	3.56m(11.67 ft.)
Aft Fan Diameter:	3.25m(10.67 ft.)
Forward Fan:	CCW looking forward
Aft Fan Rotation:	CW looking forward
Number of Blades:	8 fwd, 8 aft

Table 2-2 Test Point Summary

DATE	UHB CONFIG.	RUN NUMBER	ROTOR SPEED (RPM)	FUSELAGE CONFIG.	ALTITUDE (ft.)	MACH NUMBER
6-25-87	8x8	19510001	1280	1	35000	0.76
	"	19510002	1265	"	"	"
	"	19510003	1260	"	"	"
	"	19510004	1250	"	"	"
6-26-87	8x8	19520A01	1270	2	35000	0.76
	"	19520A02	1270	"	"	"
	"	19520A03	1260	"	"	"
	"	19520A04	1250	"	"	"
	"	19520A05	1270/1170	"	"	"
6-27-87	8x8	19530A01	1270	3	35000	0.76
	"	19530A02	1260	"	"	"
	"	19530A03	1250	"	"	"
	"	19530A04	1225	"	"	"
	"	19530A05	1270	"	"	0.77
	"	19530A06	1260	"	"	0.76
	"	19530A07	1250	"	"	"
	"	19530A08	1230	"	"	"
7-7-87	8x8	19550A01	1285	4	35000	0.76
	"	19550A02	1270	"	"	"
	"	19550A03	1260	"	"	"
	"	19550A04	1250	"	"	"
	"	19550A05	1225	"	"	"
	"	19550A06	1200	"	"	"
	"	19550A07	1170	"	"	"
8-26-87	10x8	19640A01	1200	4	22500	0.55
	"	19640A02	1210	"	"	"
	"	19640A03	1230	"	"	"
	"	19640A04	1250	"	"	"
	"	19640A05	1265	"	"	"
	"	19640A06	1290	"	"	"
	"	19640A15	1305	"	31000	0.71
8-26-87	10x8	19640B01	1275	4	35000	0.76
	"	19640B02	1265	"	"	"
	"	19640B03	1255	"	"	"
	"	19640B04	1240	"	"	0.75
2-22-88	8x8	20160H01	1250	5	35000	0.76
	"	20160H02	1255	"	"	0.77
	"	20160H05	1245	"	"	0.76
	"	20160H06	1245	"	"	"
3-05-88	8x8	2026 [†]	1200	5	33500	0.76
3-19-88	8x8	20330K01	1255	5	22500	0.69
	"	20330K02	1255	"	"	0.70
	"	20330K03	1255	"	"	0.77
	"	20330K04	1350	"	"	"
3-21-88	8x8	20340K01	1255	6	35000	0.76
	"	20340K02	1265	"	"	0.81
	"	20340K03	1285	"	"	0.84
	"	20340K04	1285	"	"	0.86
3-22-88	8x8	20350001	1265	7	35000	0.77

[†] Sound Intensity Survey Flight

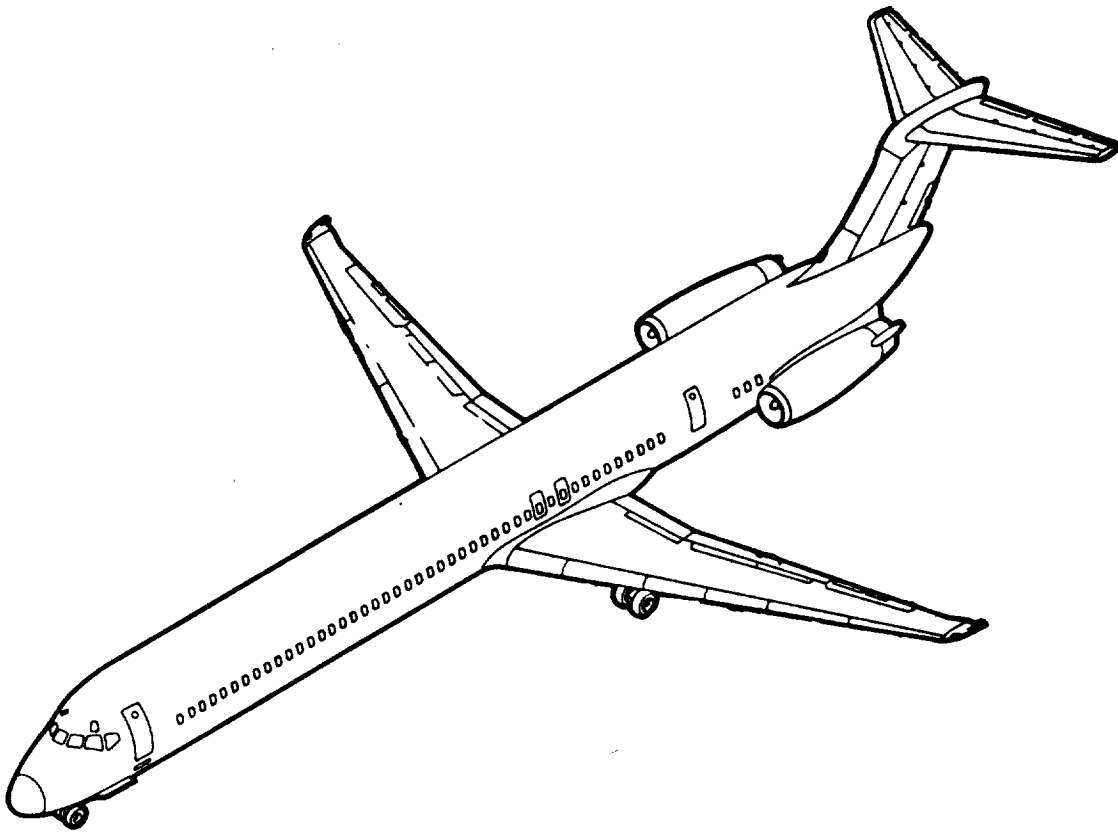


FIGURE 2-1. The MD-80 Aircraft

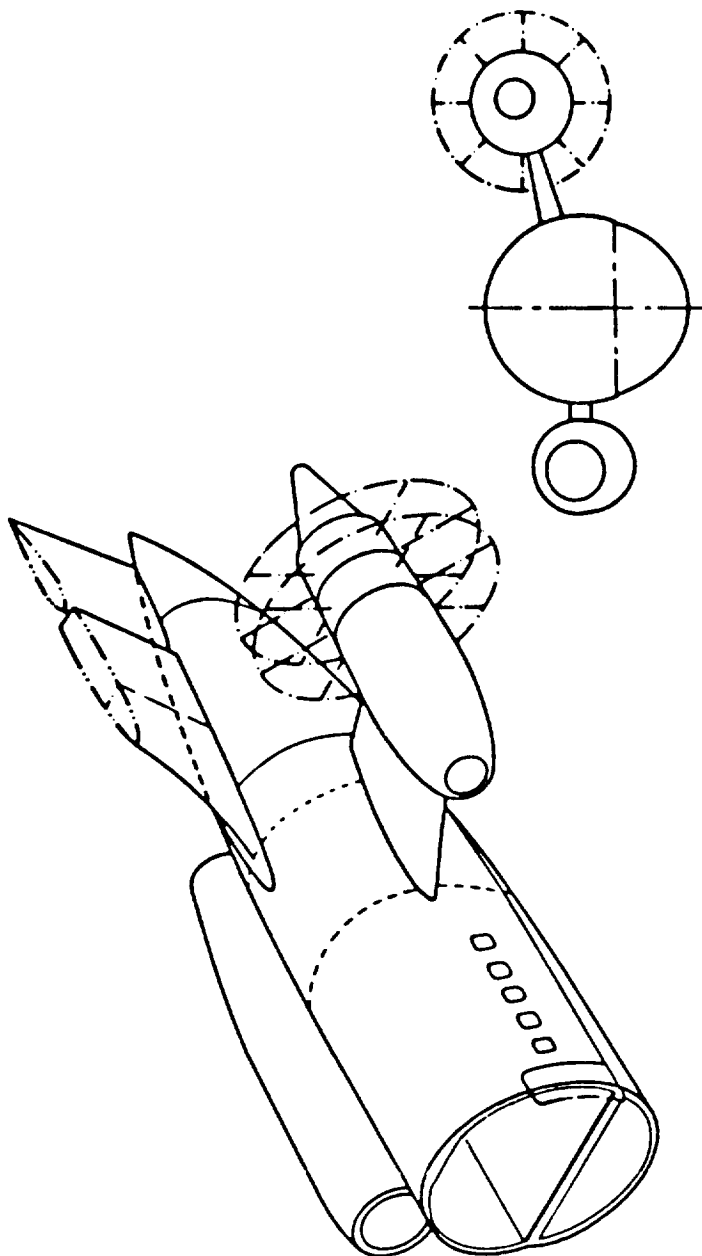


FIGURE 2-2. The UHB Engine and Pylon Installation.



FIGURE 2-3. The Demonstrator in Flight.

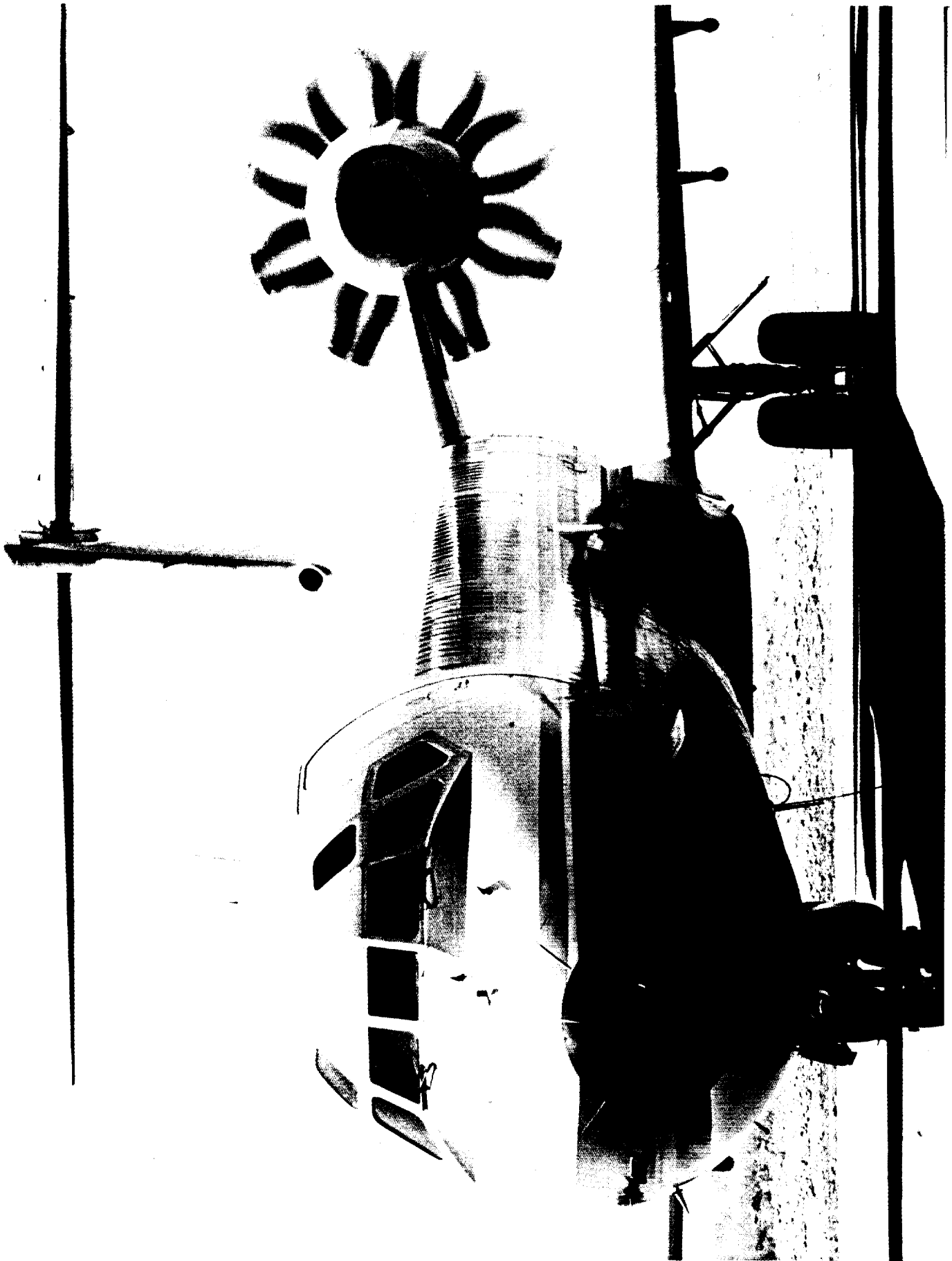


FIGURE 2-4. The Demonstrator on the Ground Showing Counter-Rotating blades.



FIGURE 2-5. View from Under the Demonstrator Showing Relative Positions of the JT8D and UDF Engines and Pylons.



FIGURE 2-6. The Furnished Cabin Showing Selected Microphone Locations.

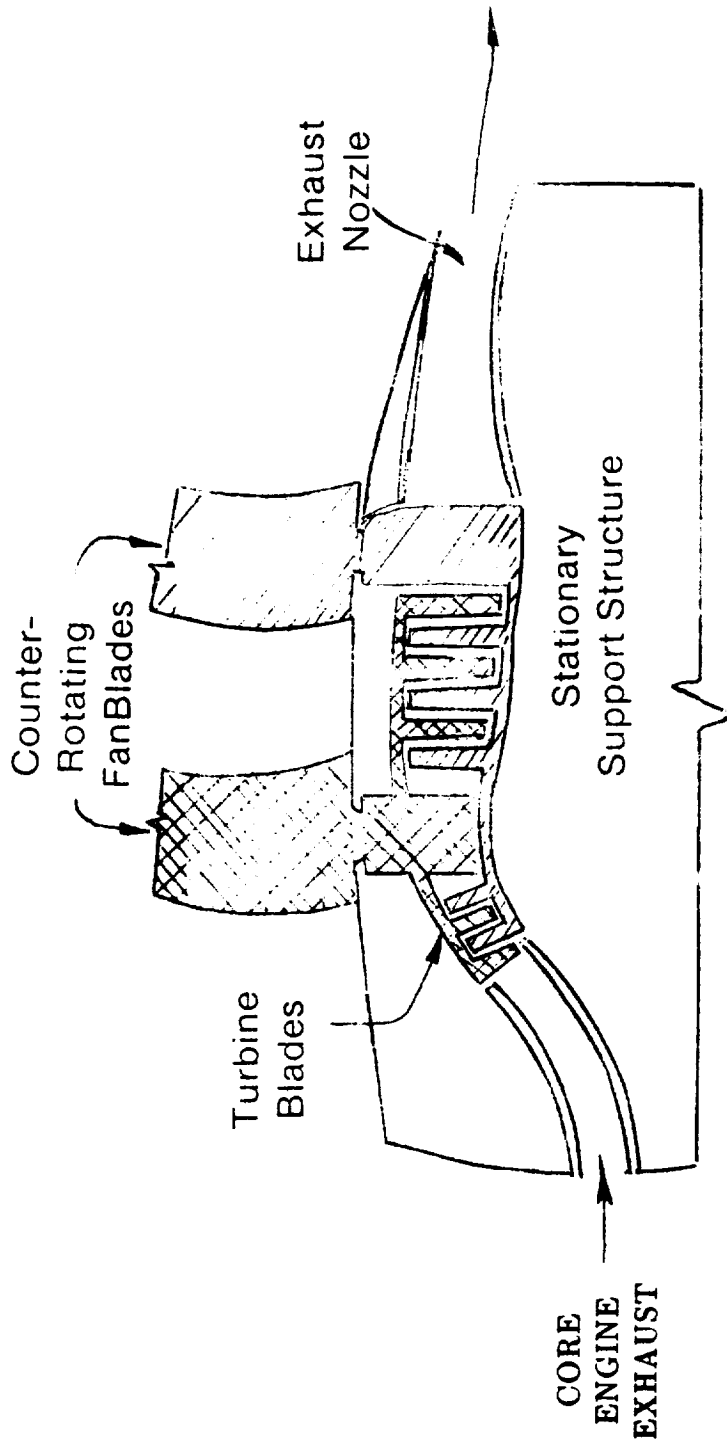


FIGURE 2-7. UDF Propulsor Design Schematic.

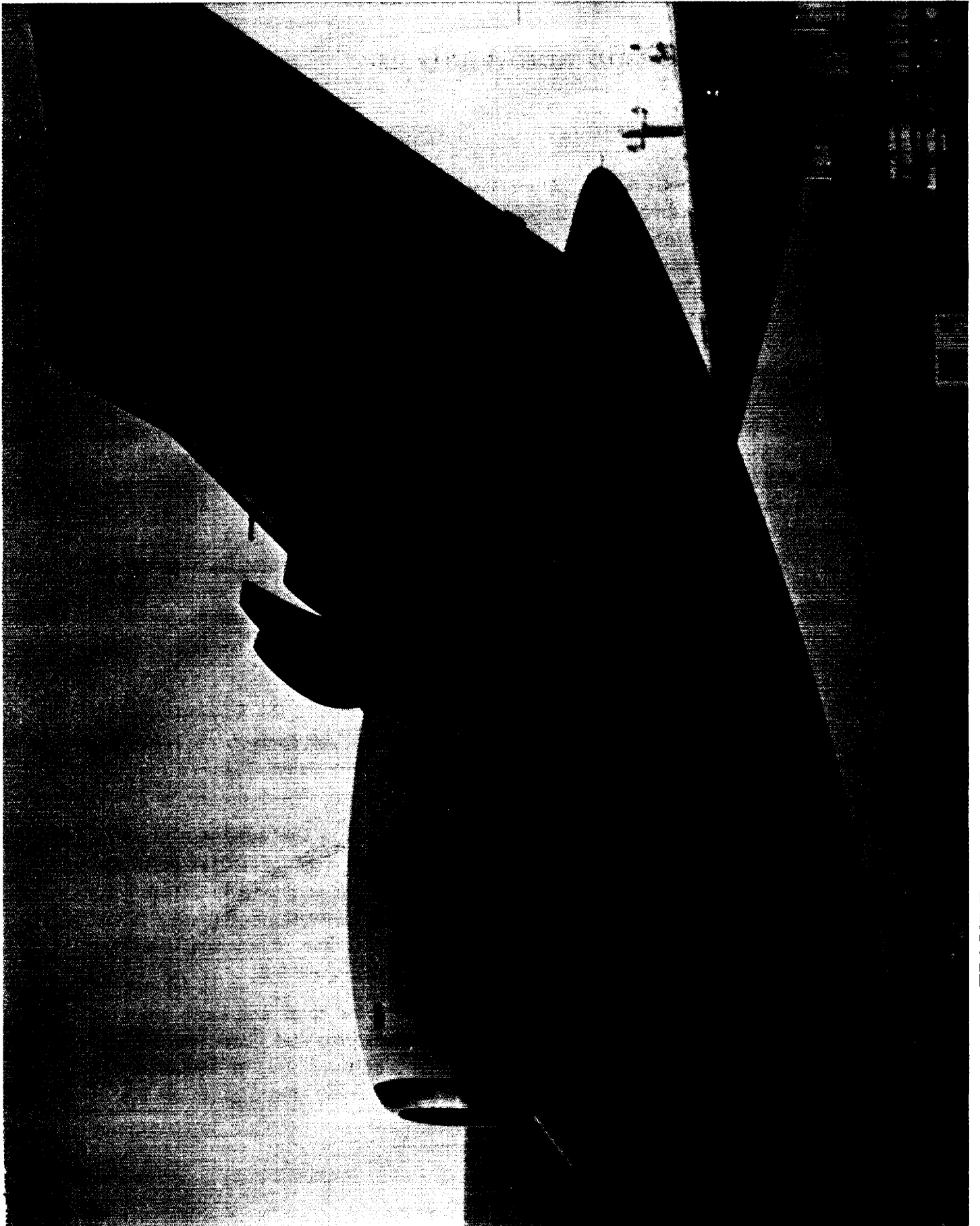


FIGURE 2-8. Close Up View of UDF 10x8 Engine on the Demonstrator.

3 Data Acquisition and Analysis

3.1 Acquisition System

The Demonstrator noise and vibration data were acquired with an airborne digital system capable of recording simultaneously up to 256 channels of digital time series data at a rate of 6400 samples per second, with a dynamic range of 80 dB. Anti-aliasing filters were chosen to provide a useful frequency band of 0 to 2000 Hz. The data were typically acquired over a period of 15 seconds.

3.2 Transducers

Since the overall objectives of the Demonstrator test program addressed many concerns including acoustics, stress, sonic fatigue, and vibration, transducers installed throughout the aircraft consisted of numerous microphones, accelerometers, and strain gauges. Of these, transducers useful for acquiring data for interior noise analysis purposes included selected exterior and interior microphones, and frame, pylon, and bulkhead accelerometers. Microphone and accelerometer measurement locations often changed during the test program, to accommodate the requirements of a specific flight. In the following, the location of all transducers used throughout the test program for interior noise-related measurements are described; transducer locations used for specific test points are defined in subsequent sections.

Exterior microphones on the fuselage surface were located in the forward and aft propeller planes and at several additional points on the fuselage surface. Microphones were also located on the upper and lower surfaces of the UHB pylon. Figure 3-1 shows these exterior microphone locations.

Interior microphones were located in the aft cabin and in the unpressurized section aft of the pressure bulkhead. The cabin microphones were located at positions approximating that of both seated and standing passengers, as shown in Figure 3-2. In each row, microphones at seat positions were 40 inches above the floor, and at aisle positions were 72 inches above the floor on the aircraft centerline. The locations of the microphones in the unpressurized aft section are shown in Figure 3-3.

Accelerometers were located at the forward and aft pylon spars and engine mount points, and on the frame at station 1437 in the forward propeller plane (see Figure 3-4). Accelerometers were also located at several points on the frames at stations 1271 and 1322, and on the aft pressure bulkhead; these locations are shown in Figure 3-5.

3.3 Data Processing and Analysis

Processing of the test data was conducted interactively with specially developed software. Frequency spectra with a bandwidth of 3.125 Hz (or 0.78125 Hz when required for finer resolution) were generated by taking the autospectrum of the time series data.

The measured spectra are typically characterized by several tones superimposed on a broadband background, as shown in the sample interior noise spectrum in Figure 3-6. The frequencies of the observed tones are related to the shaft rotational speeds of the two engines and to the blade passage frequencies associated with the two propeller rotors, plus harmonics of these various frequencies.

The rotating machinery in the engines of the Demonstrator aircraft generate tones at several frequencies. The Pratt & Whitney JT8D-209 is a dual-rotor turbofan and generates tones at two primary frequencies. The first is associated with the rotational speed (N1) of the low pressure stage and the second with the rotational speed (N2) of the high pressure stage of the engine. In this report these two frequencies are designated as JN1 and JN2, respectively. Similarly, tones are generated at frequencies associated with the rotational speeds of the low and high pressure stages of the UDF engine, and herein are designated as UN1 and UN2, respectively. In addition, tones are generated at the frequency associated with the rotational speed of the rotor shaft of each propeller. This frequency is usually referred to as the 1p frequency of the propeller; in this report the shaft speeds of the two rotors are nominally the same, so that only one 1p tone occurs.

Tones at the blade passage frequency (BPF) and harmonics are generated by each propeller. For the 8x8 engine configuration, each eight-bladed rotor generates a tone at a BPF corresponding to a frequency eight times that of the 1p frequency. Harmonics are labelled as 2BPF, 3BPF, etc. The spectrum shown in Figure 3-6 clearly exhibits the BPF and 2BPF tones. For the 10x8 engine configuration the forward ten-bladed rotor generates a tone at a BPF corresponding to ten times that of the 1p frequency, while the BPF tone from the aft eight-bladed rotor is at the same frequency (eight times 1p) as for the 8x8 configuration. To distinguish the two 10x8 blade passage frequencies, in this report they are designated as BPF(10) and BPF(8).

3.4 Sound Intensity Measurements

In addition to the digital noise and vibration data acquired routinely throughout the flight tests, a sound intensity survey was conducted during a dedicated flight (flight 2026).

For this test, the cabin sidewalls, ceiling, floor, right and left engine pylon bulkheads

and aft pressure bulkhead were divided into survey areas. Figure 3-7 shows the extent of the survey, and Figure 3-8 defines the actual grid locations on each surface. The typical grid area is approximately 7 to 8 square feet.

The sound intensity survey was conducted using Norwegian Electronics Model 216 Sound Intensity Probes. These probes utilize a single microphone to measure sound pressure, and an ultrasonic transducer to measure particle velocity. Each area was scanned approximately four inches away from the surveyed surface. Norwegian Electronics Model 830 Real Time Analyzers collected and processed the data to yield one-third octave band sound intensity levels, from which one-third octave band sound power levels were computed.

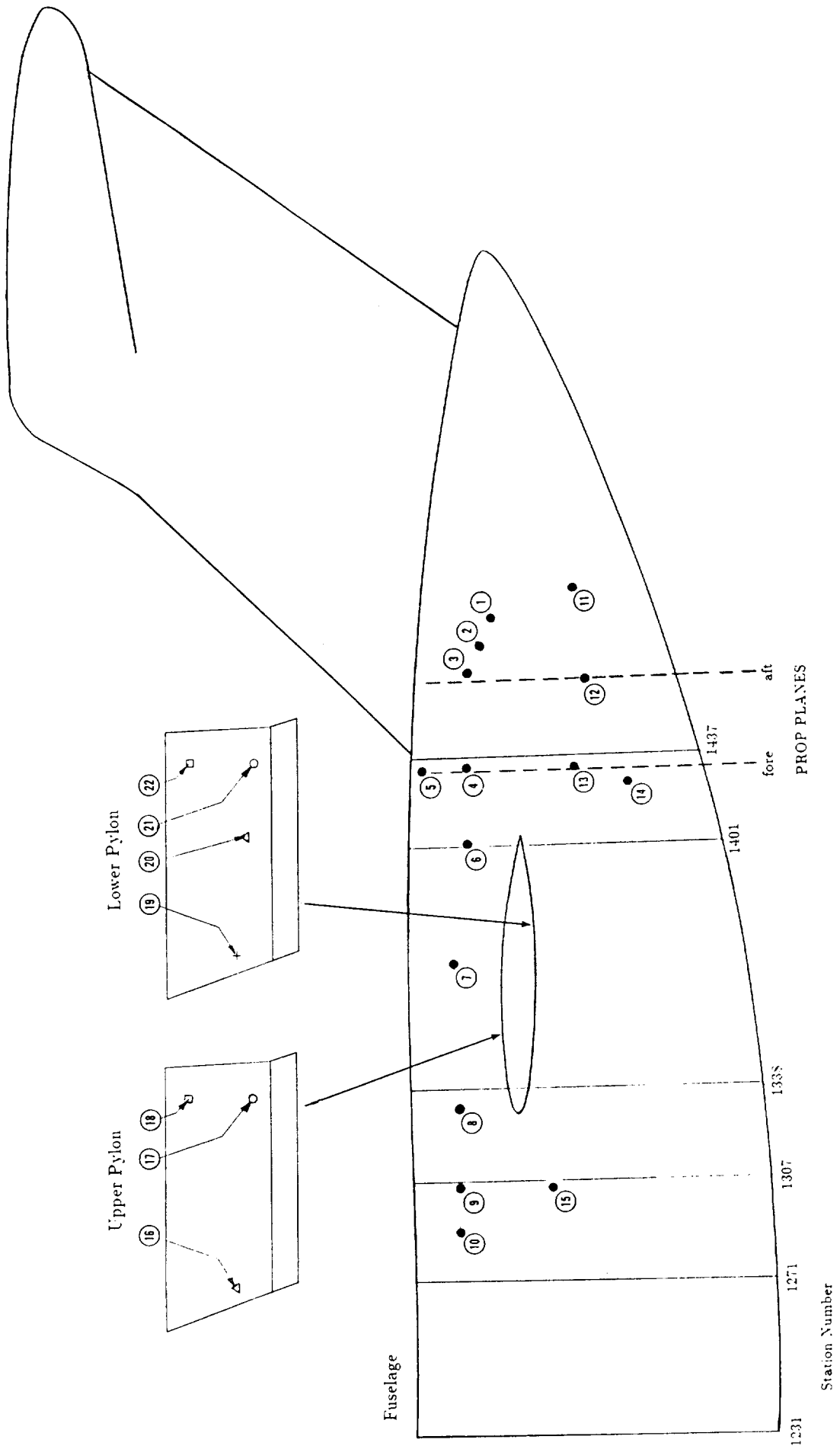


FIGURE 3-1. Exterior Microphone Locations on Fuselage and Pylon.

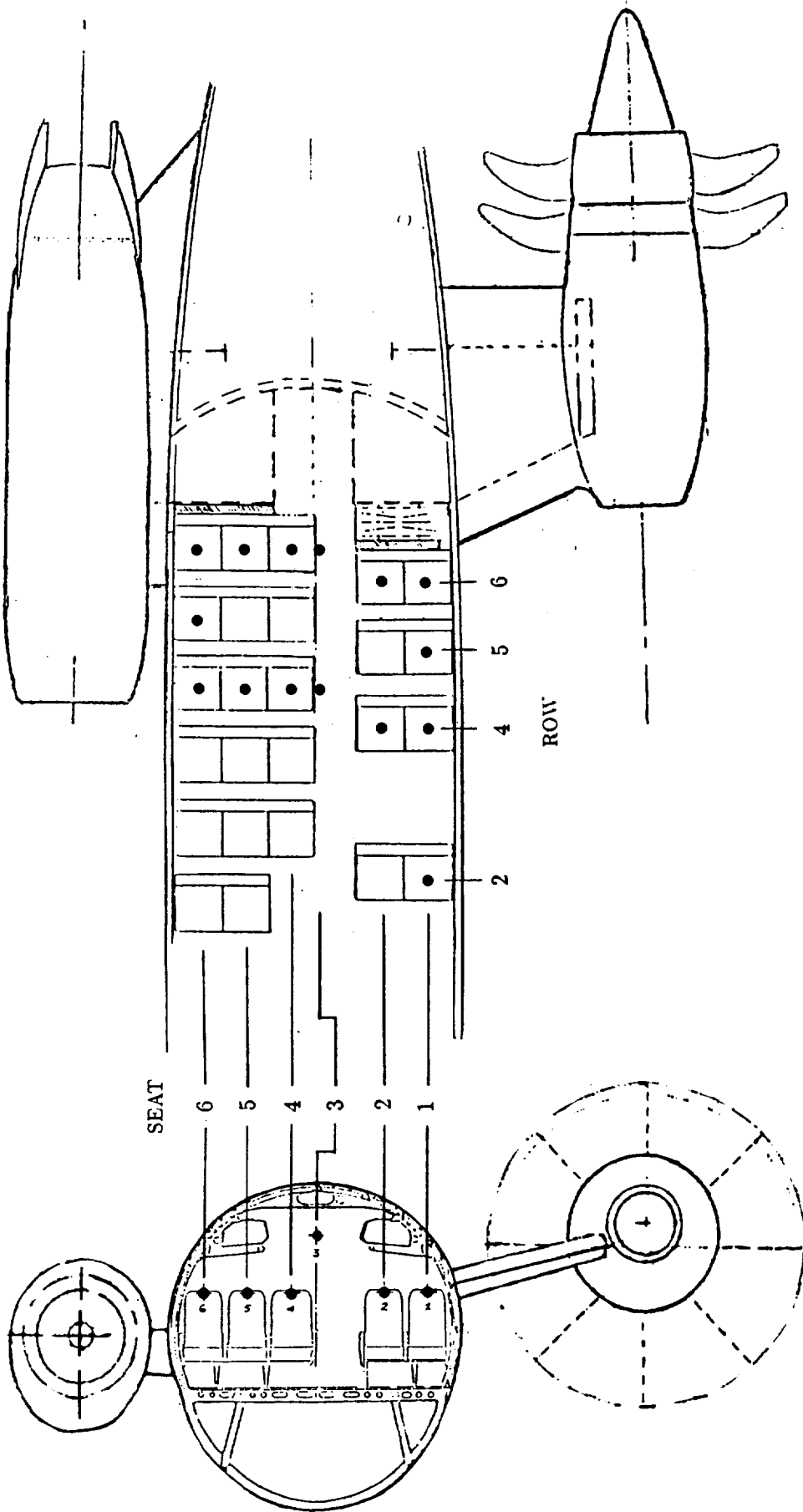


FIGURE 3-2. Cabin Microphone Locations.

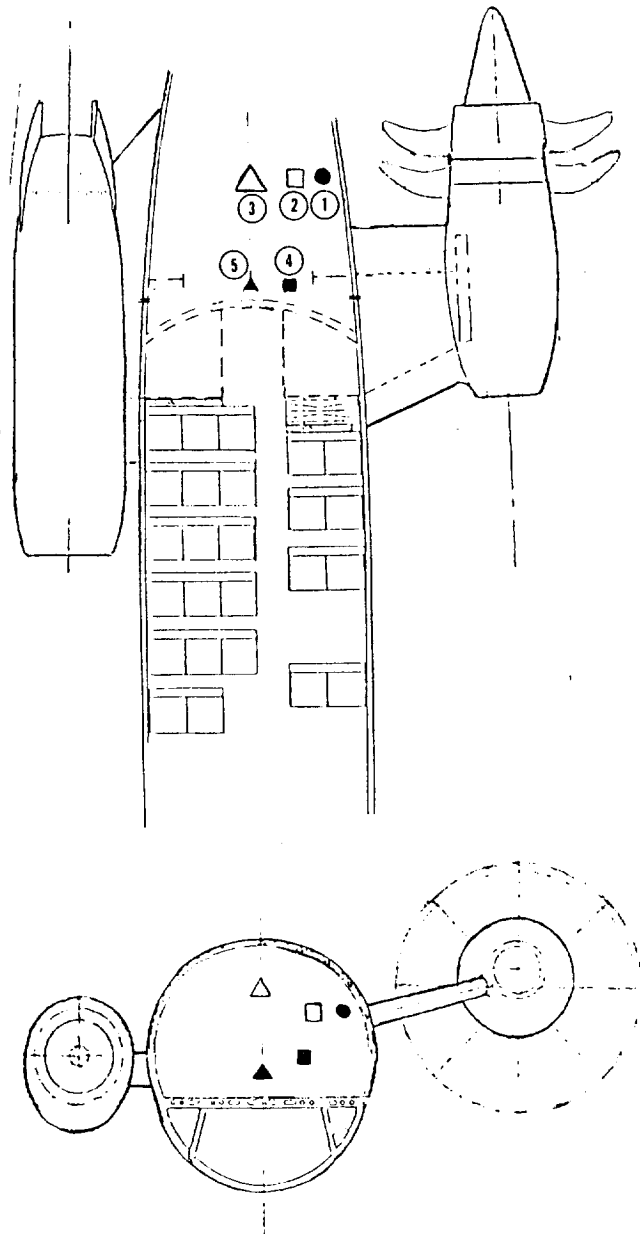
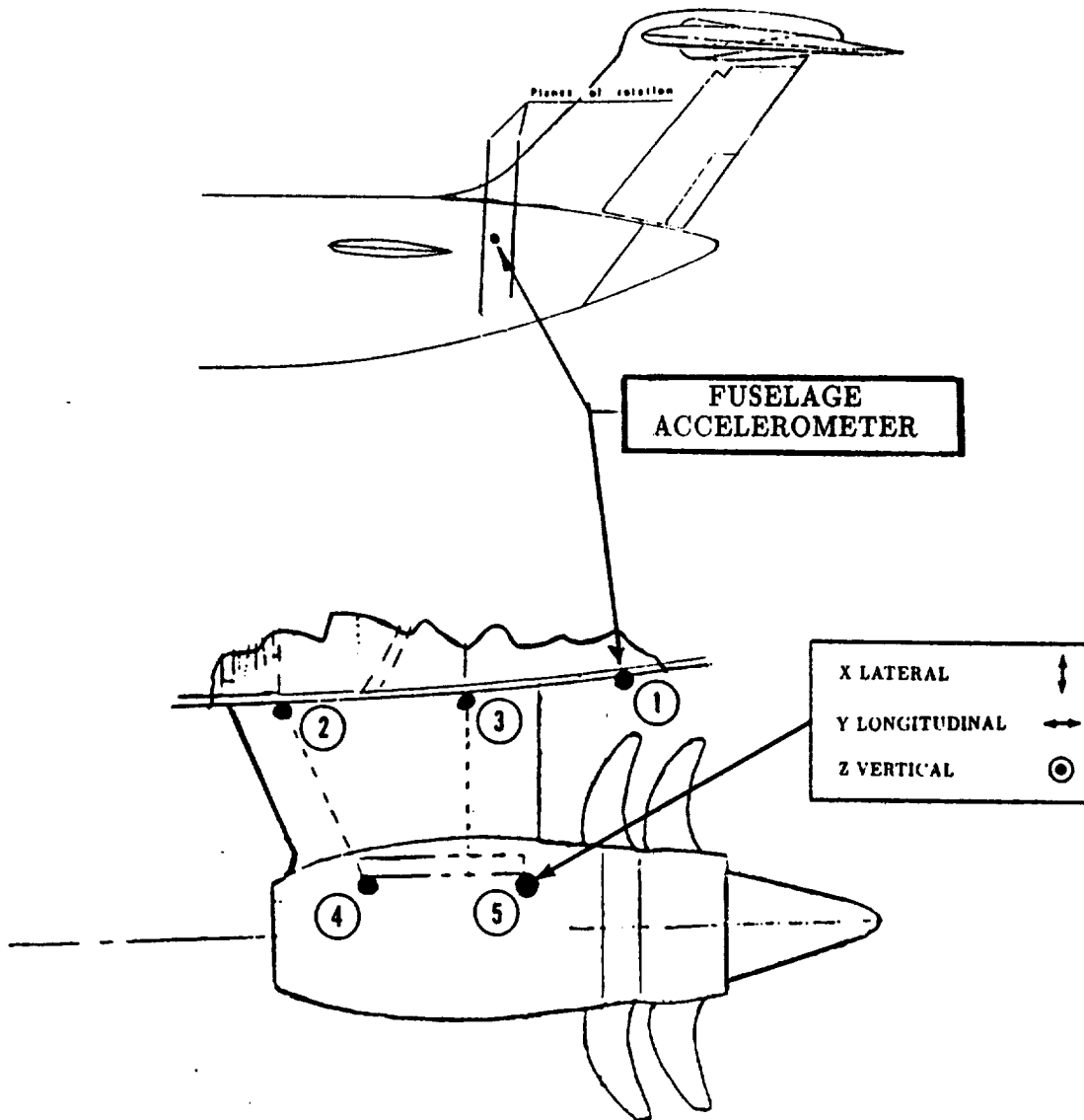


FIGURE 3-3. Aft Section Microphone Locations.



ACCELEROMETER DESCRIPTION

ACCEL#	LOCATION	DIRECTION
1	aft fuselage	radial
2	fwd. pylon spar	vertical
3	aft pylon spar	vertical
4	fwd. engine mount	vertical
5-X	aft engine mount	lateral
5-Y		longitudinal
5-Z		vertical

FIGURE 3-4. Location of Pylon and Fuselage Accelerometers.

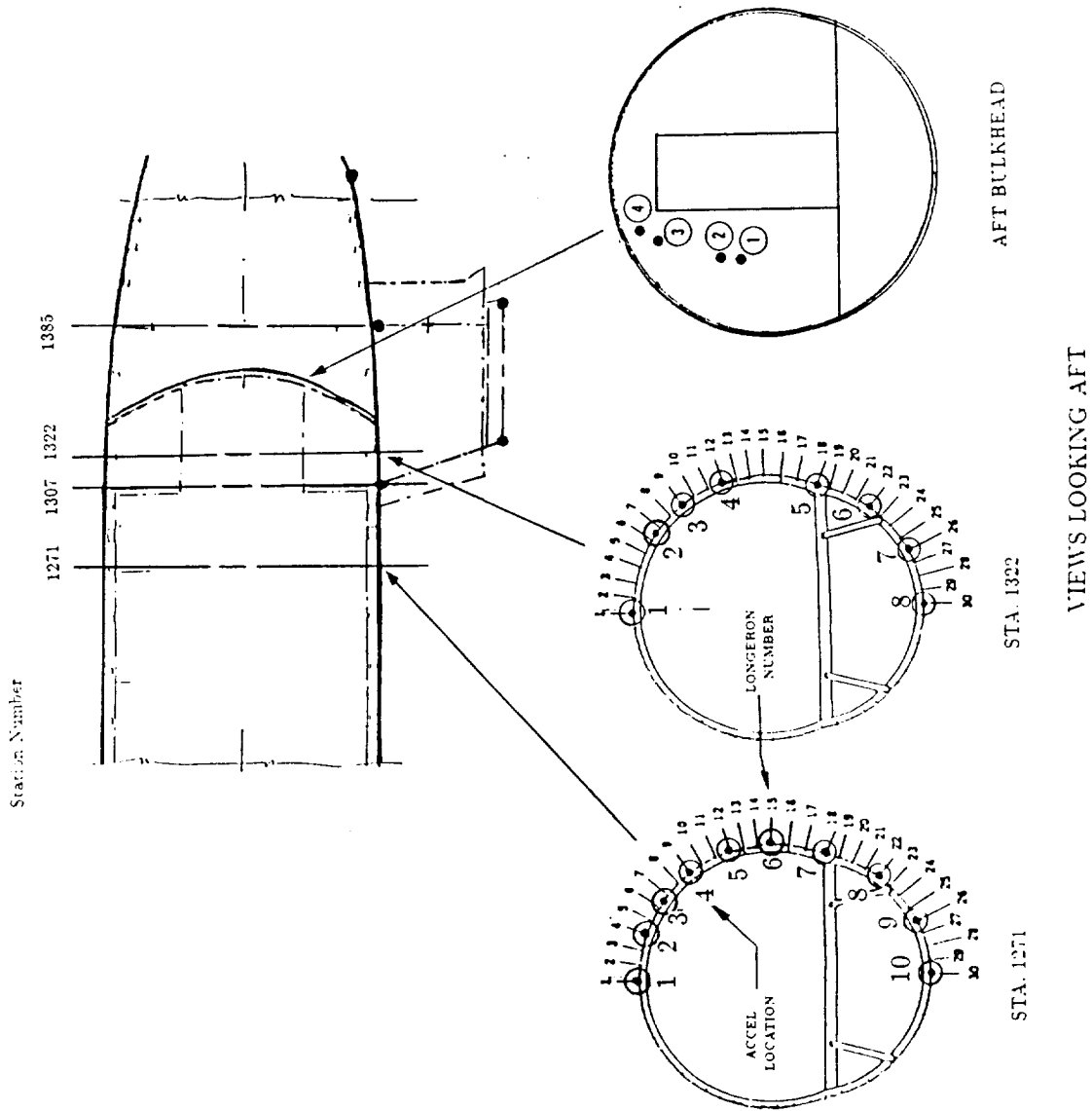


FIGURE 3-5. Location of Station 1271, Station 1322 and Aft Bulkhead Accelerometers.

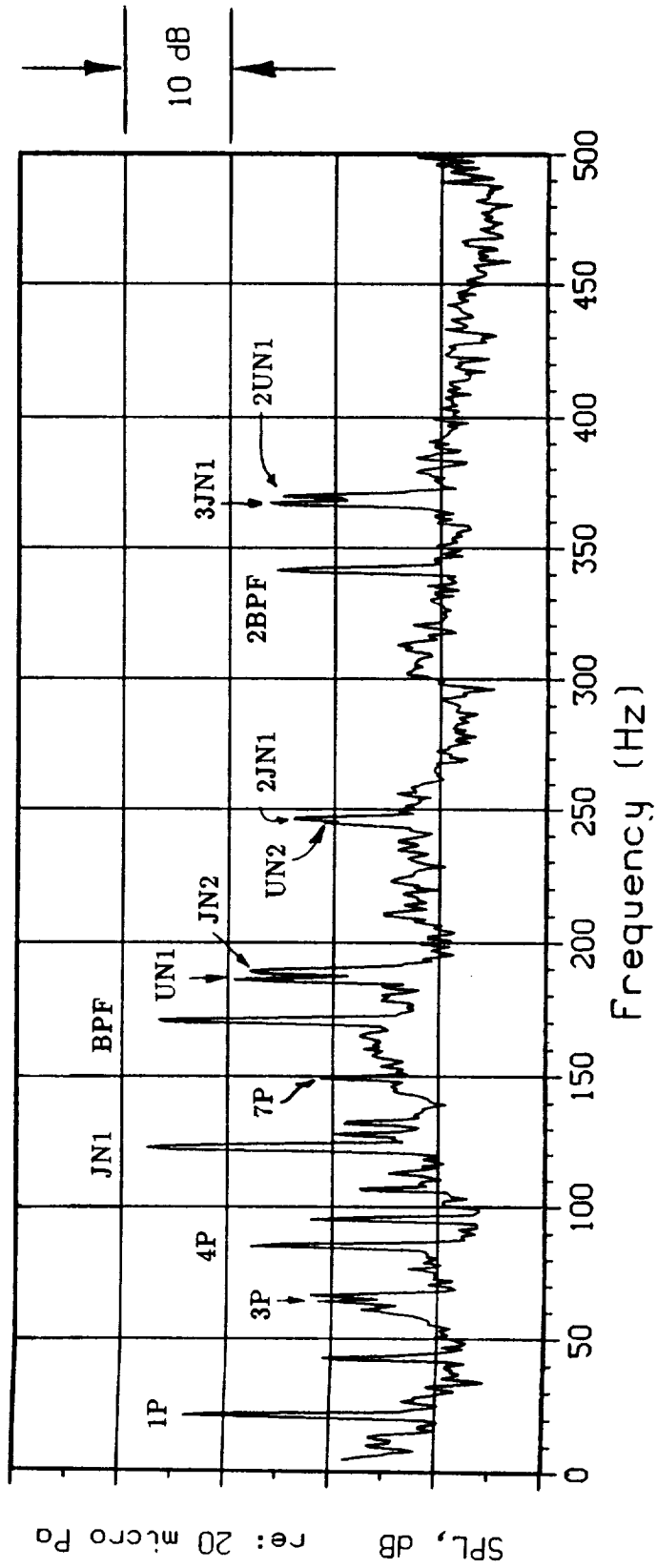


FIGURE 3-6. A Typical Interior Cabin Seat Microphone Spectrum.

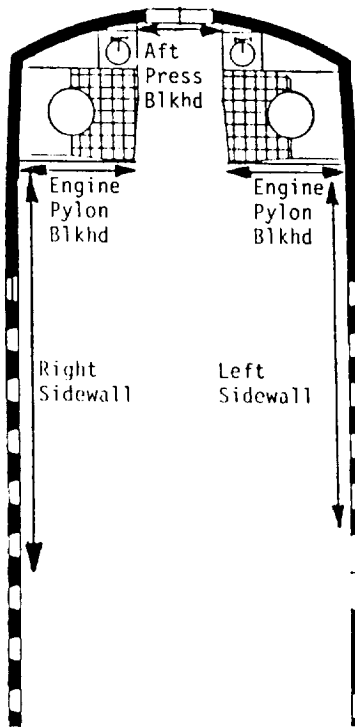
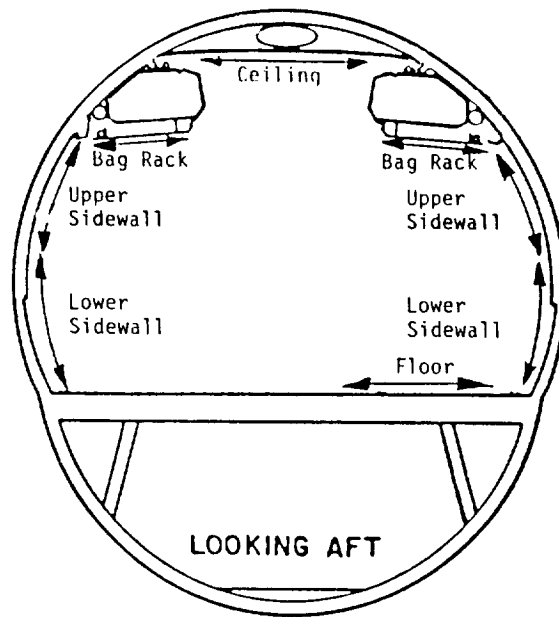


FIGURE 3-7. Sound Intensity Survey Areas.

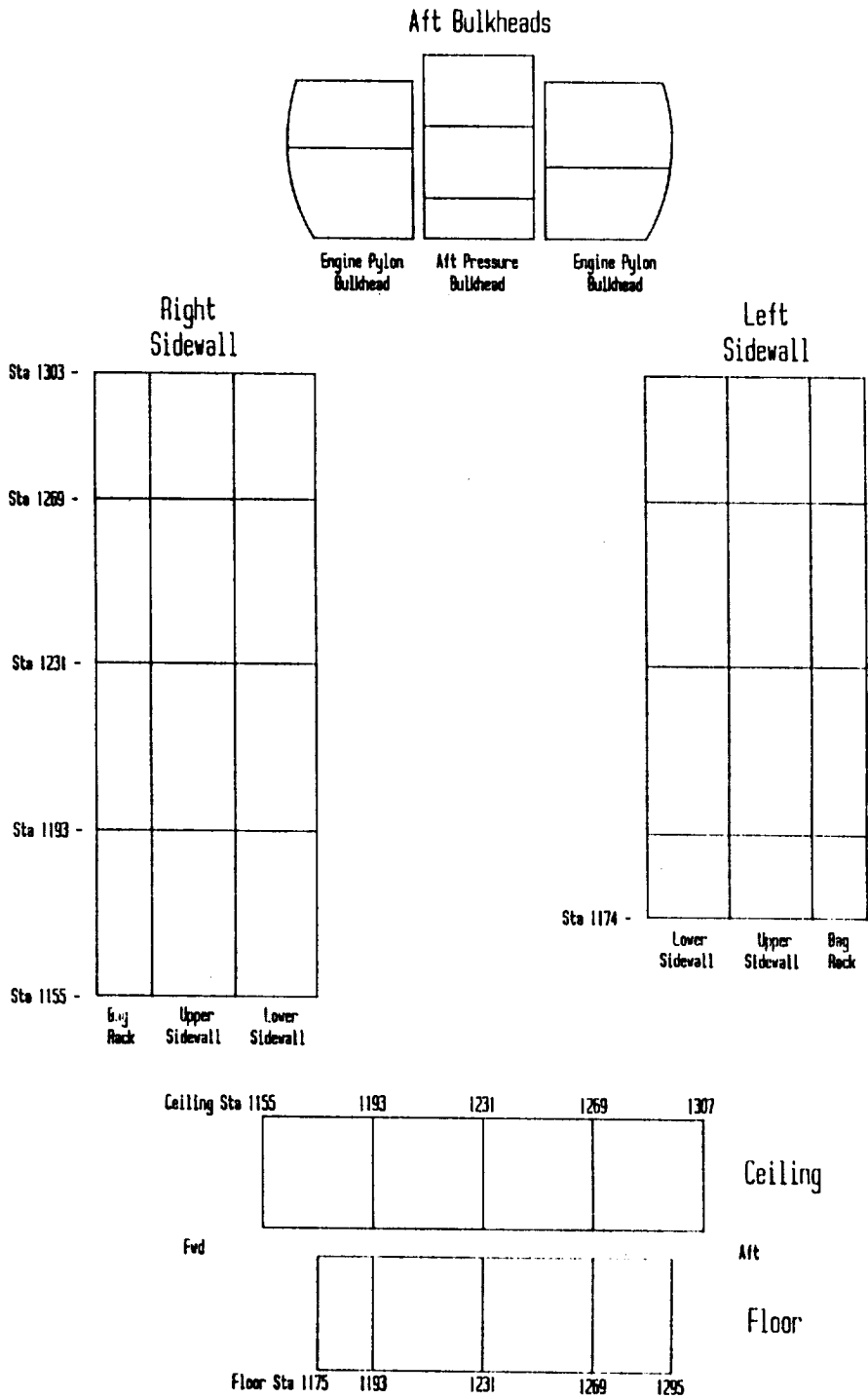


FIGURE 3-8. Location of Survey Grids.

4 Evaluation of Treatment Effectiveness

In order to achieve the UHB Demonstrator's interior noise goal of 82 dBA or less at any seat location during normal cruise conditions, several noise reduction treatments were designed and installed on the aircraft. These treatments were selected to control noise propagation along three potential paths (see Figure 4-1): an airborne path through the cabin sidewall, an airborne path into the unpressurized aft section and then through the pressure bulkhead, and a structural path through the engine pylon and into the fuselage structure. All treatments complied with FAA FAR 25 regulations and did not alter the standard dimensions and layout of the cabin.

The original plan for treatment evaluation was to install selected treatments or sets of treatments in phases, so that the effectiveness of each installation could be measured. However, this approach was constrained by the extensive time required for aircraft modifications associated with several of the treatments, and the limited number of flights available for interior noise tests. As a result, a number of treatments were installed at the same time, and comprised the "Baseline" configuration (i.e., the cabin configuration for the first interior noise test flight). Additional treatments were subsequently added, up to the fully configured Quiet Cabin, when the goal level of 82 dBA was achieved. Selected treatments believed to have little effect on cabin noise levels (based on prior flight and ground tests) were removed for later flights in an attempt to maintain the low noise level while reducing treatment weight.

In this section, treatment effectiveness is evaluated based on analysis of changes in cabin noise levels after each treatment is installed. In section 5, a detailed analysis of exterior and interior levels measured for the Quiet Cabin configuration is presented. Some of the Quiet Cabin results are used in this section to identify the major test parameters to be studied in this evaluation.

4.1 Description of Treatments

Table 4-1 lists the flight tests during which interior noise data were collected for the 8x8 UDF engine configuration, along with the interior noise treatment configuration number and a list of the treatments included. Each treatment is described below.

4.1.1 Torque Box (Structural Path)

The torque box is a device designed to greatly increase the stiffness of an existing frame, particularly to torsional motion. It consists of a new frame installed approximately four inches from an existing frame (located at station 1287), with a cover plate

over both frames (see Figure 4-2).

4.1.2 Additional Frames (Structural Path)

Four additional frames, identical to current production frames, were installed midway between existing frames in the aft cabin area. Figure 4-3 shows the locations and station numbers. The purpose of these frames is to provide additional sidewall stiffness.

4.1.3 Frame Damping (Structural Path)

Damping material was applied to the new frames, and to several existing frames to reduce structural vibration. Figure 4-3 illustrates the method of installation and the locations of the treated frames.

4.1.4 Pressure Bulkhead Double Wall (Aft Section Path)

To reduce sound transmission from the aft unpressurized fuselage section into the cabin, a double wall was constructed of 0.063 inch aluminum, and installed approximately three inches forward of the aft pressure bulkhead. The configuration also includes damping material applied to the pressure bulkhead, and isolator mounts to attach the double wall to the fuselage structure. See Figure 4-4 for details.

4.1.5 Sonic Fatigue Damping (Structural, Cabin Sidewall, and Aft Section Paths)

A damping treatment was used to reduce sonic fatigue of the fuselage skin in the vicinity of the propeller planes where high acoustic loads were expected. Since this treatment affects noise transmission into the aft section and structureborne noise propagation into the cabin, it is listed as a noise treatment. The damping material was installed on the skin between the frames and longerons, starting in the aft section at station 1510, through the passenger cabin to station 1174. The treatment is distributed on the skin from the bottom of the fuselage, extending across the UDF side, and ending at a point 30° from the top of the aircraft on the JT8D side (see Figure 4-5).

4.1.6 Cabin and Cargo Skin Damping (Structural and Cabin Sidewall Paths)

A second damping treatment was applied on all skin panels throughout the passenger cabin and the cargo compartment from stations 1098 to 1338. The treatment extended around the entire circumference of the fuselage. This treatment was added over the areas where sonic fatigue damping material was already applied.

4.1.7 Floor Isolation (Structural Path)

Floor panels from stations 1090 to 1350 were installed on isolation mounts. The isolator damping material was the same as used on the fuselage frames.

4.1.8 Aft Section Absorption (Aft Section Path)

To absorb low frequency noise in the aft, unpressurized section, 2.0 inch thick quilted fiberglass insulation blankets were installed over the pressure bulkhead and over the ventral stair cage.

4.1.9 Torque Box Damping (Structural Path)

Tests of the effectiveness of the torque box in Douglas' fuselage ground test facility indicated that this treatment could increase, rather than decrease, cabin noise levels. In an attempt to correct this situation, a damping treatment was applied to the cover plate of the torque box. The installation was similar to the damping installation used on the additional frames (see Section 4.1.3 above).

4.1.10 Engine Dynamic Absorbers (Structural Path)

Three tuned absorbers (see Figure 4-6) were added to the rear engine mounts to reduce structureborne noise, and in particular pylon vibration transmissibility. The absorbers were tuned to the nominal cruise operation blade passage frequency (168 Hz).

4.1.11 Trim Panel Damping (Cabin Sidewall Path)

From station 1098 to station 1303, damping material was applied to the trim panels within the sidewall cavity, in order to reduce panel resonant response and increase mass

density.

4.2 Selection of Test Points

To evaluate the effectiveness of the interior noise treatments, data acquired during several flights were compared. A total of seven configurations were investigated during seven different flights. To ensure the validity of this analysis, test data were selected to correspond to flight conditions with nearly identical characteristics (pressure altitude, airspeed and rotor rpm). Table 4-2 summarizes the available test points and highlights those chosen for this study.

4.3 Acoustic and Vibratory Loads

4.3.1 Exterior Noise Levels

Analysis of the Quiet Cabin data shows, among other characteristics, that :

- The propeller blade passage frequency (BPF) is the dominant propeller noise contributor to the interior noise.
- Exterior BPF levels are highest in the two prop planes, then decrease rapidly with distance forward of the prop planes.
- The boundary layer noise is a significant contributor to the interior noise, and is transmitted through the fuselage sidewall.

To accurately study treatment effectiveness using interior noise data acquired during multiple flights, it is therefore important to verify that exterior levels for the BPF tones and the boundary layer are essentially constant from flight to flight.

Figure 4-7 presents BPF tone levels measured on the fuselage surface. It can be observed that in the prop planes, the variability of the BPF tone level among the several flights is small (2 to 3 dB). The distribution of BPF levels along the fuselage is very consistent from flight to flight, showing acceptably small variations in level at each location.

Concerning boundary layer noise, Figure 4-8 presents the A-weighted broadband noise levels measured at various exterior locations along the cabin sidewall for each configuration. Again the measured levels are nearly identical from flight to flight.

4.3.2 Pylon Vibration Levels

Vibration data measured on the pylon spars show the presence of strong tones at the UN1 frequency as well as at the propeller BPF and 2BPF. Since a structureborne path along the pylon could be a contributor to the interior noise levels for these tones, it is important to also verify the consistency of the vibration data for all flights.

Figure 4-9 presents the BPF, 2BPF, and UN1 vibration levels for each configuration as measured on the inboard side of the forward pylon spar and aft pylon spar. It is readily observed that the vibration amplitudes did not vary significantly from flight to flight.

4.4 Cabin Noise and Vibration Levels

Noise levels were monitored in the cabin in seat row 6 for all seven test points, permitting a comparison of levels at identical locations for all treatment configurations. (Measurements were also obtained in either seat row 4 or seat row 5, depending on flight; these data are not included below because of the inconsistent locations.) Figure 4-10 presents the maximum overall A-weighted levels measured among the five seat locations in seat row 6 for each configuration, and the corresponding tone and broadband component levels. (The tone component is determined by summation of the various contributing tones; the broadband component is determined by subtracting the tone component from the overall.) The following observations can be drawn from this figure:

- Treatment configurations 2 (torque box damping) and 3 (engine dynamic absorbers) have a negligible effect on the maximum interior noise level,
- Treatment configuration 4 (cabin furnishings with damped trim panels) reduces that level significantly, and
- Treatment configurations 5, 6, and 7 (removal of treatments previous to configuration 4) have negligible effect on interior noise levels.

Figure 4-11 similarly presents the maximum A-weighted tone levels in seat row six observed for each configuration, at the BPF, 2BPF, UN1, and JN1 frequencies (all of which contribute to interior noise levels.) For the BPF, 2BPF, and JN1 tones, the same general observations can be made from the figure as from Figure 4-10, except for the increase in 2BPF levels for configurations 6 and 7 (which may indicate the contribution of the aft section path for this frequency when treatment is removed; see section 8.2). For the UN1 tone, the variation in level does not follow the same trends (but rather varies with nearby frame acceleration, see below).

The noise variation with cabin configuration is further investigated in Figures 4-12a, b, c, and d for selected seat locations in row 6. Again, the A-weighted overall sound levels as well as tone and broadband components are presented. An immediately recognizable trend is the noise reduction caused by the addition of the trim panels and furnishings (configuration 4), and the typically negligible change in level for the other configurations. The tone summation at the window seat on the UDF side (Figure 4-12d) does not however conform to this trend and exhibits only small changes in level among all configurations; this behavior may be the result of the modal characteristics of the cabin. Although the relative levels of the tone and broadband components vary from seat to seat, it is noted that the broadband contribution is always equal to or greater than the tone summation.

The interior noise spectra corresponding to the data in Figure 4-10 are presented in Figures 4-13 and 4-14. Figure 4-13 presents the spectra for configurations 1 through 3. The spectra for the Quiet Cabin and successive configurations (4 through 7) are shown in Figure 4-14. In Figure 4-13, the BPF tone levels at 168 Hz for all three configurations are between 90 and 95 dB. Figure 4-14 data show BPF levels between 85 and 90 dB. Similarly the broadband levels were reduced by 5 to 10 dB after installation of configuration 4. In general the spectral characteristics are similar among the three spectra in Figure 4-13; among the four spectra in Figure 4-14 the spectral characteristics are also generally similar.

Figures 4-15a, b, and c are plots of acceleration versus configuration for selected accelerometers placed on frame 1271. BPF, 2BPF, and UN1 tone levels are presented as they are the predominant tones observed on this frame. The BPF tone levels appear to vary randomly with configuration while the 2BPF tone levels remain relatively flat. No specific trends with treatment configuration can be identified for these two frequencies. For UN1 tones, a possible effect of the engine dynamic absorbers on the acceleration levels can be seen (levels generally decrease when absorbers are installed and increase when absorbers are removed at two of the three measurement locations). However, since the absorbers are tuned to 168 Hz and UN1 is 185 Hz, it is likely that the observed variation in acceleration level is unrelated to this treatment.

The acceleration of this frame at BPF and 2BPF appears unrelated to cabin noise levels, however the frame acceleration and cabin noise levels at UN1 show similar variations with configuration (see Figures 4-11 and 4-15a, c).

TABLE 4-1 UHB Demonstrator Interior Treatment Configurations.

Flight No.	Configuration No.	Treatment Description
1951	1 (Baseline)	Torque Box Additional Frames Frame Damping Double Wall Bulkhead Sonic Fatigue Damping Cabin Skin Damping Cargo Skin Damping Floor Isolation Aft Section Absorption (Cabin Unfurnished, with sidewall thermal insulation but without trim panels)
1952	2	# 1 plus: Torque Box Damping
1953	3	# 2 plus: Engine Dynamic Absorbers
1955	4 (Quiet Cabin)	# 3 plus: Cabin Furnishings Trim Panels Trim Panel Damping
2016	5	# 4 less: Engine Dynamic Absorbers
2034	6	# 5 less: Aft Section Absorption Cargo Skin Damping
2035	7	# 6 less: Double Wall Bulkhead (section over pressure bulkhead door)

TABLE 4-2

Test Point Summary for Interior Treatment Evaluation.

Run Number	Config. Num.	N3/N4 Rotor Speed (rpm)									
		1170	1200	1225	1245	1250	1255	1260	1265	1270	1280
19510001	1										•
2									•		
3								☉			
4							•				
19520A01	2									•	
2										•	
3								☉			
4							•				
(split)5		•									•
19530A01	3									•	
2								•			
3							•				
4					•						
5										•	
6								☉			
7							•				
8					•						
19550A01	4									•	•
2								☉			
3											
4							•				
5					•						
6			•								
7		•									
20160H01	5										
2							•	☉			
5						•					
6					•						
20340K01	6							☉			
20350O01	7								☉		

• Available Test Points

☉ Test Points Selected for Treatment Effectiveness Study

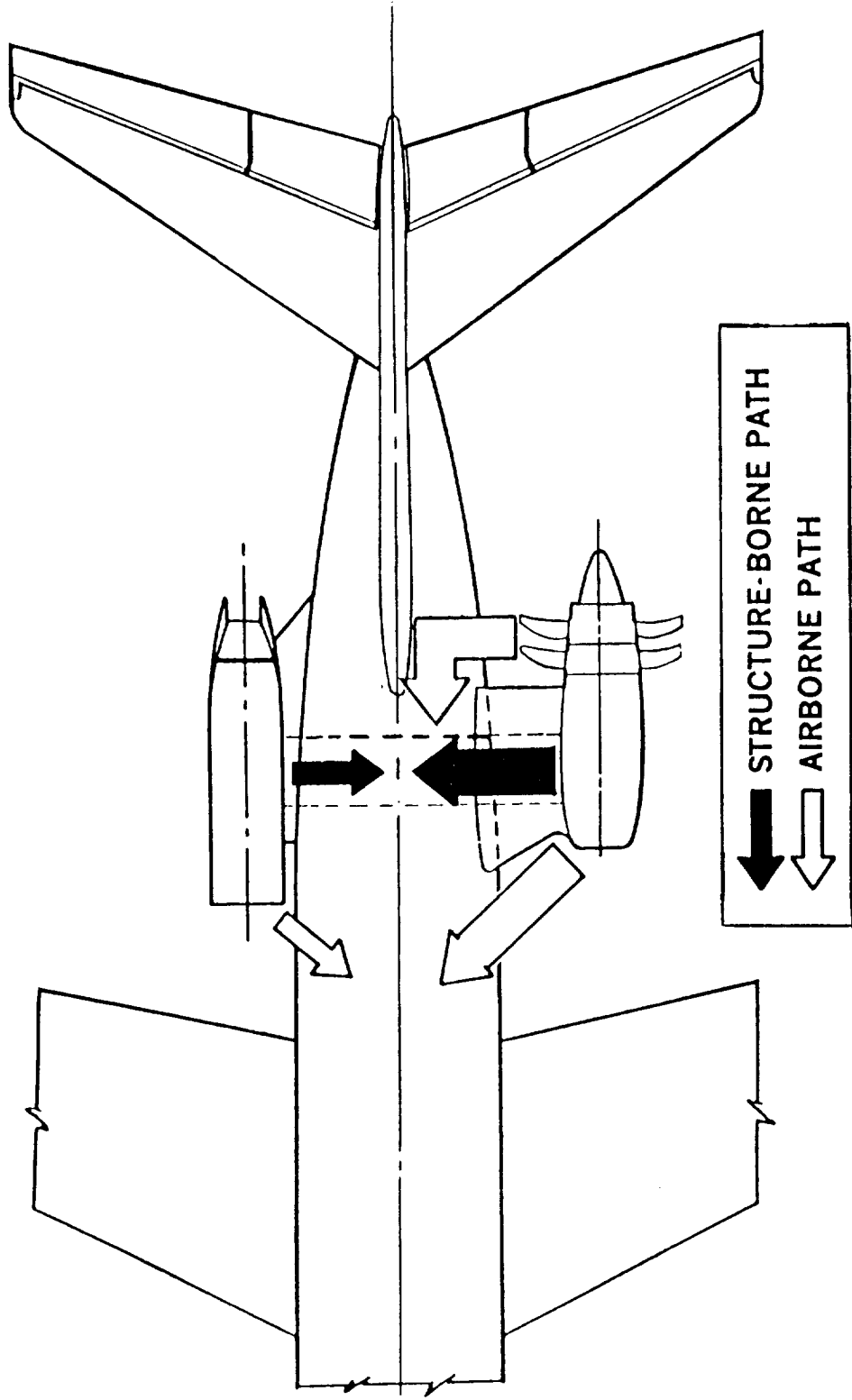
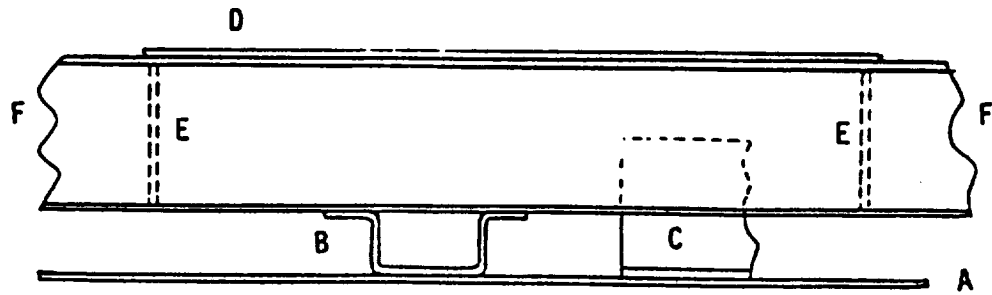
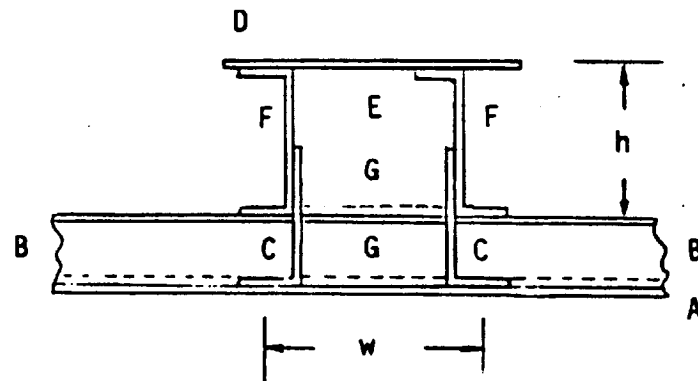


FIGURE 4-1. Predicted Noise Transmission Paths for the MD-UHB Demonstrator.



LONGERON CROSS-SECTION

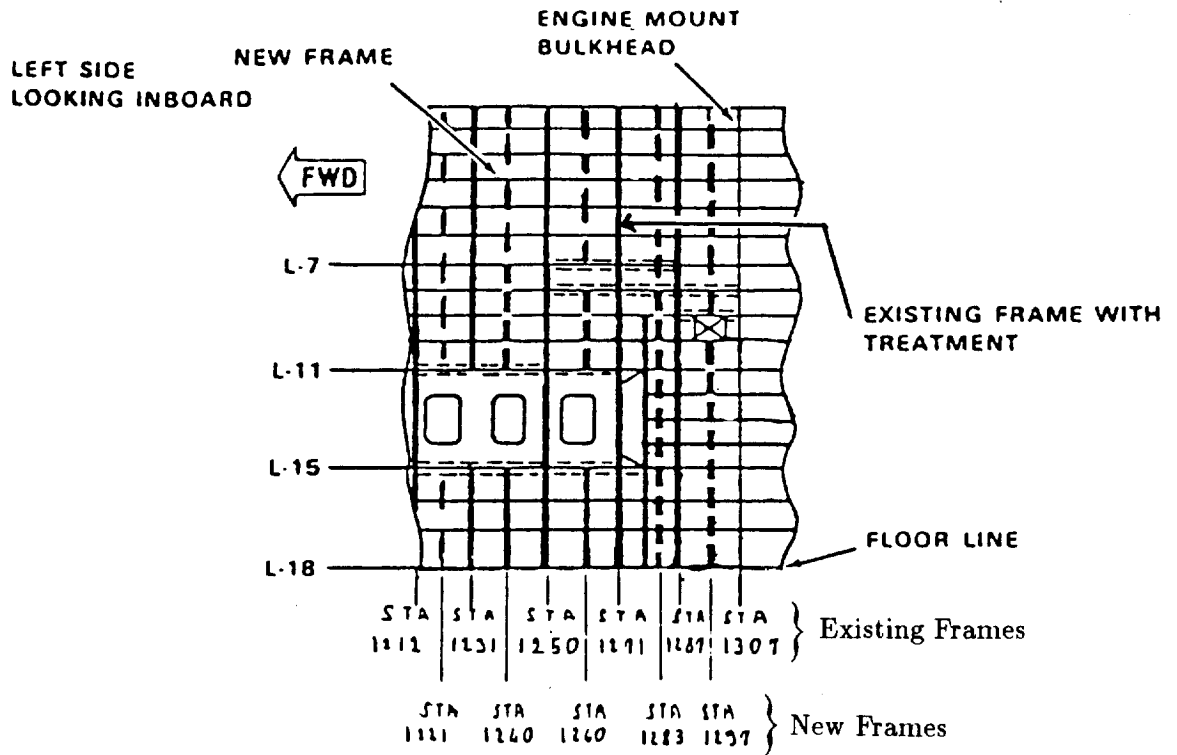


FRAME CROSS-SECTION

- A - SKIN
- B - LONGERON
- C - CLIP ANGLES OF TORSIONAL RING FRAME TO SKIN BETWEEN LONGERONS
- D - COVER PLATE OF TORQUE BOX (LIGHTENING HOLES CIRCUMFERENTIALLY)
- E - WEB STIFFENERS TO PREVENT BUCKLING
- F - FRAME CHANNELS
- G - DAMPING MATERIAL - ON SKIN BETWEEN LONGERONS
- ON LONGERONS BETWEEN RING CHANNEL

FIGURE 4-2. Torque Box Design.

SIDEWALL STIFFNESS/DAMPING MOD



TREATMENT DESIGN

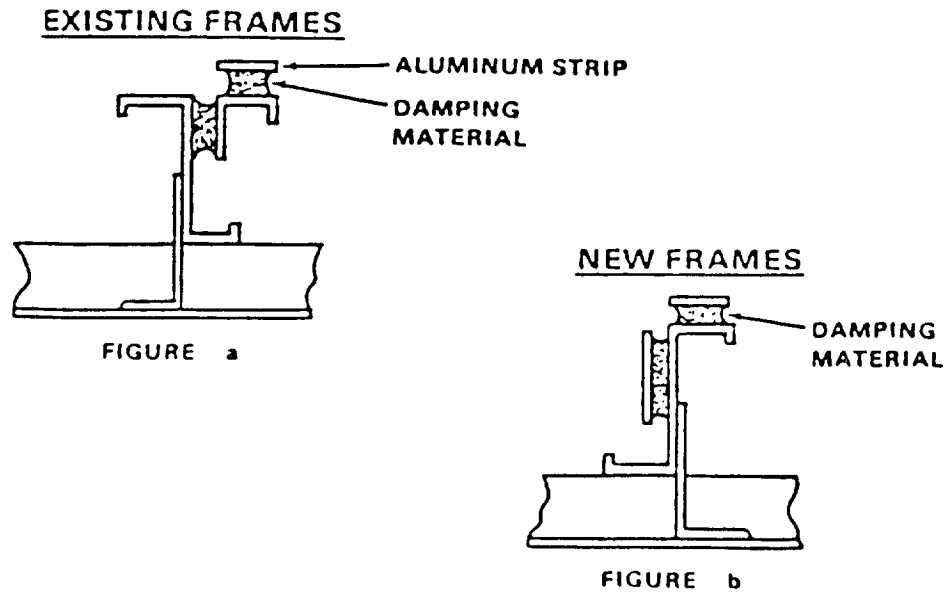


FIGURE 4-3. Frame Modifications and Additions.

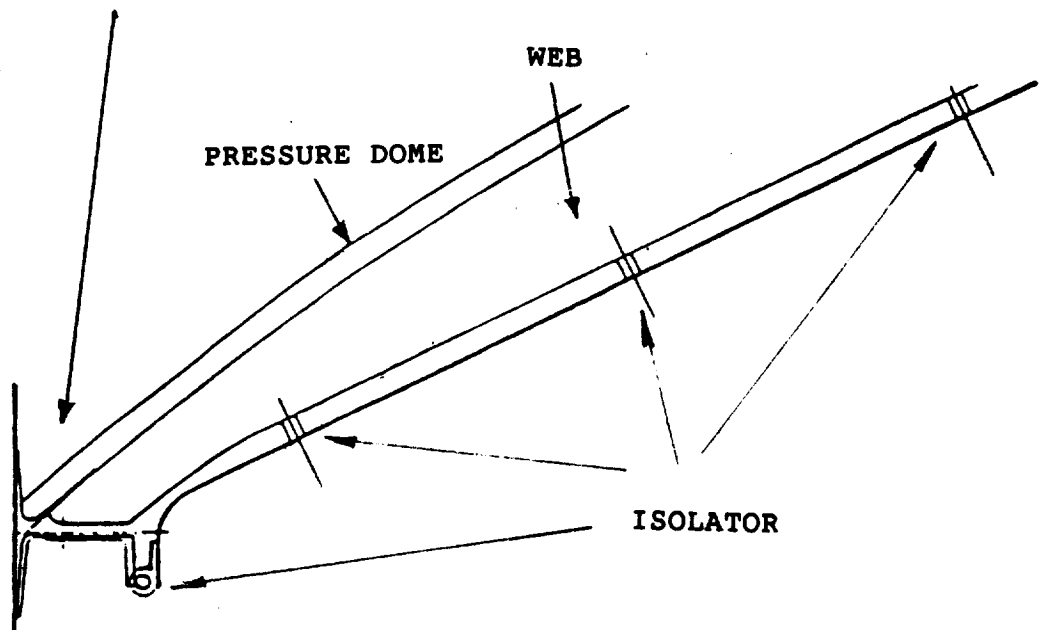
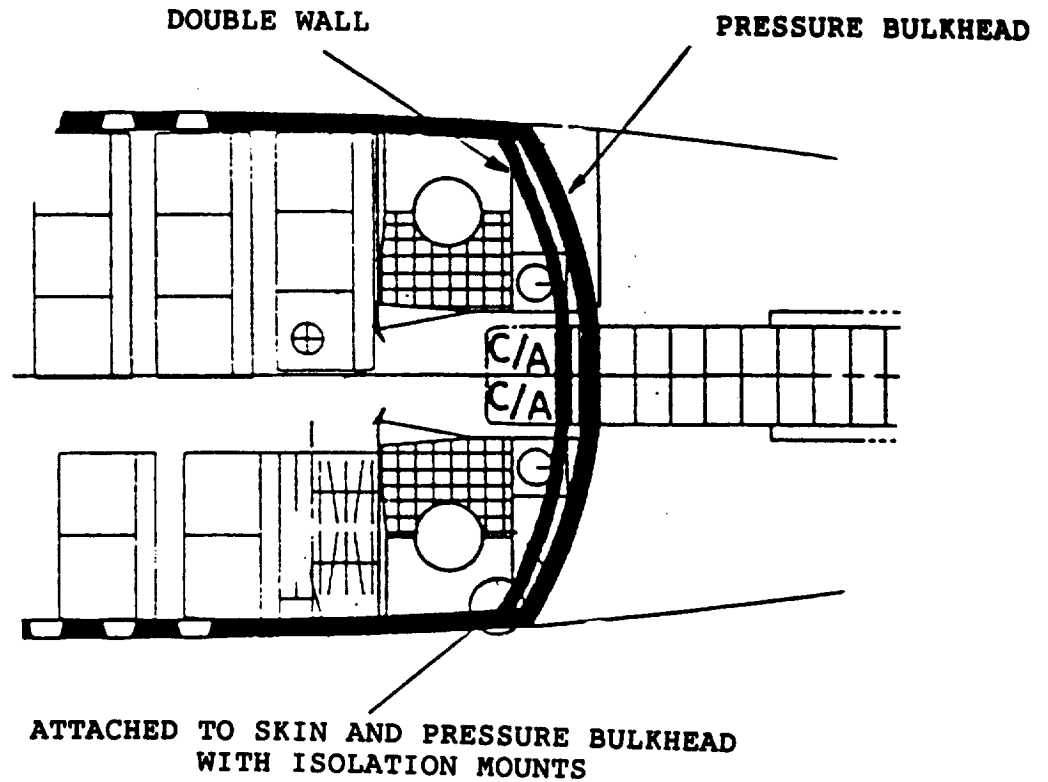


FIGURE 4-4. Pressure Bulkhead Double Wall Design.

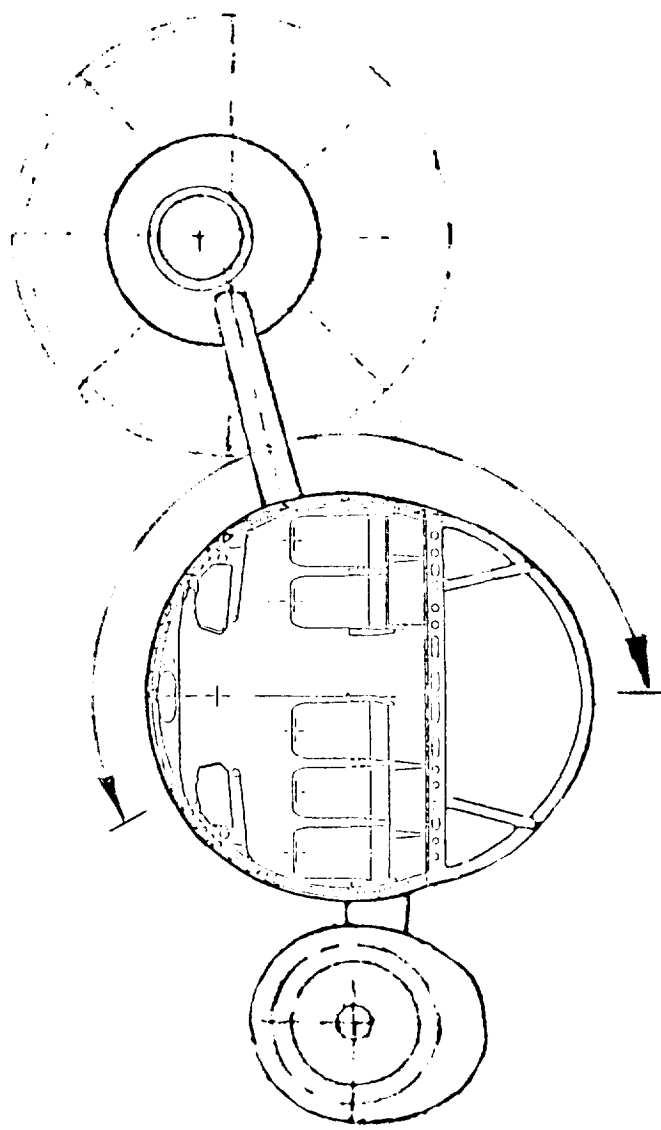


FIGURE 4-5. Distribution of Sonic Fatigue Treatment Between Stations 1174 and 1510.

AFT

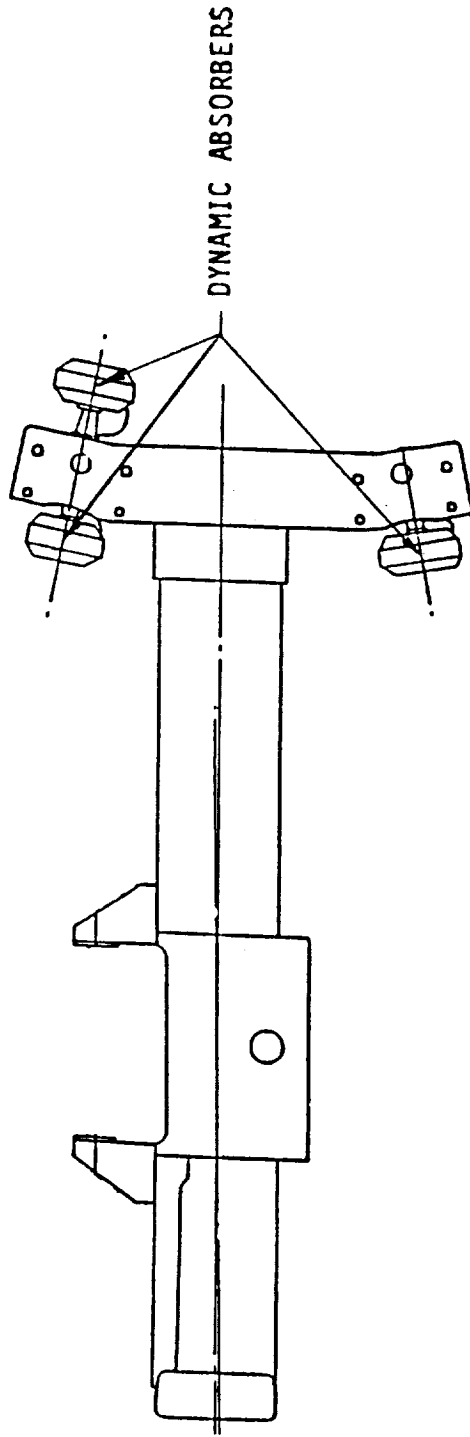


FIGURE 4-6. ENGINE DYNAMIC ABSORBER LOCATIONS ON MOUNT BEAM.

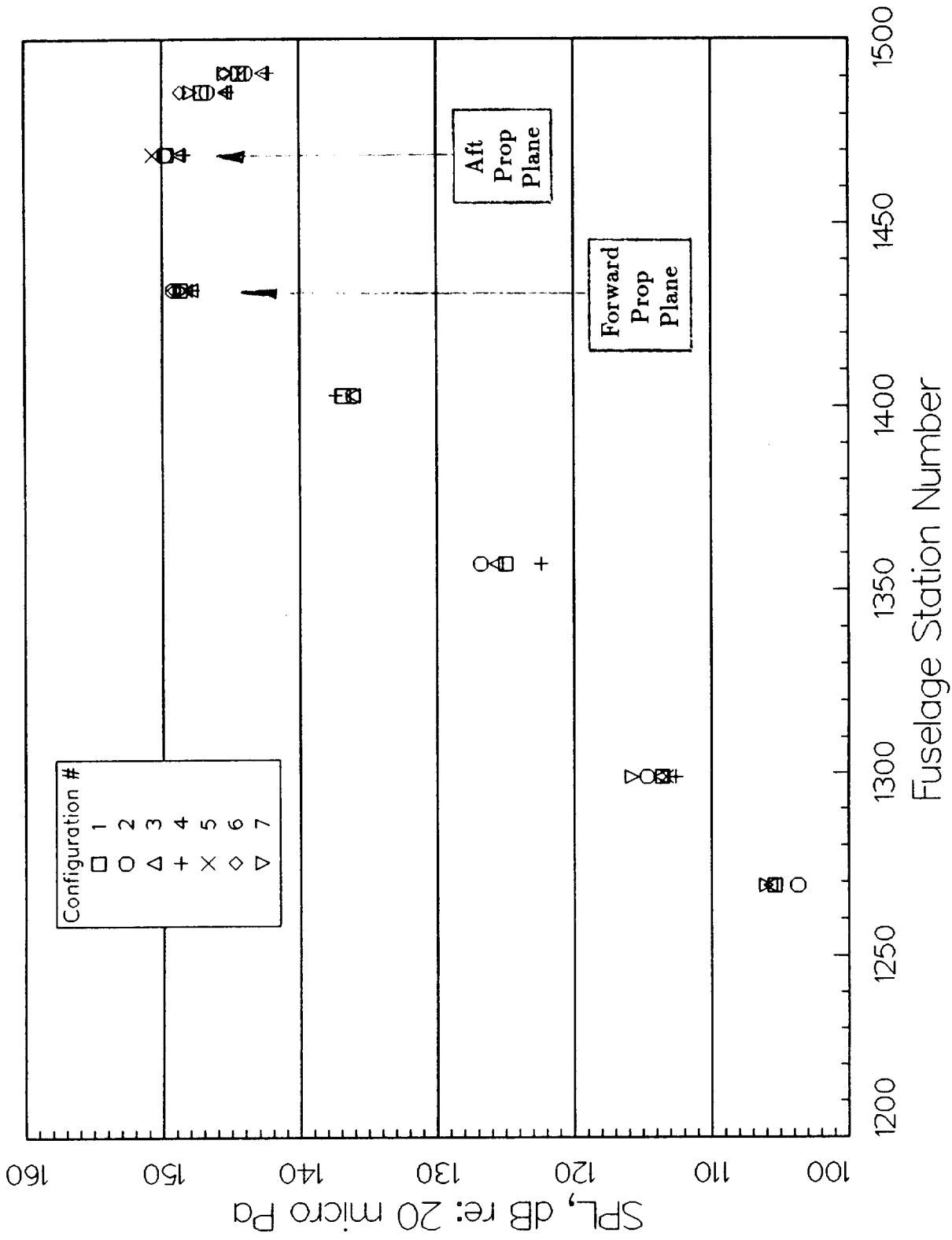


FIGURE 4-7. Exterior Acoustic Loads Distribution of the 8x8 Propeller Blade Passage Frequency for Each Test Point.

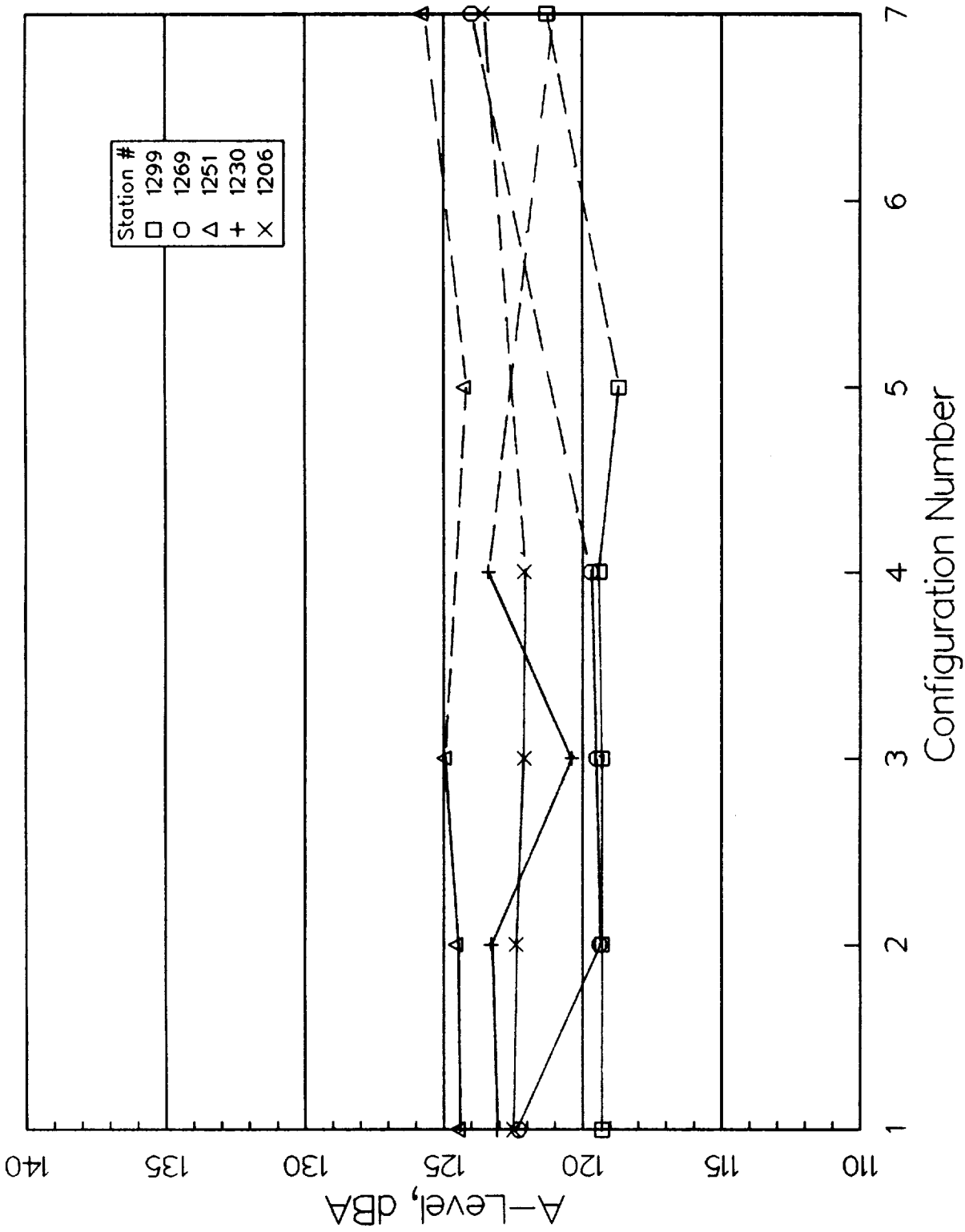


FIGURE 4-8. Fuselage Acoustic Loads: A-Weighted Broadband Levels

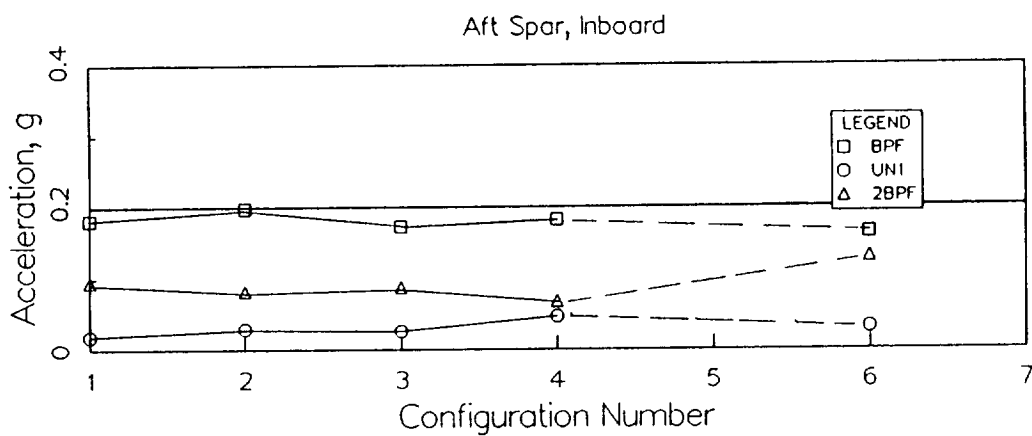
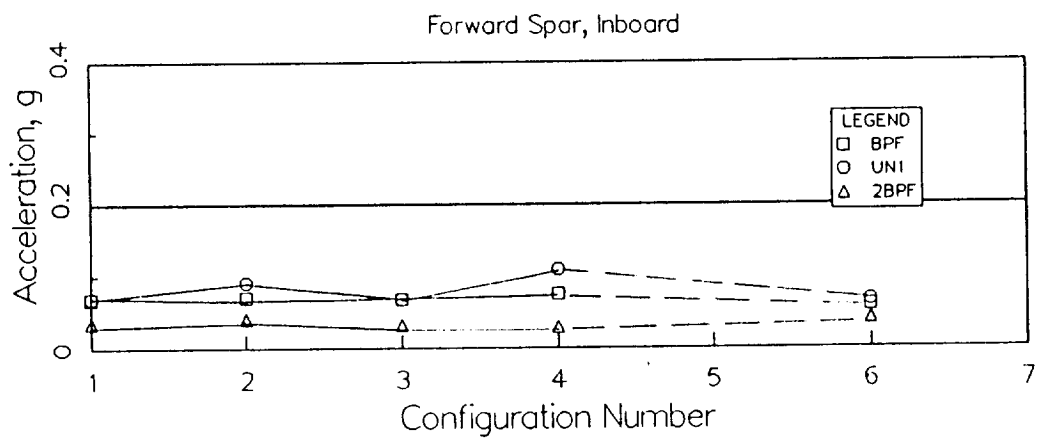
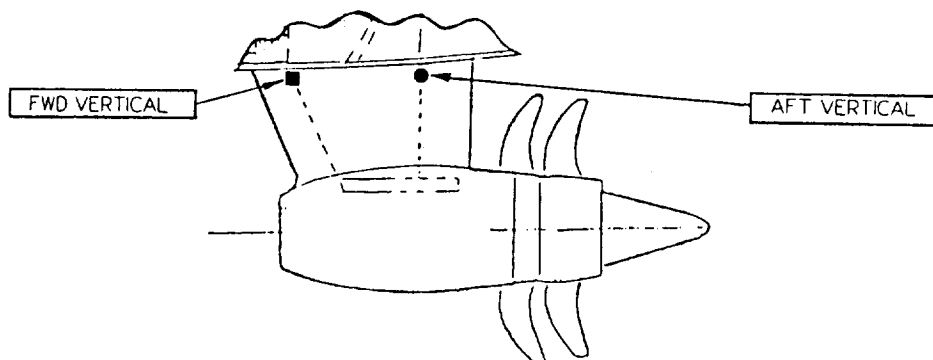


FIGURE 4-9. Acceleration levels at BPF, 2BPF and UN1 Measured at the Inboard Location of the Pylon Spar.

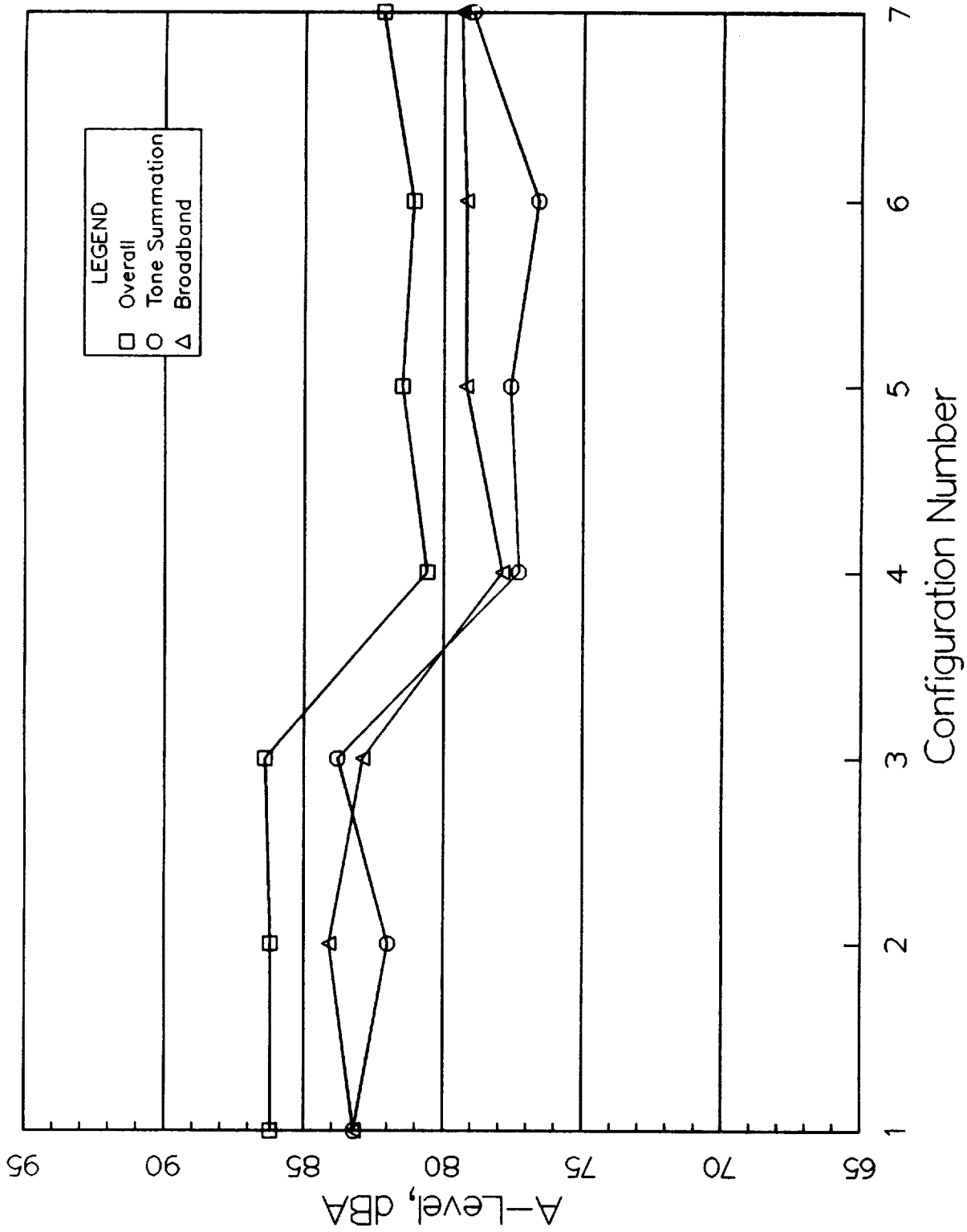


FIGURE 4-10. Maximum A-Weighted Levels at Seated Positions of Row 6.

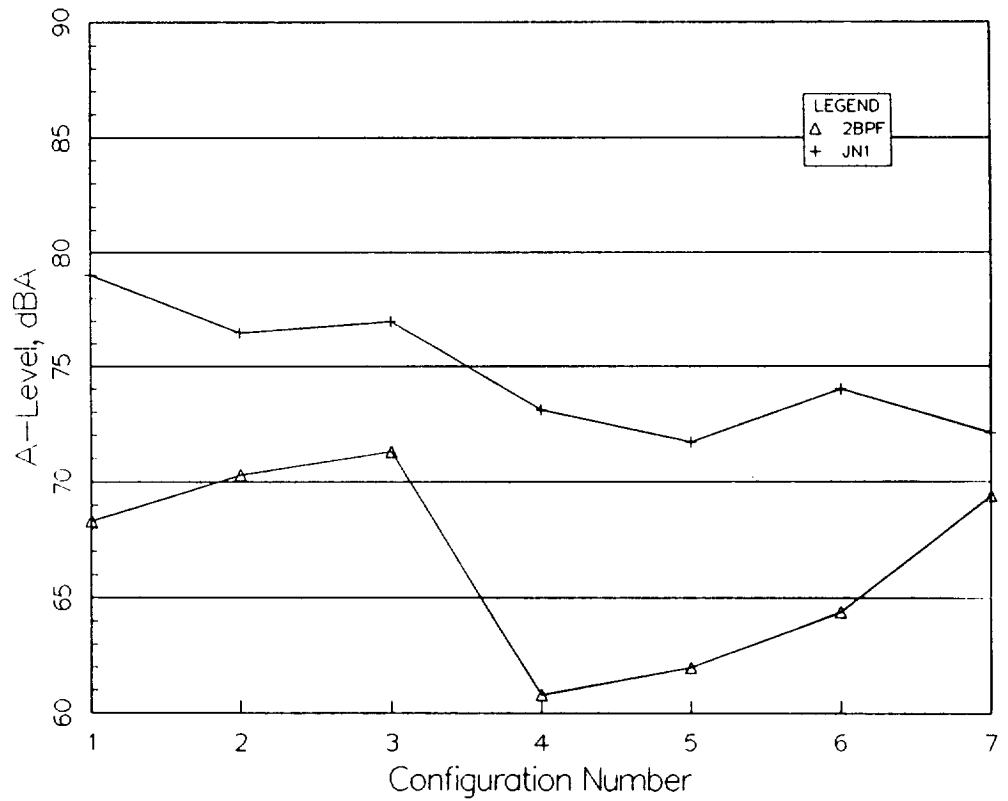
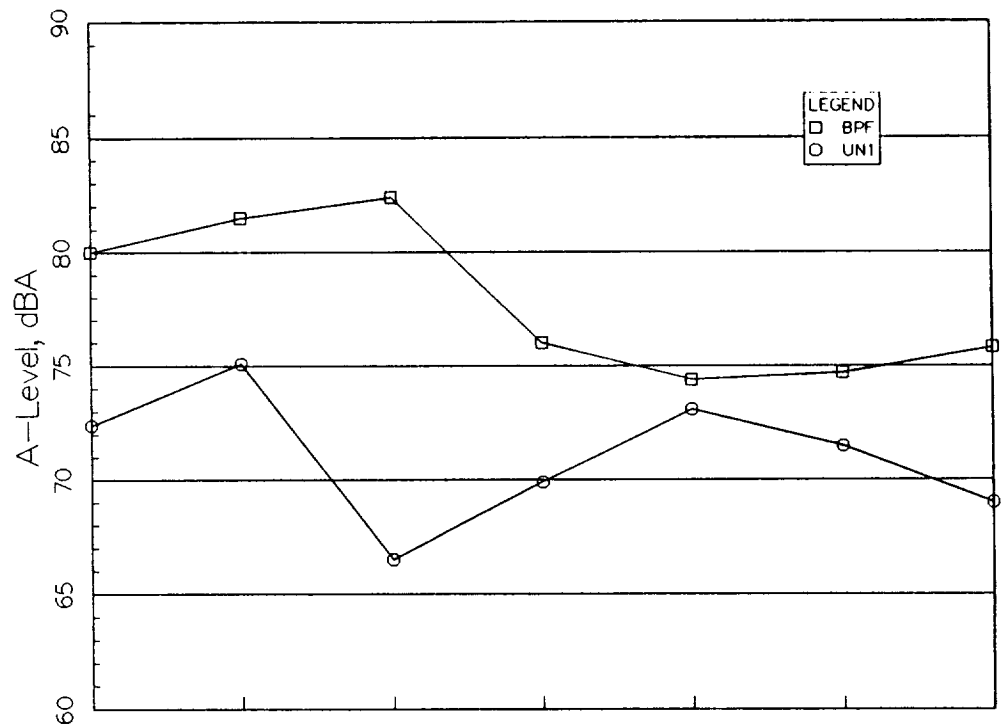


FIGURE 4-11. Maximum A-weighted Tone Levels at Seated Positions of Row 6.

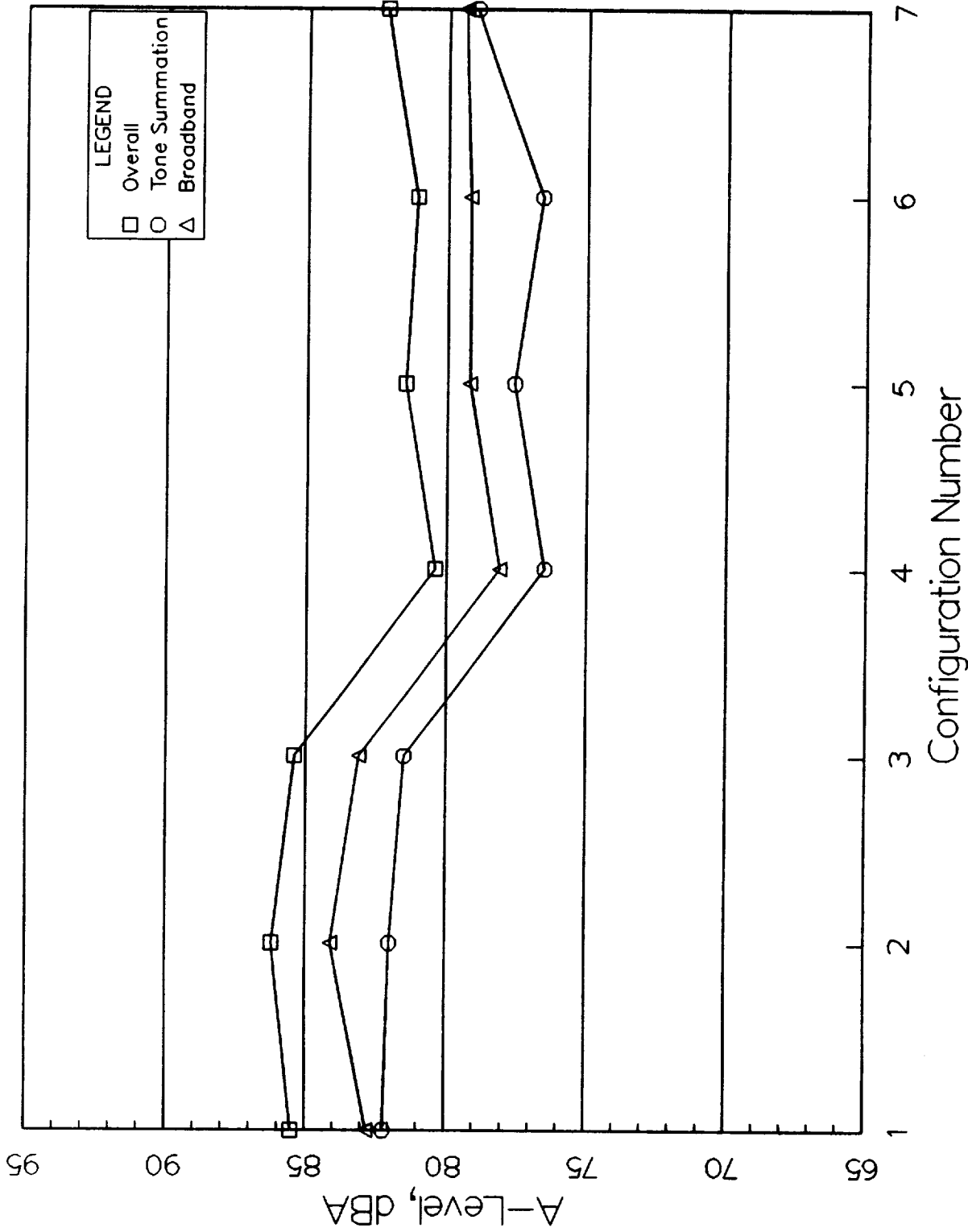


FIGURE 4-12a. A-Weighted Levels measured at Microphone 6 in Row 6 (Window Seat, JT8D Side).

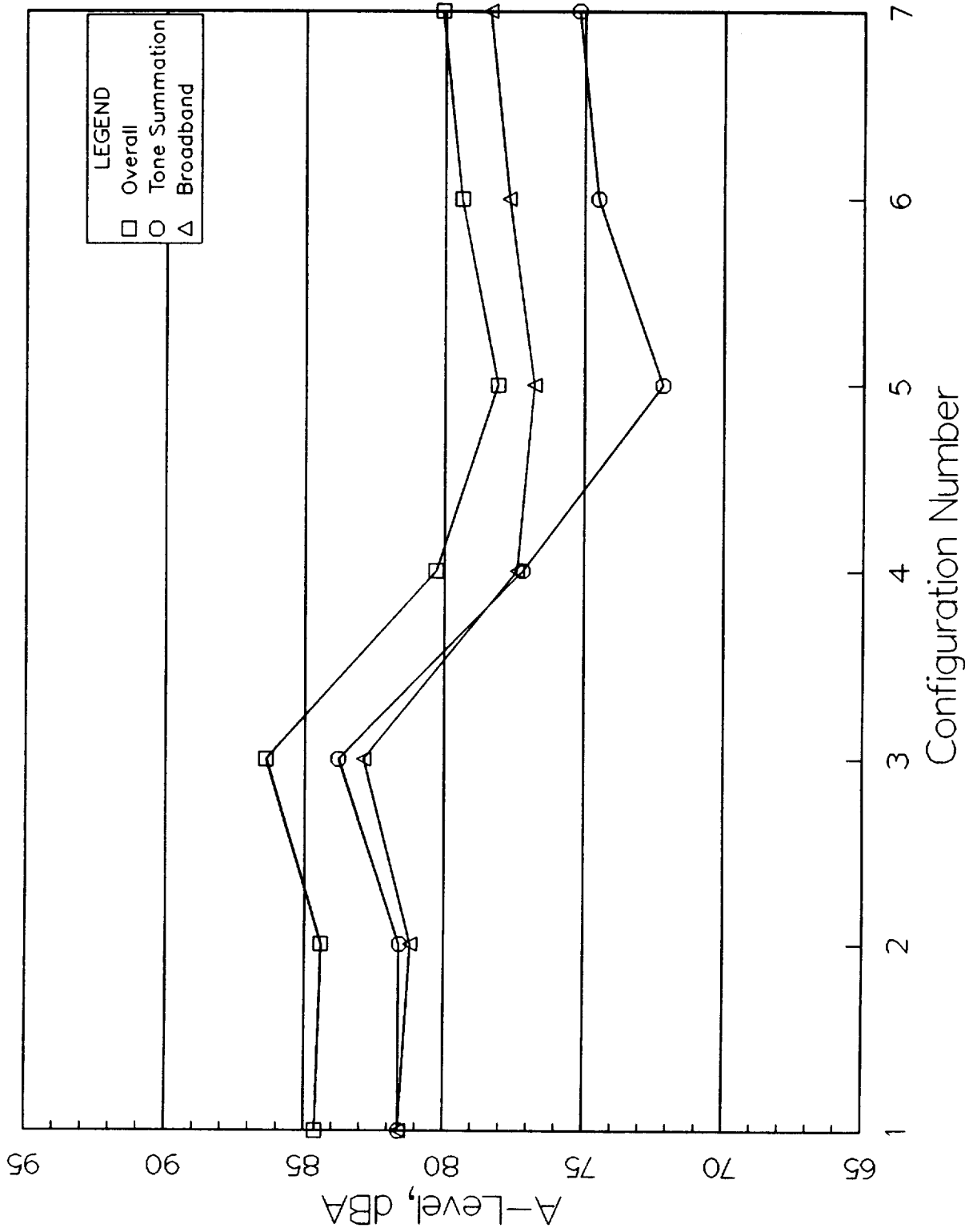


FIGURE 4-12b. A-Weighted Levels Measured at Microphone 4 in Row 6
(Aisle Seat, JT8D Side).

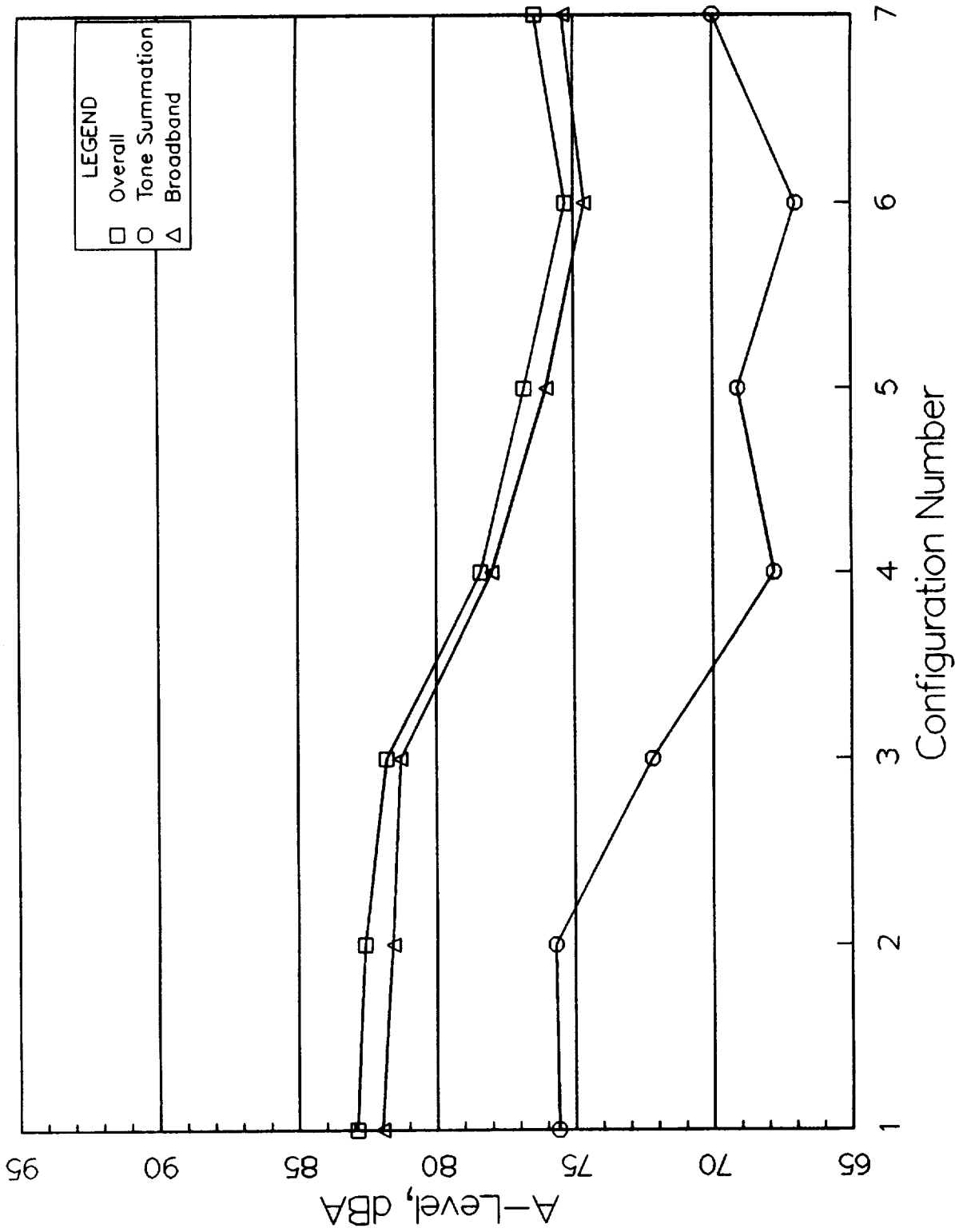


FIGURE 4-12c. A-Weighted Levels Measured at Microphone 2 in Row 6 (Aisle Seat, UDF Side).

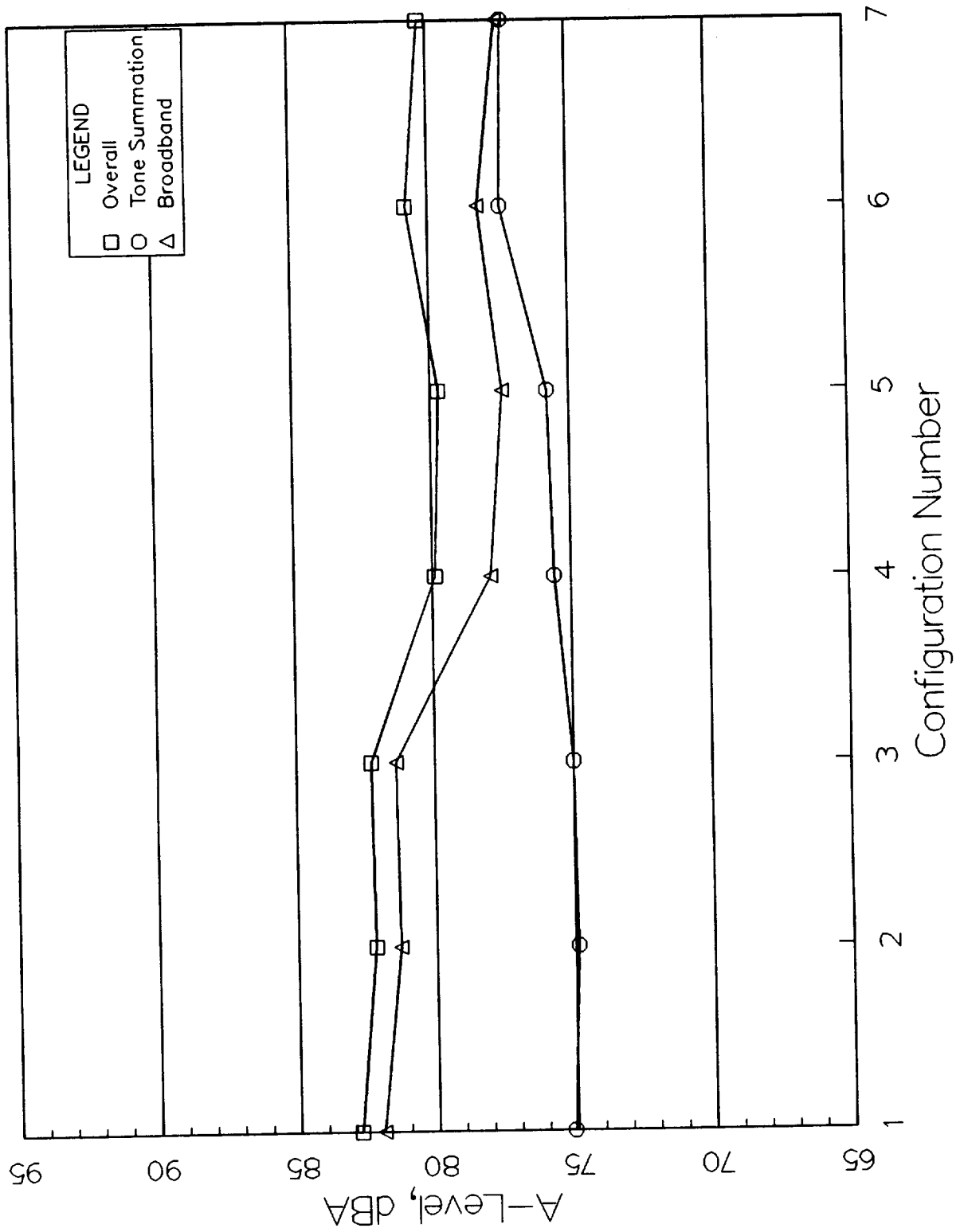


FIGURE 4-12d. A-Weighted Levels Measured at Microphone 1 in Row 6 (Window Seat, UDF Side).

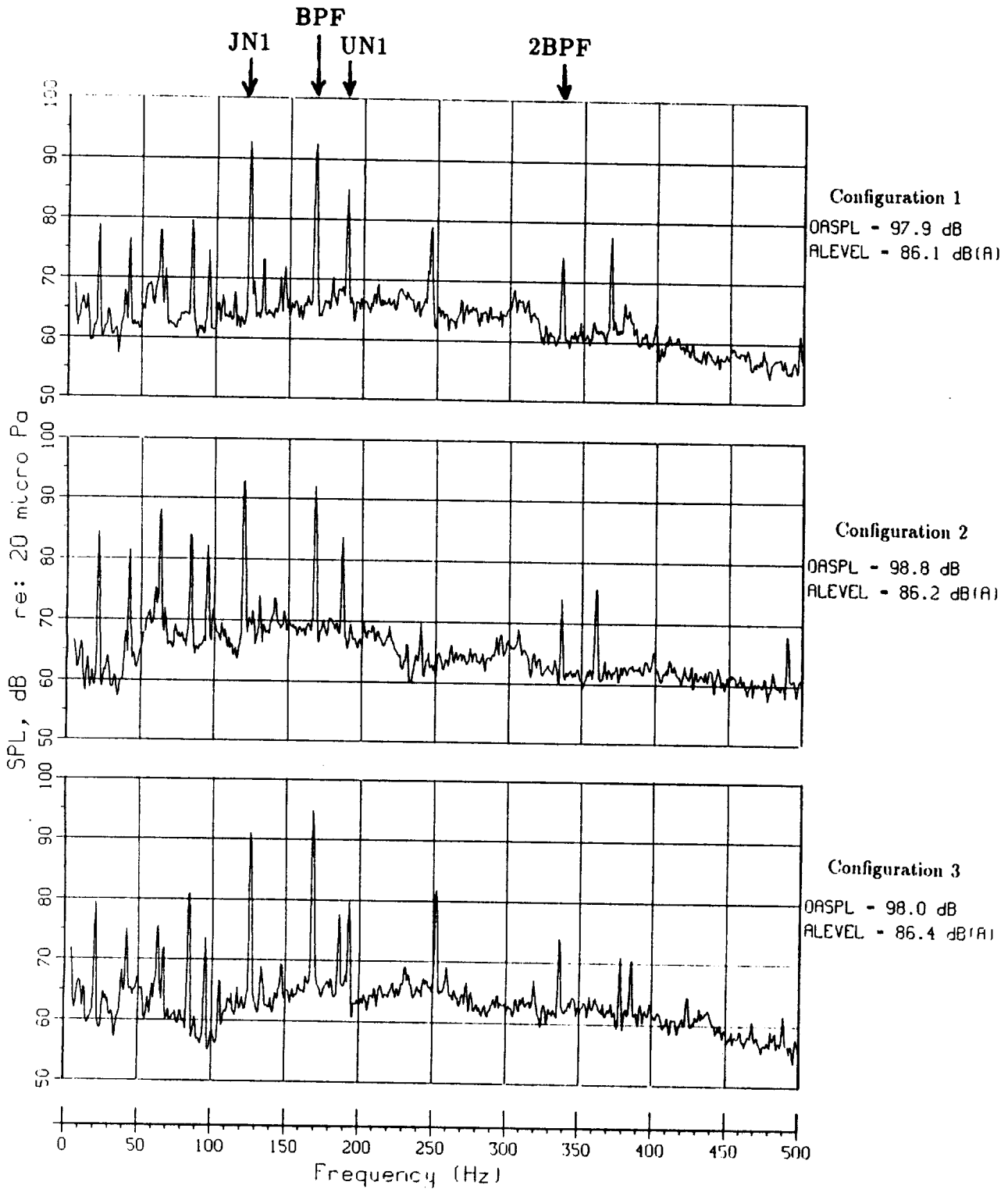


FIGURE 4-13. Measured Interior Noise Spectra in Row 6 for the Seat with the Maximum A-Level (Configurations 1, 2 and 3).

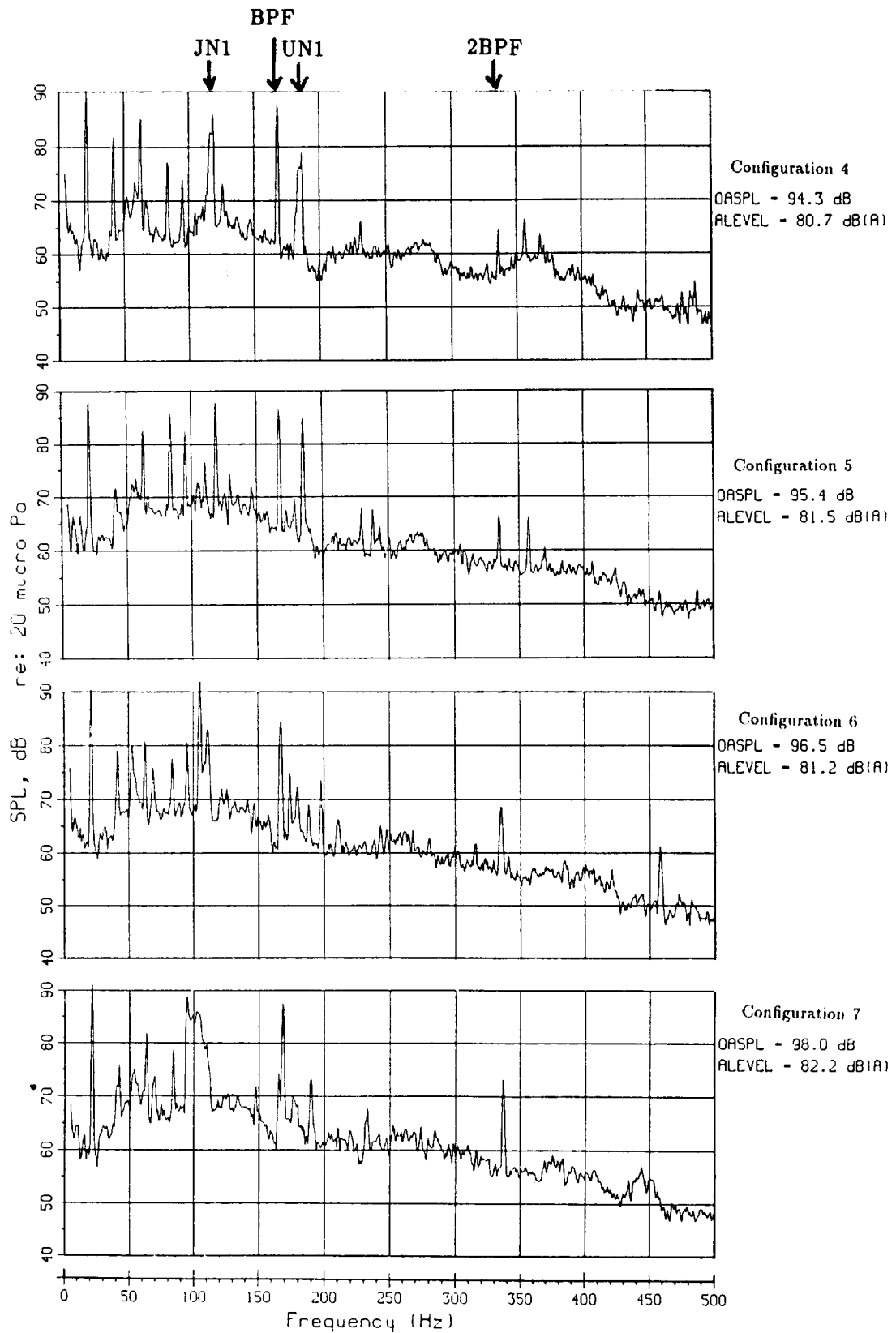


FIGURE 4-14. Measured Interior Noise Spectra in Row 6 for the Seat with the Maximum A-Level (Configurations 4, 5, 6 and 7).

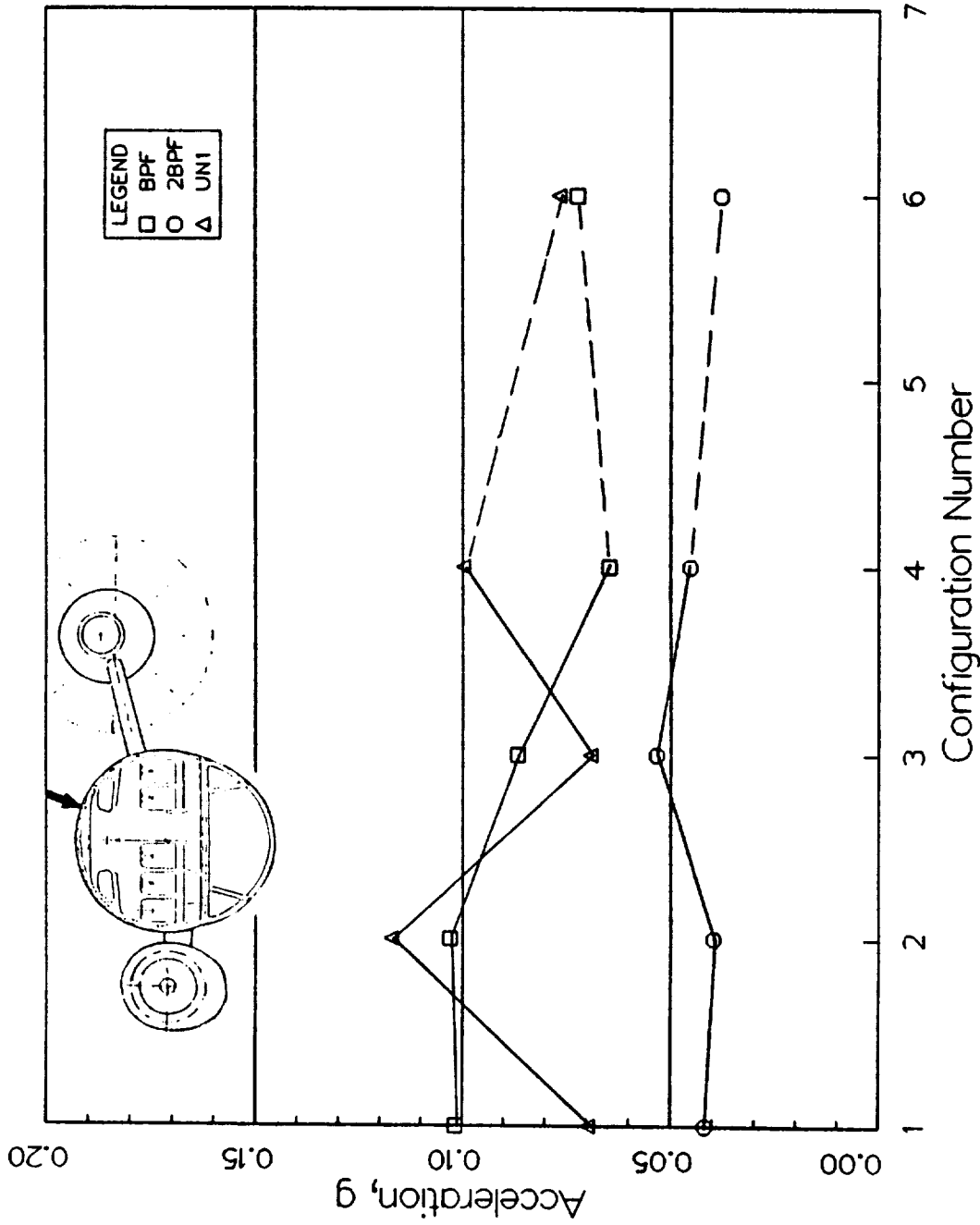


FIGURE 4-15a. Frame Acceleration at BPF, 2BPF and UNI at Fuselage Station 1271, Longeron 2.

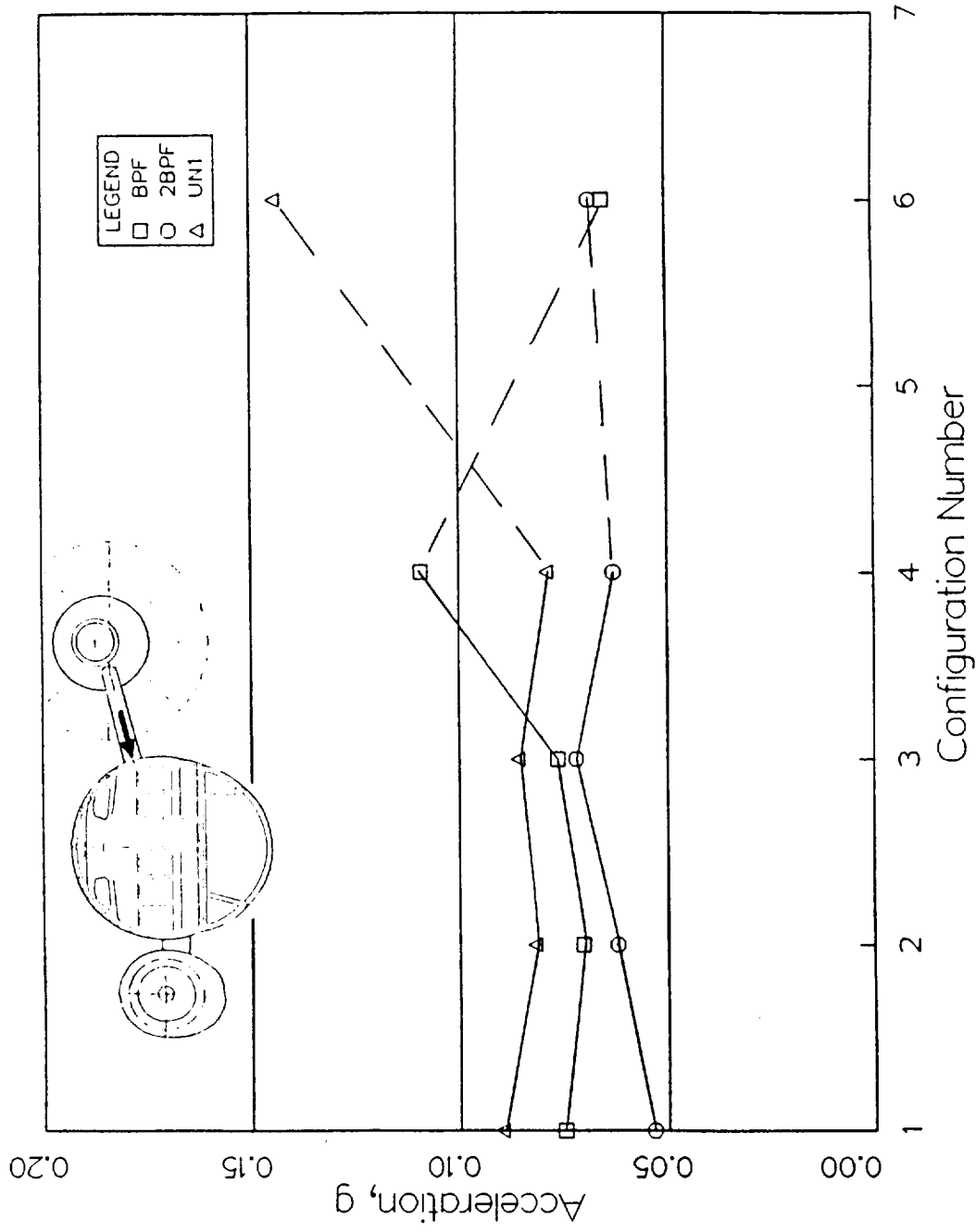


FIGURE 4-15b. Frame Acceleration at BPF, 2BPF and UN1 at Fuselage Station 1271, Longeron 5.

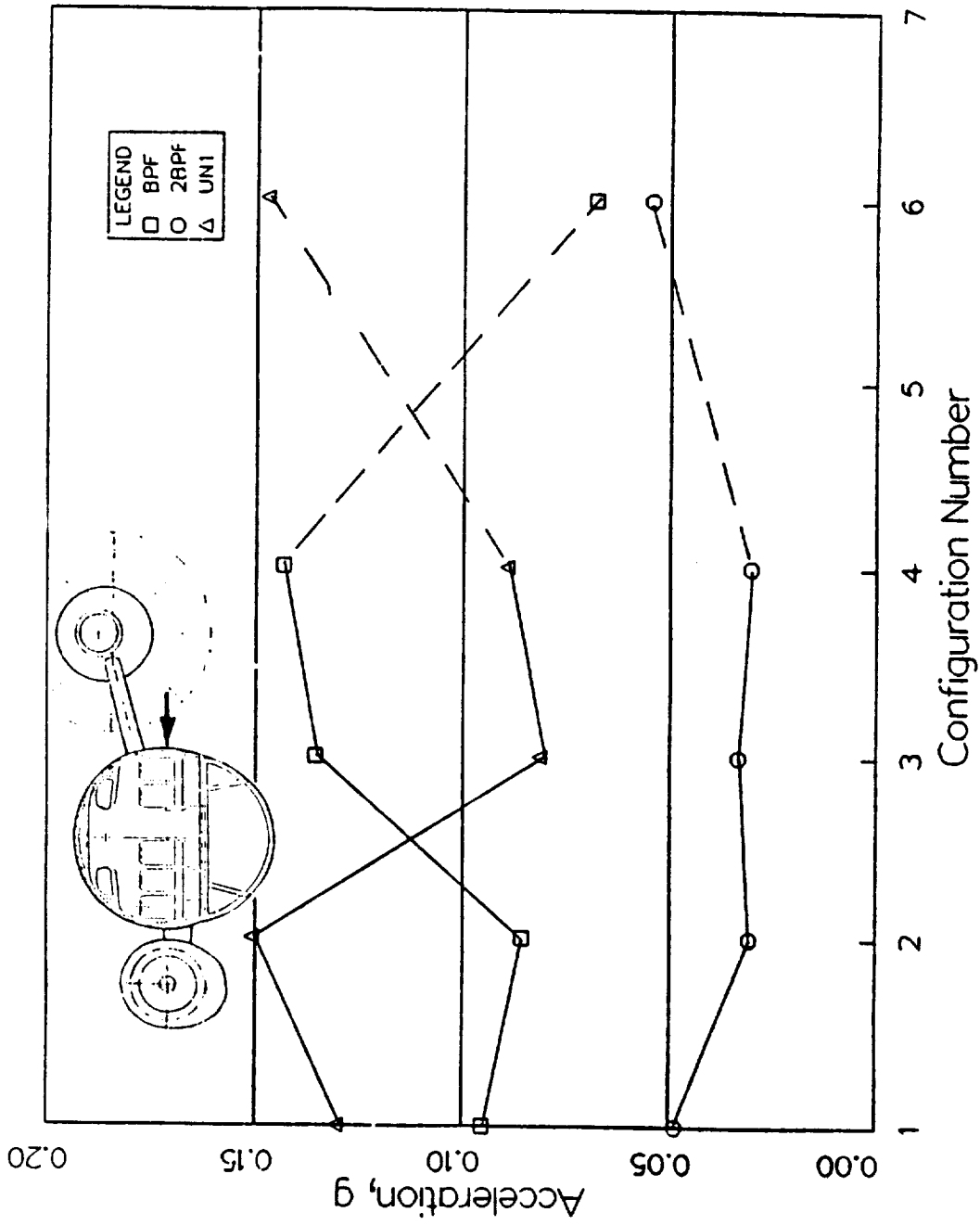


FIGURE 4-15c. Frame Acceleration at BPF, 2BPF and UNI at Fuselage Station 1271, Longeron 6.

5 Analysis of Quiet Cabin Noise Levels

The fully treated Quiet Cabin configuration (configuration 4) was tested during 8x8 Flight 1955. The test was conducted at 35,000 ft and at a Mach number of 0.76. To investigate the noise characteristics of this configuration, data were acquired at each of the following rotor speeds: 1170, 1200, 1225, 1250, 1260, 1270 and 1280 rpm. The BPFs associated with these speeds are 156.0, 160.0, 163.2, 166.4, 168.0, 169.6 and 171.2 Hz, respectively.

5.1 Acoustic and Vibratory Loads

5.1.1 Exterior Noise Levels

Since the BPF is the dominant propeller noise contributor to the interior noise (see Figure 4-11), the variation of the BPF tone level with propeller speed (at constant aircraft Mach number) was reviewed. As shown in Figure 5-1, the BPF level measured in the forward propeller plane of rotation generally increases with increasing propeller speed, while the level in the aft plane of rotation does not vary significantly with propeller speed.

It is interesting to observe that in the forward plane noise levels are highest at the lower microphone, and in the aft plane noise levels are highest at the upper microphone. This is primarily the result of the dynamic effects of the rotational direction of the blades, combined with the shielding effects of the fuselage curvature. Looking forward from the left side of the aft fuselage, the forward rotor turns counterclockwise towards the bottom of the fuselage, while the aft rotor turns clockwise towards the top of the fuselage. Thus noise levels are highest where the blades advance towards the fuselage, and lowest where the blades recede.

5.1.2 Pylon Vibration Levels

Earlier, it was shown that the three dominant components of the pylon vibration are the tones at the BPF, 2BPF and UN1 frequencies. Figure 5-2a presents the data acquired on the aft engine mount in the vertical, lateral and longitudinal directions and Figure 5-2b the data acquired on the inboard side of the pylon, on each of the two spars in the vertical direction. The BPF data acquired on the engine mount in the lateral direction exhibits a strong dependence on the propeller rotational speed with a peak at 1250 rpm. For all practical purposes, the 2BPF response at the engine mount is very low. The UN1 tone also exhibits a propeller speed dependence but is characterized by

a generally decreasing amplitude with increasing speed. Also, the lateral response for UN1 is weaker than the longitudinal and vertical responses.

The behavior of the data acquired on the pylon spars on the inboard side of the pylon is different than on the engine mount. The vibration levels at BPF and 2BPF increase with increasing propeller speed, a trend similar to that shown in Figure 5-1 for the BPF SPL in the forward propeller plane. Acceleration levels on the aft pylon spar are greater than those on the forward spar for both BPF and 2BPF. The vibration at the UN1 frequency measured at these locations does not appear to be influenced by propeller speed; acceleration is higher on the forward spar than on the aft spar.

5.2 Cabin Noise Levels

For these test points interior noise levels were measured in seat rows 4 and 6. Figures 5-3 and 5-4 present the measured levels in these two rows, respectively. Each figure presents the A-weighted overall levels along with the corresponding broadband and tonal component contributions. Also, the data acquired at microphone position 3 (the aisle measurement location) are presented separately from the data acquired at the other positions (seat measurement locations).

At position 3, it can be observed that the noise level does not vary substantially with propeller speed. Further inspection of the data reveals that the contribution of the tones to the overall level is indeed fairly constant. The data acquired at the row 4 measurement location exhibits a small increase with increasing propeller speed, however the variation is too small to be clearly distinguished from the expected experimental scatter. At the seated positions, the maximum measured levels are shown to increase with increasing propeller speed, and peak near 1250 rpm. Inspection of the tone contribution shows the same trend.

The overall levels measured at each seat row are very similar. However the tone contribution to the level of seat row 4 is generally 1 to 3 dB higher than that observed at seat row 6 while the reverse is true for the broadband contribution.

The variation with propeller speed of the maximum amplitude measured for each major contributing tone is presented in Figure 5-5. It is readily observed that BPF is the only tone that exhibits a level increase with increasing propeller speed. Another feature of the data presented is that the JN1 and BPF tone levels are higher in row 4 than in row 6.

Figures 5-6 through 5-9 present the variation of the amplitude of each of the major tones at each seat location of each row. In Figure 5-6, one can observe that the distribution of the BPF tone amplitude in each seat row does not follow a particular

pattern. For example, at 1225 rpm the amplitude of the BPF tone is nearly constant across row 6, while at 1170 rpm it decreases toward the right side (JT8D side) of the aircraft and at 1280 rpm it increases toward the same side. It can however be noted that, on the right side of the aircraft, higher propeller speeds generally result in higher BPF tone amplitudes. The data scatter is also observed to increase from slightly more than 5 dB on the UDF side to slightly more than 10 dB on the JT8D side. In row 4, levels vary more abruptly from seat to seat for each rotor speed. The trend observed in Figure 5-5 of higher tone levels in row 4 at 1250 and 1260 rpm can be seen in these data.

In Figure 5-7, the 2BPF data reveal no apparent trends. The levels typically vary 4 to 7 dB across each seat row, except for the small data scatter at locations 1 and 3 of row 4.

Figures 5-8 and 5-9 present the data associated with the UN1 and the JN1 tones, respectively. Both sets of data exhibit a very small scatter. This might have been expected as each of the two engine spools were rotating at nearly constant speed, while the rotor speed was varied among the seven test points. The other striking feature for both tones is the low levels observed at seat location 2 of row 6, nearly 10 dB lower than measured at any other seat location. For JN1, seat location 2 of both row 4 and row 6 exhibit low levels.

Finally, Figure 5-10 presents the amplitude variation of the tone summation in the same manner. The scatter is generally small (5 dB or less). No particular trend can be observed, except on the right side of row 6 where higher propeller speed results in higher tone summation levels, a trend similar to that observed for the BPF tone. Also, the decrease in level at seat location 2 of row 6 observed for the UN1 and JN1 tones occurs for the tone summation levels as well.

Comparison of the levels in Figures 5-6 through 5-10 shows that for most seat positions and propeller speeds, the tone component of the interior noise is dominated by the BPF tone, followed in importance by the JN1 tone and then the UN1 tone. The 2BPF tone is not a major contributor to the total tonal energy.

The broadband component of the interior noise is shown in Figure 5-11. The broadband level is naturally independent of the propeller speed and remains constant across the cabin. The slightly higher levels at location 3 are expected since they were measured at a standing location, closer to the air conditioning ducts at the top of the cabin.

The overall level variation shown in Figure 5-12 indicates very little dependence on the propeller speed as expected from the data presented in Figures 5-3 and 5-4. Comparison of the levels in Figures 5-10, 11, and 12 indicates that generally the level of the broadband component is equal to or higher than the level of the tone component, in agreement with the data presented in Section 4.5.

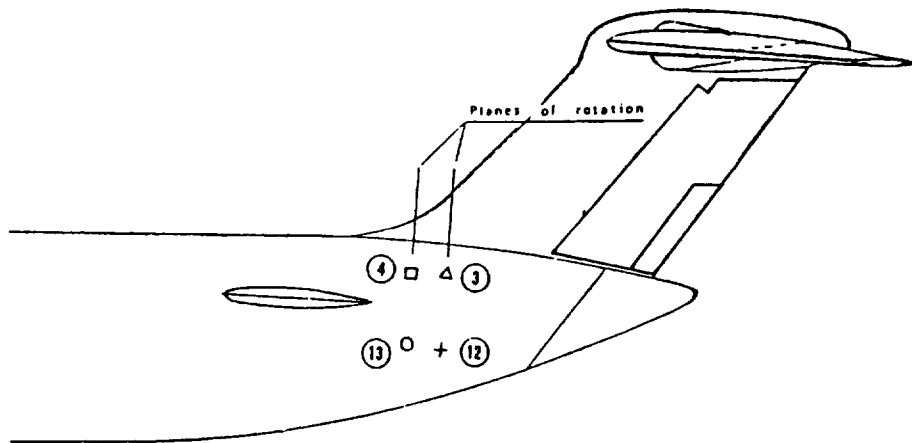
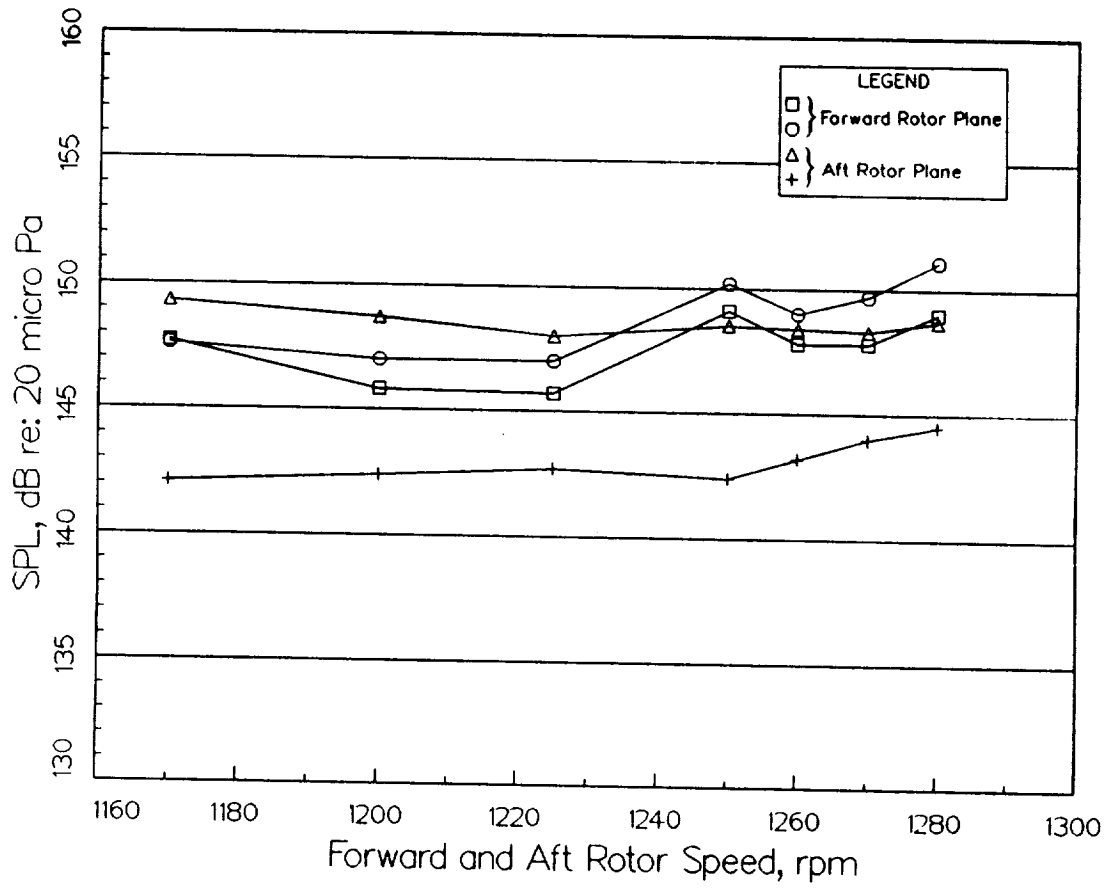


FIGURE 5-1. Variation of BPF Sound Pressure Level with Propeller Speed.

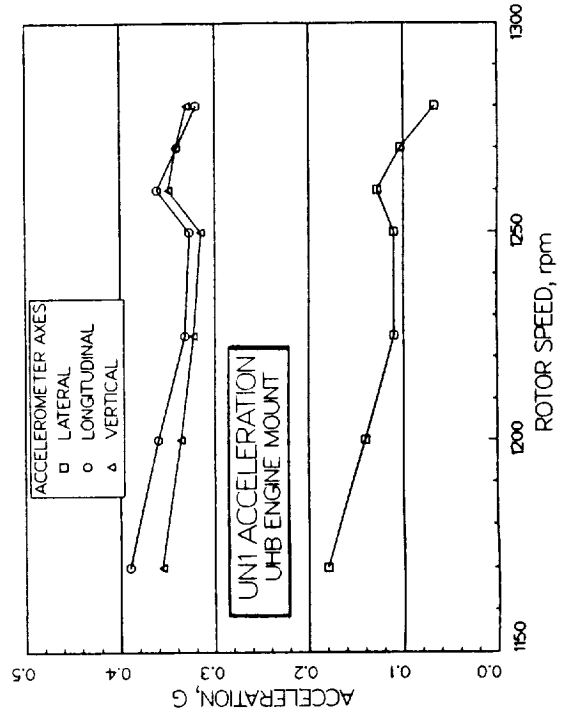
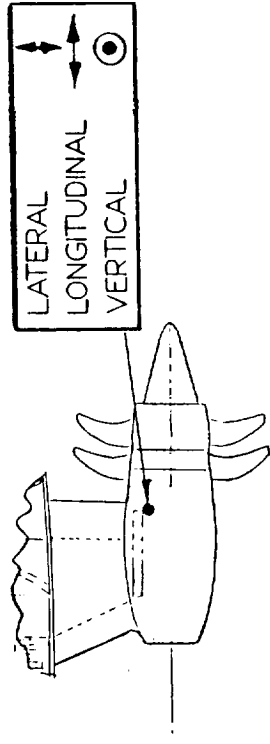
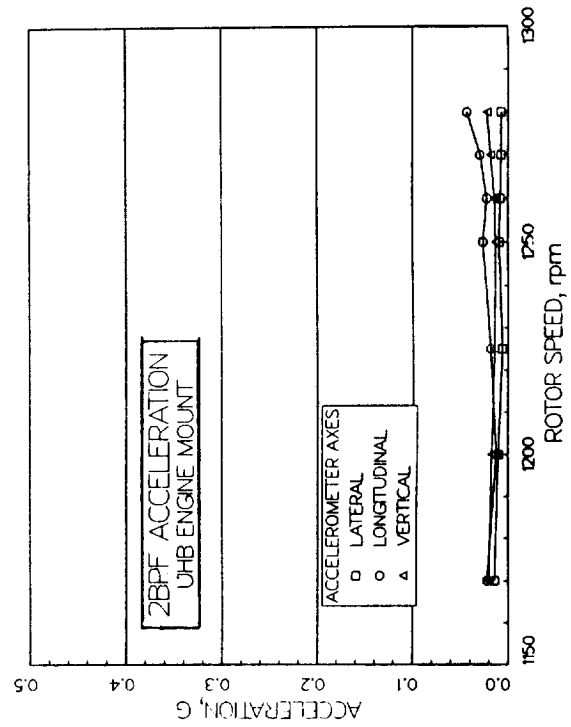
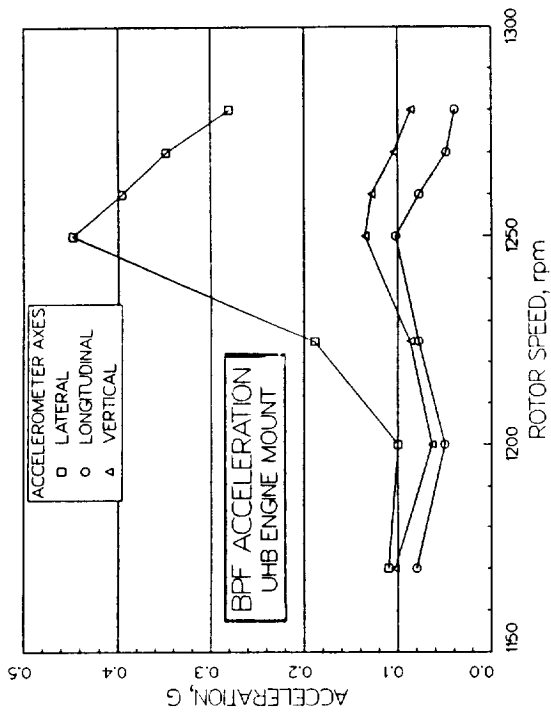


FIGURE 5-2a. Aft Engine Mount Accelerations at BPF, 2BPF and UNI.

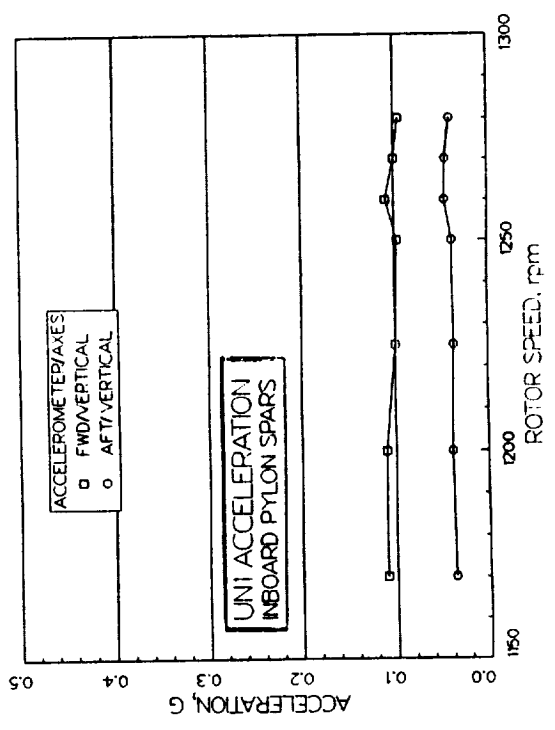
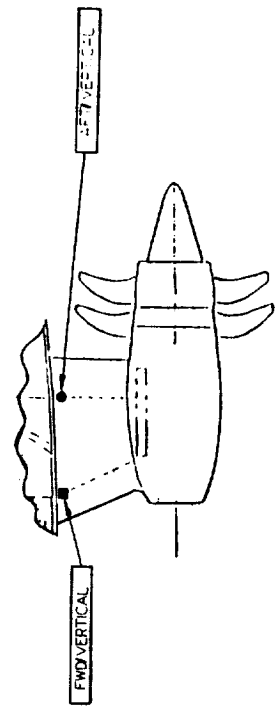
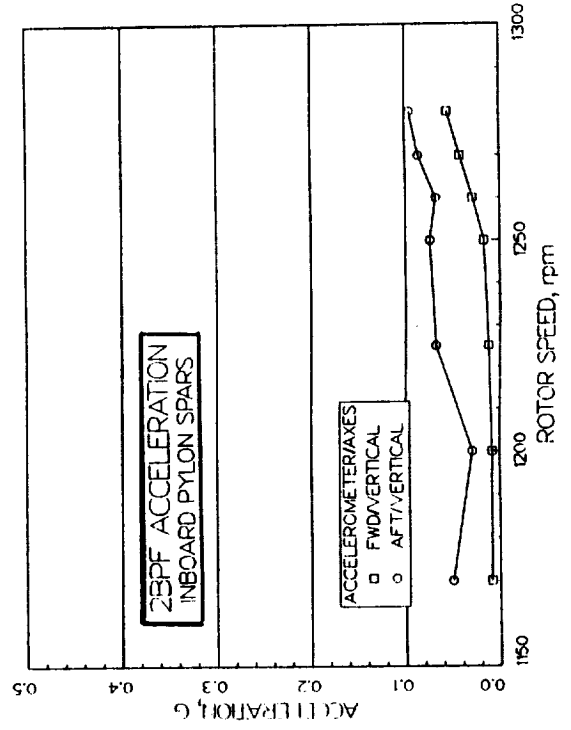
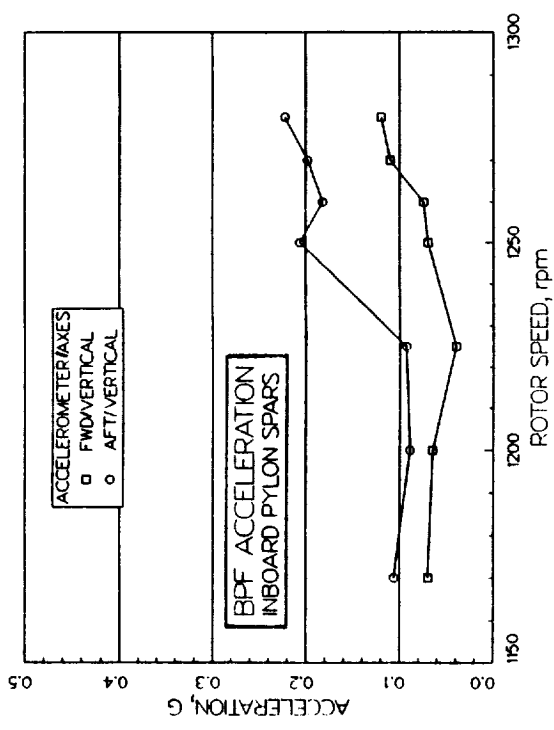
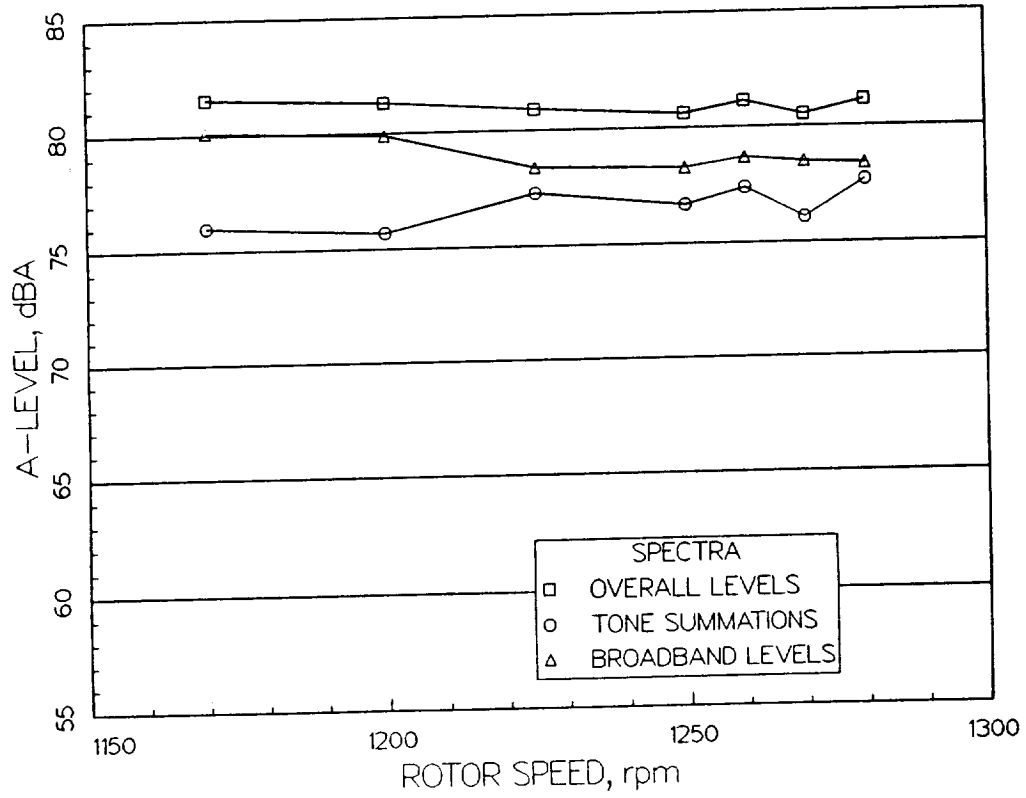


FIGURE 5-2b. Inboard Pylon Spar Accelerations at BPF, 2BPF and UNI.

MAXIMUM LEVELS AT POSITION 3 ONLY



MAXIMUM LEVELS AT ALL POSITIONS EXCEPT 3

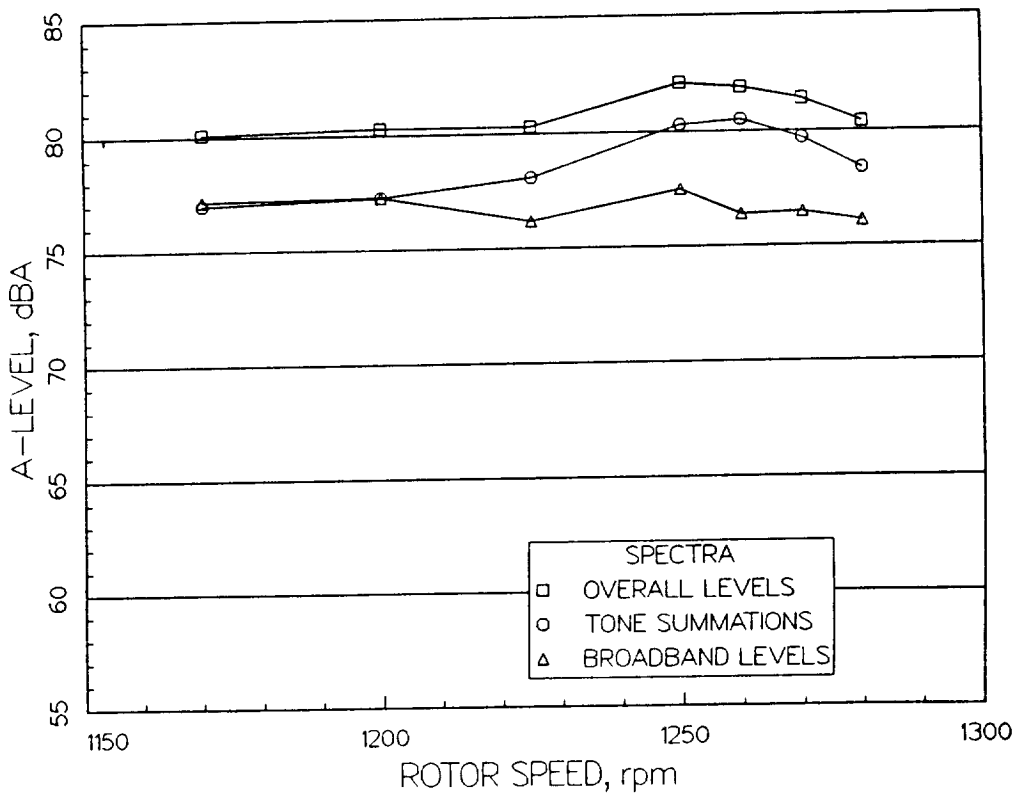
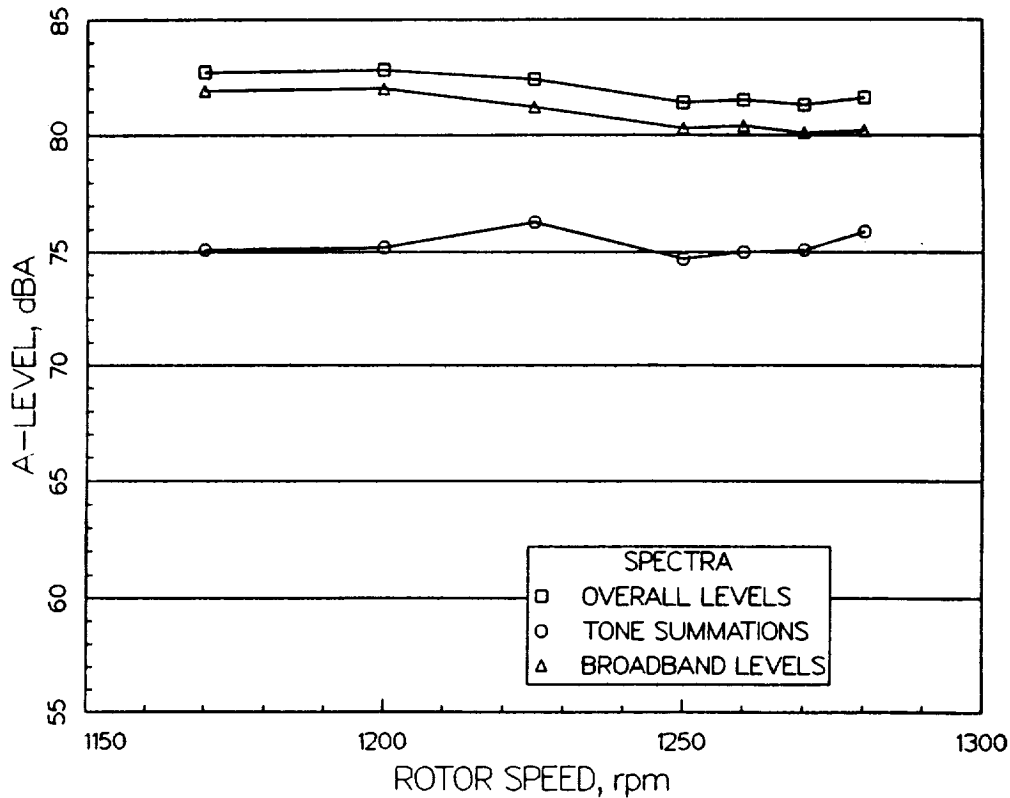


FIGURE 5-3. A-weighted Interior Noise Levels At Row 4 (Configuration 4).

MAXIMUM LEVELS AT POSITION 3 ONLY



MAXIMUM LEVELS AT ALL POSITIONS EXCEPT 3

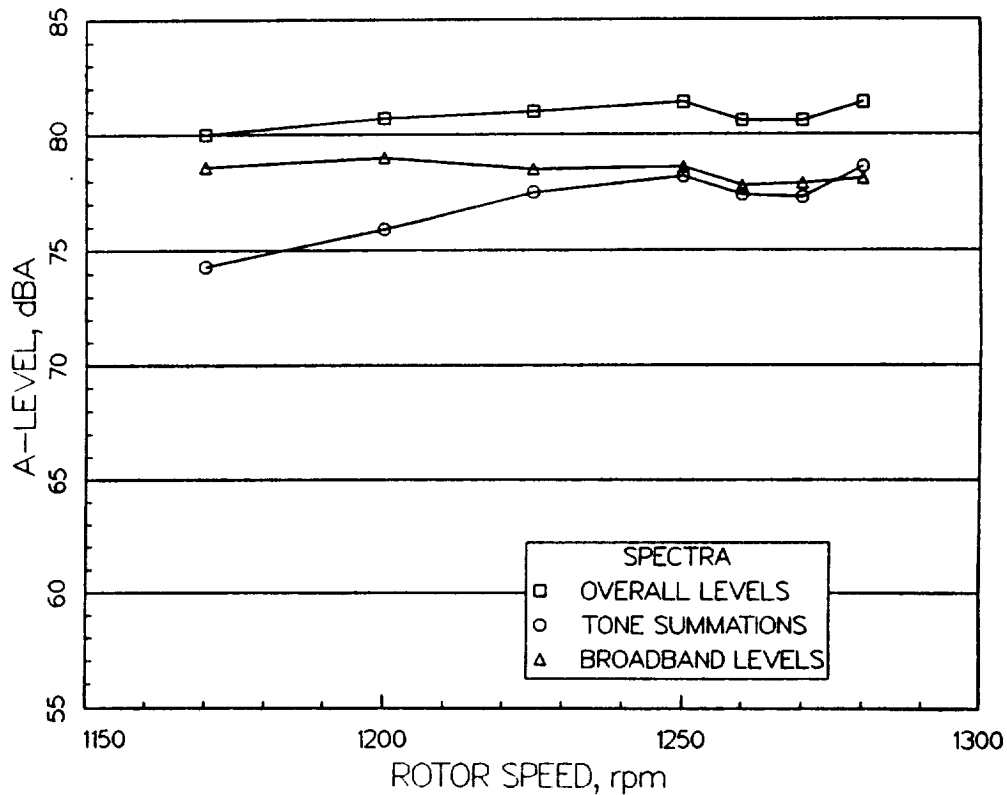


FIGURE 5-4. A-weighted Interior Noise Levels At Row 6 (Configuration 4).

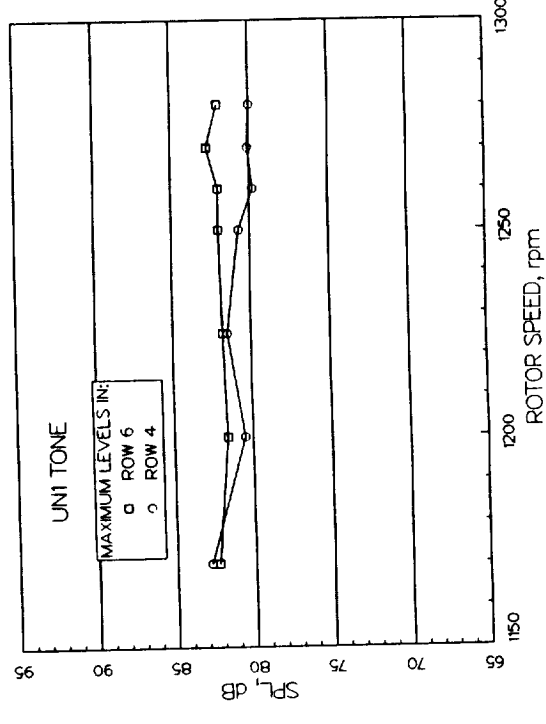
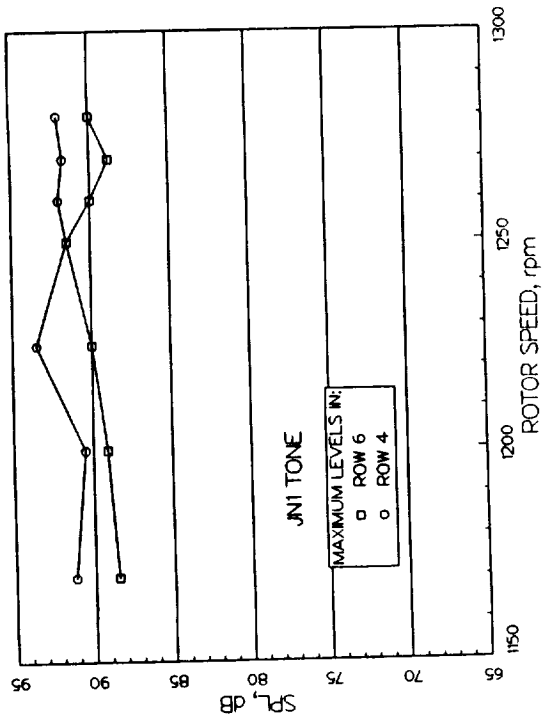
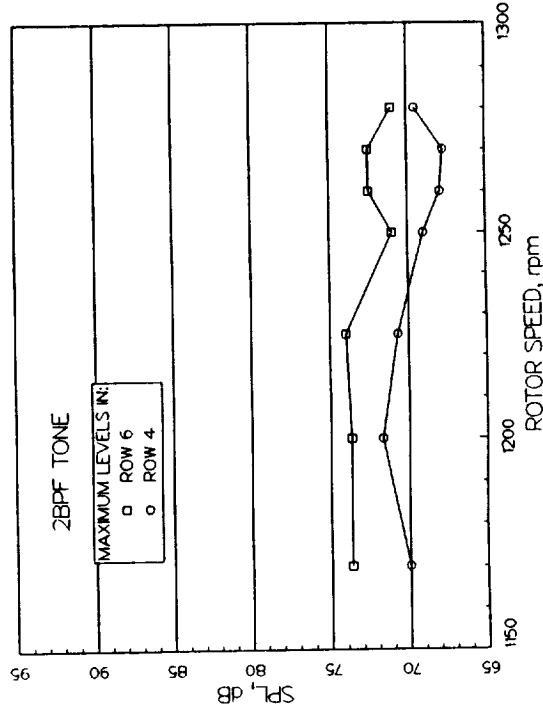
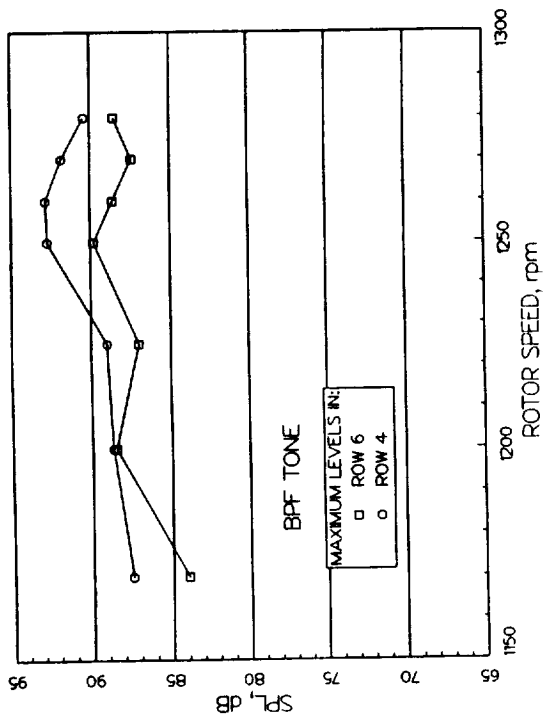


FIGURE 5-5 Maximum Measured Sound Pressure Levels at BPF, 2BPF, UN1 and JN1 Frequencies.

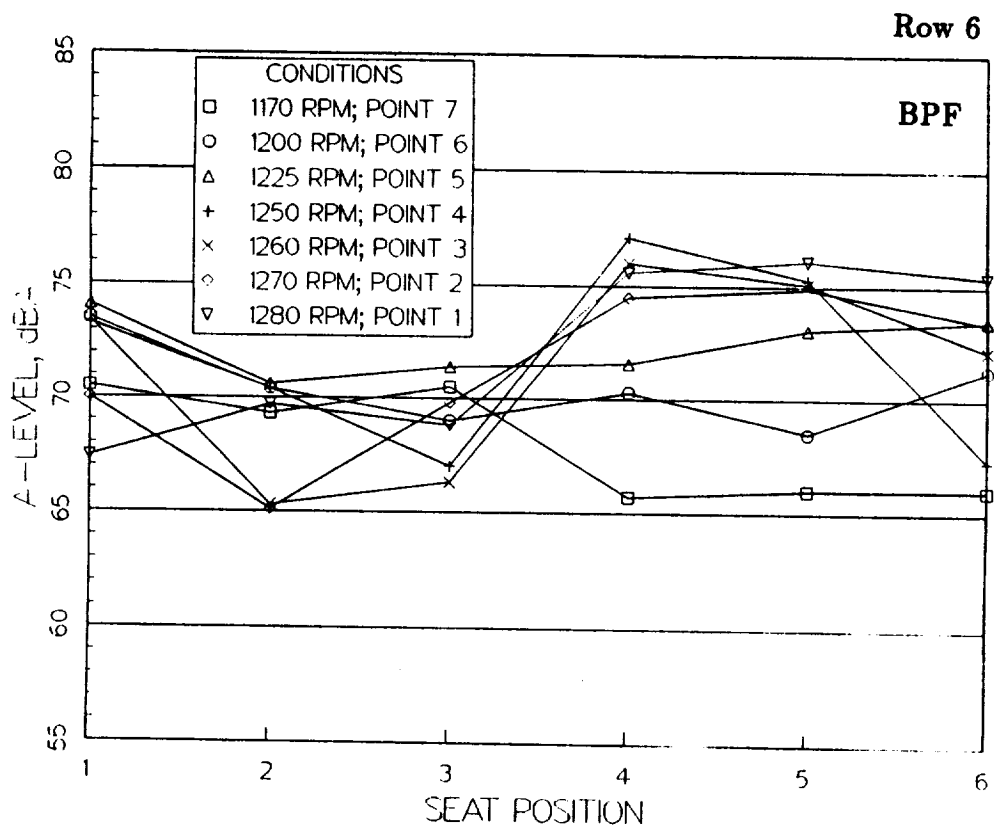
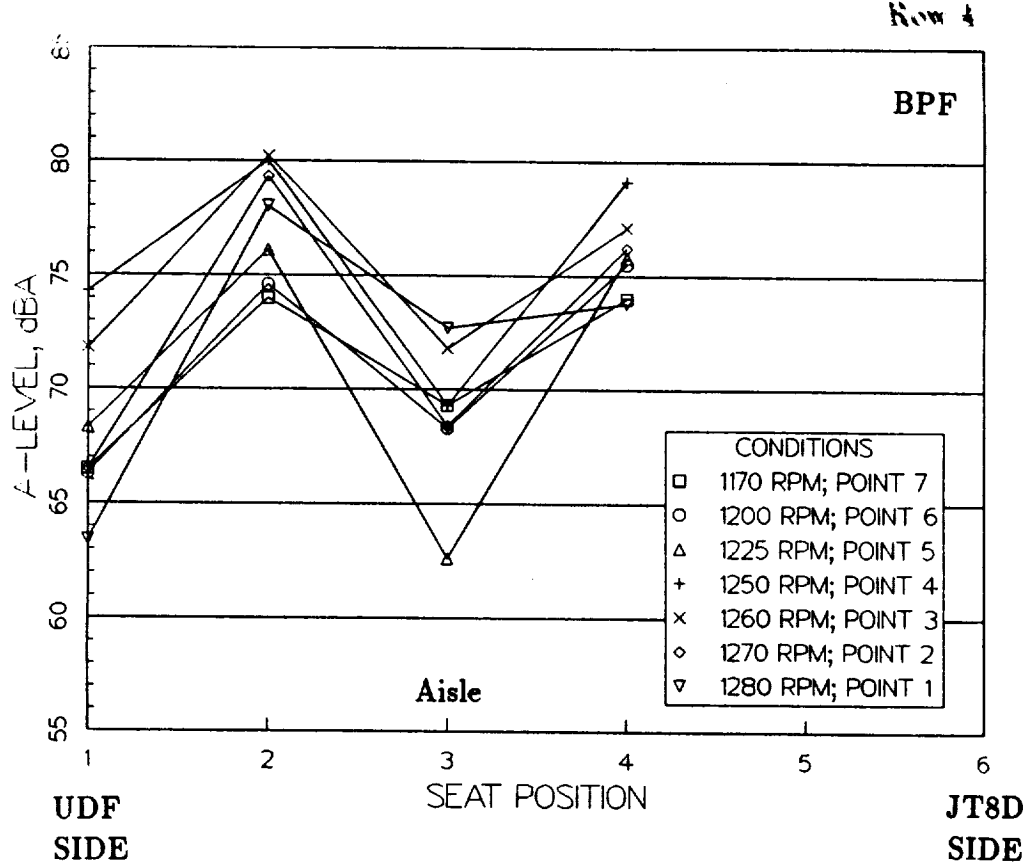


FIGURE 5-6. Variation of the BPF A-weighted Level in Row 4 and Row 6.

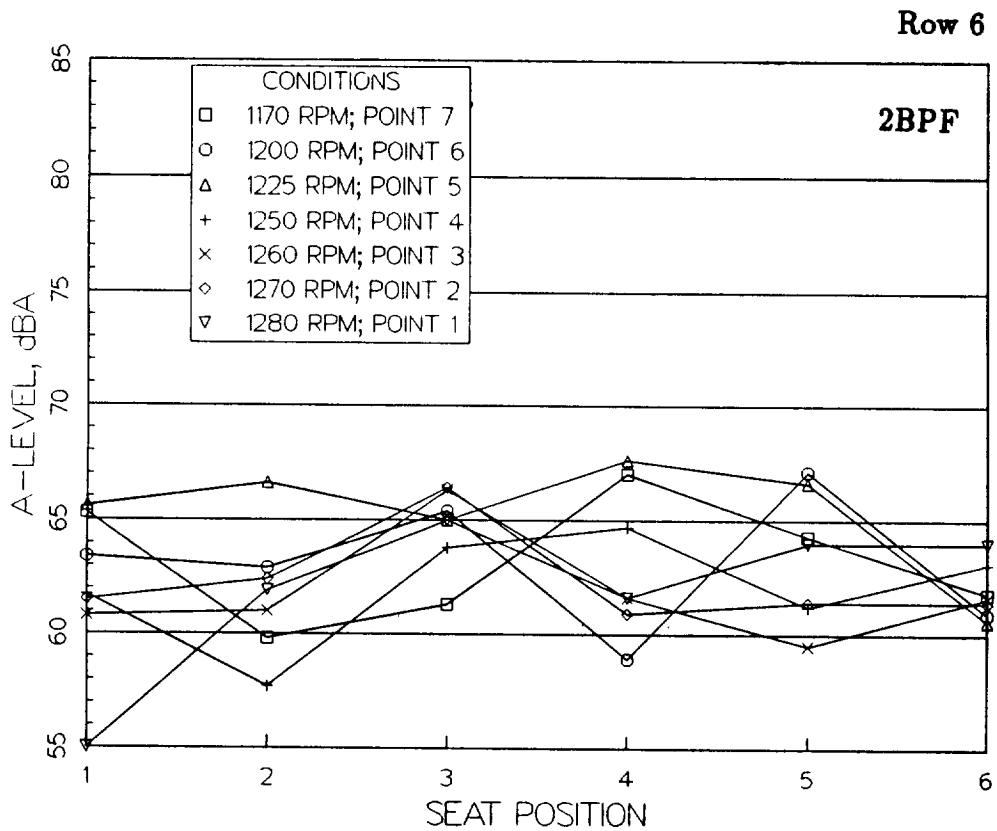
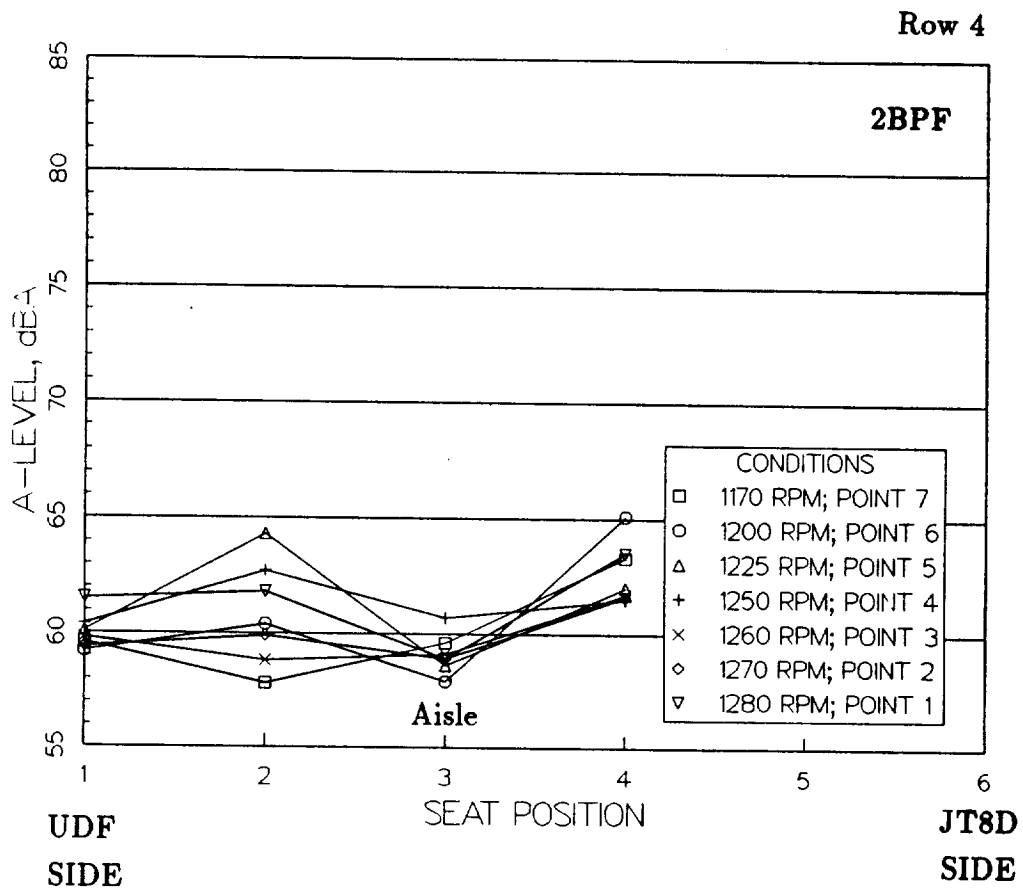


FIGURE 5-7. Variation of the 2BPF A-weighted Level in Row 4 and Row 6.

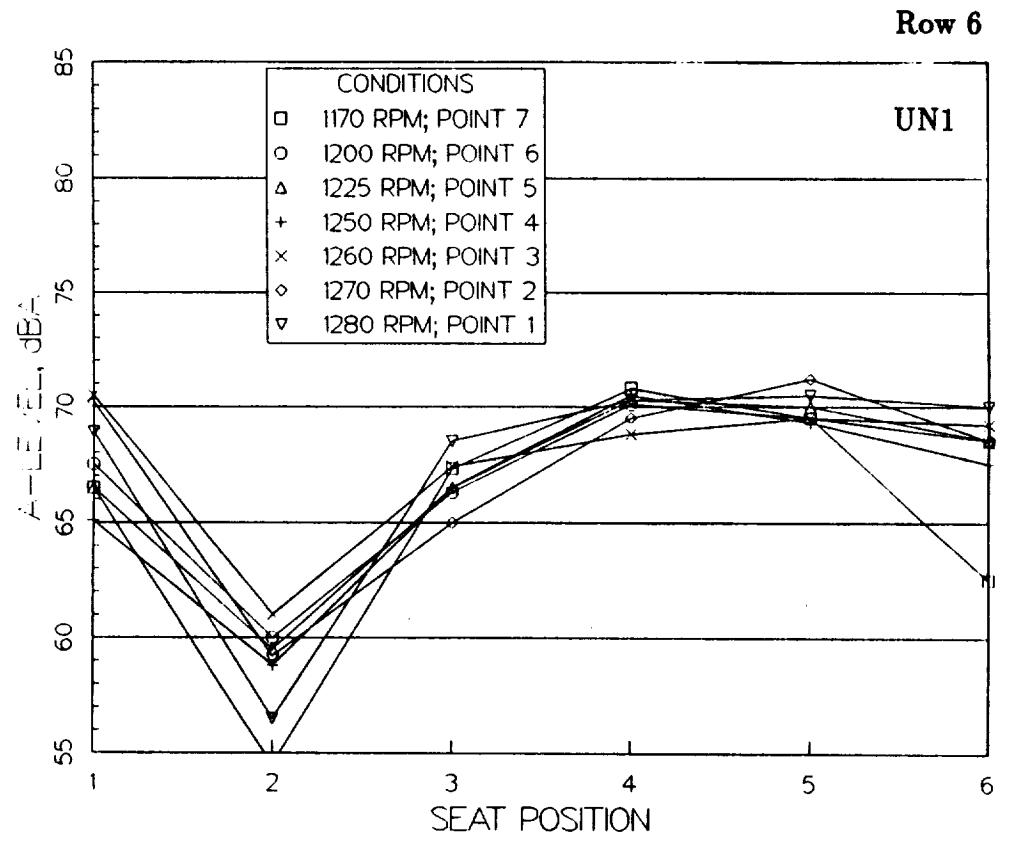
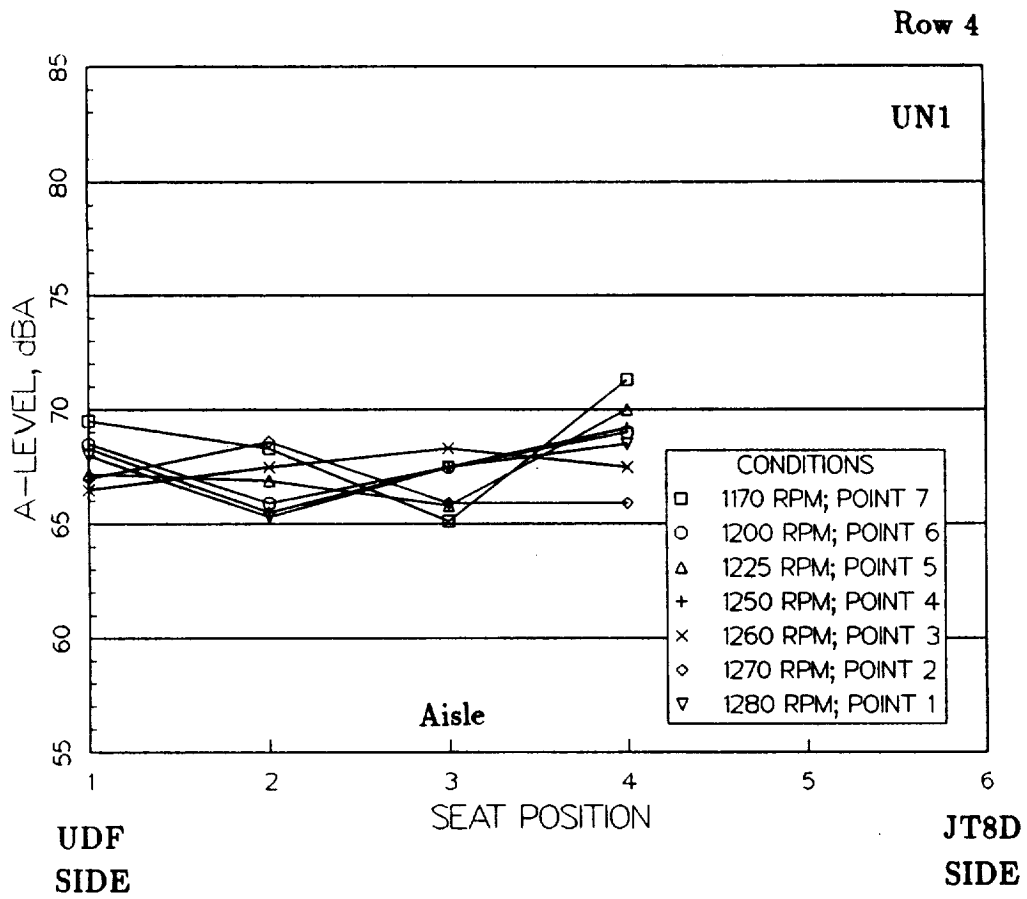


FIGURE 5-8. Variation of the UN1 A-weighted Level in Row 4 and Row 6.

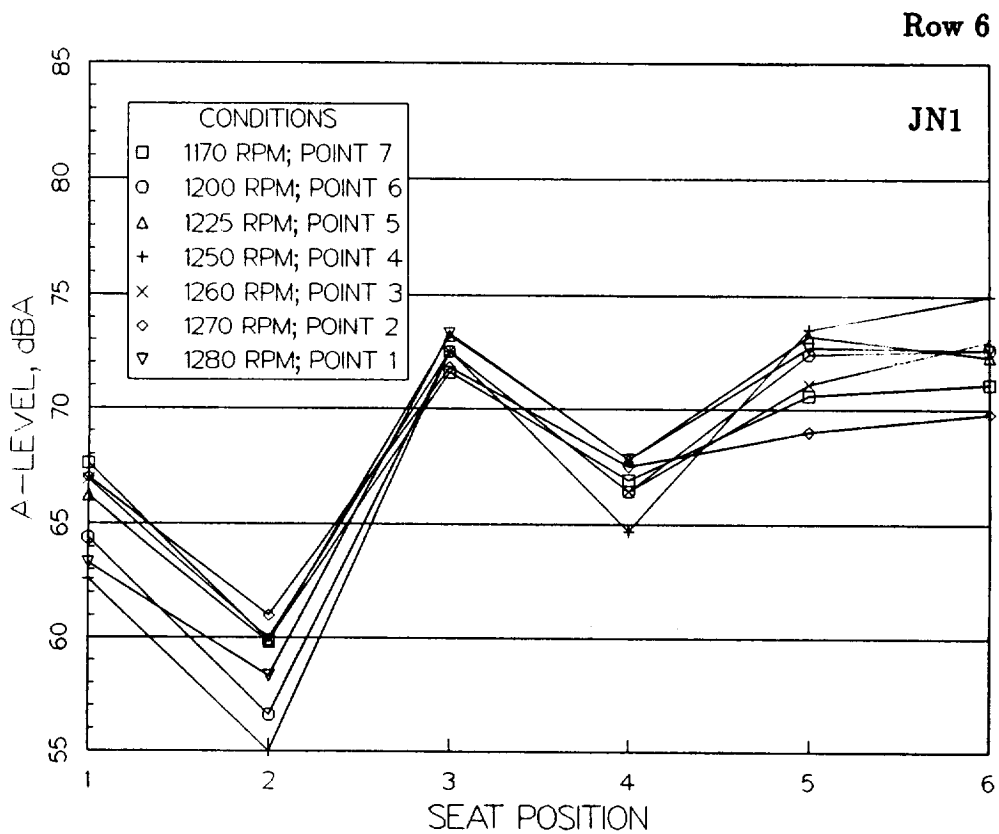
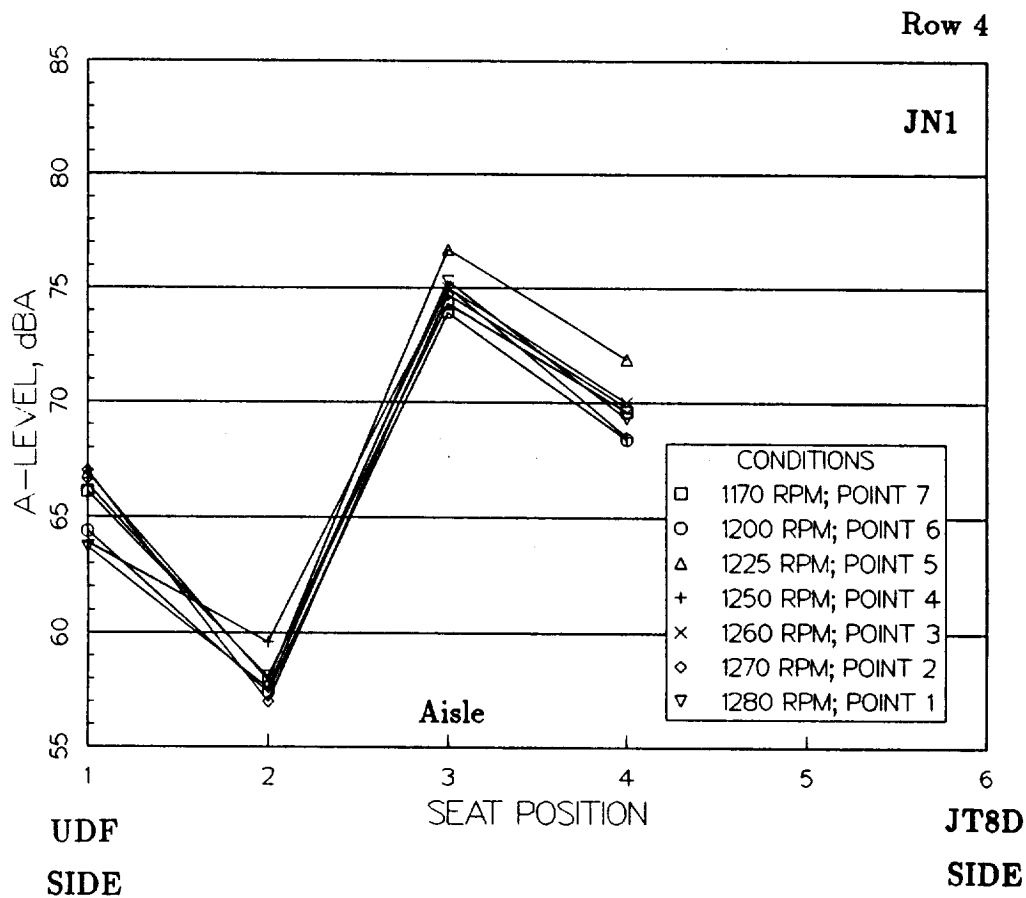


FIGURE 5-9. Variation of the JN1 A-weighted Level in Row 4 and Row 6.

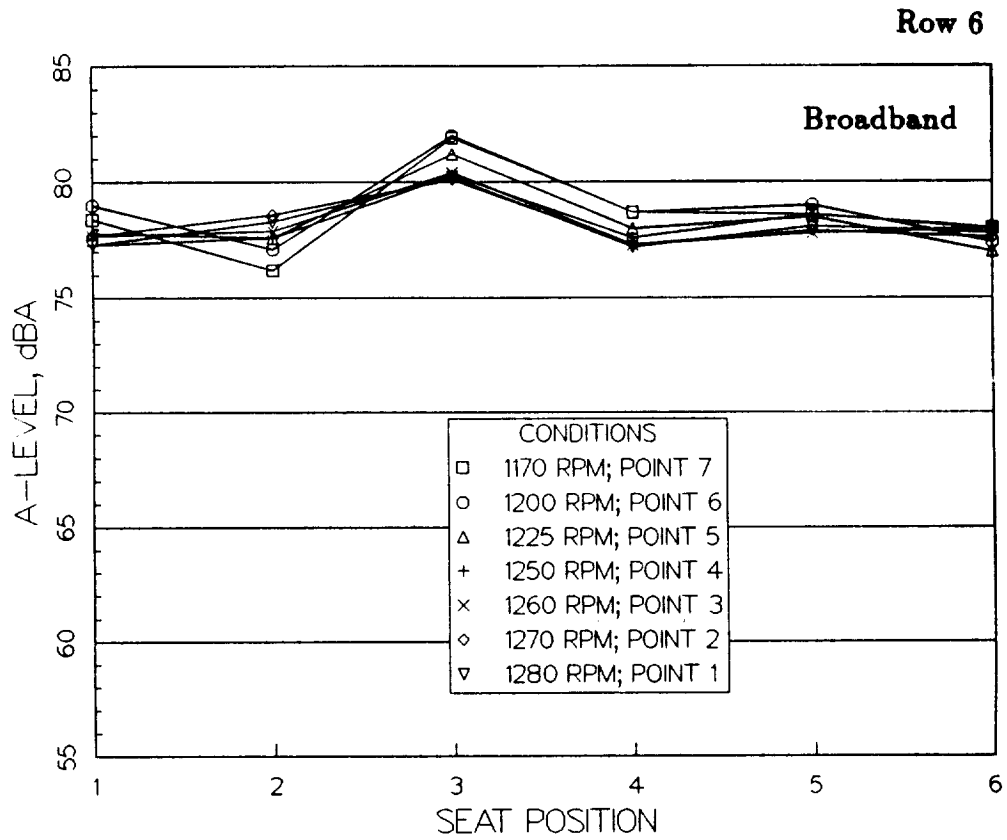
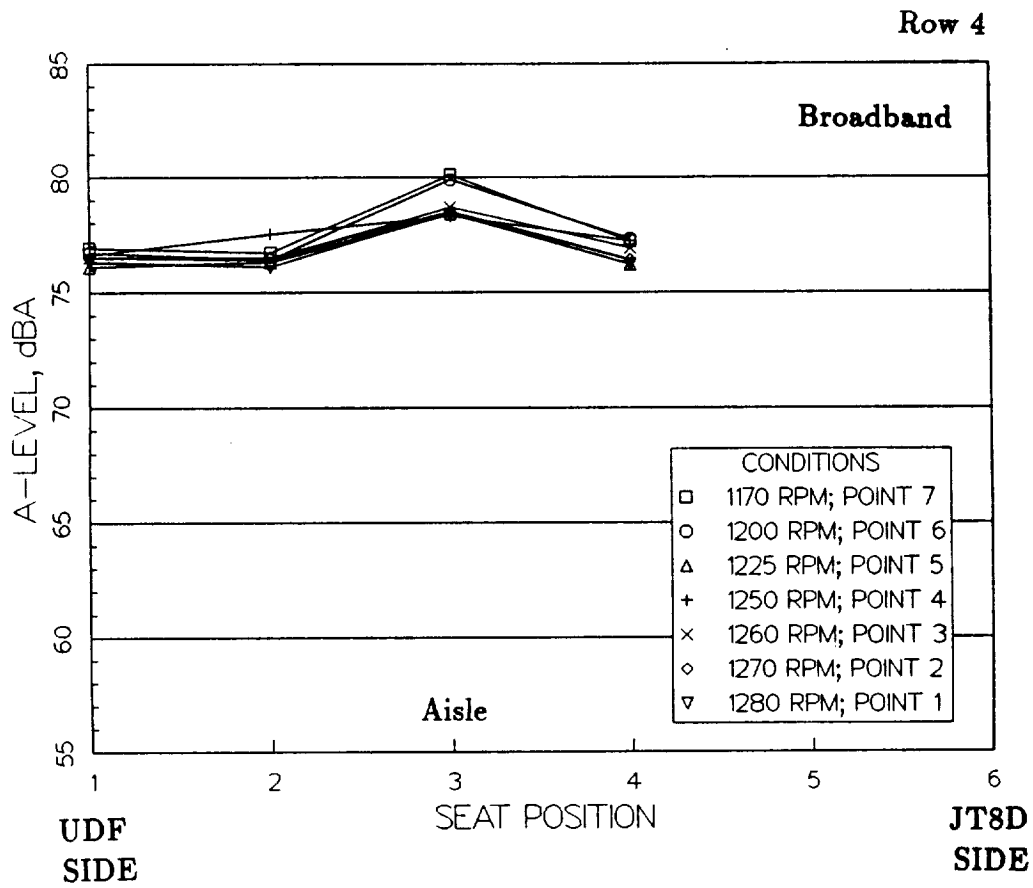


FIGURE 5-11. Variation of the Broadband Noise Levels in Row 4 and Row 6.

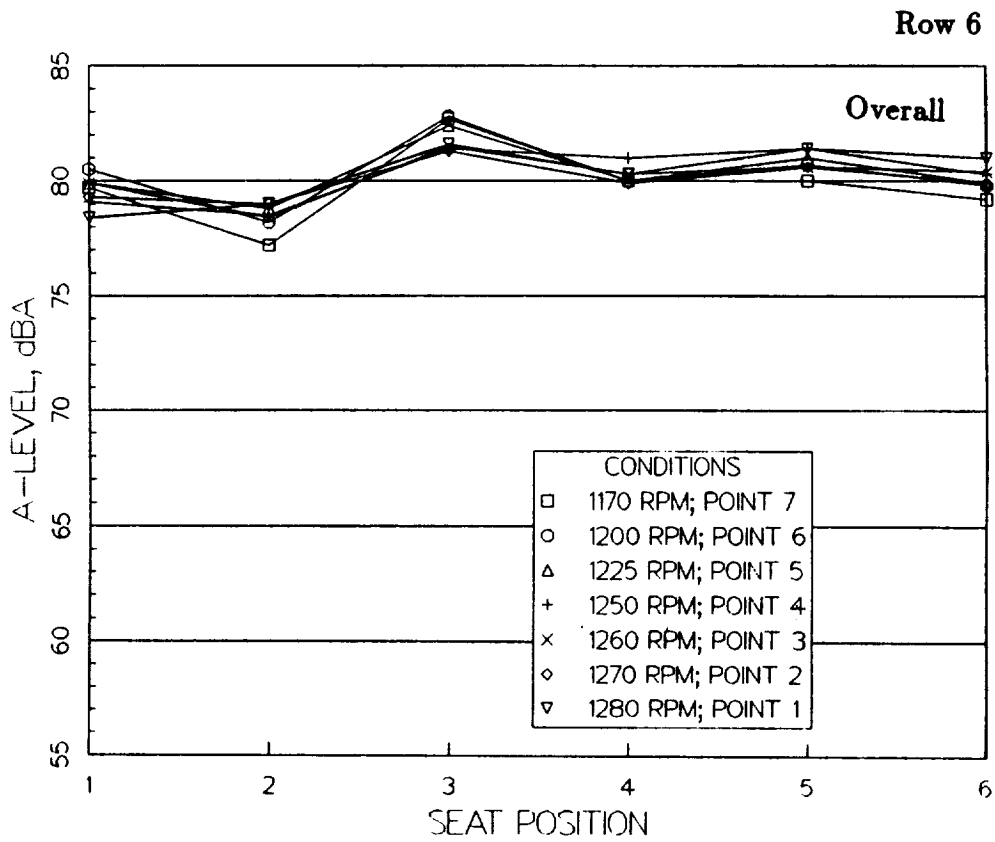
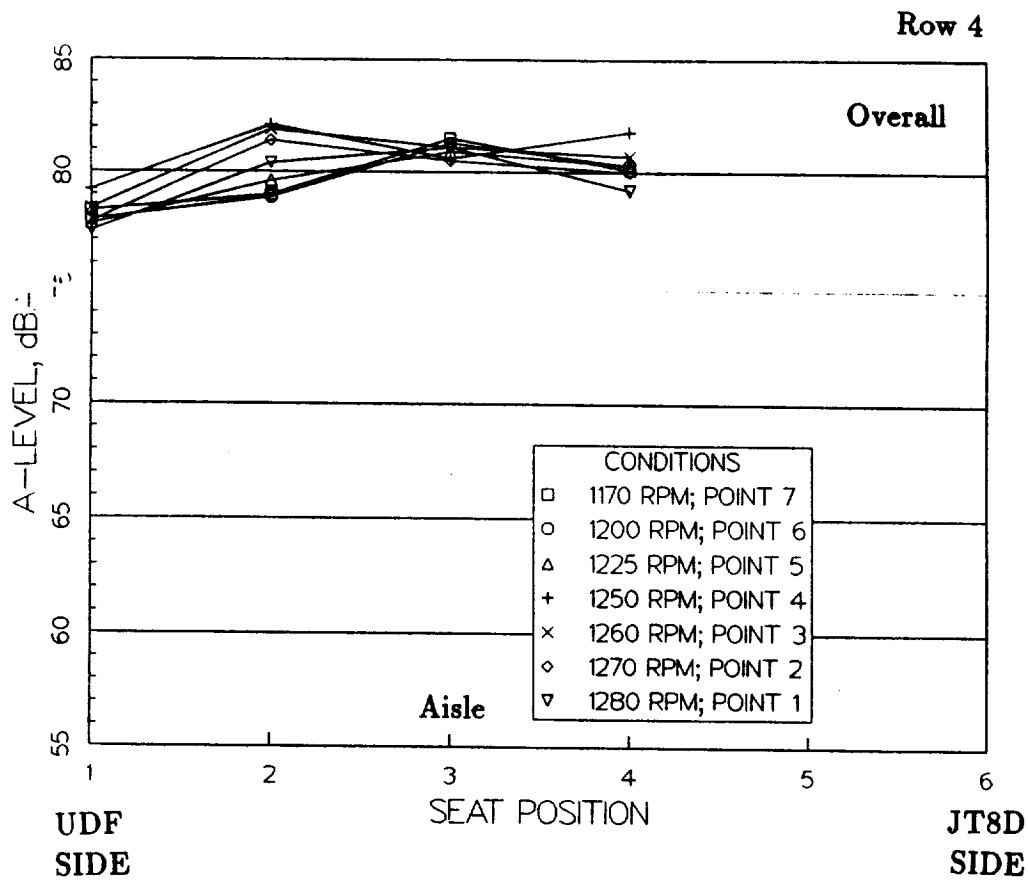


FIGURE 5-12. Variation of the Overall A-weighted Levels in Row 4 and Row 6.

6 Comparison of 10x8 and 8x8 Data

In this section, comparisons between 10x8 and 8x8 measurements are presented. The 10x8 data were collected during Flight 1964, flown at 35,000 ft at a Mach number of 0.76. As for 8x8 Flight 1955, the aircraft interior was fully furnished and configured with the complete Quiet Cabin package of noise control treatments (that is, Configuration 4). The 10x8 data were acquired at nominal rotor speeds of 1240, 1256, 1264 and 1278 rpm. The blade passage frequencies of the forward/aft rotors associated with these speeds are 207/165, 209/168, 211/169, and 213/170 Hz, respectively.

It should be noted that this rotor speed range for the 10x8 flights is much narrower than the range for the 8x8 flights, thereby limiting comparisons. In addition, selected exterior and interior transducers were relocated: some fuselage microphones were moved to the pylon, some pylon accelerometers were moved to fuselage frames, and the number of interior microphones was reduced and several were relocated either inside the cabin or elsewhere. While these changes reveal new information, they also limit direct comparisons between transducers.

6.1 Acoustic and Vibratory Loads

6.1.1 Exterior Noise Levels

Figure 6-1 compares narrowband spectra measured at the same aft fuselage location (above the pylon, in the forward rotor plane). In the 8x8 spectrum, tones at BPF(8) and its harmonics are evident, as are the individual subharmonic tones at approximately 21 Hz intervals. In the 10x8 spectrum there are two sets of BPF tones, for the BPF(10) and BPF(8) harmonics. In addition, occasional interaction tones appear in the spectrum (at BPF(10) + BPF(8), for example).

Comparisons of BPF levels versus rotor speed on the fuselage in the rotor planes are shown in Figures 6-2a and 6-2b. Figure 6-2a shows 8x8 engine BPF(8) levels above the pylon in the forward and aft rotor planes (from Figure 5-1). Superimposed on the figure are the 10x8 engine levels measured at the same locations. For this comparison, the BPF(10) and BPF(8) levels of the 10x8 engine have been added together, since the 8x8 engine BPF(8) levels are due to the combined effect of both 8-bladed rotors. However, at both measurement locations the BPF(8) level is significantly higher than the BPF(10) level for the 10x8 engine, so that the summed level is dominated by the contribution from the aft rotor. Figure 6-2a shows that the 10x8 levels are 3 to 5 dB higher in the aft plane than the 8x8 levels, and 1 dB lower in the forward plane.

In contrast, Figure 6-2b shows corresponding data measured on the fuselage below

the pylon in the forward plane (note that the two measurement points are shifted slightly). Here, the 10x8 engine levels, which are dominated by the BPF(10) levels, are 3 to 4 dB lower than the 8x8 engine levels.

It should be noted that at the upper microphone locations the 10x8 BPF levels are dominated by the noise of the aft (8-bladed) rotor, while at the lower microphone locations the 10x8 BPF levels are dominated by the noise of the forward (10-bladed) rotor. As discussed in Section 5 for the 8x8 exterior data, this reflects the clockwise rotation of the aft rotor towards the top of the fuselage and the counterclockwise rotation of the forward rotor towards the bottom of the fuselage.

Figures 6-2a and 6-2b indicate that the variation of level with rpm is similar for the two engine configurations, although the speed range may be too narrow for significant trends to emerge. For the measurement locations studied, the highest aft fuselage levels were measured during the 10x8 engine flight tests.

When the 8x8 engine flight tests were conducted, the blade pitch was varied from test point to test point to maintain constant shaft horsepower for all rotor speeds. However, during the 10x8 engine flight tests shaft horsepower varied with rotor speed. Estimates of the relative differences between 10x8 and 8x8 engine BPF levels were made, taking these shaft horsepower differences into account, as well as the differences in rotor diameter, blade count, and tip clearance between the two propulsor configurations. These estimates agree in trend with the measurement results discussed above: higher BPF levels in the aft rotor plane and lower BPF levels in the forward plane for the 10x8 engine compared to the 8x8 engine, and higher maximum levels on the aft fuselage for the 10x8 engine.

6.1.2 Pylon and Fuselage Vibration Levels

Figures 6-3a and 6-3b present comparisons between 10x8 and 8x8 pylon accelerations. In Figure 6-3a, the accelerations measured at the aft engine mount are compared. In the vertical direction, 10x8 accelerations are considerably lower than 8x8 accelerations. In the longitudinal direction, 10x8 accelerations are comparable to or lower than 8x8 accelerations.

In Figure 6-3b, comparisons of 10x8 and 8x8 accelerations measured inboard at the forward spar show that BPF(8) vertical accelerations are considerably lower for the 10x8 engine, while BPF(10) vertical accelerations for the 10x8 engine are somewhat higher than 8x8 BPF accelerations in the lower portion of the rpm range, and somewhat lower than 8x8 BPF accelerations in the higher portion of the rpm range. The vertical accelerations at UN1 are comparable for the two systems.

Summarizing, these figures show that 10x8 vibration levels in the pylon are typically

the same or lower than 8x8 levels.

Finally, Figure 6-4 compares 10x8 and 8x8 acceleration levels measured on the fuselage in the forward rotor plane; the 10x8 levels are a summation of the BPF(10) and BPF(8) levels, but are dominated by the BPF(8) levels. The variation with rpm is similar for the two systems. However, the figure shows that 10x8 levels are higher than 8x8 levels; this observed trend is opposite to the trend in noise levels at the nearby fuselage location (shown in Figure 6-2a).

6.2 Cabin Noise Levels

Figures 6-5a through 6-5e present comparisons between 10x8 and 8x8 cabin noise levels, for each of five seat positions in the aft cabin where levels were monitored in both sets of tests. On each figure, the overall A-level and broadband and tonal components measured during 10x8 and 8x8 flights over the same range of rotor speeds are presented.

The figures show that overall levels for the two systems are comparable at positions 1 and 3 in row 6 and position 1 in row 4, and are lower (by about 2 dB) for the 10x8 configuration at position 4 in row 6 and position 3 in row 4. Broadband levels are comparable for the two engine configurations at each seat; the differences in overall levels at the latter two positions are due to lower tone levels during the 10x8 flights.

At position 4 in row 6, the tone component is 2 to 3 dB lower for the 10x8 configuration, while at position 3 in row 4 the 10x8 tonal component is 5 dB lower. Figures 6-6a and 6-6b compare the 10x8 and 8x8 spectra measured at these positions for comparable rotor speed. The JN1, JN2, and UN1 tones are seen to be roughly comparable in level between the 10x8 and 8x8 spectra at both positions, but the 10x8 BPF tones are lower (and at position 3 in row 4 are much lower) than the 8x8 BPF tones.

For the 10x8 engine, exterior acoustic levels at the blade passage frequencies were found to be higher but pylon vibration levels were found to be comparable to or lower than the corresponding levels of the 8x8 engine for the same frequencies. The reduction in interior BPF noise levels in spite of the increase in the exterior BPF acoustic loads suggests that these cabin tones are due to the structureborne propagation of pylon vibrations through the fuselage.

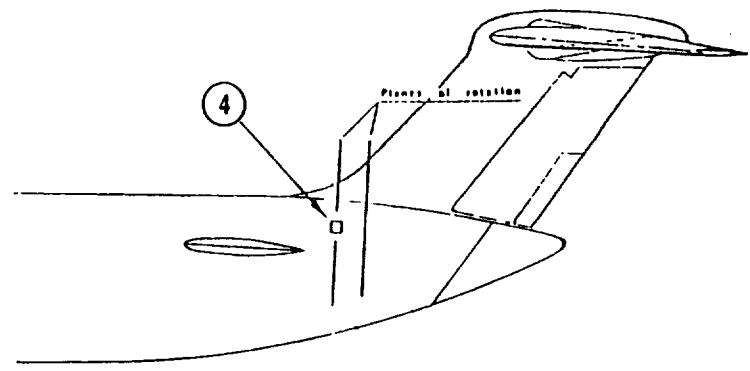
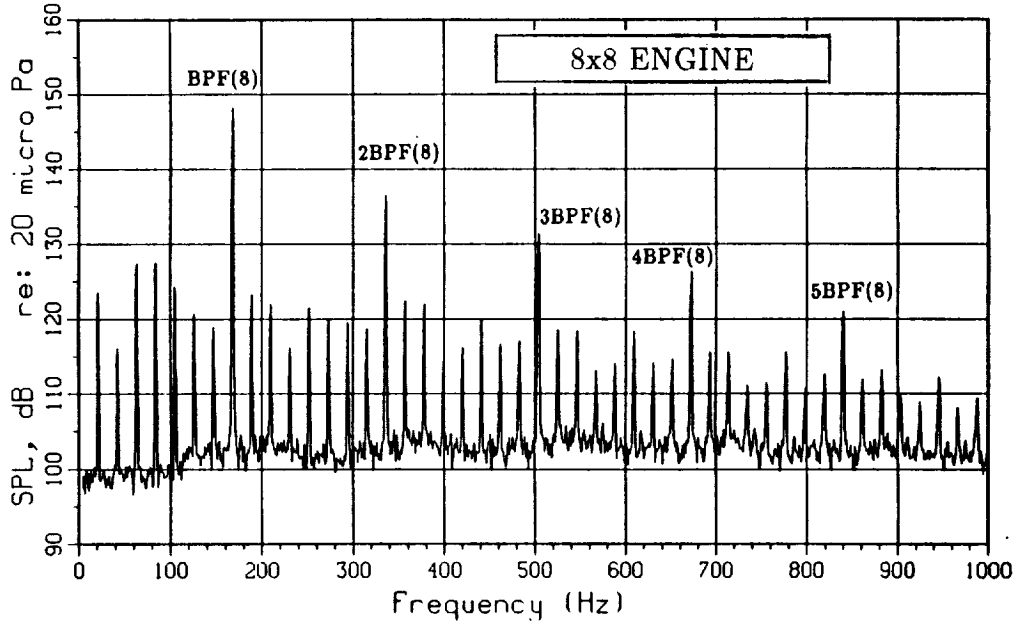
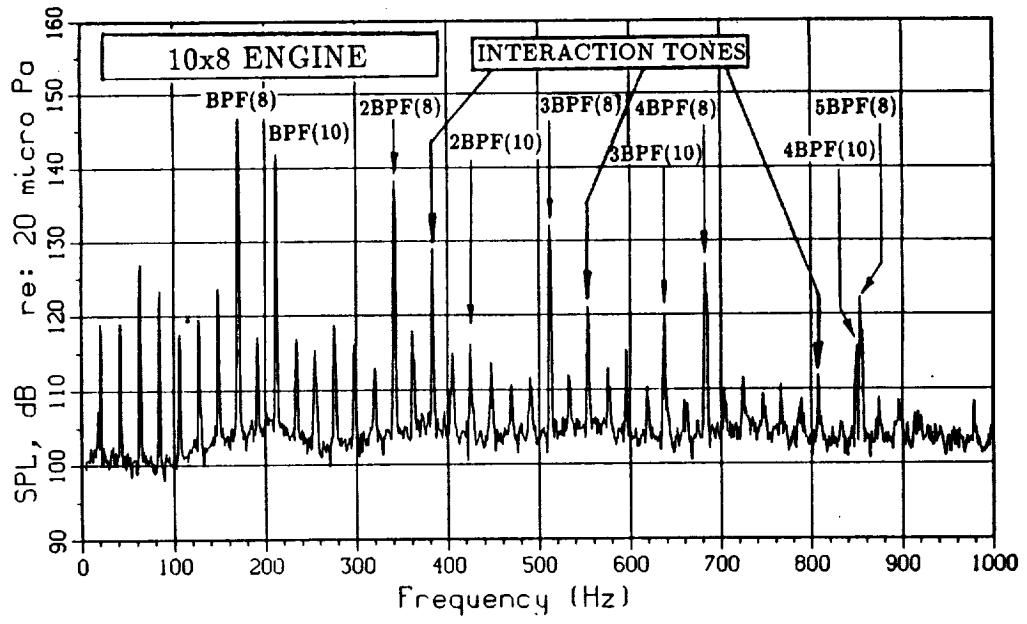


FIGURE 6-1. Comparison of 10x8 and 8x8 Spectra at Exterior Mircophone 4.

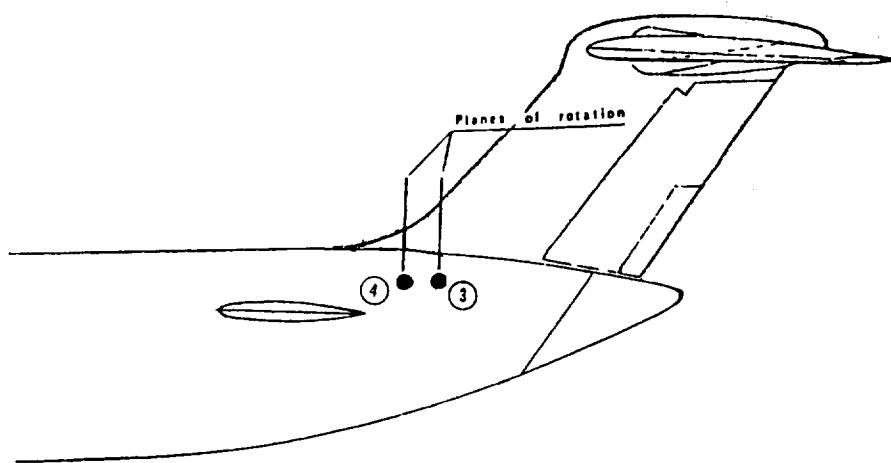
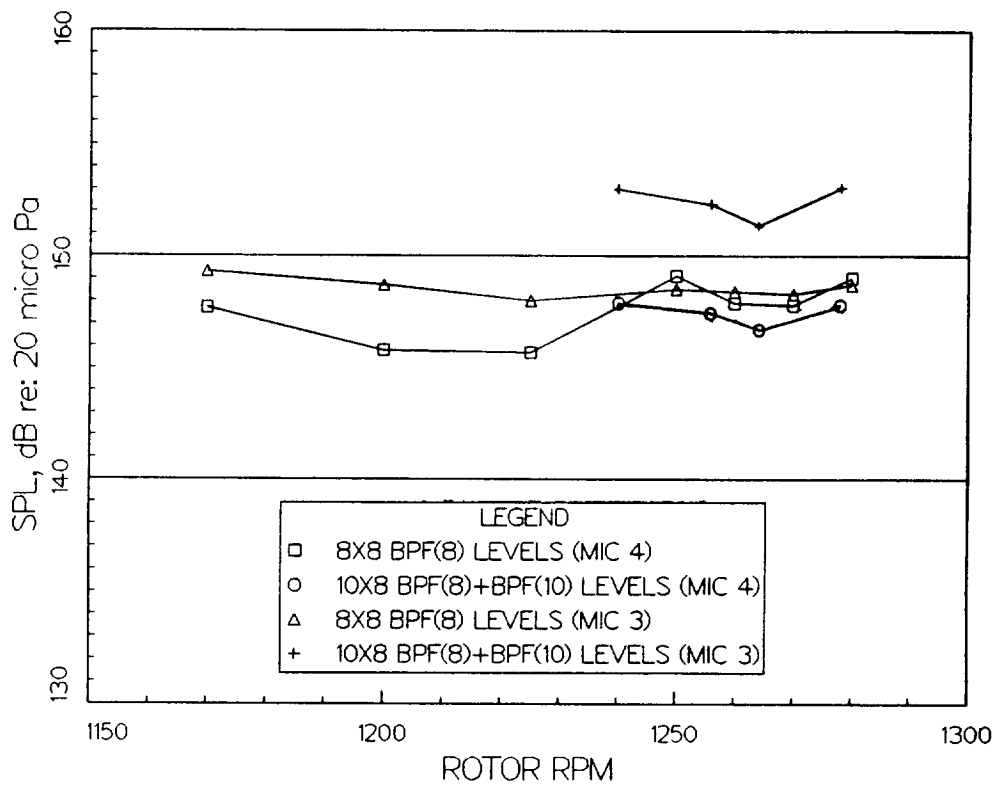


FIGURE 6-2a. Comparison of 10x8 and 8x8 BPF Tones on the Aft Fuselage.

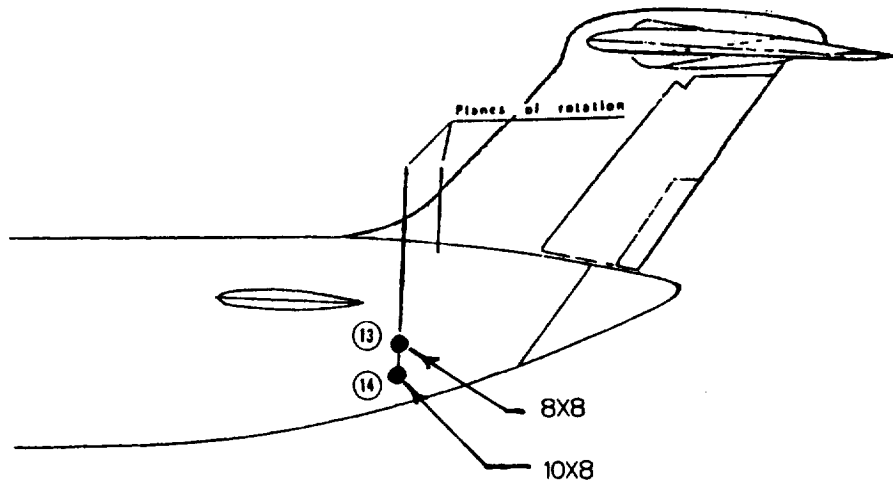
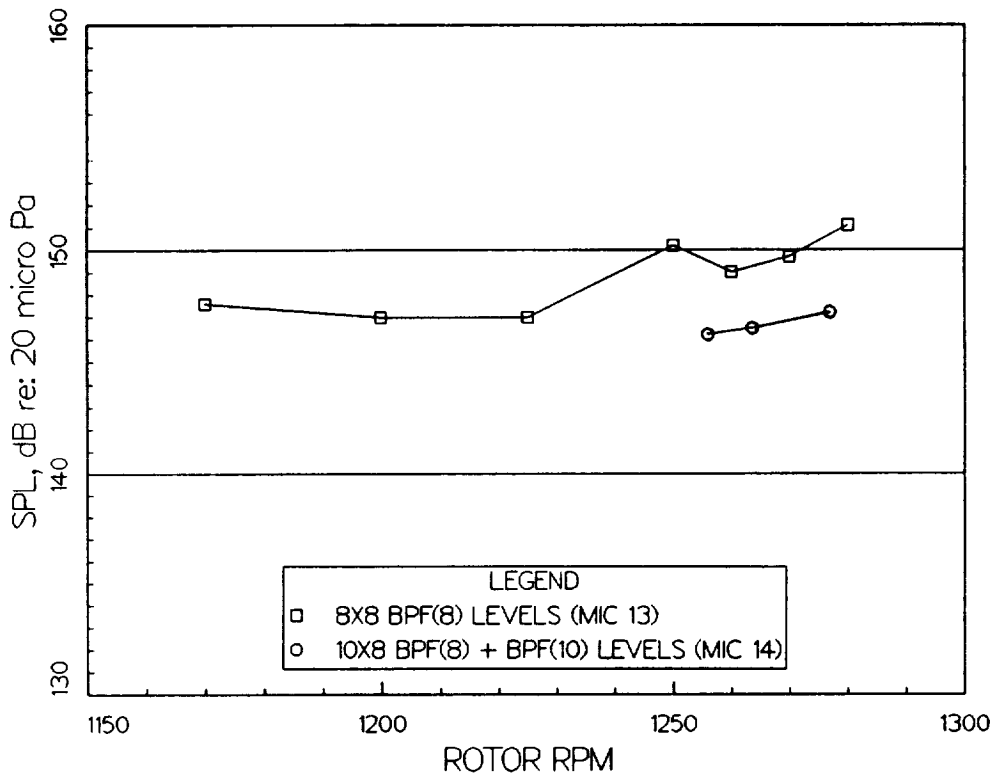


FIGURE 6-2b. Comparison of 10x8 and 8x8 BPF Tones on the Aft Fuselage.

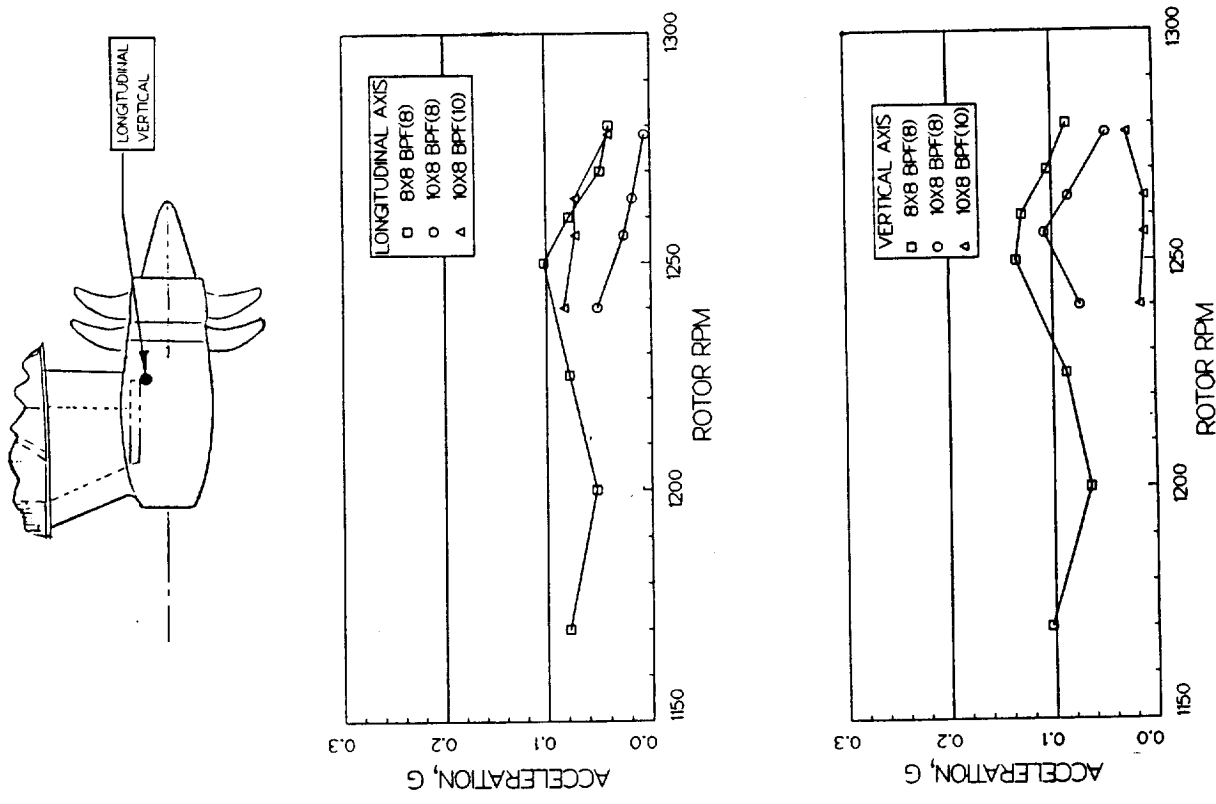
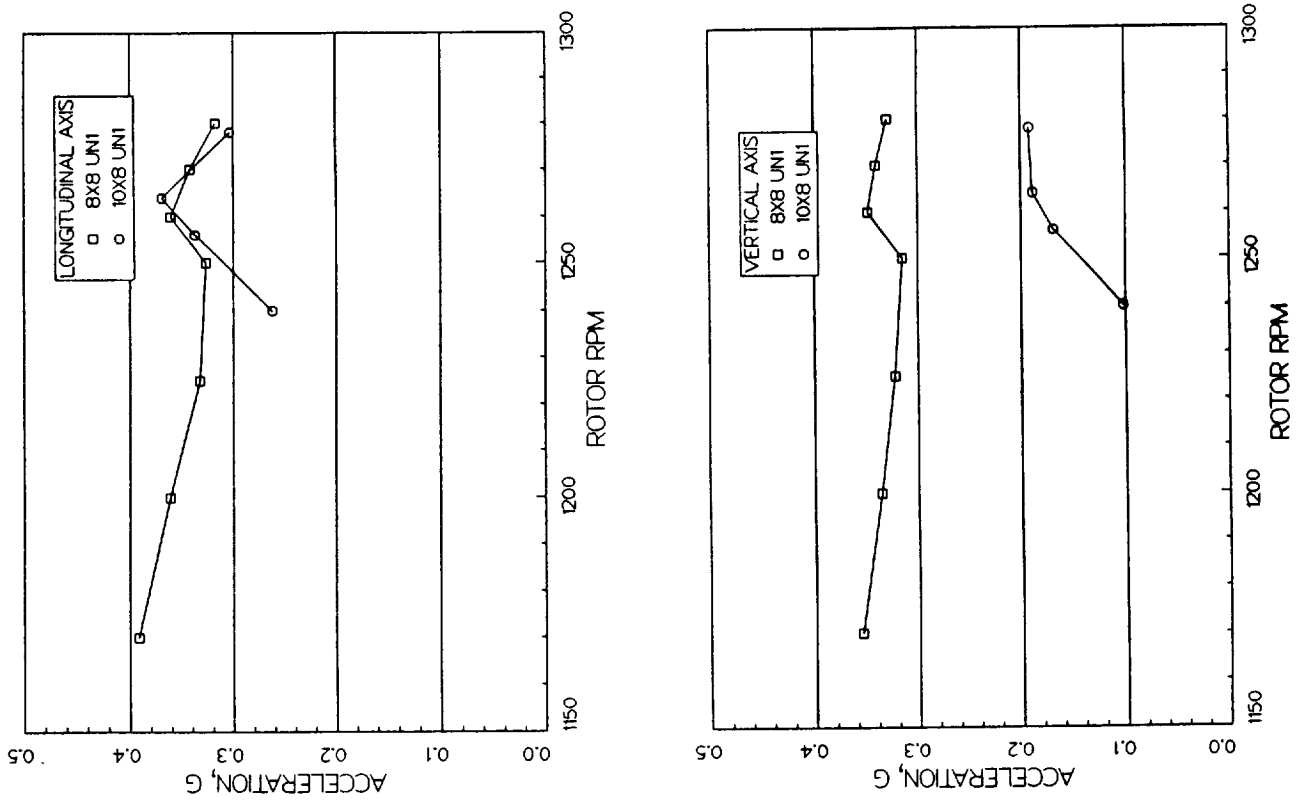


FIGURE 6-3a. Comparison of 10x8 and 8x8 Engine Mount Accelerations.

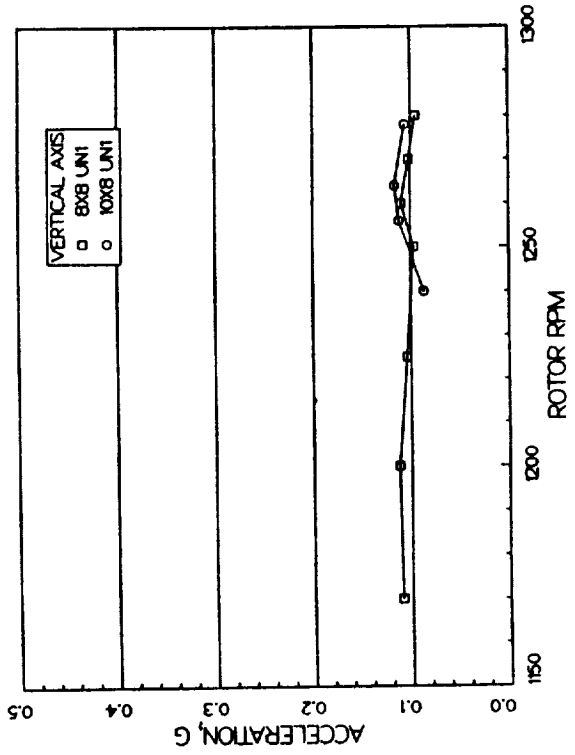
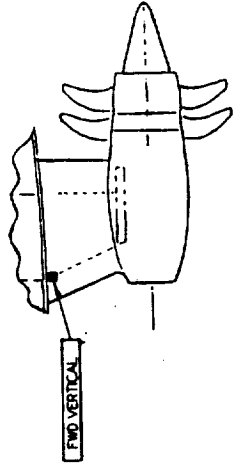
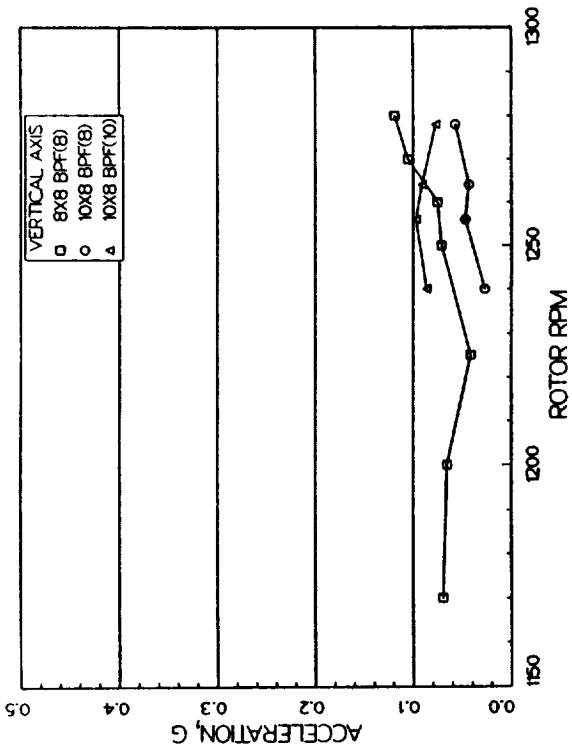


FIGURE 6-3b. Comparison of 10x8 and 8x8 Pylon Accelerations.

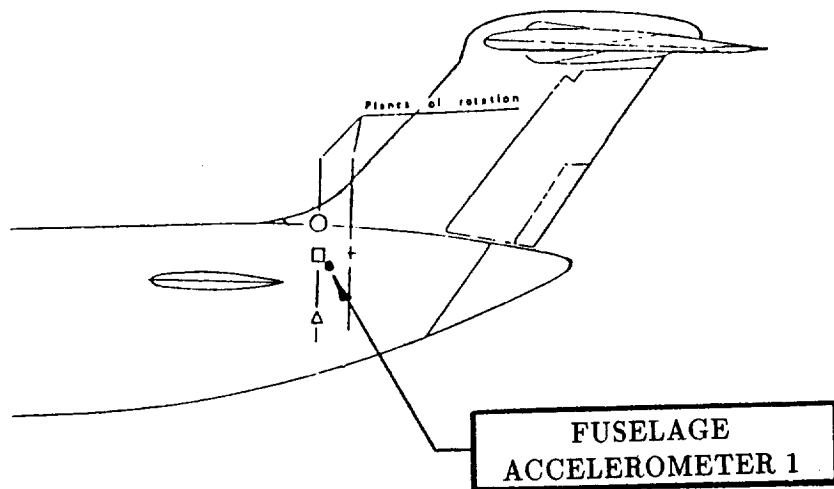
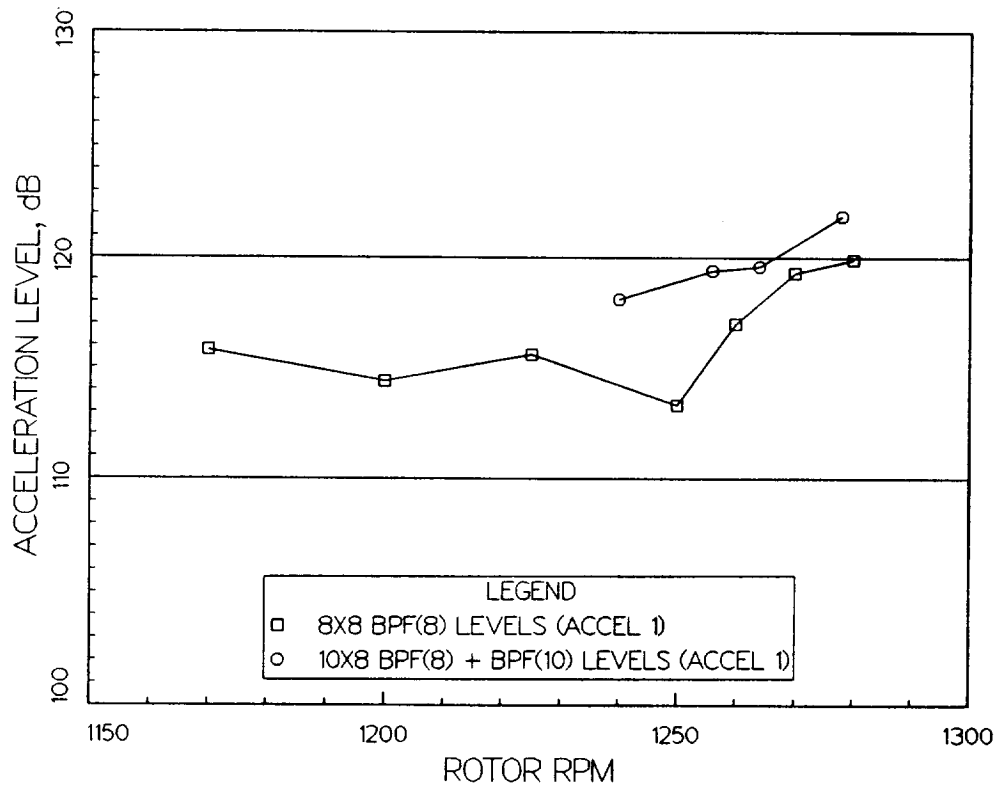


FIGURE 6-4. Comparison of 10x8 and 8x8 Fuselage Acceleration Levels.

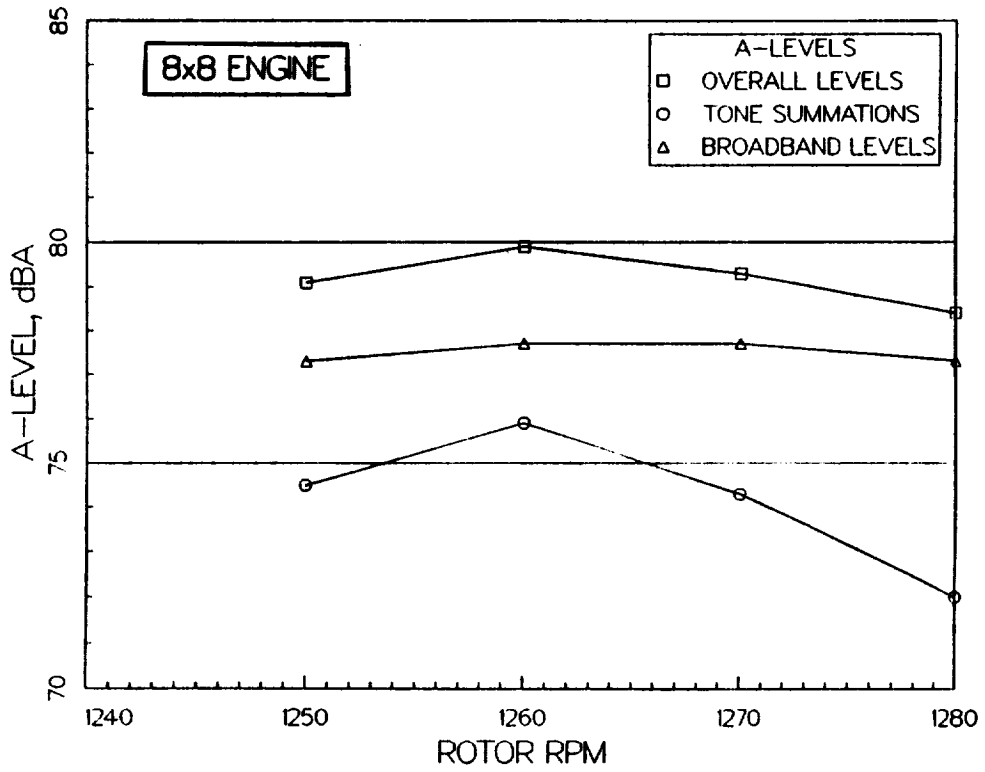
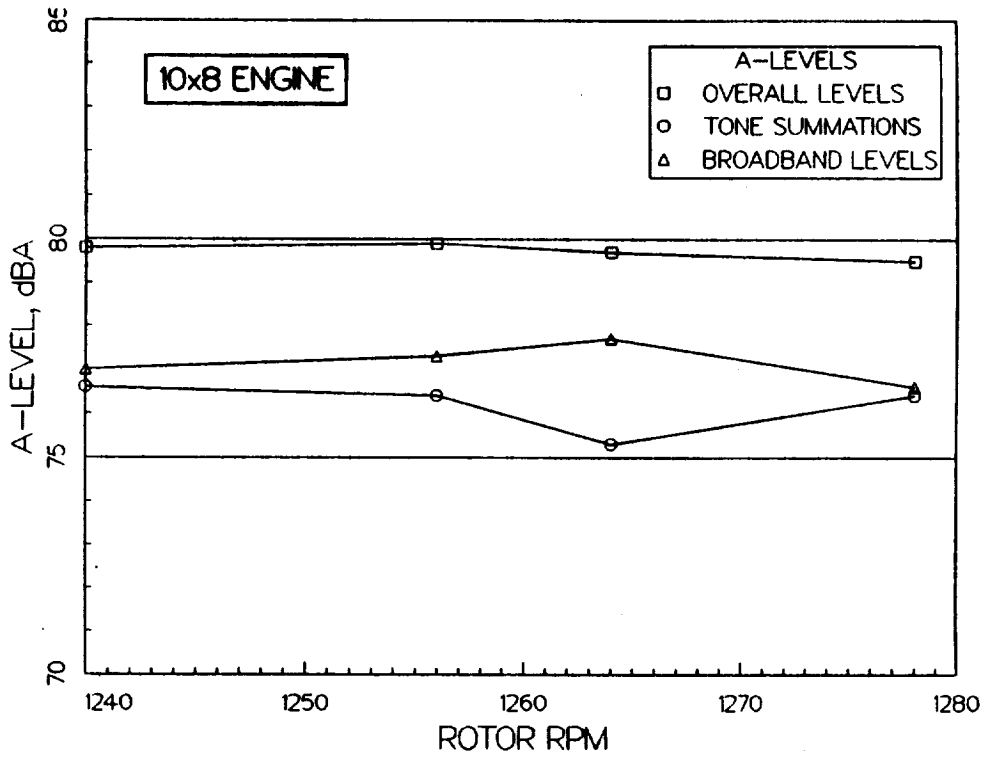


FIGURE 6-5a. Comparison of 10x8 and 8x8 Noise Levels at Row 6 Seat 1.

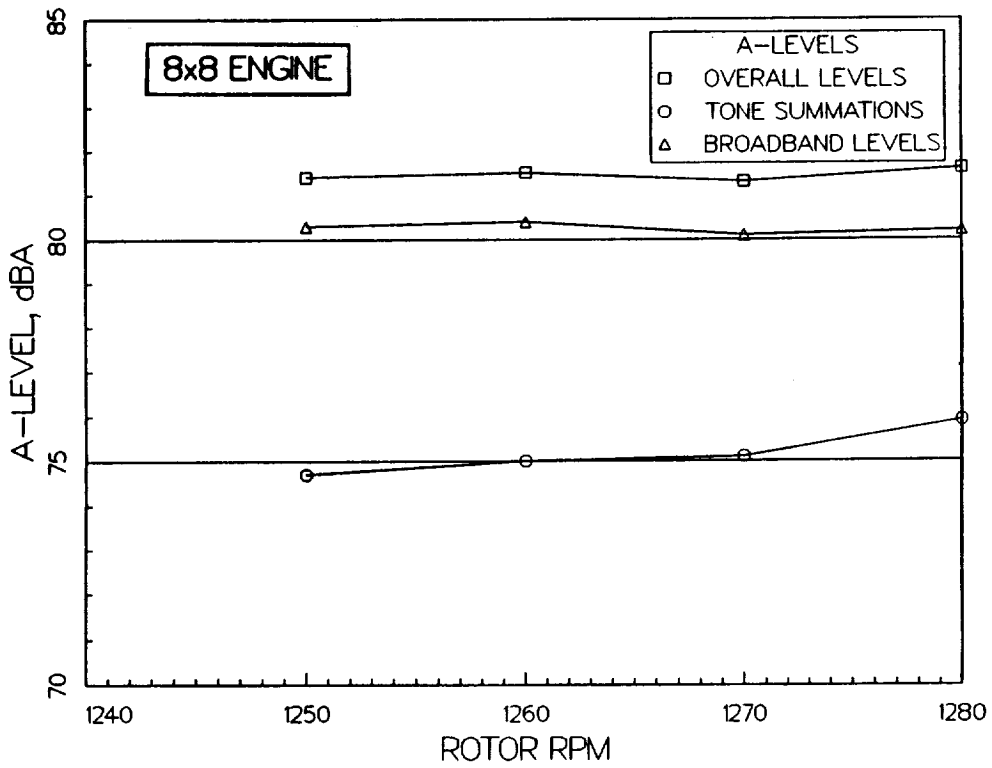
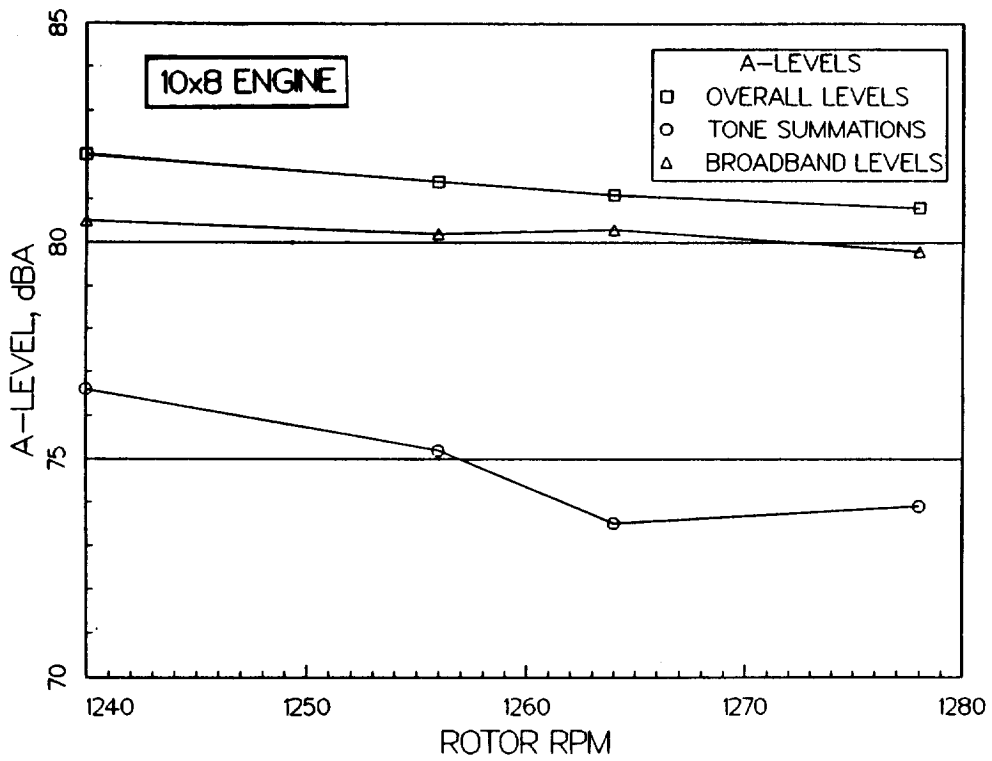


FIGURE 6-5b. Comparison of 10x8 and 8x8 Noise Levels at Row 6 Seat 3.

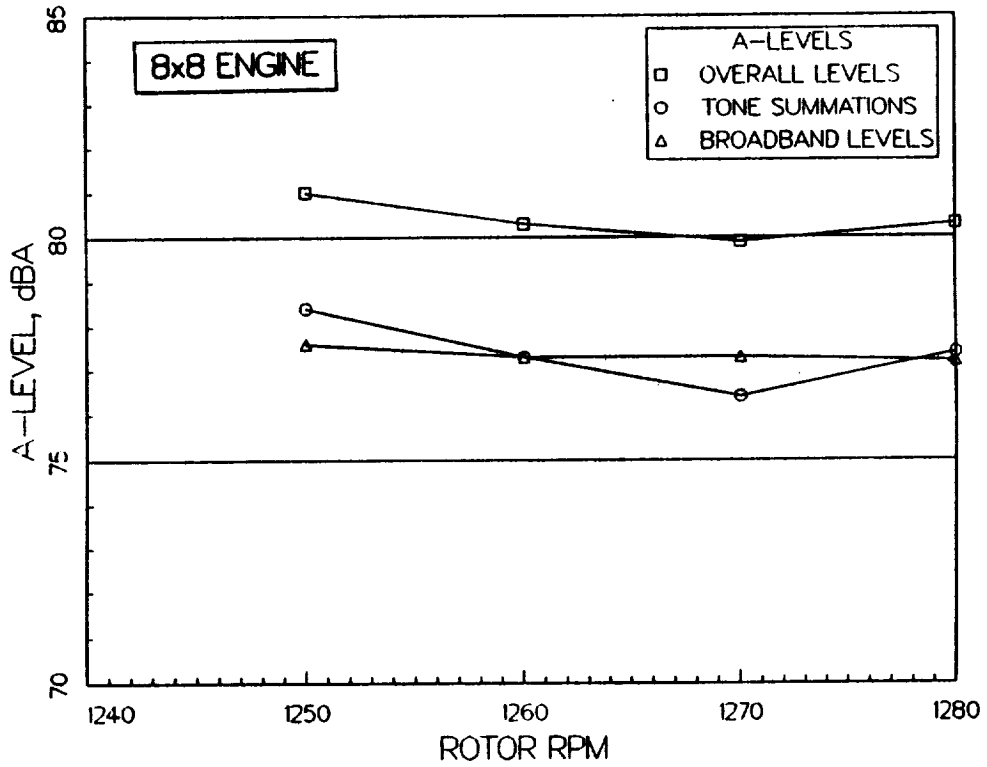
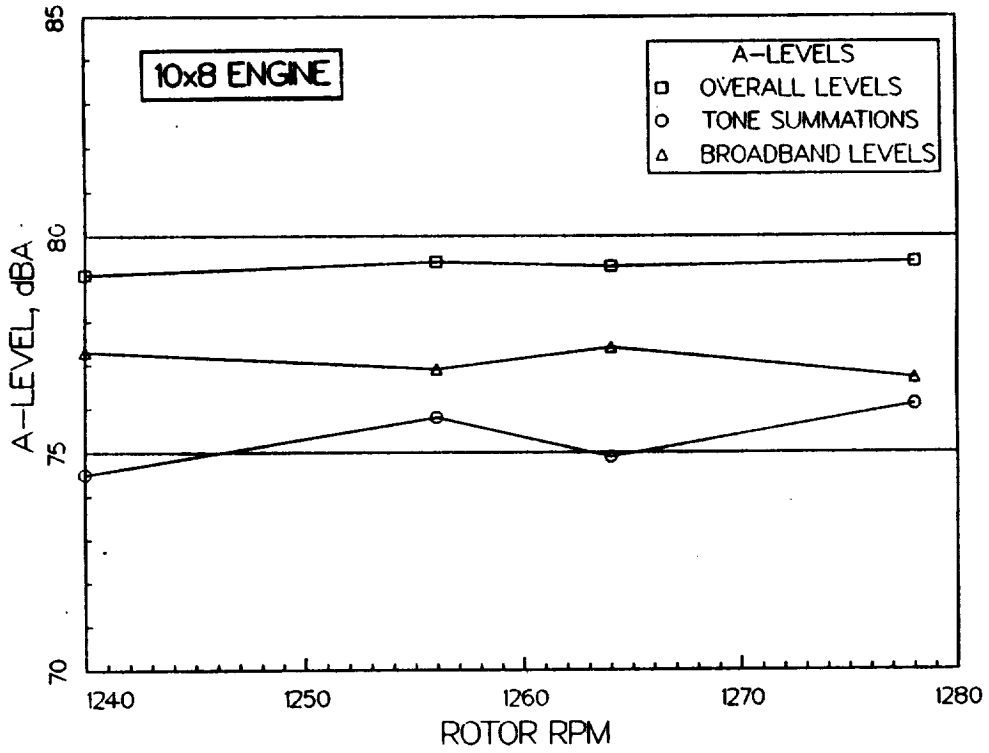


FIGURE 6-5c. Comparison of 10x8 and 8x8 Noise Levels at Row 6 Seat 4.

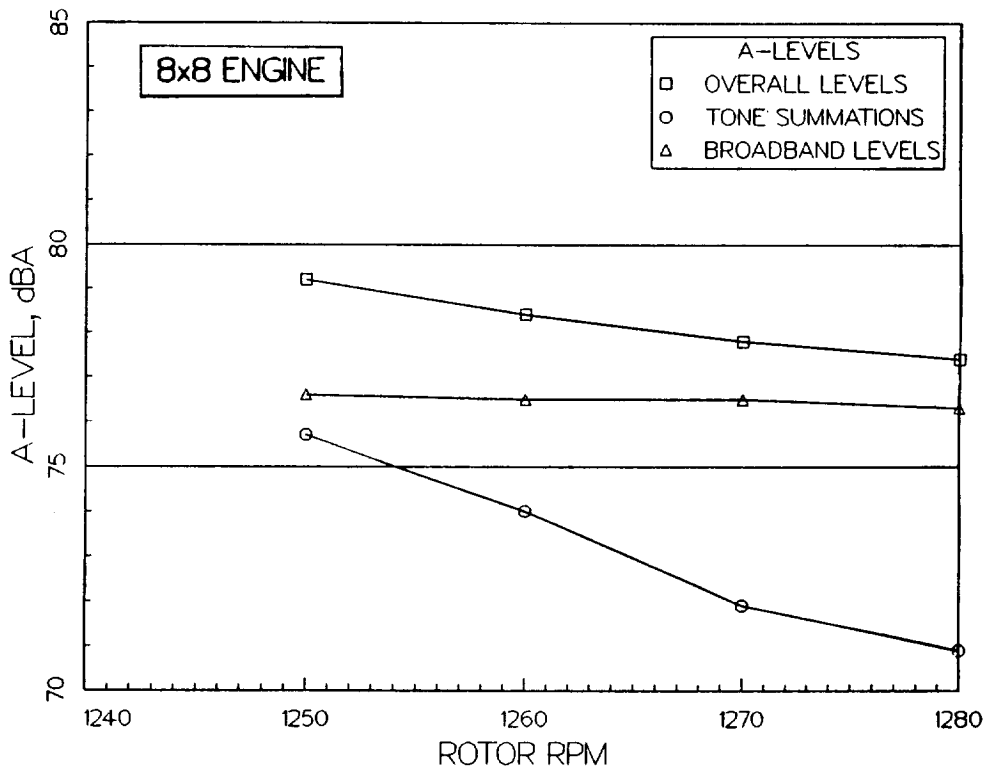
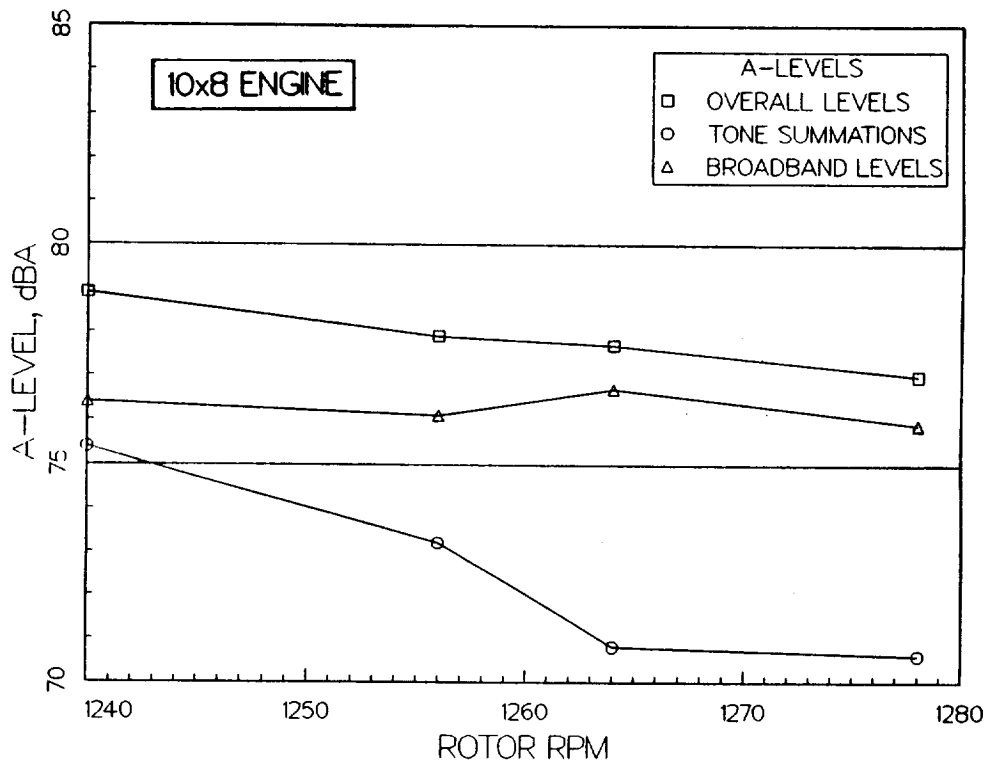


FIGURE 6-5d. Comparison of 10x8 and 8x8 Noise Levels at Row 4 Seat 1.

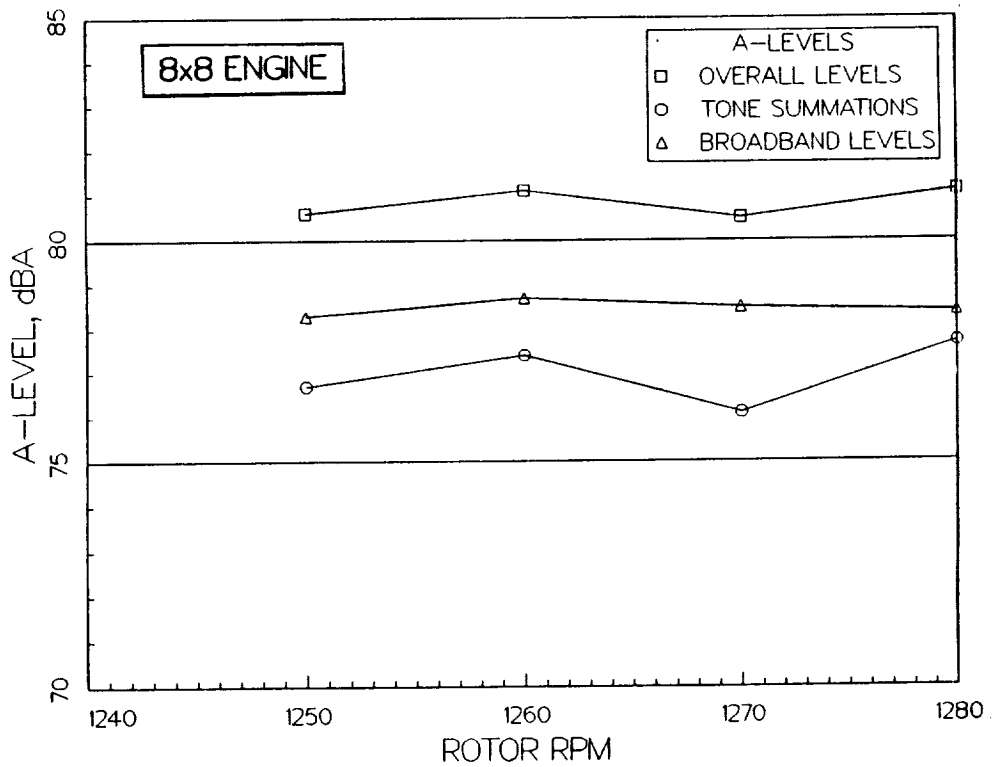
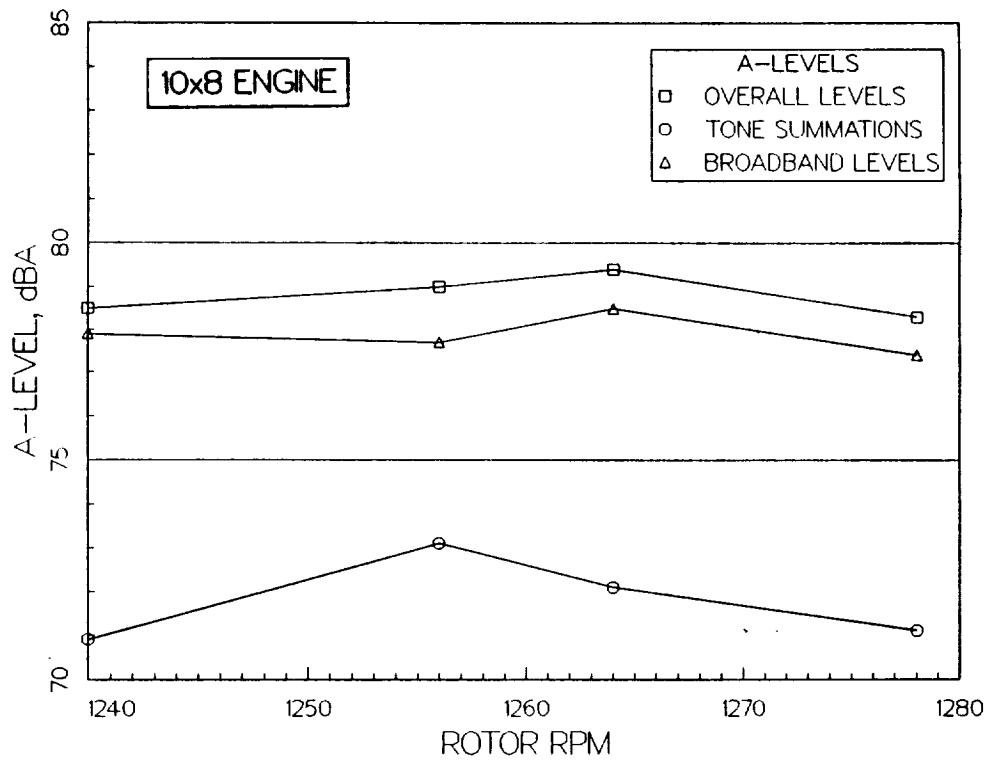


FIGURE 6-5e. Comparison of 10x8 and 8x8 Noise Levels at Row 4 Seat 3.

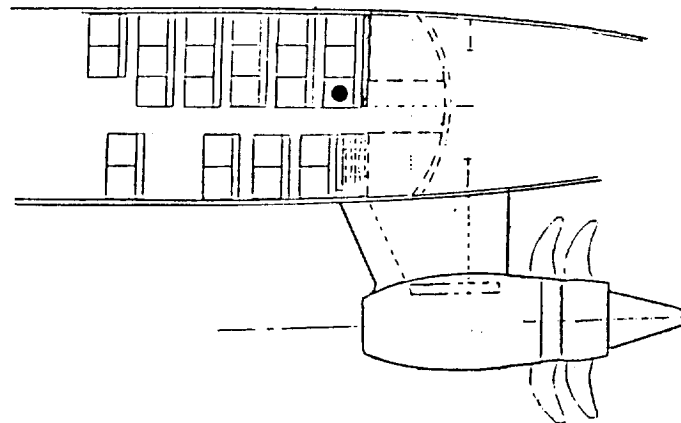
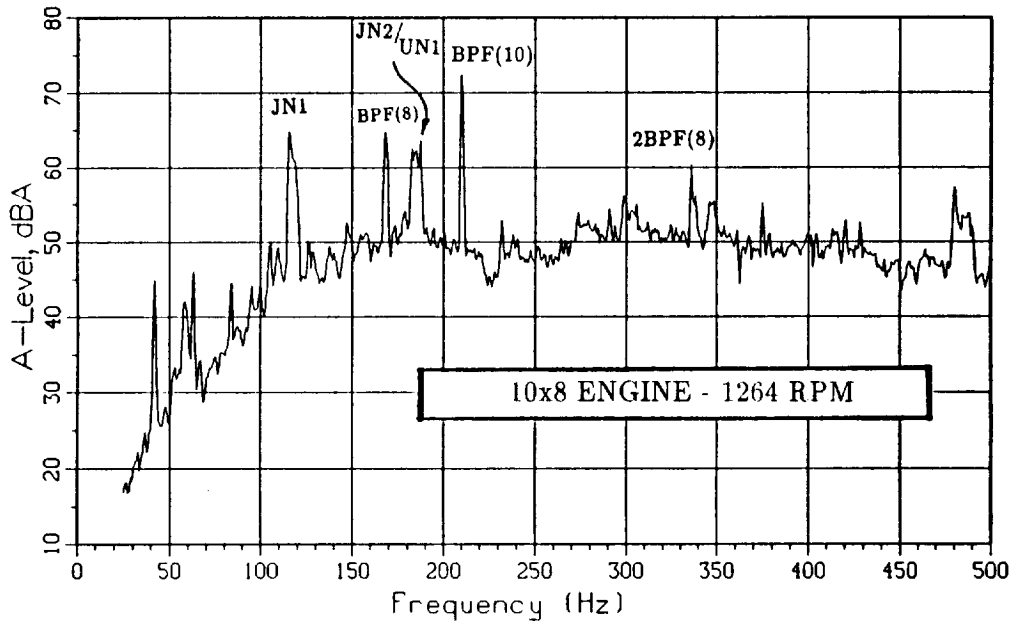
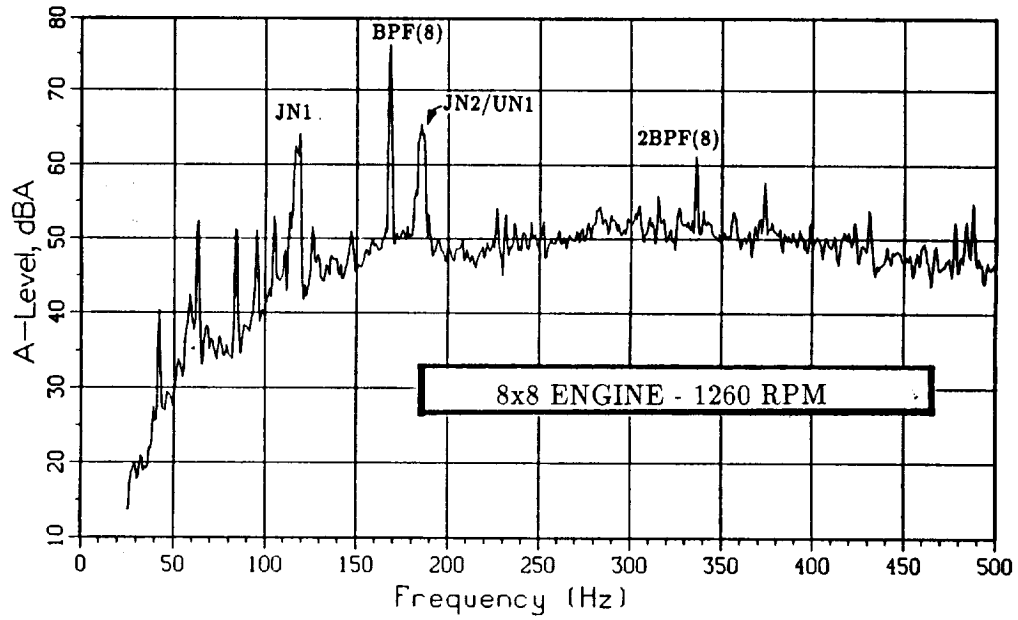


FIGURE 6-6a. Comparison of 10x8 and 8x8 Spectra
Row 6 Seat 4.

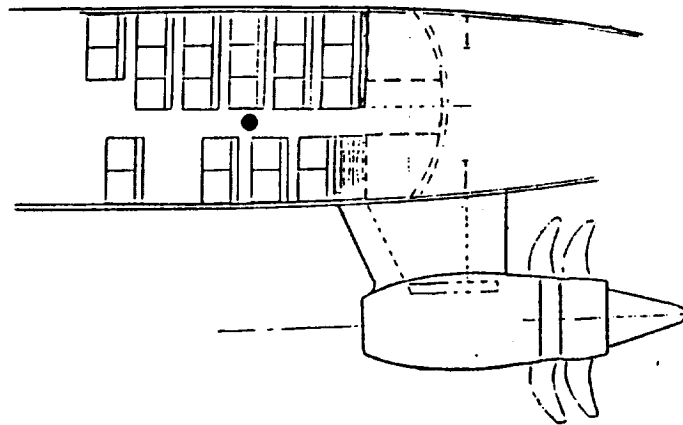
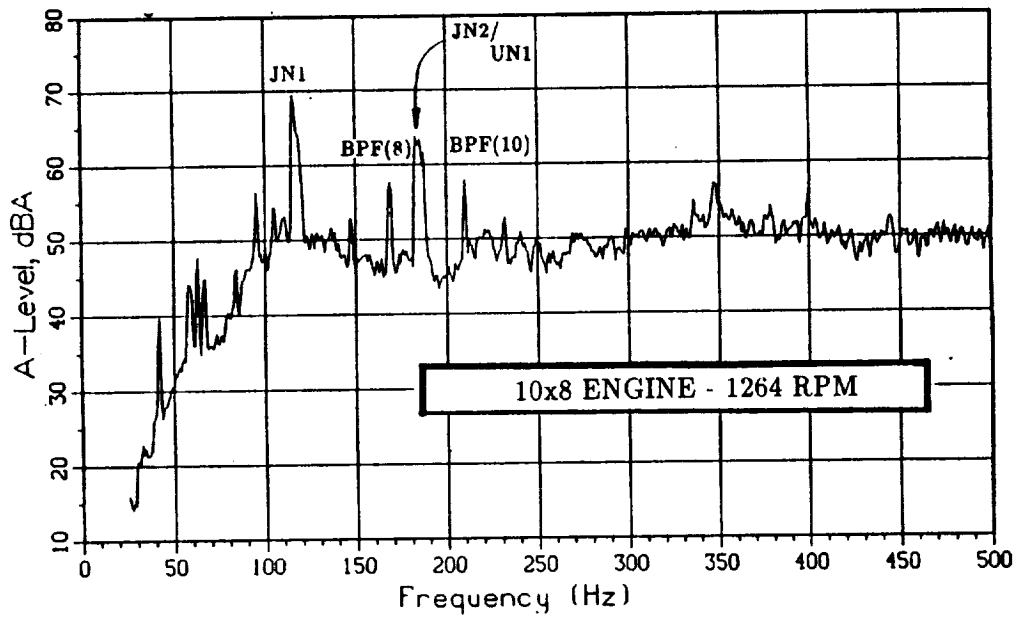
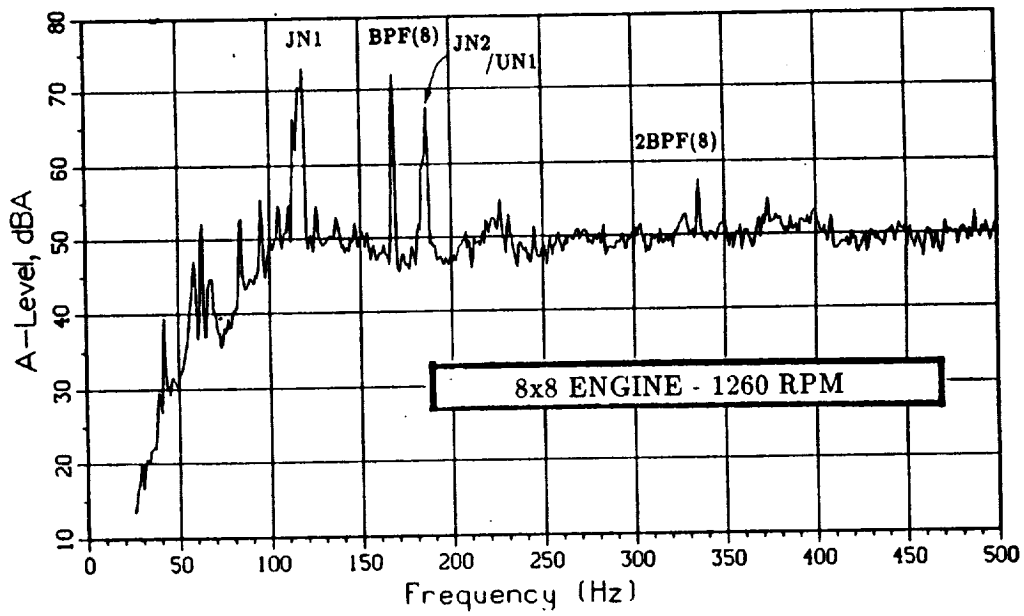


FIGURE 6-6b. Comparison of 10x8 and 8x8 Spectra
Row 4 Seat 3.

7 Comparison of Cruise and Non-Cruise Data

In this section, comparisons between cruise and non-cruise measurements are presented, for both 8x8 and 10x8 engine configurations. "Cruise" refers to the standard high altitude, high speed cruise conditions of 35,000 ft. and Mach 0.76 at which all of the data reported previously were obtained. "Non-cruise" refers to flight conditions at lower altitudes and at the same or lower Mach numbers, although the aircraft is operating in a cruise mode at these non-standard conditions.

Only a limited number of test points containing interior noise data are available for the non-cruise conditions. Table 7-1 lists the non-cruise test points included in this analysis, and the corresponding cruise test points used for comparison. These test points were selected to have overlapping rotor speed ranges to the extent possible, and to have the Quiet Cabin (or subsequent) treatment configuration. To facilitate comparisons, cruise conditions are labelled with a "C", and non-cruise conditions are labelled with an "N".

7.1 Acoustic and Vibratory Loads

7.1.1 Exterior Noise Levels

Figure 7-1 compares 8x8 BPF levels for four flight conditions measured at two locations on the fuselage exterior in the forward propeller plane. The figure shows a 2 to 4 dB increase between cruise levels (Condition C) and the levels at Condition N3, but nominally no difference between cruise levels and the levels at Conditions N1 and N2.

Estimates of the expected differences in BPF tone levels between the cruise and non-cruise conditions were made, based on empirical adjustments for differences in altitude (due to pressure and speed of sound differences) and helical tip Mach number. For Condition N3, the estimated difference in level is 3.5 dB; for Conditions N1 and N2 the estimated difference is -0.5 dB. These agree well with the measured exterior data shown in Figure 7-1.

In Figure 7-2, 10x8 BPF(10) and BPF(8) levels for three flight conditions are compared, at the upper measurement location. The levels for Condition N5 are 7 to 11 dB lower than the cruise levels for both BPFs. The single data point for Condition N4 is higher than cruise levels by 2 dB for BPF(8), and lower than cruise levels by about 4 dB for BPF(10).

The estimated difference between the BPF levels for cruise conditions and Condition

N5 is -7.5 dB, again in agreement with the measured data. However, for Condition N4 the estimated difference in levels relative to cruise levels is -0.5 dB. The BPF levels for the single data point in Figure 7-2 for this condition is at variance with this estimate.

7.1.2 Pylon Vibration Levels

Vibration levels on the pylon are available for the 10x8 flights only, and only at the rear engine mount in the longitudinal and vertical directions. Figures 7-3 and 7-4 compare vibration levels measured in these two directions, respectively, for the BPF(10), BPF(8), and UN1 tones for the three 10x8 flight conditions.

In the longitudinal direction, Figure 7-3 shows that the levels of the three tones for the cruise conditions and Condition N5 are generally comparable, depending on rotor speed. The single point for Condition N4 varies inconsistently in comparison with the other data, as was the case for the exterior noise levels for this data point.

In Figure 7-4 it can be seen that in the vertical direction, BPF(8) vibration levels for cruise conditions are higher than for Condition N5, while the opposite is true for BPF(10) levels. UN1 levels tend to overlap for these two conditions. Again, the tone levels for the single data point for Condition N4 are at variance with the levels for the other conditions.

7.2 Cabin Noise Levels

The maximum BPF tone levels measured among several aft cabin seats are shown in Figure 7-5, for the various flight conditions. In the top of the figure, the maximum 8x8 BPF levels measured among seats 1, 3, 4, 5, and 6 in row 6 are compared. The general trends of the data in this figure reflect the exterior levels shown in Figure 7-1: higher tone levels compared to cruise by 2 to 4 dB for Condition N3, and comparable tone levels for Conditions N1 and N2.

Changes in the BPF tone levels measured in the aft cabin for non-cruise conditions relative to cruise conditions for the 8x8 flights thus appear to be directly related to corresponding changes in the exterior acoustic loads. This relationship is not as clearcut, however, for the 10x8 flights. BPF(10) and BPF(8) levels are shown in the middle and bottom portion of the figure, respectively, and represent the maximum levels measured among seats 1, 3, and 4 of row 6 and seats 1 and 6 of row 5. The decrease in level of 7 to 11 dB from cruise conditions to Condition N5 observed in the exterior data of Figure 7-2 for both BPF tones is not clearly reflected in the interior noise levels. For BPF(10), this trend does occur for the lower rotor speeds, but the difference decreases significantly for the higher rotor speeds. For BPF(8), the levels for the two conditions

tend to overlap. These relative levels also appear unrelated to the measured pylon vibration levels shown in Figures 7-3 and 7-4. Finally, the BPF levels for Condition N4 also vary differently compared with cruise levels than either the exterior noise data or the pylon vibration data.

It is reasonable to expect that the maximum BPF tone levels measured in the cabin vary in accordance with the maximum BPF tone levels measured on the aft fuselage, as was seen to be the case for the 8x8 data. For the 10x8 data, the only available exterior microphones were not those at which the maximum near field levels were expected to occur, based on the data presented in Section 6. Thus the discrepancies observed between the exterior and interior data for the 10x8 flights may be a result of using inappropriate exterior levels.

Figures 7-6 and 7-7 present the interior noise levels for the 8x8 and 10x8 flights, respectively, in terms of the overall A-levels, and the tone and broadband components of the A-level. Each figure consists of several pages, one for each seat position.

The overall A-levels for the 8x8 flights depicted in Figure 7-6 show typically a 5 dB increase for all seats for Condition N3 as compared with levels under cruise conditions. For Conditions N1 and N2, overall levels are 0 to 5 dB higher than for cruise conditions, averaging about 3 dB higher. In each case, these increases are the result of higher broadband levels, which dominate the interior levels for the non-cruise conditions. The estimated change in boundary layer noise levels for the non-cruise conditions relative to cruise conditions is a 5 dB increase for 22,500 ft altitude and Mach 0.77 (Condition N3), and a 3 to 4 dB increase for 22,500 ft altitude and Mach 0.69 to 0.70 (Conditions N1, N2). These expected changes in exterior levels are reflected in the observed changes in broadband interior levels measured at each of the aft cabin seats. Although BPF tone levels also increase for non-cruise conditions (as seen in Figure 7-5), the larger increases in broadband noise levels have the more significant effect on the overall cabin noise levels.

For the 10x8 flights, Figure 7-7 shows that in seat row 6 overall A-levels decrease by 1 to 3 dB for Condition N5, relative to levels for cruise conditions. As for the 8x8 data, this change reflects the corresponding change in broadband levels in seat row 6. The estimated change in boundary layer noise level is a 1.5 dB decrease for these non-cruise conditions relative to cruise conditions; the measured interior broadband levels are in good agreement with this prediction. For seat row 6 measurements, the levels of the broadband component exceeds the levels of the tone component, especially for the non-cruise data where the tone component has been significantly reduced, resulting in lower overall levels which track the lower broadband levels.

The seat row 5 data for the 10x8 configuration also show lower broadband levels for these non-cruise conditions, but the tone levels are higher in this row than in row

6. The net result is that overall levels in seat row 5 for these non-cruise conditions are comparable to (and for some rotor speeds higher than) the overall levels for cruise conditions.

As noted for the 10x8 BPF data, the levels measured during Condition N4 varied considerably, and were inconsistent among locations. Similarly the interior noise levels for this condition are also variable, and do not follow expected trends.

TABLE 7-1. Test Point Summary for Non-Cruise Comparisons

RUN NUMBER	UHB CONFIG.	ROTOR SPEED (RPM)	ALTITUDE (ft.)	MACH NUMBER	OPERATIONAL CONDITION
19550A01	8x8	1285	35000	0.76	C
19550A02	"	1270	"	"	C
19550A03	"	1260	"	"	C
19550A04	"	1250	"	"	C
19550A05	"	1225	"	"	C
19550A06	"	1200	"	"	C
19550A07	"	1170	"	"	C
19640A01	10x8	1200	22500	0.55	N5
19640A02	"	1210	"	"	N5
19640A03	"	1230	"	"	N5
19640A04	"	1250	"	"	N5
19640A05	"	1265	"	"	N5
19640A06	"	1290	"	"	N5
19640A15	"	1305	31000	0.71	N4
19640B01	10x8	1275	35000	0.76	C
19640B02	"	1265	"	"	C
19640B03	"	1255	"	"	C
19640B04	"	1240	"	0.75	C
20330K01	8x8	1255	22500	0.69	N1
20330K02	"	1255	"	0.70	N2
20330K03	"	1255	"	0.77	N3
20330K04	"	1350	"	"	N3

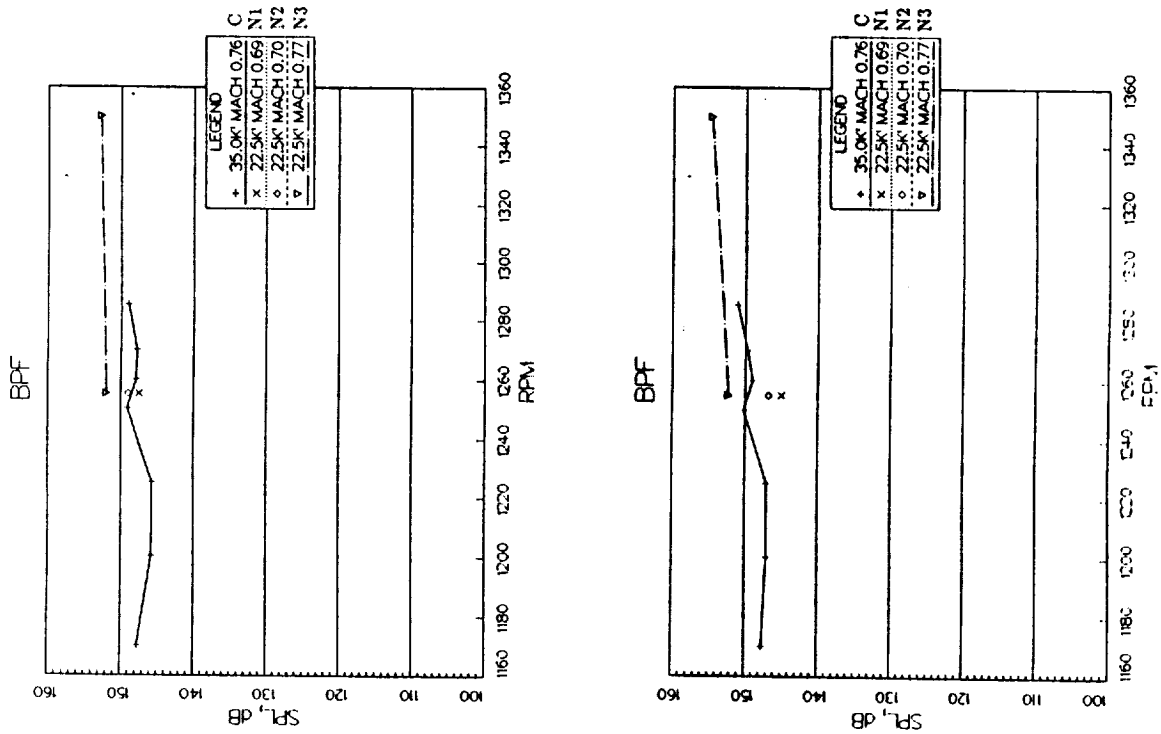


FIGURE 7-1. Variation of 8x8 Exterior Sound Pressure Level at BPF

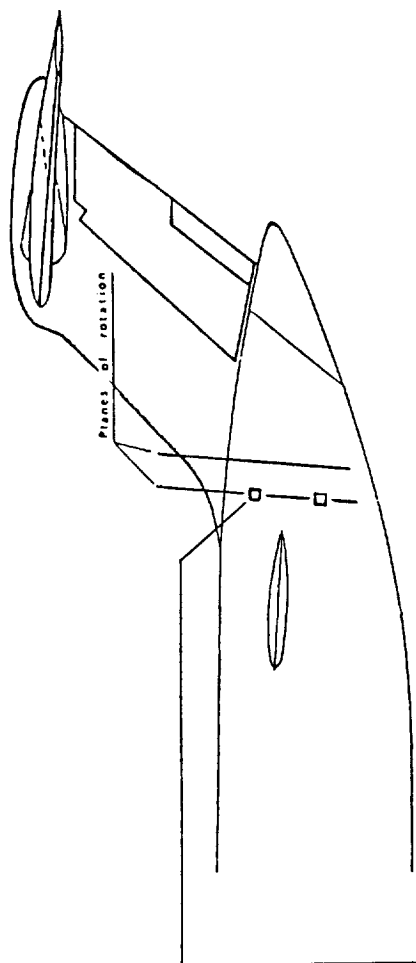
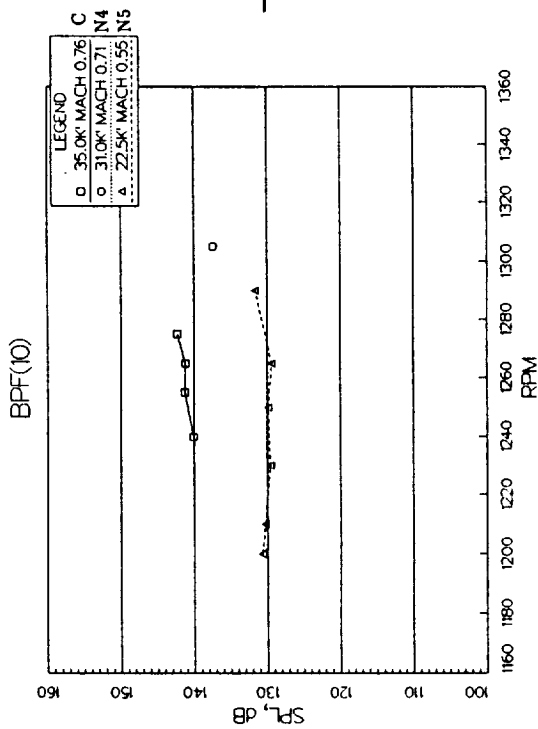
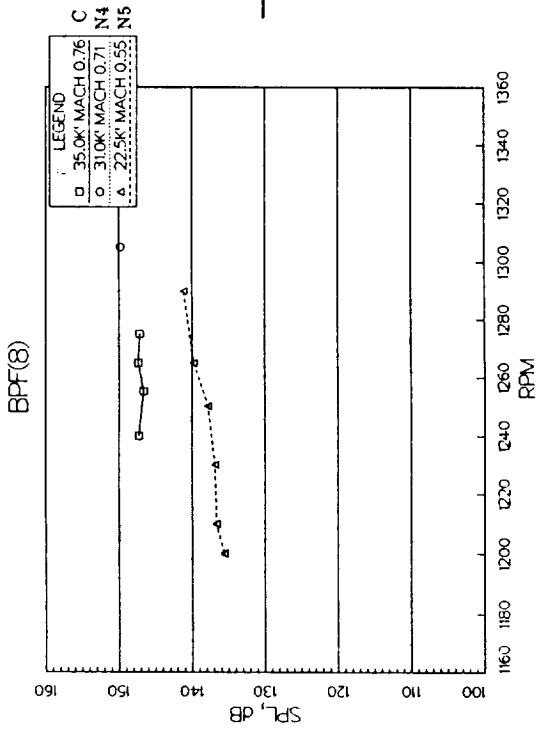


FIGURE 7-2. Variation of 10x8 Exterior Sound Pressure Level at BPF

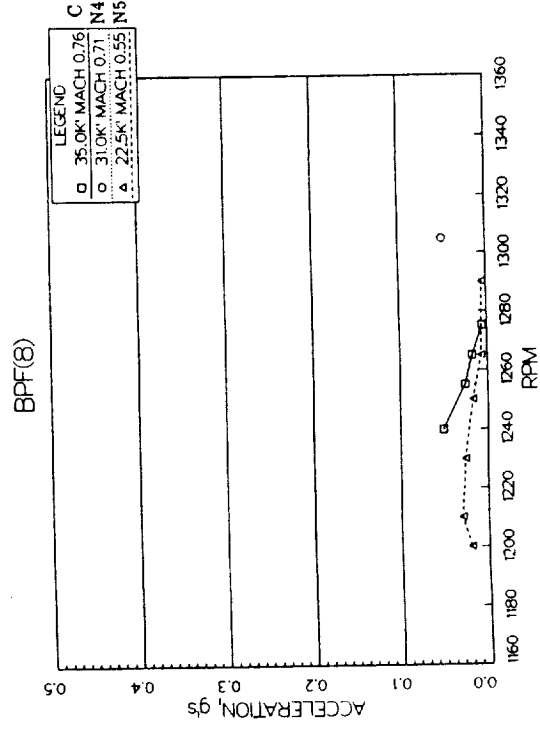
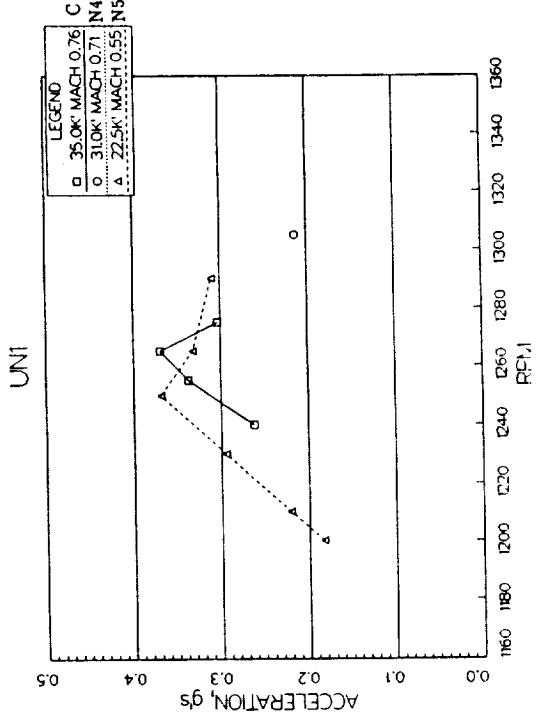
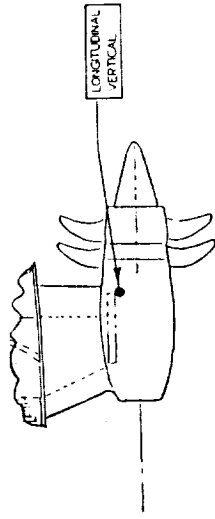
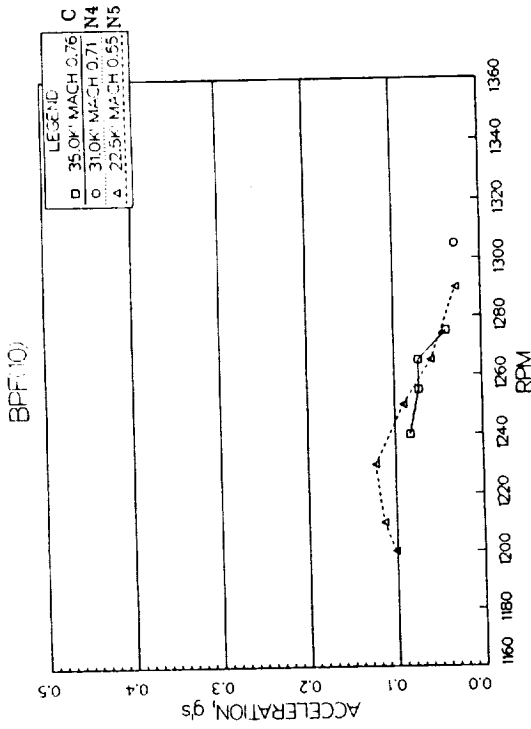


FIGURE 7-3. Variation of 10x8 Longitudinal Pylon Acceleration

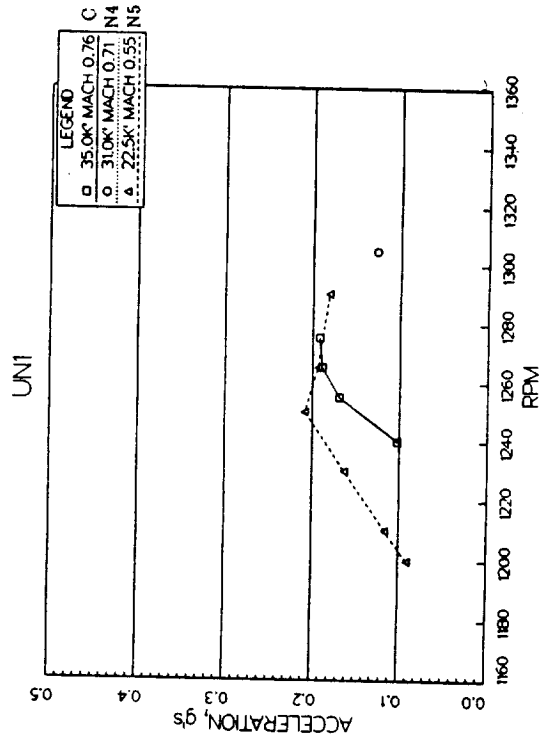
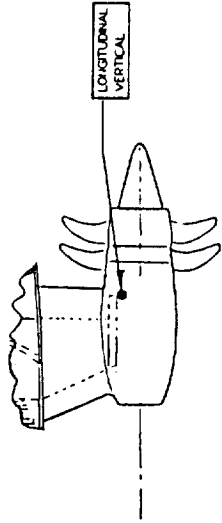
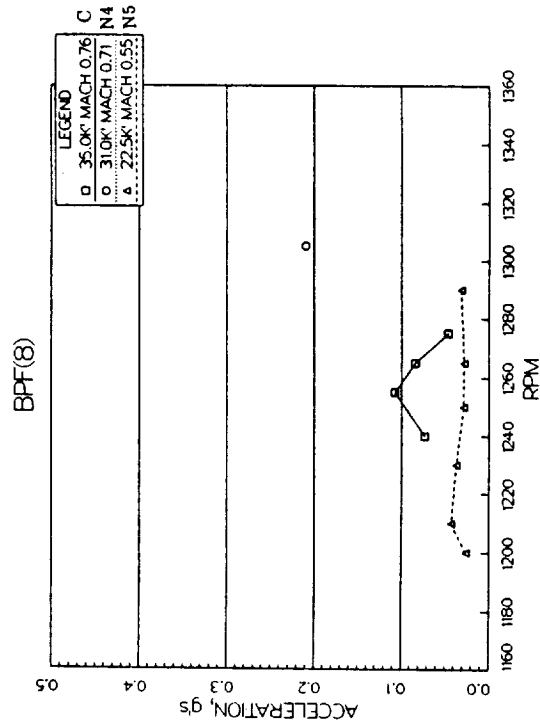
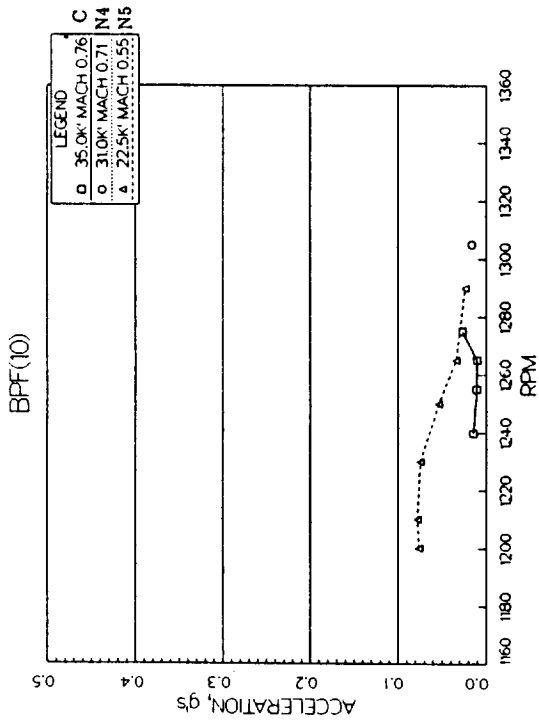


FIGURE 7-4. Variation of 10x8 Vertical Pylon Acceleration

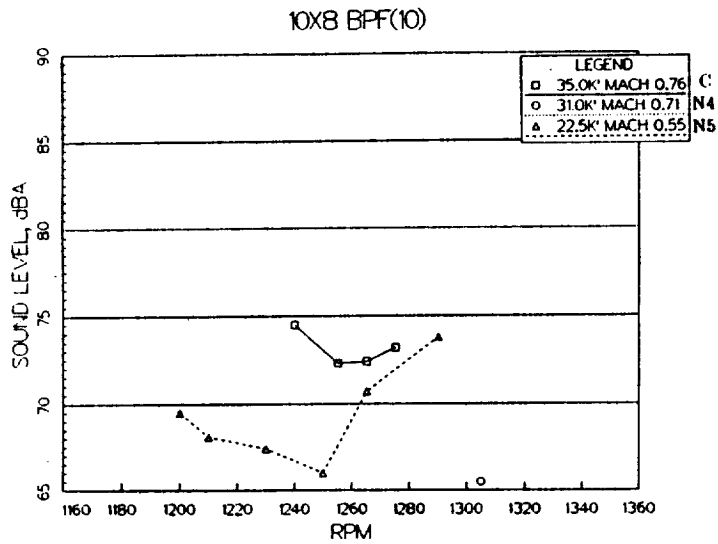
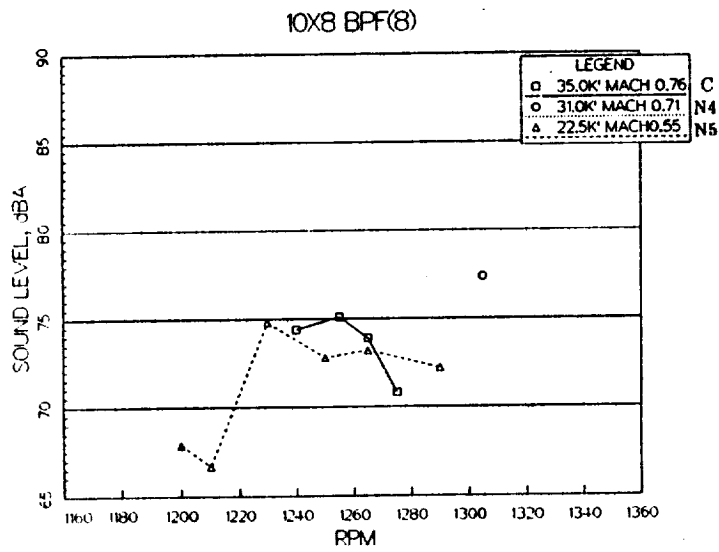
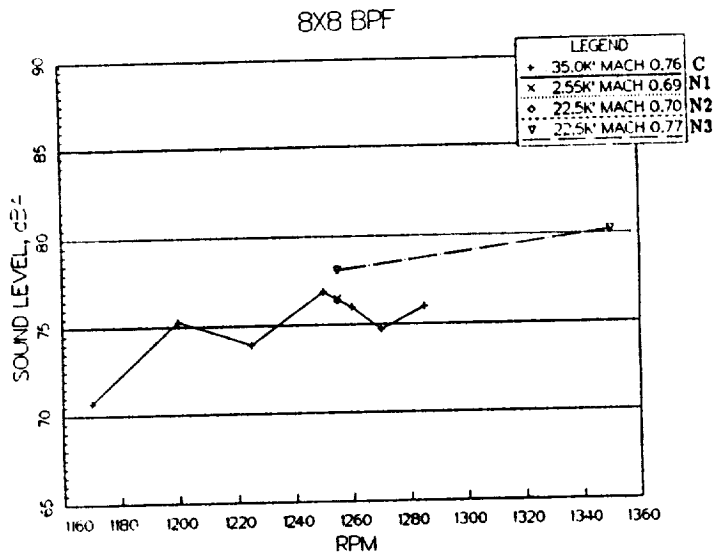


FIGURE 7-5. Maximum Measured Sound Pressure Level in row 6 at each BPF.

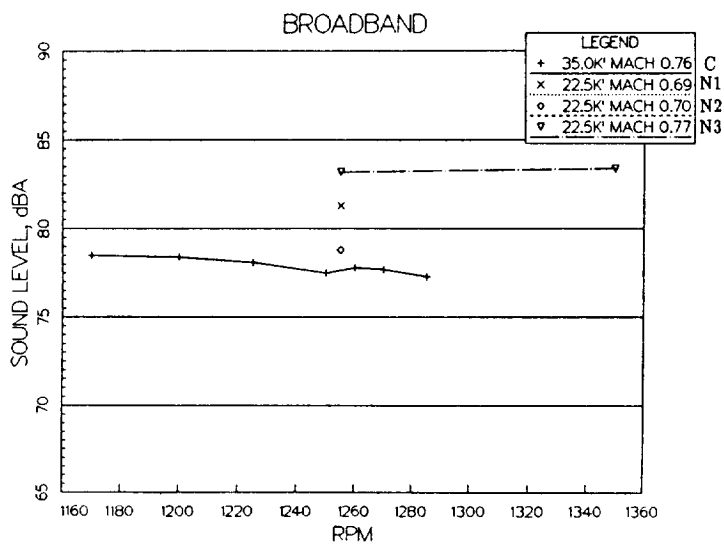
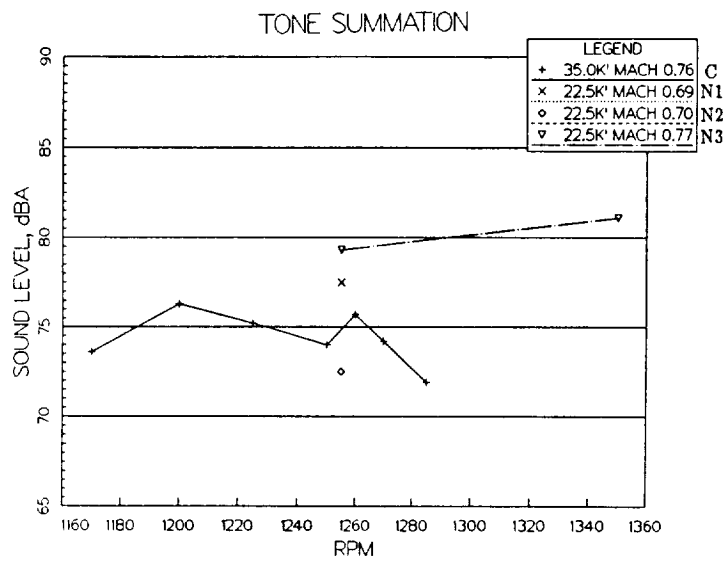
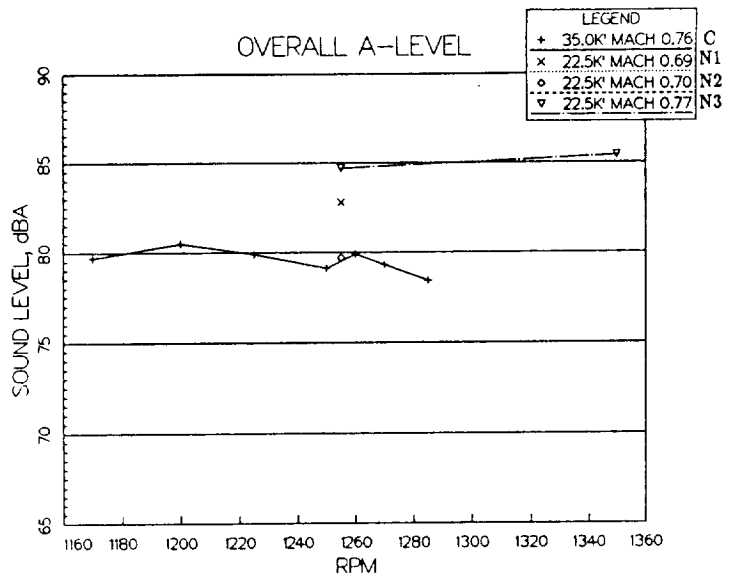


FIGURE 7-6a. Variation of 8x8 interior Noise Components with RPM at Row 6 Seat 1

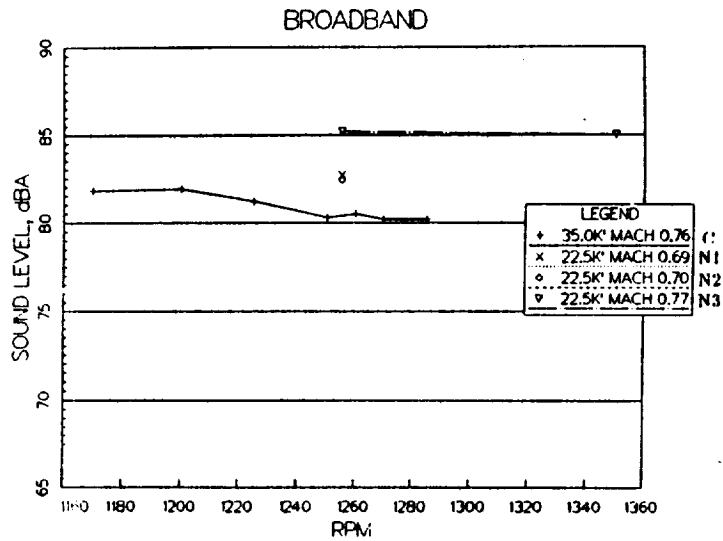
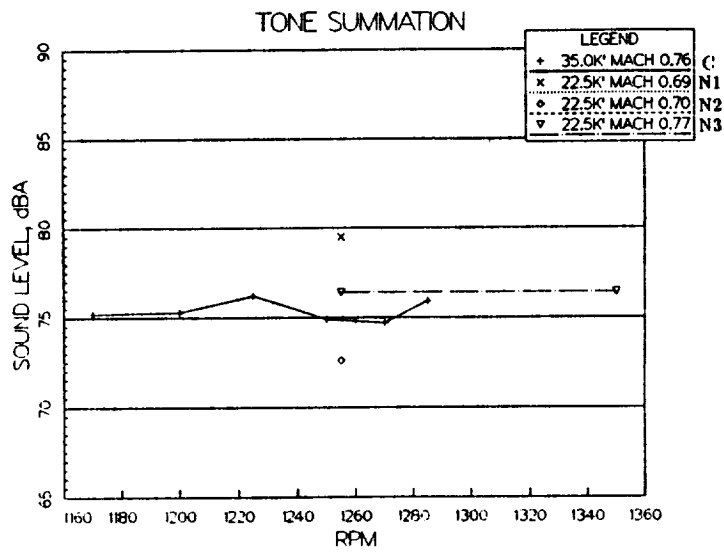
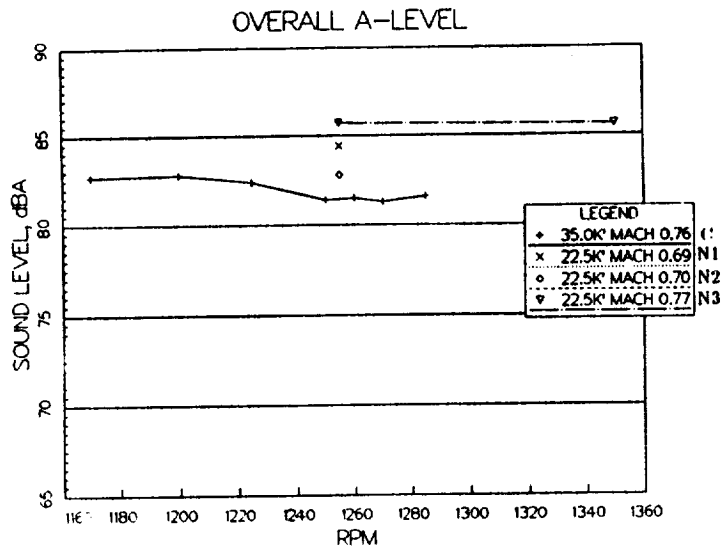


FIGURE 7-6b. Variation of 8x8 interior Noise Components with RPM at Row 6 Seat 3

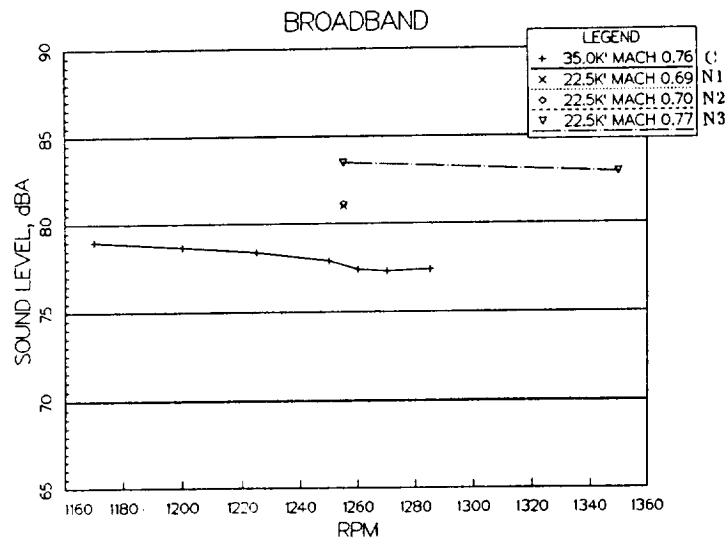
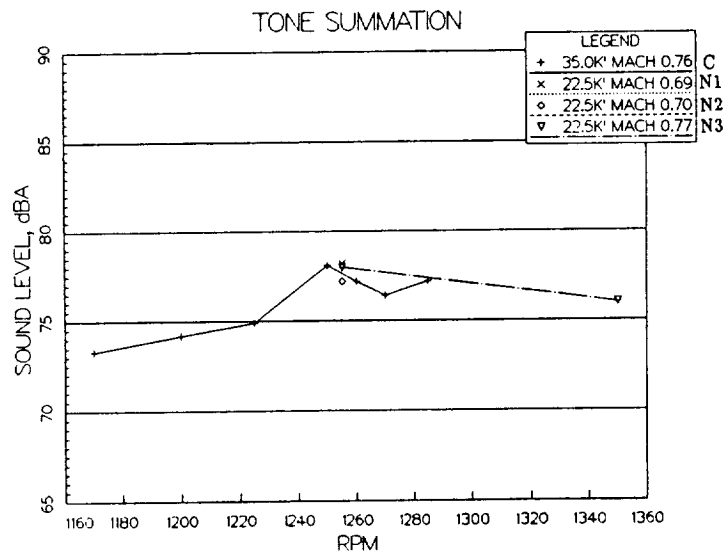
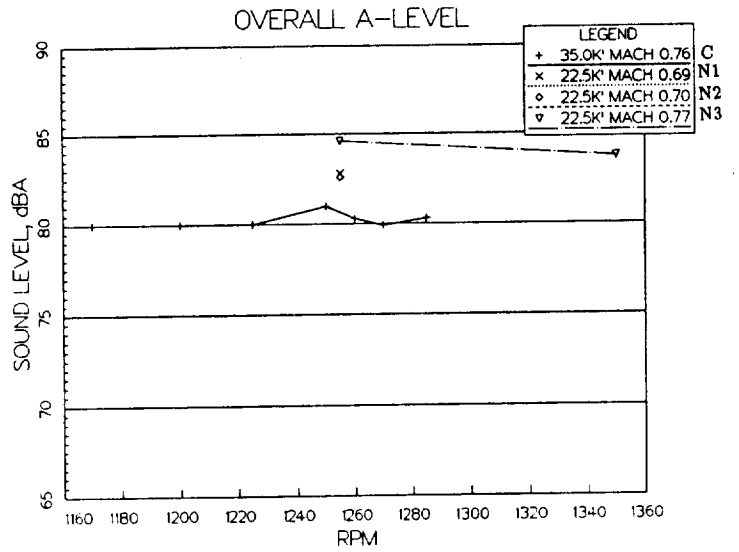


FIGURE 7-6c. Variation of 8x8 interior Noise Components with RPM at Row 6 Seat 4

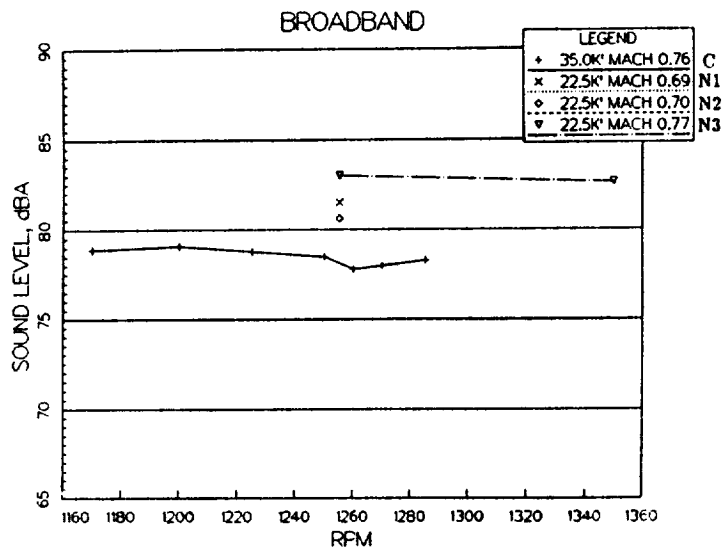
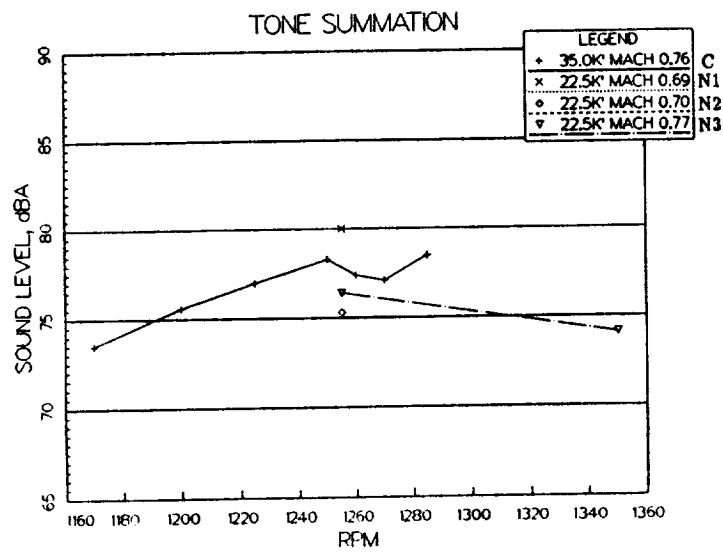
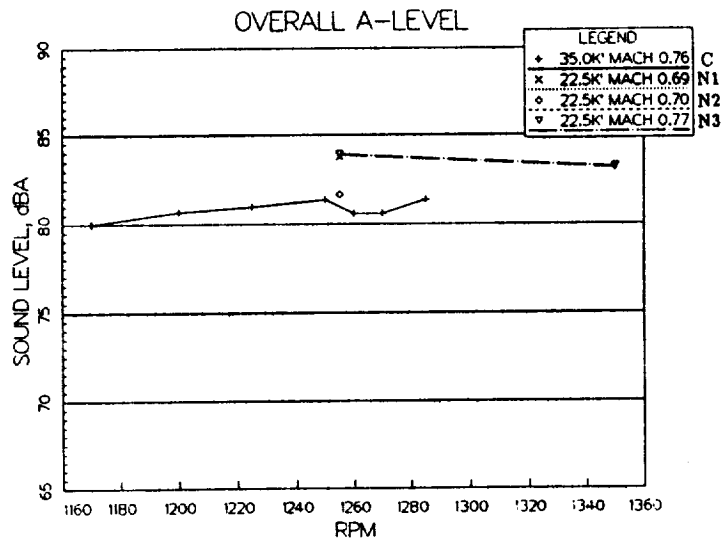


FIGURE 7-6d. Variation of 8x8 interior Noise Components with RPM at Row 6 Seat 5

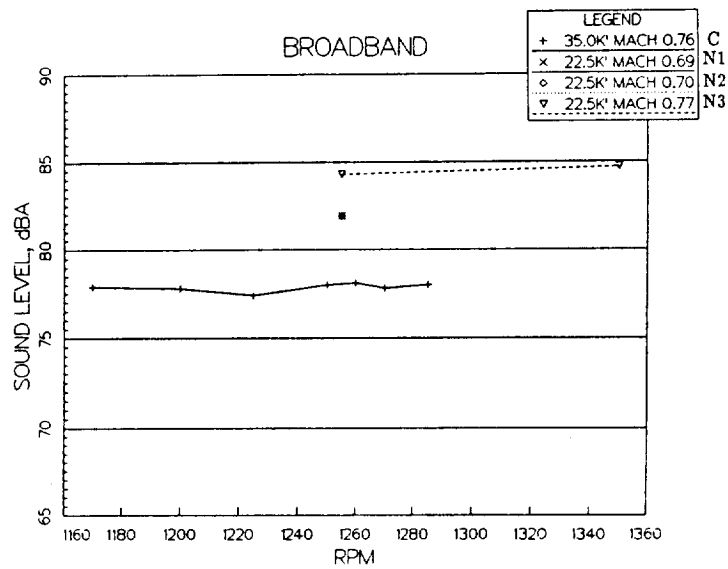
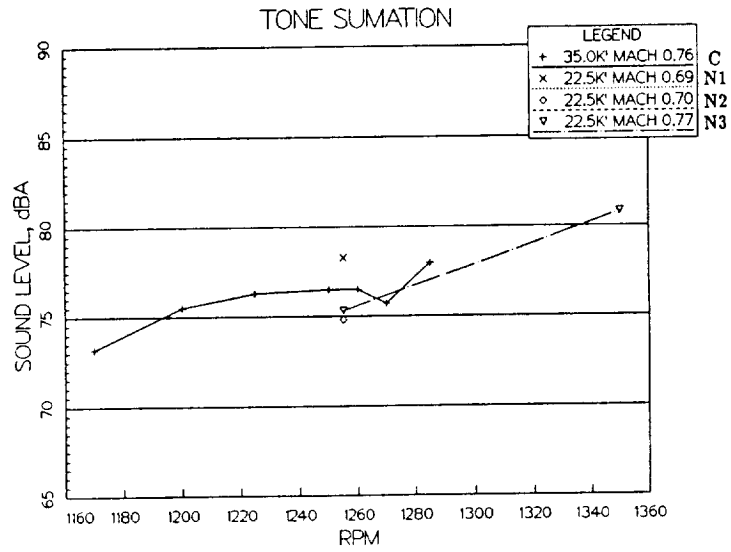
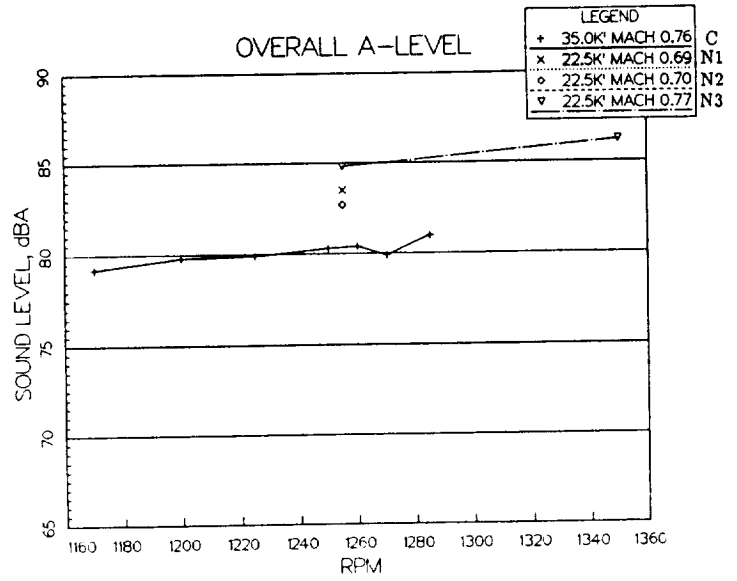


FIGURE 7-6e. Variation of 8x8 interior Noise Components with RPM at Row 6 Seat 6

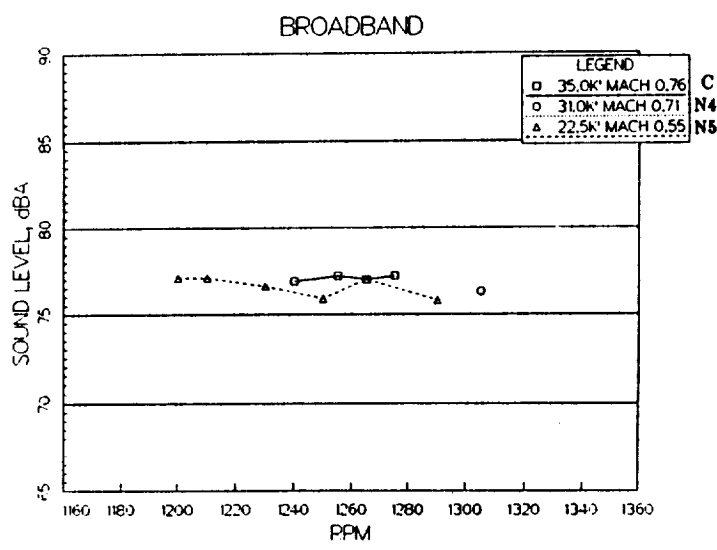
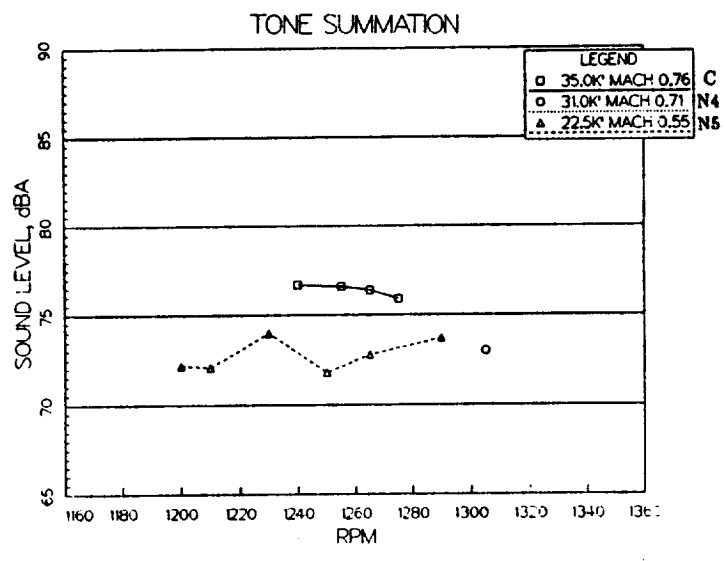
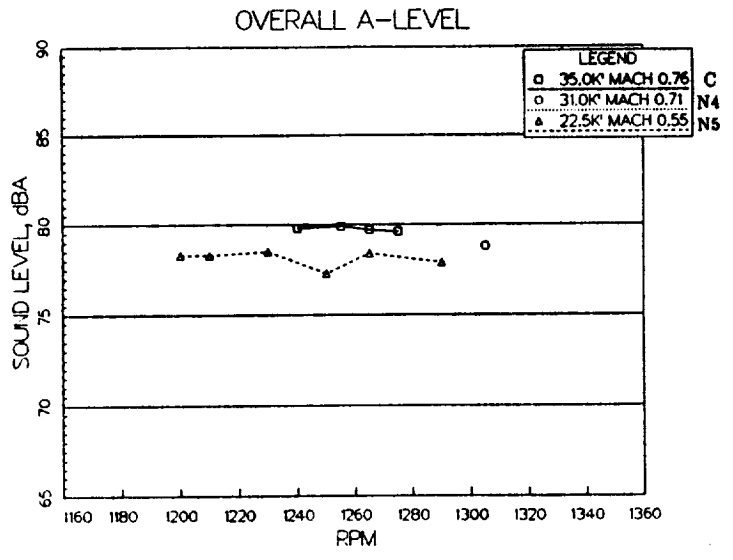


FIGURE 7-7a. Variation of 10x8 interior Noise Components with RPM at Row 6 Seat 1

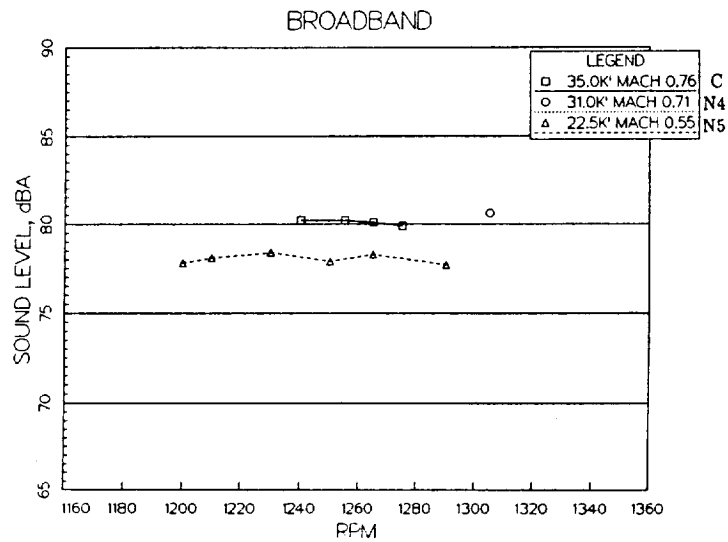
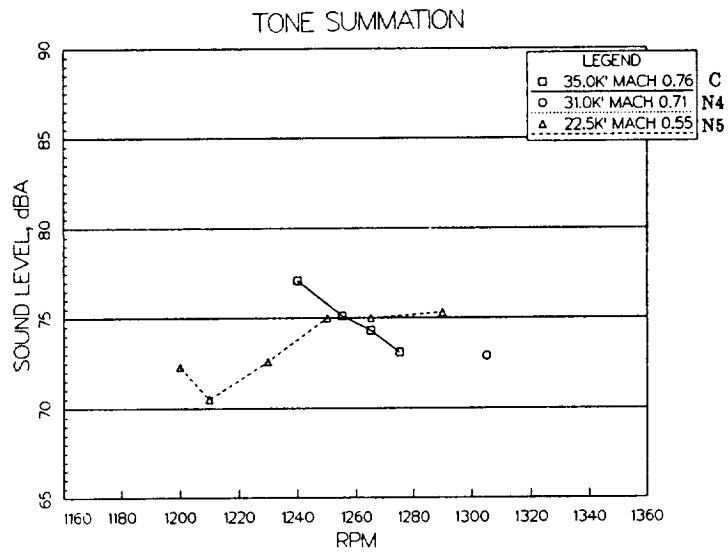
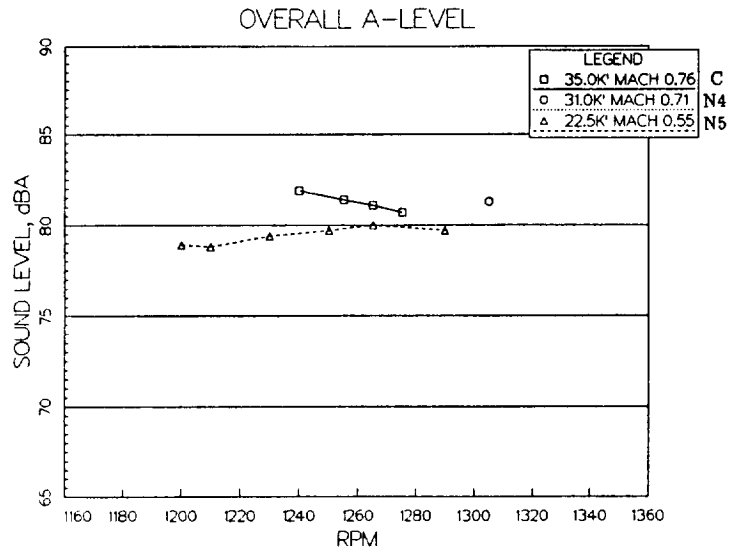


FIGURE 7-7b. Variation of 10x8 interior Noise Components with RPM at Row 6 Seat 3

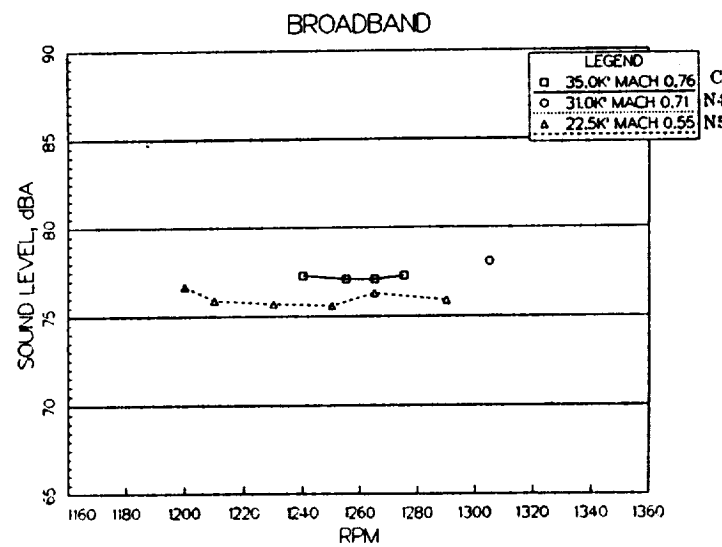
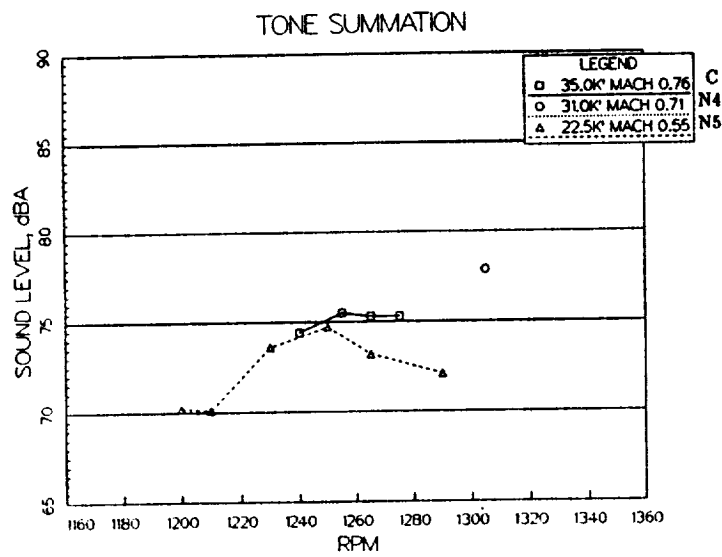
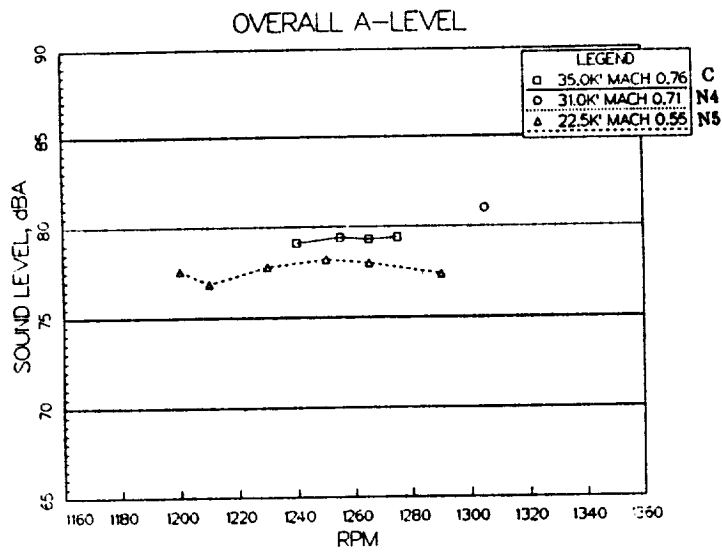


FIGURE 7-7c. Variation of 10x8 interior Noise Components with RPM at Row 6 Seat 4

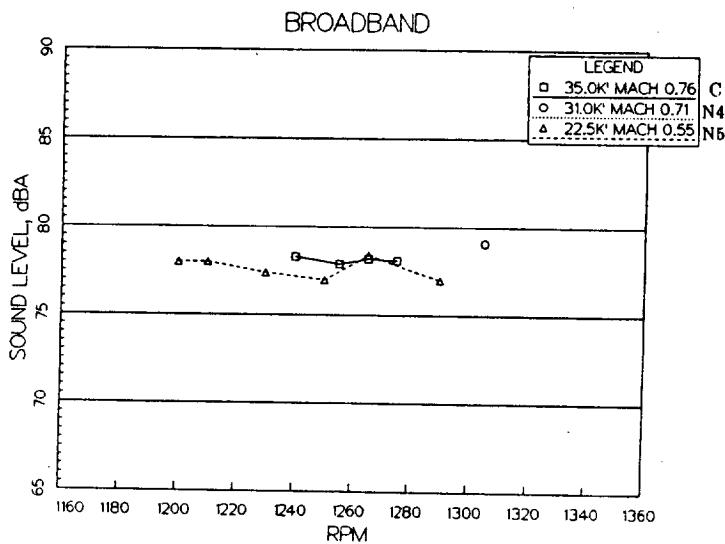
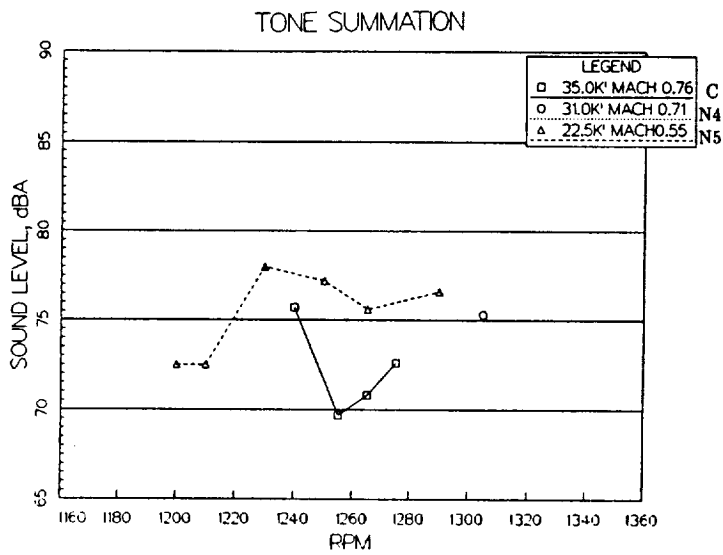
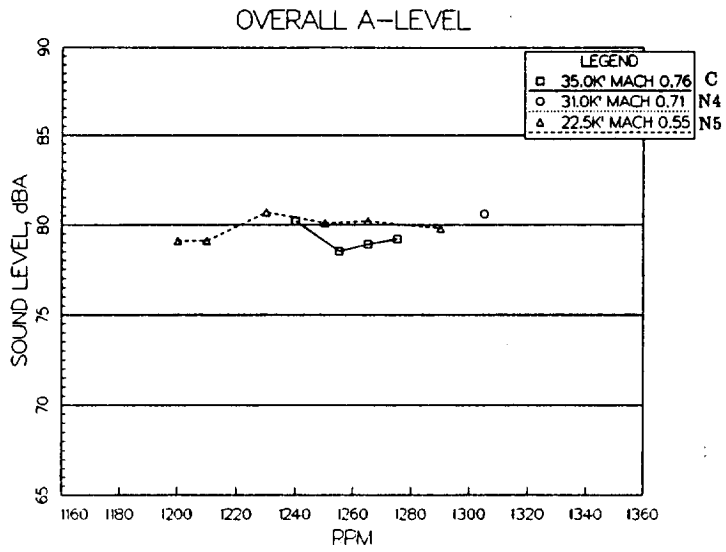


FIGURE 7-7d. Variation of 10x8 interior Noise Components with RPM at Row 5 Seat 1

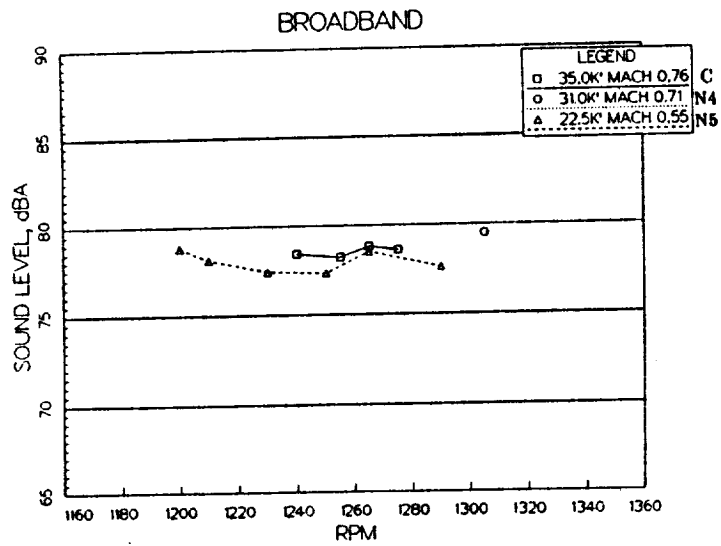
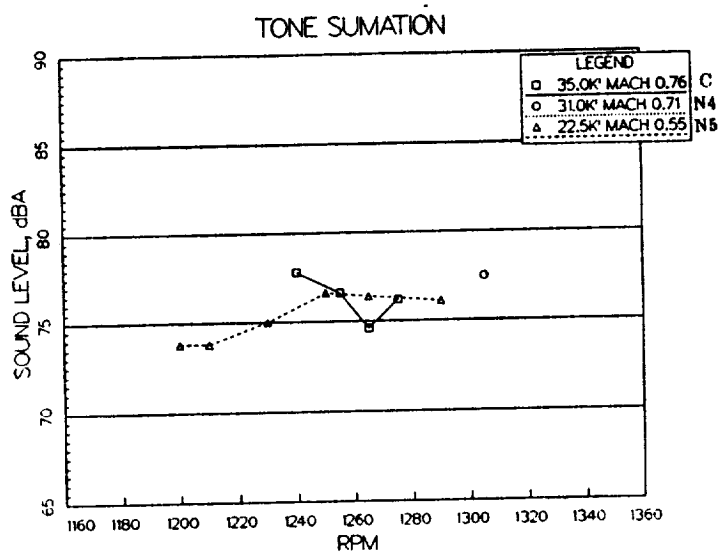
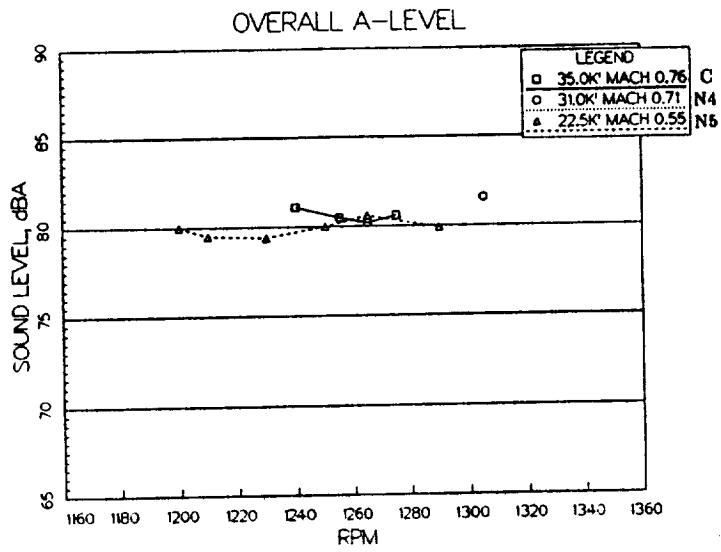


FIGURE 7-7e. Variation of 10x8 interior Noise Components with RPM at Row 5 Seat 6

8 Identification of Major Transmission Paths

When exterior acoustic and mechanical forces excite a complex structure, determination of the major transmission paths by direct measurements is generally not feasible. Several analysis methods are available, however, which provide a partial definition of transmission paths. For example, various techniques to compare measured interior and exterior noise and vibration levels can be used to infer the relative strengths of specific paths. Measured sound intensity data can be used to identify major radiating surfaces and thereby aid in the interpretation of other measurement results. Partial coherence techniques can be used to examine the degree to which individual signals measured in the interior or along specific transmission paths are related to selected source signals, to further deduce transmission path strengths. Taken together, the results of these various analyses can provide a complete understanding of the transmission characteristics into the aircraft cabin.

In this section, all of these analysis techniques are utilized to determine the major transmission paths on the Demonstrator. Prior to the flight test program, the three paths shown in Figure 4-1 were predicted to be the major paths. The various analyses of measured flight test data have focused on developing a better understanding of the transmission characteristics on these, and other, paths.

In the first subsection below, the results of a sound intensity survey conducted on a dedicated 8x8 flight are presented. In the following three subsections, each of the transmission paths shown in Figure 4-1 is examined using a variety of interior and exterior data measured during 8x8 flight 1955. The relative strength of each path is assessed using these data and the sound intensity survey results. Finally, the last subsection presents the results of partial coherence analyses of selected data from 8x8 flight 1955 and 10x8 flight 1964, which provide an independent assessment of transmission path strengths.

8.1 Results of Sound Intensity Survey

Figures 8-1 and 8-2 show sound intensities and sound power levels, respectively, for various scanned surfaces in the passenger cabin measured during 8x8 flight 2026. Measurement locations are defined in Figures 3-7 and 3-8. It should be noted that for these sound intensity measurements, the fuselage configuration (configuration 5) was different from the Quiet Cabin configuration (configuration 4). In addition to removal of the engine dynamic absorbers, several items were removed from the cabin to facilitate the survey: the seats, the carpeting on the floor, the carpeting on the left engine pylon bulkhead, and the section of the double wall bulkhead over the aft pressure bulkhead.

On each figure, the measured levels are listed for the four one-third octave bands of 100, 160, 200, and 315 Hz; these bands contain the JN1, BPF, UN1, and 2BPF tones, respectively. Positive values indicate energy flow from the scanned surface, while negative values indicate energy flow into the surface. Levels in parentheses indicate that the pressure intensity index is greater than 20 dB, and therefore the data are questionable.

For all four tones of interest, the highest intensities and power levels arise from the aft bulkheads (both engine pylon bulkheads and the aft pressure bulkhead) and the right upper and lower sidewalls (in the aft part of the cabin). There are also significant but lower levels from the left sidewall (for UN1) and from the aft floor (for BPF).

8.2 Cabin Sidewall Path

Figure 8-3a shows exterior spectra for several locations on the fuselage for 8x8 flight 1955, test point 0A03 (with a rotor speed of 1260 rpm). While tones at the BPF, 2BPF, and subharmonics are very prominent in the vicinity of the propeller planes of rotation, these tones rapidly diminish as the location moves forward. Outside the passenger cabin the tones have nearly completely disappeared, with levels at or below the broadband noise (due to the boundary layer).

Interior spectra measured in the last seat row, as shown in Figure 8-3b, depict strong tones at the BPF and 2BPF superimposed on a broadband background (also due to the boundary layer). If these BPF and 2BPF tones measured in the cabin were the result of transmission through the cabin sidewall, their levels would be at or below the broadband levels, corresponding to the spectral characteristics of the acoustic loads on the fuselage exterior. Since this is not the case, it is clear that the tones in the interior are not the result of direct transmission through the cabin sidewall.

To further support this conclusion, the power levels presented in Figure 8-2 show that the left sidewall is not a major source for tones at the BPF and 2BPF frequencies (note the higher power levels from the right sidewall at these frequencies). Thus the tones observed in the cabin are not transmitted along the airborne path from the UHB engine through the cabin sidewall.

The broadband background noise in the cabin, however, is likely the result of transmission of exterior boundary layer noise through the cabin sidewall, as is the case on most conventional aircraft. In Section 7, estimates of the differences in exterior boundary layer noise levels for several flight conditions were in good agreement with measured differences in interior broadband levels for the same conditions. This agreement tends to verify the concept that interior broadband levels are the result of the exterior boundary layer noise.

8.3 Aft Section Path

Figure 8-4 shows spectra measured at two locations just behind the aft pressure bulkhead. This figure shows major tones at the BPF and 2BPF, with maximum levels on the order of 110 dB and 100 dB, respectively (note the absence of engine rotational tones in these spectra). For comparison, the interior noise spectra of Figure 8-3b show maximum BPF levels on the order of 90 dB, and maximum 2BPF levels on the order of 70 dB. If the tones in the cabin are the result of transmission through the pressure bulkhead, the bulkhead is providing a reduction in level of about 20 dB at the BPF, and about 30 dB at 2BPF.

Independent measurements were conducted in a Douglas Aircraft Company ground test facility using a DC-9 test article and a loudspeaker located in the aft section as a source (see NASA CR 181819). With the same double wall treatment applied to the pressure bulkhead, the reduction in level between a corresponding location behind the bulkhead and a typical seated position in the aft seat row was on the order of 35 dB for the frequency range corresponding to the BPF, and on the order of 45 dB for the frequency range corresponding to 2BPF. Thus, if the cabin tones were strictly a result of transmission through the pressure bulkhead, their levels would be approximately 15 dB lower than the levels actually measured.

The ground measurements also showed that with the double bulkhead removed, the pressure bulkhead still provides about 35 dB noise reduction for the frequency range corresponding to the BPF. This would tend to confirm the results reported in Section 4 for Treatment 7, i.e. that interior BPF levels were relatively unchanged with the removal of the section of the double wall bulkhead over the pressure bulkhead door.

For higher frequencies (typically above 200 Hz), the ground measurements showed an improvement in noise reduction due to the double wall treatment of 10 to 20 dB, generally increasing with frequency. This improvement was also observed in the UHB Demonstrator measurements. For example, Figure 8-5 compares spectra at the same seat location for the flight tests corresponding to the Quiet Cabin configuration (treatment configuration 4), and treatment configurations 6 and 7. In this figure, the spectra are plotted to 2000 Hz. The presence of the tones at the higher multiples of the BPF when the double wall bulkhead was removed (configuration 7) is clear, indicating that this path would be important for these higher frequencies if the bulkhead were not treated. Although these tones do not contribute significantly to the A-level in the cabin, they would be perceptible to passengers. Note also the increasing level of the 2BPF tone from configurations 4 to 7, as observed earlier in Figure 4-11.

The discussion above has shown that the transmission path from the aft unpressurized section through the pressure bulkhead into the cabin is not significant, particularly when the pressure bulkhead is treated with a double wall. Nevertheless, it is interesting

to examine the first portion of this "aft section path", i.e. the transmission of sound (and particularly BPF tones) from the UHB engine into the aft unpressurized section. At first thought, it would appear that acoustic forces from the two blade rows would impinge on the aft fuselage, and then transmit directly through the fuselage wall into the aft unpressurized section. Analysis of measured data, however, shows that this is not exactly the situation.

Figure 8-6 compares BPF levels measured at several transducers as a function of UDF rotor speed for flight 1955. The data are plotted for selected fuselage exterior microphones in the two propeller planes, for a fuselage accelerometer in the forward prop plane, and for two microphones in the aft unpressurized section. The similarity between the levels at both aft section interior microphones and the fuselage accelerometer levels is easily seen. In fact, the computed linear regression between the levels at the centerline interior microphone and the accelerometer levels has a correlation coefficient of 0.98. Thus, it appears that the BPF levels in the aft unpressurized section are directly related to (and caused by) the structural motion of the fuselage.

In comparing the accelerometer levels to the exterior microphone levels, there are dissimilar variations with rpm. A linear regression of the accelerometer levels with any of the microphone levels shows small correlation. However, the primary area of disagreement is at 1250 rpm, where accelerometer levels do not rise with increased acoustic levels (as measured by the two microphones in the forward prop plane). If this test point is (temporarily) neglected, the agreement improves. The computed linear regressions between the accelerometer levels and the microphone levels in the forward prop plane for the remaining six test points have correlation coefficients of 0.84 for the upper microphone, and 0.96 for the lower microphone.

The exterior microphones measure the acoustic loads impinging on the fuselage (generated by the dynamic loads on the rotating propellers, which may include steady and unsteady components), while the accelerometer measures the structural response of the fuselage to these loads. This response is not necessarily linear with frequency, particularly given the complex vertical and canted frame structure and the use of damping treatment in this area. Conceivably, there is a dip in the structural response at 166 Hz, the BPF corresponding to 1250 rpm. This nonlinear behavior could explain the dissimilarity in the accelerometer/microphone data at the 1250 rpm test point.

In summary, the BPF levels in the aft unpressurized section are likely the result of the structural response of the fuselage to the impinging acoustic loads. With the aft pressure bulkhead treated (with a double wall), these levels do not propagate significantly into the passenger cabin.

8.4 Structural Path

As has been discussed earlier, the noise levels measured in the cabin consist of a broadband component due to boundary layer noise, and a tone component which is comprised of the BPF, 2BPF, JN1, and UN1 tones superimposed on the broadband spectrum. In the previous sections it was observed that the broadband component arises from external boundary layer noise transmitted through the cabin sidewall, and that the various tones did not result from transmission through either the cabin sidewall or the aft pressure bulkhead. In the following, it will be demonstrated that these tones are transmitted structurally through the engine pylon and fuselage.

The sources of the tones at the engine rotational frequencies are mechanical forces within the engines which do not generate airborne noise but which propagate structurally. This is substantiated by review of the noise spectra for the exterior fuselage microphones (Figure 8-3a), in which the UN1 tone is absent, and review of pylon vibration data (Figure 5-2) which shows a strong UN1 component at both the engine mount and pylon spar locations.

Indeed, the sound intensity measurements (Figures 8-1 and 8-2) show that for both UN1 and JN1 tones, the aft bulkheads are major radiating surfaces, as are the rear sidewalls. It appears that the JN1 tone propagates through the JT8D pylon into the fuselage, through the pressure bulkhead, the right pylon bulkhead and the right sidewall. The UN1 tone similarly propagates through the UDF pylon into the fuselage, through the pressure bulkhead, the left pylon bulkhead and the left sidewall. However, the UN1 tone also propagates through the entire pylon bulkhead structure to the right side of the aircraft, and into the right sidewall.

It should be noted that in order to support the UDF pylon, a new left pylon bulkhead was installed which is significantly stiffer and more massive than the right pylon bulkhead. Structural energy from the UDF pylon thus has a ready transmission path through this structure to the other side of the aircraft. It should also be remembered that the double wall bulkhead section over the aft pressure bulkhead door was removed during the sound intensity measurements. Although high sound power levels are shown in Figure 8-2 for the aft pressure bulkhead, it is likely that the sound power flow from this bulkhead is reduced in the fully treated cabin configuration.

For the BPF and 2BPF tones, the sound intensity measurements again show that the major radiating surfaces are the aft pressure bulkhead, the two engine pylon bulkheads, and (for the BPF tone) the right sidewall in the rear of the cabin. Since it was shown above that these tones do not propagate along an airborne transmission path through the pressure bulkhead, the sound power flow from the bulkhead must be structurally induced. Also, the presence of sound radiation at the BPF and 2BPF frequencies from the right side of the aircraft can only be structurally generated. As a final point, Figure

5-2b shows that the vertical acceleration levels measured at the inboard pylon spar for the BPF tone follow the same trend with rpm as the exterior microphone levels (Figure 8-6) in the forward prop plane. The computed linear regression of the acceleration levels with the lower microphone levels has a correlation coefficient of 0.97. Thus the BPF tones propagating through the fuselage are likely caused by the impinging acoustic loads on the UDF pylon.

In Section 5.2, the cabin noise level distribution for the various tones was discussed. The sound intensity data provide an explanation for some of the observed trends. For example, the BPF tone measured in the last seat row appeared to be higher on the right (JT8D) side than the left (UDF) side for most of the engine rpm settings. Since the pressure bulkhead had a double wall treatment and the left engine pylon bulkhead was covered by a coat closet during the flight tests, thereby greatly reducing the acoustic energy from these two surfaces, the high sound power levels from the right engine pylon bulkhead and right sidewall would explain the higher measured levels on the right side of the cabin.

The JN1 tones were also observed to be higher on the right side. Figure 8-2 shows that the greatest sound power at this frequency emanates from the right sidewall, as might be expected.

In contrast, the sound intensity results show radiation from both sidewalls and the aft bulkheads into the cabin for the UN1 tone, and primarily from the aft bulkheads for the 2BPF tone. These two tones show roughly the same levels on both sides of the cabin.

In summary, all the tones observed in the cabin appear to be generated by energy that is propagated structurally, resulting in acoustic radiation from various cabin surfaces. The major surfaces include all the aft bulkheads and the right rear cabin sidewall.

8.5 Results of Partial Coherence Analyses

Partial coherence analyses were conducted for 8x8 flight 1955 test point 0A03 and 10x8 flight 1964 test point 0B03. The purpose of these analyses is to identify the major sources and paths for the BPF tones measured in the cabin. An overview of the analysis technique and major results are described in this subsection. The mathematical basis of the partial coherence analysis technique is contained in Appendix B.

8.5.1 Partial Coherence Analysis Concepts

The degree to which two signals are related can be measured by the “ordinary coherence function”. A coherence value of 0.1 or less between two signals is low enough for an assumption of linear independence, while a value of 0.9 or higher indicates that the signals are highly dependent. The coherency between two signals, however, is not an indication of a cause and effect relationship. For example, when there is a single periodic source impinging on a structure, the measured signals throughout the structure are all likely to be highly coherent; nevertheless one cannot draw conclusions about transmission paths from these coherence values alone. Thus the coherence between an interior microphone signal and a trim panel accelerometer signal may be nearly 1, but the sound at the microphone is not necessarily caused by the vibration of the trim panel, nor is the trim panel vibration necessarily caused by sound in the cabin. Similarly if the periodic source in this example is a rotating propeller generating acoustic energy, the signals at nearby exterior microphones and accelerometers will also likely be highly coherent with each other and with the signals at the two interior transducers, but the presence of airborne and/or structureborne transmission paths cannot be deduced from these coherence values.

In this example, the signal at the exterior microphone could be considered a measure of the noise source, while the signal at the interior microphone could be considered a measure of the response to this source. In other terms, the aircraft structure could be considered a system with inputs and outputs; the source signal would be an input, and the response signal would be an output. When there are multiple sources (such as dual propeller rotors generating multiple acoustic sources and mechanical forces in the engine generating vibration sources), the noise measured at a specific interior location can be modeled as a multiple-input single-output process.

A “partial coherence” analysis involves selectively removing the effects of individual inputs from the output. The partial coherence function is then a measure of the coherence between a single input and a single output, after removing the effects of specified inputs. The process of removing these specified inputs from the output is called “conditioning”. The partial coherence analysis begins with the output spectrum. This spectrum is then “conditioned” as the effect of the first selected input is removed. This conditioned spectrum is then further conditioned as the effect of the second selected input is removed, and so on.

If this technique is applied to a specific tone in the output spectrum, then as each input is removed the level of the tone in the conditioned spectra will sequentially diminish, for those inputs which have a real effect on the output. That is, if there are three inputs but only the first two of them affect the output, the conditioned spectra will show reductions in level only when these two inputs are removed. Conditioning

the input with the third output will produce no reduction in level.

There are several subtleties implicit in the use of this technique, some of which were uncovered during the analyses described below. First, the tone level will decrease to a background noise floor as the conditioning process occurs, if the set of selected inputs completely reflects the noise source(s). In practical application the number and location of transducers may not be sufficient for complete measurement of the source, resulting in a residual level remaining after the output is conditioned with all the inputs. Second, for a fixed set of inputs, the overall results of the conditioning process were found to be independent of the ordering of the inputs. That is, the final conditioned output spectrum does not depend on the order of removal of the inputs; this is in contrast with current thinking which holds that the input order is important to the final conditioned output. However, the intermediate conditioned spectra are highly dependent on input ordering, and thus the relative importance of each input to the output cannot be determined from the intermediate spectra alone. Third, if the inputs are independent of each other the relative reduction in level as each input is separately removed from the output will provide a rank ordering of the importance of each to the output. This however is not always the case, since the signal measured at a specific input transducer may include the effect of multiple sources. Finally, it is critical to identify inputs and outputs properly. Often transducers selected as inputs are actually intermediate outputs, resulting in misleading conclusions (particularly in systems with high coherency among all transducers).

8.5.2 Analysis of 8x8 Data

Figure 8-7 shows the transducers used in the partial coherence analysis of the 8x8 flight test data. The five interior microphones in seat row 6 are used as output transducers. For input transducers, the four exterior microphones in the two rotor planes (3, 4, 12, 13) are used to represent acoustic sources, while the four accelerometers on the engine mount (4, 5X, 5Y, 5Z) are used to represent vibration sources. Accelerometers 1, 2, and 3 and aft section microphone 5 are considered to be (intermediate) output transducers, that is, they measure the response of the fuselage to either acoustic or vibration excitation, rather than the source of the excitation itself. (In this analysis, the cabin sidewall path is ignored since the noise spectra measured on the fuselage outside the cabin do not contain BPF tones.)

As a starting point, Table 8-1 lists the ordinary coherence between the various inputs and each cabin output. It is surprising to note that, with a few exceptions, the coherence values are relatively low. Further, there is considerable variability in the coherence between a single input and several outputs. For example, the coherence values between exterior microphone 3 (which directly measures the acoustic energy from

the rear propeller) and interior microphones 1, 4, and 5 lie between 0.6 and 0.8, while the coherences with interior microphones 3 and 6 are significantly lower. Similar trends are seen in the accelerometer coherence values. This may imply a complex interaction among the various acoustic and vibration sources with regard to the interior noise environment.

The results of conditioning each output with the various inputs (both individually and sequentially) are shown in Table 8-2. The table lists the reduction in the level of the BPF tone at each of the five interior microphones, as a result of the conditioning process. The first four entries in the table show the effect on the output microphones of the removal of each input microphone, individually. The reductions seem to correspond with the coherence values in Table 8-1; removal of inputs with high coherence result in large reductions, while removal of inputs with low coherence results in small reductions.

In contrast, the next set of entries in the table show the effect on the output microphones of the sequential removal of the same input microphones, in the order listed. Thus for output microphone 1, removal of the effects of input microphone 4 reduces the BPF level by 1.5 dB (as was also seen in the first entry in the table), but the subsequent removal of the effects of input microphone 13 further reduces the BPF level by 13.5 dB, for a total reduction of 15 dB. Although the individual effects of conditioning the output with these two inputs are small (1.5 and 0 dB), the combined effect is substantial. This implies that the two input microphones are measuring different sources (or different combinations of two sources), and both of these sources are contributing to the level at output microphone 1.

It is likely that these two sources are in fact the two propellers. Although the frequency of the tones generated by these propellers is the same (within the resolution of the spectral analysis), at any point on the fuselage there is a phase difference between the signals received from each blade row, which varies with location. This varying phase shift arises from the fact that the propellers are counter-rotating, and at different distances from the fuselage. Thus there are two separate acoustic sources, of the same frequency, impinging on the aft fuselage; the level in the cabin is affected by both.

Returning to Table 8-2, it can be seen that for the same output microphone, further conditioning with input microphones 3 and 12 produces no further reduction in level. It would appear that two exterior microphones (4 and 13) are sufficient to include the effects of the two exterior sources.

The same trends observed for output microphone 1 can be observed for the other output microphones, to varying degrees.

The next portion of the table contains the results of conditioning the output with the accelerometer inputs. As for the microphone inputs, the accelerometer inputs exhibit the characteristic that the individual reductions correspond to the coherence

values. In contrast to the microphone inputs, however, the sequential reductions for the accelerometer inputs are more in line with reductions that would be expected based on the individual reductions.

Finally, the reductions in level at the output microphones can be compared for three sets of conditioning inputs: all microphone inputs, all accelerometer inputs, and all microphone and accelerometer inputs combined. The table shows that for each output microphone, conditioning with all the inputs produces the greatest reductions; these reductions for all the outputs eliminate the BPF tone from the conditioned spectra (within 1 dB). This implies that all the acoustic energy at the output is accounted for by the inputs used in the analysis, and further that both sets of inputs (microphone and accelerometer) are needed. Thus it can be concluded that the interior BPF levels result from both acoustic and vibration excitation of the structure. Furthermore, the relative magnitudes of the reductions produced separately by the microphone and accelerometer inputs give an indication of the relative strengths of the two types of sources: for output microphones 1, 3, and 5 the acoustic sources appear to contribute more to the interior level than the vibration sources, while the reverse occurs for output microphones 4 and 6.

Since the source of the BPF tones in the cabin is a combination of acoustic and vibration excitation, the issue of transmission path identification still remains. Is the acoustic energy transmitted solely along the aft section path and the vibration energy transmitted solely along the structural path, or is there a more complex propagation scenario? To investigate this further, accelerometers 2 and 3 were analyzed as outputs. Each was conditioned with the various exterior microphone and accelerometer inputs used previously. For both outputs, the results of the partial coherence analysis showed that the BPF levels arose from a combination of acoustic and vibration excitation. Thus the structural path, through the pylon and fuselage structure, transmits both acoustic energy (from acoustic loads impinging on the pylon) and vibration energy (from engine mechanical forces) into the cabin.

In the unpressurized section behind the pressure bulkhead, aft section microphone 5 was also conditioned with the various exterior microphone and accelerometer inputs. Conditioning this output with these several inputs together only partially reduced the BPF tone level. Since a relationship between the BPF levels at this microphone and at exterior accelerometer 1 was observed in Section 8.3, this accelerometer was also used as an input to further condition the aft section microphone 5 output (despite the fact that this accelerometer is considered to be an output transducer itself). Again the level at this output microphone was not fully reduced to the background. The presence of residual energy at this output after conditioning with these inputs implies that other sources may affect the BPF levels in the aft section. For example, radiation of the pressure bulkhead (due to propagation of structural energy through the pylon spars

and fuselage structure into this bulkhead) may contribute to the aft section microphone levels. It should be noted that among the five microphones in this aft unpressurized section (see Figure 3-3), the BPF level is highest at two microphones: microphone 1 adjacent to the fuselage wall near the forward propeller plane and microphone 5 adjacent to the pressure bulkhead. This supports the hypothesis that vibration of fuselage structural members contributes to the BPF levels measured in the aft section.

From this discussion it can be inferred that the aft section path is not significant in the transmission of acoustic energy into the cabin. It would appear, then, that acoustic and vibration excitation of the pylon is transmitted into the fuselage structure, and then propagated into the passenger cabin. Structural energy is also propagated into the aft unpressurized section. These results are in agreement with the conclusions developed independently in Section 8.3 and 8.4.

8.5.3 Analysis of 10x8 Data

The partial coherence analysis of the 10x8 flight test data was conducted in a similar manner to that of the 8x8 data. There were, however, some differences in transducers. For outputs, interior microphones in row six were available for seat positions 1, 3, and 4. Available inputs were limited to exterior microphones 3 and 4, and accelerometers 5Y and 5Z. Additional available transducers included accelerometers 1 and 2, plus four accelerometers mounted on the pressure bulkhead (which were not available for the 8x8 analysis; see Figure 3-5 for locations).

Table 8-3 lists the ordinary coherence values between the various inputs and outputs, for BPF(8) and BPF(10) tones. The table shows that there is a highly coherent environment on the Demonstrator for the 10x8 engine configuration. The coherence values are all nearly unity, except for coherence values of about 0.7 between accelerometer 5Z and each output microphone for the BPF(10) tone. These uniformly high coherence values are in contrast to the coherence values for the 8x8 data (Table 8-1), where the two sources of the same frequency combined to generate incoherent signals.

Conditioning the three output microphones with the various inputs results in the reductions in BPF tone levels listed in Table 8-4. As for the 8x8 data, the reductions in levels shown in the table due to conditioning with the individual inputs reflect the coherence values. The results of conditioning with the combined inputs suggest that both acoustic and vibration excitation contribute to the levels at the output microphones, at about equal strength. However, since there is high coherence among the various inputs for both BPF tones, the relative importance of acoustic and vibration sources to the outputs cannot be determined with certainty.

Conditioning accelerometer 2, the bulkhead accelerometers, and aft section micro-

phone 5 as outputs with the same inputs as above also indicates approximately equal contributions from acoustic and vibration sources for each of these outputs. Again, since the levels between these output transducers are all highly correlated with each other as well as with all the available input transducers, and since several input transducers are missing for this 10x8 analysis, no further conclusions can be drawn concerning transmission paths from the acoustic and vibration sources into the passenger cabin.

TABLE 8-1
 Coherence Between Inputs and Outputs
 for BPF Tone (168 Hz), Testpoint 19550A03

<i>Input Transducer</i>	<i>Output Microphone</i>				
	1	3	4	5	6
Mic 4	0.30	0.38	0.98	0.97	0.40
13	0.08	0.75	0.75	0.77	0.79
3	0.80	0.18	0.78	0.65	0.08
12	0.84	0.50	0.45	0.28	0.19
Accel 4	0.79	0.05	0.34	0.46	0.47
5Z	0.70	0.31	0.78	0.60	0.03
5X	0.60	0.39	0.87	0.69	0.03
5Y	0.50	0.39	0.94	0.81	0.18

TABLE 8-2
Reduction in BPF Tone Level at
Interior Output Microphones Conditioned with
Exterior Microphone and Accelerometer Inputs,
Test Point 19550A03

<i>Input Transducer</i>	<i>Output Microphone</i>				
	1	3	4	5	6
Mic 4	1.5	2.0	17.5	15.0	3.0
13	0.0	6.0	5.5	6.0	7.0
3	7.0	1.0	6.0	4.5	0.5
12	8.0	3.0	2.5	1.0	0.5
Mic 4	1.5	2.0	17.5	15.0	3.0
+13	15.0	11.5	20.5	21.5	7.0
+ 3	15.0	12.0	21.0	21.5	7.5
+12	15.0	12.0	21.0	21.5	8.0
Accel 4	6.0	1.0	1.5	2.5	3.0
5Z	6.0	2.0	6.5	4.0	0.5
5X	4.0	2.0	8.5	5.0	0.5
5Y	3.0	2.0	12.0	7.5	1.0
Accel 5Z	6.0	2.0	6.5	4.0	0.5
+5X	9.0	6.0	15.5	12.5	7.0
+5Y	12.5	10.0	19.5	16.5	12.0
+4	13.0	11.0	22.5	18.5	13.0
Accel 5Z	6.0	2.0	6.5	4.0	0.5
+5X	9.0	6.0	15.5	12.5	7.0
+5Y	12.5	10.0	19.5	16.5	12.0
+4	13.0	11.0	22.5	18.5	13.0
+Mic 4	13.0	11.5	23.5	22.0	15.5
+13	15.5	13.0	24.5	22.5	18.5
+3	15.5	13.0	24.5	22.5	19.0
+12	15.5	14.0	24.5	22.5	19.0

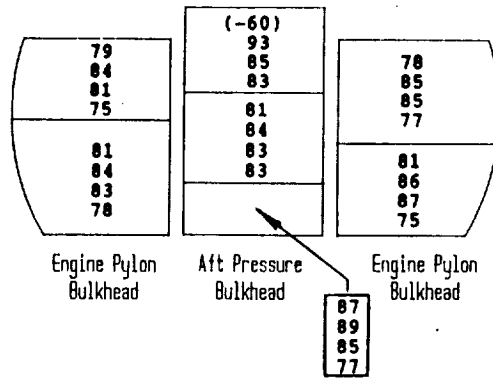
TABLE 8-3
Coherence Between Inputs and Outputs
for BPF Tone (168 and 210 Hz), Test Point 19640B03

<i>Input Transducer</i>	Output Microphone					
	1		3		4	
	BPF(8)	BPF(10)	BPF(8)	BPF(10)	BPF(8)	BPF(10)
Mic 4	0.98	0.94	0.95	0.92	0.97	0.97
3	0.98	0.93	0.95	0.89	0.97	0.96
Accel 5Z	0.98	0.72	0.95	0.69	0.98	0.75
5Y	0.96	0.95	0.93	0.92	0.95	0.97

TABLE 8-4
Reduction in BPF Tone Level at
Interior Output Microphones Conditioned with
Exterior Microphone and Accelerometer inputs,
Test Point 19640B03

<i>Input Transducer</i>	Output Microphone					
	1		3		4	
	BPF(8)	BPF(10)	BPF(8)	BPF(10)	BPF(8)	BPF(10)
Mic 4	16.5	12.5	13.0	11.0	13.5	14.5
3	16.0	11.5	13.0	9.5	13.5	13.5
Mic 4	16.5	12.5	13.0	11.0	13.5	14.5
+3	16.5	13.0	13.5	11.5	14.0	15.0
Accel 5Z	17.5	5.5	13.0	5.0	14.5	6.0
5Y	14.0	12.5	11.0	11.0	12.5	14.5
Accel 5Z	17.5	5.5	13.0	5.0	14.5	6.0
+5Y	17.5	12.5	13.5	11.0	15.0	15.0
Accel 5Z	17.5	5.5	13.0	5.0	14.5	6.0
+5Y	17.5	12.5	13.5	11.0	15.0	15.0
+Mic 4	18.0	13.0	13.5	11.5	15.0	15.5
+3	18.5	13.5	14.0	12.0	15.0	15.5

Aft Bulkheads



(JT8D Side)

Right Sidewall

-83	87	91
-78	85	84
66	81	80
-69	73	79
-78	84	84
-83	82	80
-78	82	77
-67	73	72
-75	78	78
73	79	79
-73	80	76
-71	75	73
-77	77	79
-83	80	78
-78	77	76
-68	70	73

Bag Rack Upper Sidewall Lower Sidewall

(UDF Side)

Left Sidewall

76	-76	-79
77	77	-75
83	81	-79
74	-65	-73
76	(-62)	-75
(-62)	79	-82
76	79	-79
65	67	-71
72	66	-71
-82	(-61)	-78
-78	-66	-71
63	(59)	-68
-69	-67	-66
-84	-79	-77
-75	-68	-75
68	-62	-69

Lower Sidewall Upper Sidewall Bag Rack

ONE-THIRD OCTAVE BAND CENTER FREQUENCY IN EACH BOXED AREA

First Row, JN1: 100 Hz
 Second Row, BPF: 160 Hz
 Third Row, UN1: 200 Hz
 Fourth Row, 2BPF: 315 Hz

-79	-74	-75	-78
-82	(-71)	-80	-82
-78	-76	-78	-74
-65	69	73	72

Ceiling

Fwd

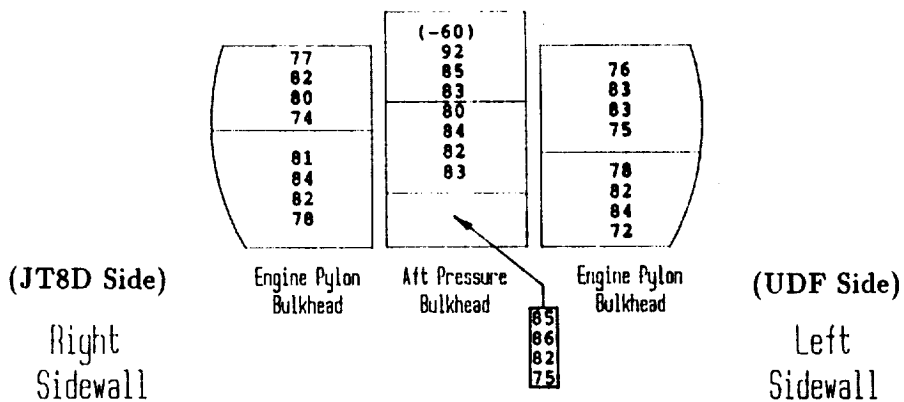
Aft

-69	64	72	77
-71	-71	84	86
69	(-66)	(63)	79
72	71	69	77

Floor

FIGURE 8-1. Measured Sound Intensities for the 100, 160, 200 and 315 Hz One-Third Octave Bands, 8x8 Flight 2026.

Aft Bulkheads



-80	85	89
-75	84	82
63	80	78
-66	72	78

-76	82	82
-80	80	78
-75	80	75
-64	71	70

-72	76	76
70	77	77
-70	75	74
-68	73	71

-74	75	77
-81	78	76
-75	75	74
-70	68	71

Bag Rack Upper Sidewall Lower Sidewall

ONE-THIRD OCTAVE BAND
CENTER FREQUENCY
IN EACH BOXED AREA

First Row, JN1: 100 Hz
Second Row, BPF: 160 Hz
Third Row, UN1: 200 Hz
Fourth Row, 2BPF: 315 Hz

74	-74	-76
75	75	-72
81	79	-76
72	-63	-70

74	(-60)	-73
(-60)	77	-79
74	77	-76
63	65	-68

70	65	-68
-80	(-59)	-75
-76	-64	-69
61	(57)	-65

-64	-62	-61
-79	-74	-72
-70	-63	-70
63	-58	-63

Lower Sidewall Upper Sidewall Bag Rack

-78	-73	-73	-77
-81	(-69)	-79	-81
-77	-75	-77	-73
-64	68	73	71

Fwd Aft

Ceiling

-65	63	72	75
-67	-71	84	84
66	(-65)	(63)	77
69	71	68	74

Floor

FIGURE 8-2. Measured Sound Power Levels for the 100, 160, 200 and 315 Hz One-Third Octave Bands, 8x8 Flight 2026.

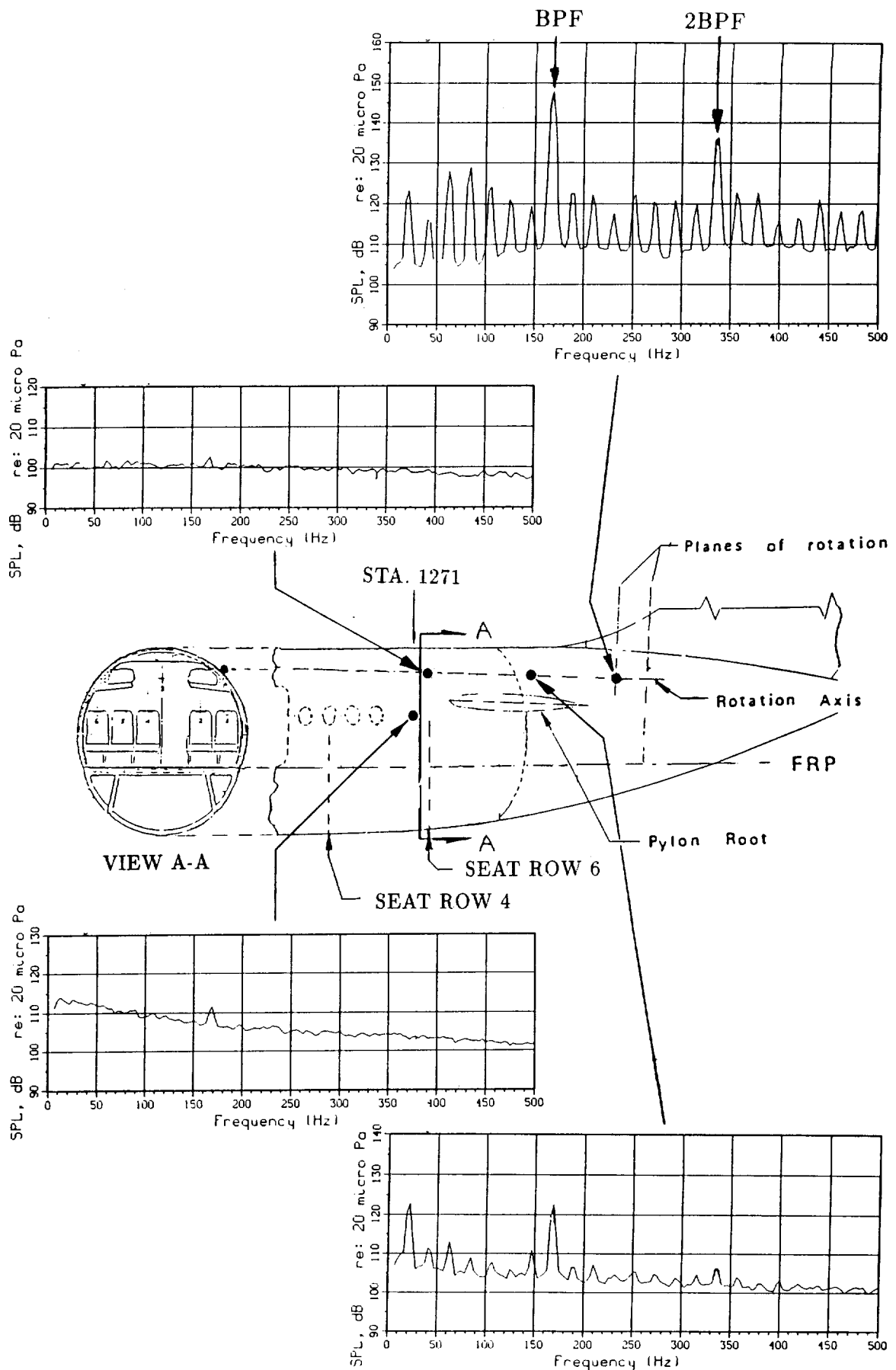


FIGURE 8-3a. Cabin Sidewall Transmission Path: Exterior Noise Spectra Measured on the Aircraft Fuselage. Test Point 19550A03.

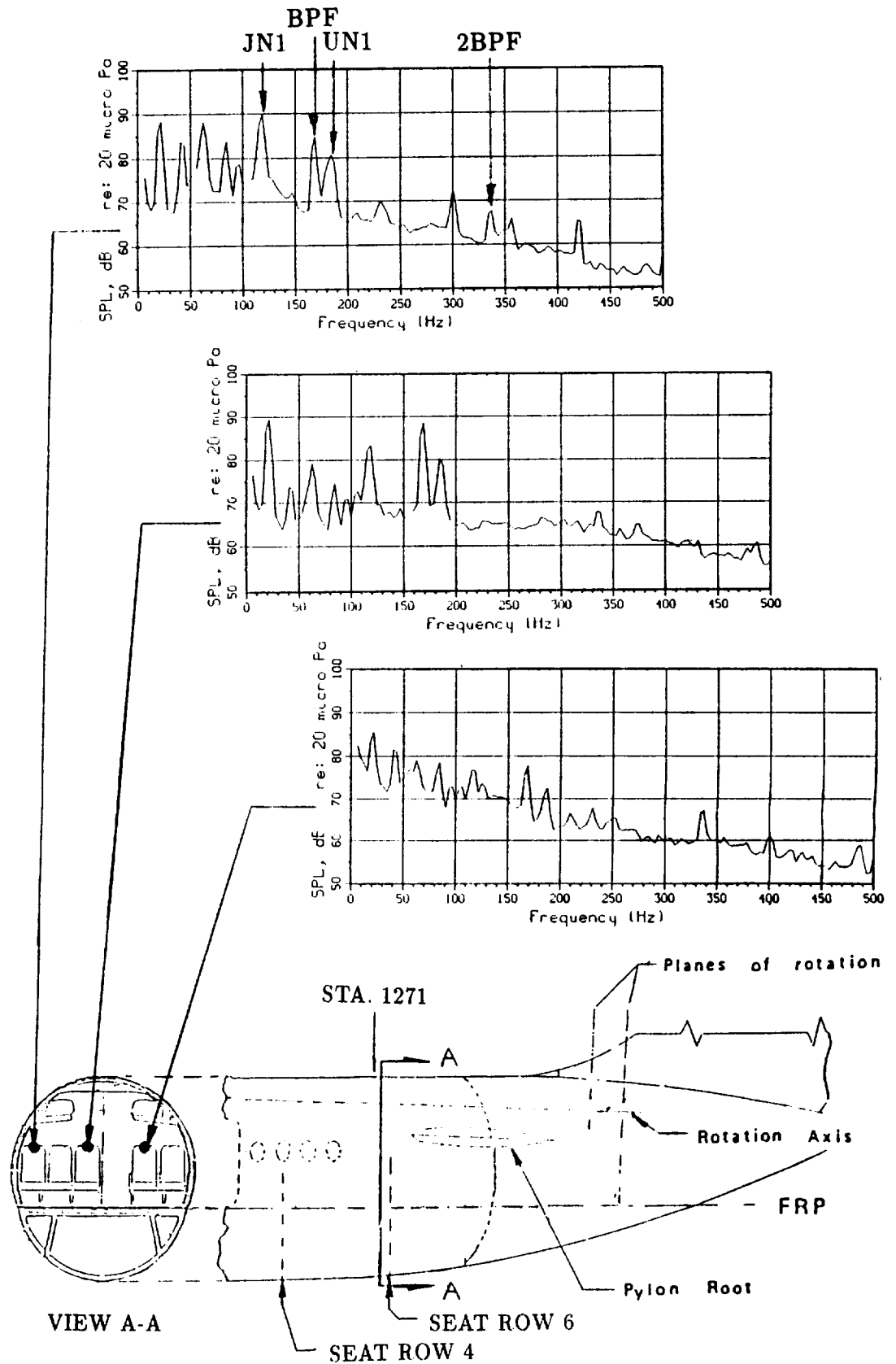


FIGURE 8-3b. Cabin Sidewall Transmission Path: Interior Noise Spectra, Test Point 19550A03.

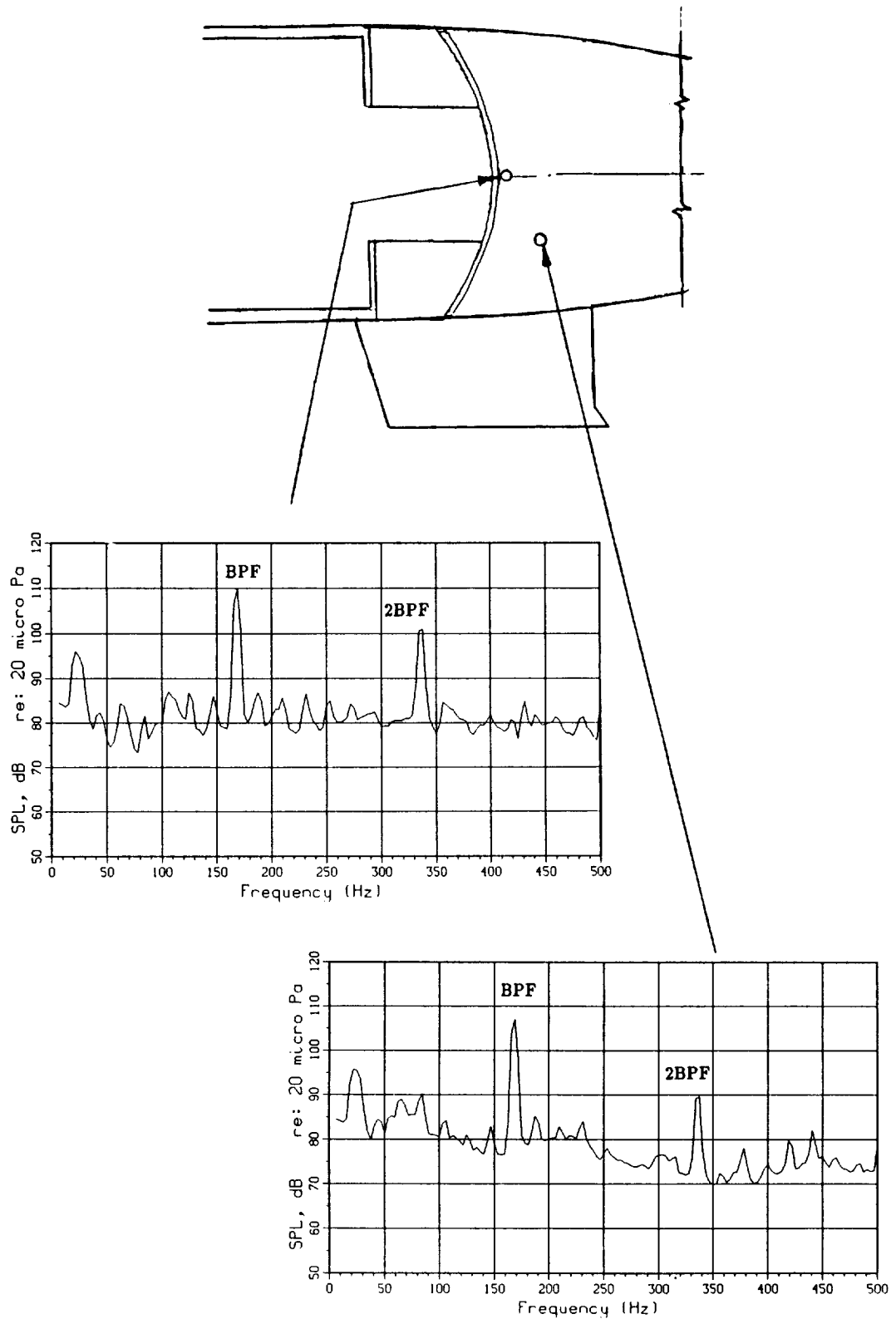


FIGURE 8-4. Aft Section Transmission Path: Unpressurized Section Noise Spectra, Test Point 19550A03.

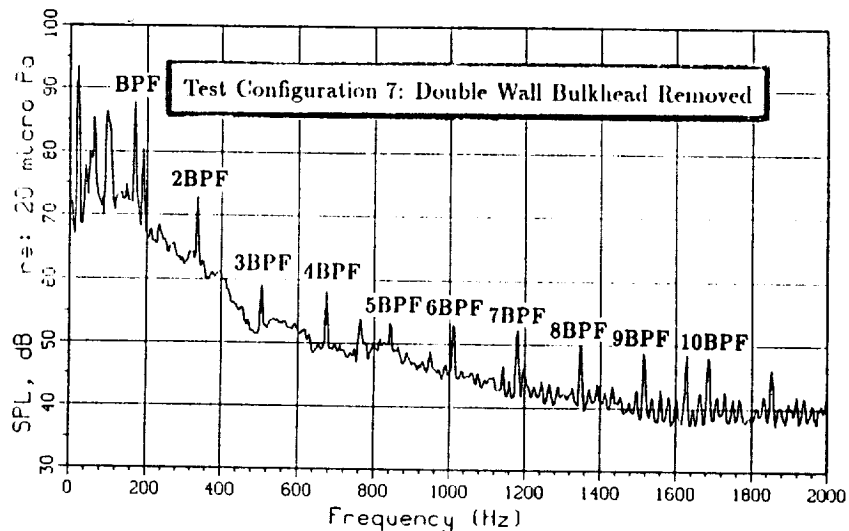
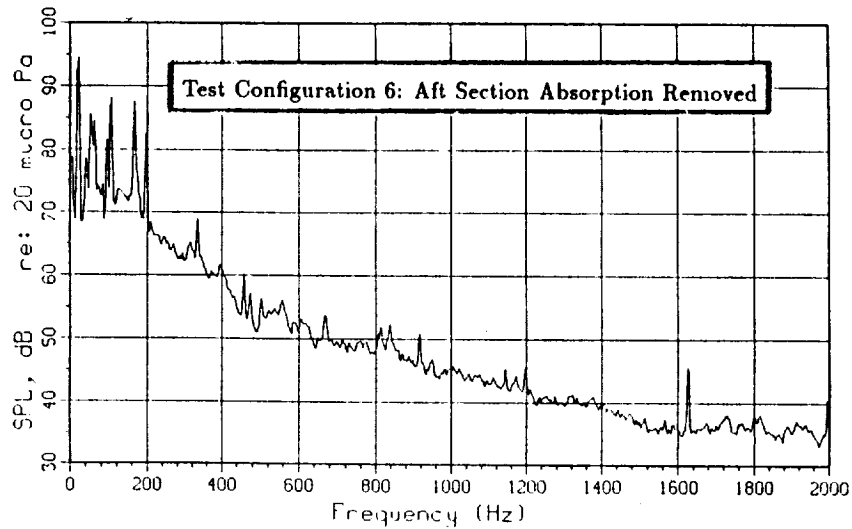
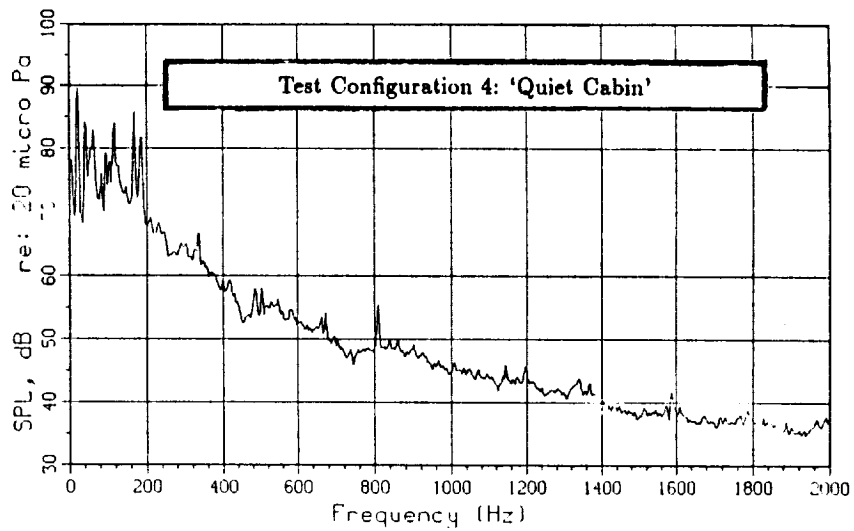


FIGURE 8-5. Aft Section Transmission Path: Comparison of Interior Noise Spectra at Row 6, Seat 1.

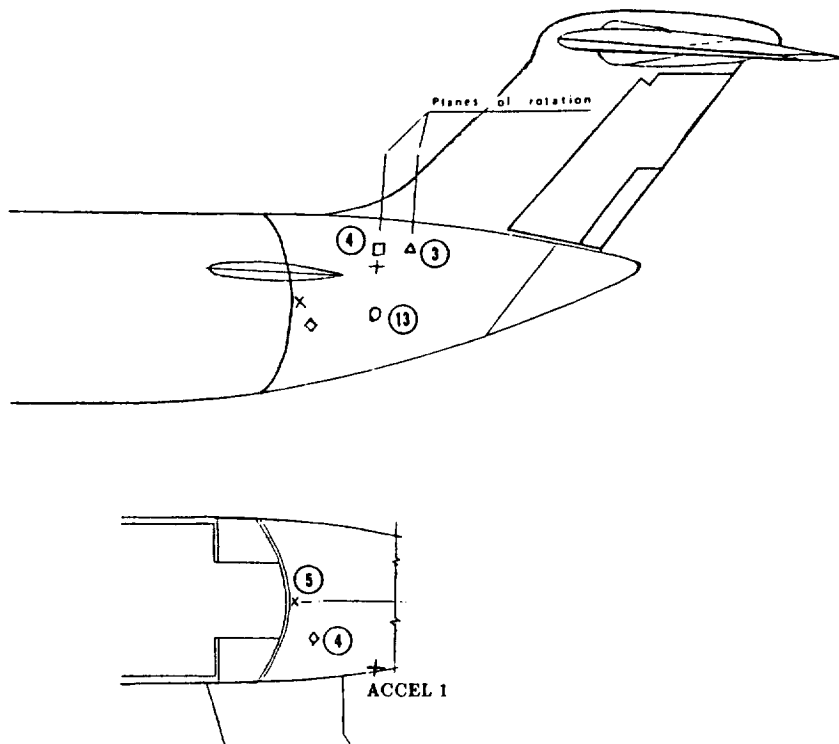
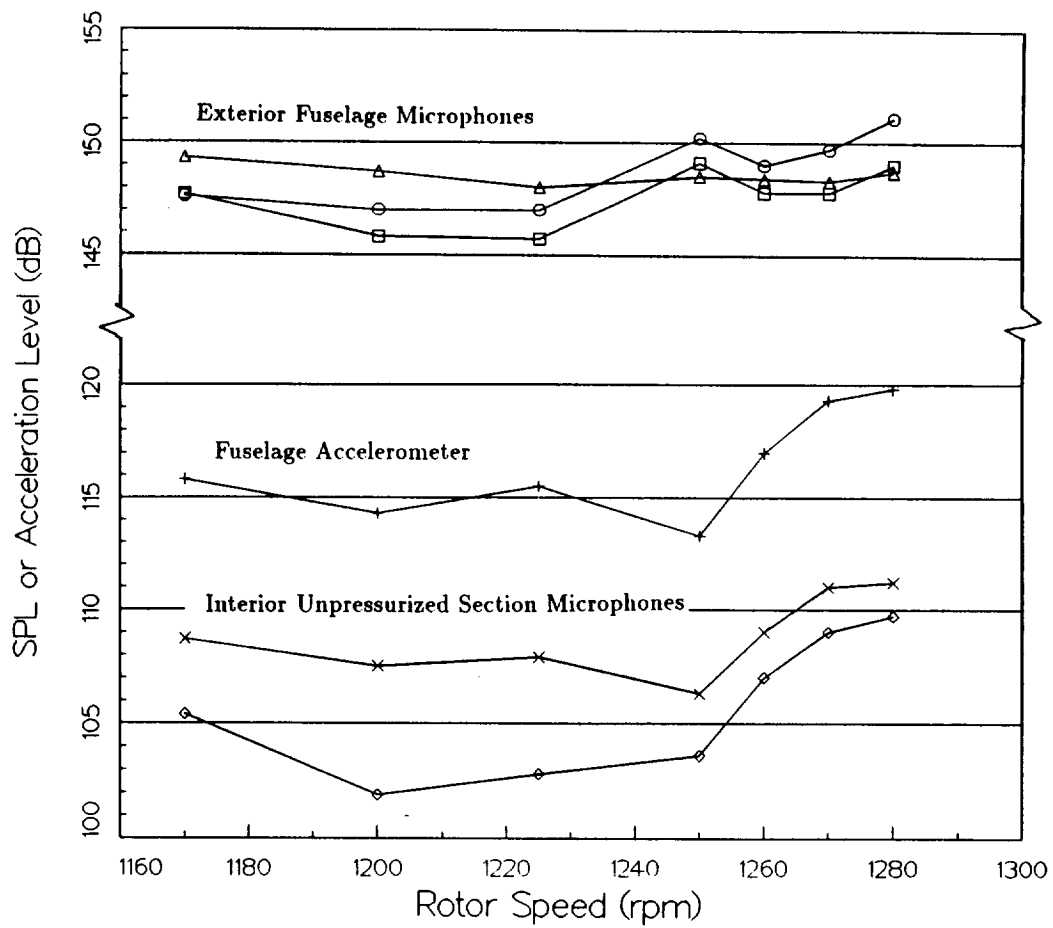
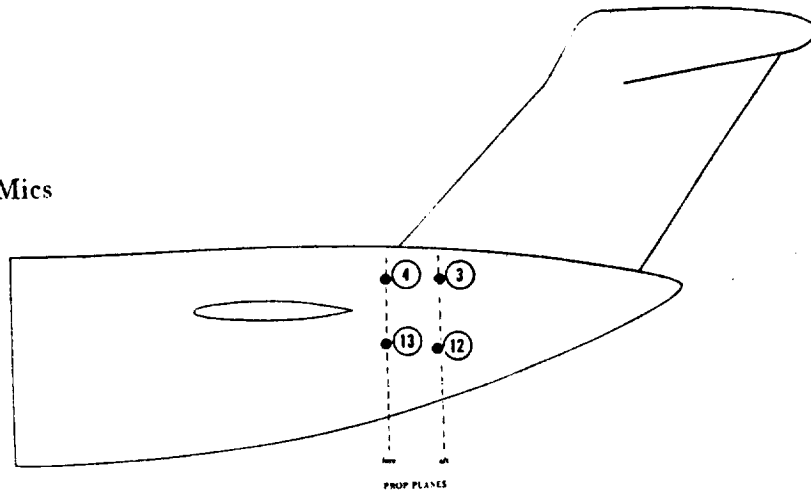
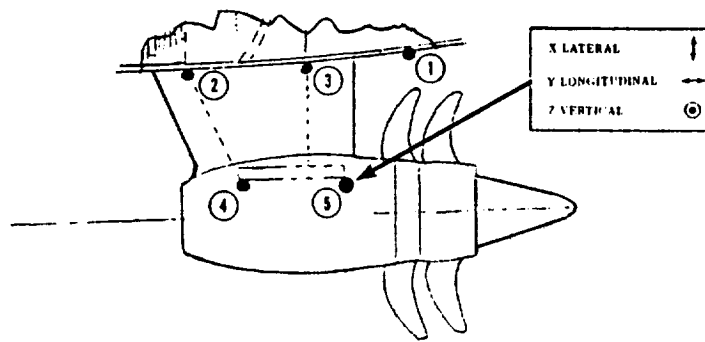


FIGURE 8-6. Comparison of Noise and Vibration Data Acquired in the Aft Section of the Aircraft, Flight 1955.

Exterior Mics



Pylon/Fuselage Accels



Interior Mics

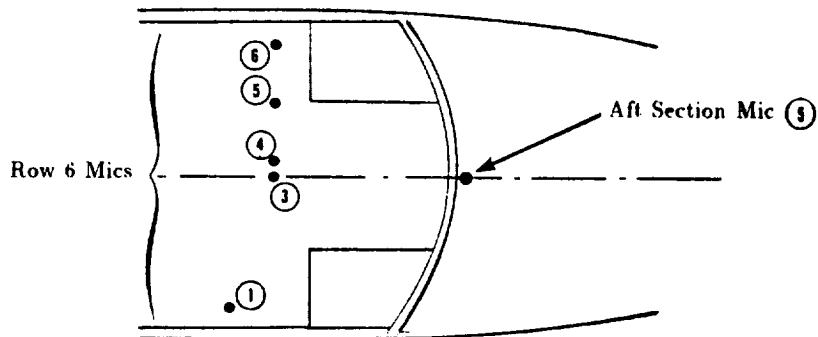


FIGURE 8-7. Transducers Used in the Partial Coherence Analysis of 8x8 Data

9 Summary and Conclusions

Noise and vibration data acquired during flight tests of the UHB Demonstrator with a GE UDF engine were analyzed to evaluate the effectiveness of selected noise control treatments in reducing interior noise levels, and to investigate cabin noise characteristics and transmission paths. Most of the flight data were acquired at high altitude, high speed cruise conditions (35,000 ft. and 0.76 Mach), with an 8x8 engine configuration. Additional tests were conducted with a 10x8 engine configuration and at lower altitudes and speeds, permitting a comparison of interior noise levels among the various engine configurations and operating conditions.

Noise control treatments were installed on the Demonstrator to reduce cabin noise to a maximum level of 82 dBA. Seven configurations were evaluated; in the first four, treatments were added up to the Quiet Cabin configuration for which the goal level of 82 dBA was achieved. The final three configurations involved removal of selected treatments without increasing cabin noise levels. The treatment evaluation analysis showed that:

- the torque box damping and the engine dynamic absorbers have a negligible effect on cabin noise levels,
- the cabin furnishings (including damped trim panels) reduce cabin noise levels significantly, and
- removal of engine dynamic absorbers, cargo skin damping, and double wall pressure bulkhead treatments has a negligible effect on cabin noise levels.

Interior noise spectra in the aft cabin were found to contain several tones, superimposed on a broadband background. These tones correspond to the blade passage frequencies of the two propellers, the propeller shaft rotational frequency, the core rotational frequencies of the UHB and JT8D engines, and various harmonics of these several tones. The broadband background is due to the exterior boundary layer noise.

In terms of A-weighted sound levels, at a particular seat location the broadband component of the noise level is typically equal to or higher than the tonal component (which is the summation of the levels of all the tones in the spectrum). Since there is little variation in the broadband noise in the aft cabin, the range in overall noise levels is small, typically from 78 to 82 dBA over the last five seat rows.

The main contributors to the tonal component, in order of importance, are the BPF tones, the JN1 tone, the UN1 tone, and the 2BPF tones. The BPF tone levels increase with increasing rotor speed, reflecting the increase in exterior noise levels observed in

the forward rotor plane as rotor speed increases. The BPF levels are typically highest in the aft cabin, on the right side of the aircraft.

Comparison of interior noise levels for high speed, high altitude cruise operations measured during 8x8 and 10x8 flights showed comparable maximum overall levels for the two engine configurations. Broadband levels were nearly identical; BPF tone levels were lower at selected locations during the 10x8 flights. These lower levels correspond to the measured lower noise levels in the forward rotor plane and lower vibration levels on the engine mount for the 10x8 flights.

Noise data from several flights at lower altitudes and speeds than the standard 35,000 ft., Mach 0.76 cruise conditions were reviewed for 8x8 and 10x8 configurations. For these "non-cruise" conditions, the levels of the broadband and tonal components were different than for cruise conditions. Differences in the broadband levels were traced to expected differences in exterior boundary layer noise levels (due to altitude and speed differences). Differences in the tonal levels corresponded in most cases with differences in exterior noise levels in the forward propeller plane, which are attributable to altitude and helical tip Mach number effects.

The sound intensity survey showed that most of the tone energy in the cabin emanates from the engine mount bulkheads and the pressure bulkhead (if untreated), and the sidewall on the JT8D side. Study of the various interior and exterior noise and vibration data, in conjunction with the results of the sound intensity survey and the partial coherence analyses, yields the following conclusions about noise sources and transmission paths into the cabin:

- the cabin sidewall path is not a propeller noise path but is the likely path of the broadband noise component,
- the aft section path does not appear to be a transmission path for the propeller noise at low frequencies, but if left untreated may allow higher harmonics of the propeller noise to be transmitted and become perceptible in the cabin, and
- the tones found in the interior noise spectra are the result of structureborne transmission through the pylon and the fuselage. The transmitted energy is caused by a combination of acoustic loads from the propeller blades impinging on the pylon, and mechanical forces within the engine propagating through the pylon. The major radiating surfaces are the aft bulkheads (primarily the engine mount bulkheads) and the right (JT8D side) sidewall.

Finally, two analysis techniques were evaluated using measured Demonstrator flight test data. The partial coherence analysis technique was found to be very useful in identifying the relative strengths of the sources of BPF tones in the cabin, but of limited

usefulness in sorting out transmission path strengths. The weakness of this technique was in part related to the limited availability of transducers, at appropriate locations. Nevertheless, the conclusions drawn from the partial coherence analyses agreed with conclusions developed independently from other data analyses, demonstrating that the technique has good potential for source/path diagnosis.

The second technique (described in Appendix A) is a spectral analysis method of estimating turbulent boundary layer pressure fluctuations using a fixed microphone probe on the fuselage exterior. Good agreement was found between predicted levels and wavenumber-frequency levels estimated from the flight data, in the mid-wavenumber and frequency range. This demonstrates that the fixed probe technique works, and can be used successfully to measure turbulent boundary layer spectra in flight.

A Estimation of The Turbulent Boundary Layer Pressure Wavenumber-Frequency Spectrum

The pressure and vibrational fields associated with turbulent flows over various vehicles have been the subject of continuing research over the past 30 years. In commercial aircraft, the turbulent boundary layer (TBL) pressure fluctuations represent one of the dominant sources of interior noise during cruise, as was also observed on the UHB Demonstrator. The modeling of the turbulent boundary layer pressure frequency spectrum for interior noise prediction is generally based on an empirical fit to laboratory wind tunnel measurements. As a result, cabin flight test data are not in good agreement with predicted levels based on such models. In addition, it has been reasoned that the absence of wavenumber information leads to an overprediction of interior levels. Wavenumber information is also useful since the relative importance of nonresonant transmission at low wavenumber can be determined by the wavenumber-frequency spectra of the TBL fluctuations.

The main objective of the study described in this Appendix is to examine a new spectral analysis method of estimating turbulent boundary layer pressure fluctuations using a fixed probe consisting of two microphones. Demonstrator flight test data have been used to examine the applicability of this spectral analysis method to in situ flight measurements of TBL pressure fluctuations. TBL pressure wavenumber-frequency spectra on the fuselage surface were determined from measurements using two exterior microphones, for several flight conditions. These estimated inflight spectra were then compared with existing wind tunnel data, and with selected prediction models. The behavior of the TBL wavenumber-frequency spectra in the lower wavenumber region was also examined with regard to the “wavelength white” region of the wind tunnel TBL spectra.

A.1 Definition of Wavenumber-Frequency Spectra

Turbulent flow is a random process in both space and time, and cannot be specified deterministically. The turbulent pressure field is, therefore, modeled as a zero-mean random process with a space-time correlation function given by

$$R_{pp}(\mathbf{r}_1, \mathbf{r}_2; t_1, t_2) = \mathcal{E}\{p(\mathbf{r}_1, t_1)p(\mathbf{r}_2, t_2)\},$$

where \mathbf{r}_1 and \mathbf{r}_2 denote two observation points, and \mathcal{E} is the expectation operator. A common property of the random field is temporal stationarity which implies a dependence of R_{pp} only on the difference $t_1 - t_2$, i.e.

$$\begin{aligned} R_{pp}(\mathbf{r}_1, \mathbf{r}_2; t_1, t_2) &= R_{pp}(\mathbf{r}_1, \mathbf{r}_2; t_1 - t_2, 0), \\ &= R_{pp}(\mathbf{r}_1, \mathbf{r}_2; \tau), \end{aligned}$$

where $\tau = t_1 - t_2$. In this case the field can be characterized in terms of its cross-spectral density as follows:

$$S_{pp}(\mathbf{r}_1, \mathbf{r}_2; \omega) = \int R_{pp}(\mathbf{r}_1, \mathbf{r}_2; \tau) e^{-i\omega\tau} d\tau,$$

which is obtained as the Fourier transform of R_{pp} over the τ variable.

Another property of some fields is spatial homogeneity which implies that R_{pp} depends only on the spatial separation $\mathbf{r}_1 - \mathbf{r}_2$, giving:

$$\begin{aligned} R_{pp}(\mathbf{r}_1, \mathbf{r}_2; \tau) &= R_{pp}(\mathbf{r}; \tau) \\ \text{and } S_{pp}(\mathbf{r}_1, \mathbf{r}_2; \omega) &= S_{pp}(\mathbf{r}; \omega), \end{aligned}$$

where $\mathbf{r} = \mathbf{r}_1 - \mathbf{r}_2$. The wavenumber-frequency spectrum can now be defined as the Fourier transform of the spatial-time correlation on the spatial separation vector \mathbf{r} and the time difference τ . For spatially homogeneous fields, the wavenumber-frequency spectrum is given by:

$$S_{pp}(\mathbf{k}, \omega) = \iint R_{pp}(\mathbf{r}; \tau) e^{-i(\mathbf{k}\cdot\mathbf{r} + \omega\tau)} d\mathbf{r} d\tau.$$

The wavevector \mathbf{k} is the Fourier conjugate variable of the spatial separation vector \mathbf{r} , and the circular frequency ω is the conjugate variable of the time difference τ .

For a nonhomogeneous field, the wavenumber-frequency spectrum can be defined as a space-varying spectrum, i.e.,

$$S_{pp}(\mathbf{x}, \mathbf{k}, \omega) = \iint R_{pp}(\mathbf{x}, \mathbf{r}; \tau) e^{-i(\mathbf{k}\cdot\mathbf{r} + \omega\tau)} d\mathbf{r} d\tau.$$

The space-averaged spectrum for a nonhomogeneous process may be written:

$$S_{pp}(\mathbf{k}, \omega; A) = \frac{1}{A} \int S_{pp}(\mathbf{x}, \mathbf{k}, \omega) d\mathbf{x},$$

where A is the area of the measurement surface.

The measurement of the wavenumber-frequency spectral density, in general, requires an array of transducers carefully placed in the field under investigation. The space-time sampled data is then Fourier transformed to obtain the wavenumber-frequency spectrum.

A.2 Spectral Modeling of TBL Pressure Fluctuations

The pressure fluctuations in an incompressible flow have classically been examined by relating the phenomenon to velocity fluctuations through Poisson's equation. Some of the theoretical knowledge seems to be contradicted by experiments, however, particularly the behavior of the spectrum at long wavelengths. For example, the theories of Kraichnan [1,2] and Phillips [3] indicated that the spectrum should vanish at long wavelengths whereas the experimental results are best described by models in which the spectrum approaches a constant in that region, e.g. Corcos' model [4]. As a result, several semi-empirical/empirical models have been developed primarily on the basis of experimental data. (A complete description of the vast amount of work related to TBL theoretical and empirical models is beyond the scope of this report.)

In the present investigation, the TBL wavenumber-frequency spectra obtained from flight test data were compared with three different prediction models: Corcos' convective ridge model [4], a spectral model proposed by Laganelli et al. [6], and Witting's burst and sweep model [5]. These models appear to match a broad variety of experiments and provide a basis for wavelength-white spectra at long wavelengths.

Many measurements of two point wall pressure statistics were carried out through the 1960's and early 1970's. Those conducted using cross-spectral techniques, e.g. Bull [7] and Blake [8], are of more significance for TBL pressure spectrum estimation than those conducted using cross-correlation techniques, e.g. Willmarth and Wooldridge [9]. The cross-correlation measurements did not provide sufficient accuracy when Fourier transformed to the frequency ranges of interest for such problems as aircraft cabin noise.

On the basis of the wind tunnel measurements, it has been recognized that the wavenumber-frequency spectrum of the wall pressure is sharply peaked with regard to the longitudinal (streamwise) wavenumber at a value $k_1 \approx \omega/U_c$, where U_c is the convection velocity and ω is the circular frequency. The decrease with lateral (spanwise) wavenumber k_3 is much slower, so that $S_{pp}(\mathbf{k}, \omega)$ possesses a convective ridge centered at $(k_1, k_3) \approx (\omega/U_c, 0)$ and is oriented towards the flow. Wind tunnel measurements by Willmarth and Wooldridge [9] and Corcos [4] support the conclusion that $S_{pp}(k_3) \approx S_{pp}(0)$. The fundamental problem, then, is the description of the longitudinal component $S_{pp}(k_1)$.

Although a large number of laboratory wind tunnel measurements have been performed, only a few have addressed the wavenumber-frequency description, particularly in the lower wavenumber-frequency region of the turbulent fields. Blake and Chase [10], Farabee and Geib [11], and Martini, Leahy, and Moeller [12] among others used a flush mounted array of microphones to measure the low wavenumber turbulent pressure spectrum. Wavenumber measurements were also carried out using structural elements

such as membranes and plates, e.g. Martin and Leehy [13] and Jameson [14].

Figure A-1 shows a possible shape of the wavenumber spectrum for zero lateral wavenumber and at a fixed frequency in terms of the longitudinal wavenumber [5,12]. The shape of this spectrum near the convective ridge ω/U_c is rather well established by cross-spectral measurements, but the shape near and below the acoustic wavenumber, $k_a = \omega/c_0$ (where c_0 is the speed of sound in the ambient medium), has not been conclusively established. The figure also shows two possible spectral characteristics in the low wavenumber region: the upper dashed curve shows a flat region where S_{pp} is independent of k_1 , while the lower solid curve has a region where S_{pp} is proportional to k_1^2 , and so would tend to zero in the absence of the acoustic peak. Most existing low wavenumber wall pressure measurements become independent of wavenumber ("wavenumber white") beginning at a wavenumber substantially above the acoustic wavenumber, and thus favor the upper curve. There is no indication that the incompressible k_1^2 low wavenumber limit of Kraichnan [1], as shown in the lower curve, is approached in any way.

On the other hand, an extensive search of the available published literature has revealed that no attempt has been made to estimate, in situ, the wavenumber-frequency spectrum of the turbulent boundary layer pressure spectrum on the exterior of an airplane fuselage. Most of the flight test investigations reported in the past are limited to pressure power spectral density, correlation, and cross spectrum analysis [15-17].

The estimation procedure used here for determining the wavenumber-frequency spectrum is unique in the sense that it requires the use of a fixed probe consisting of two microphones and can be easily applied to inflight measurements. The theory and assumptions behind this estimation technique are described in the following sections.

A.3 Estimation Procedure

As mentioned earlier, wavenumber-frequency spectra can be determined through measurements using an array of carefully placed transducers. In recent years, new techniques applicable to homogeneous and stationary fields have been developed for estimating wavenumber-frequency spectra which use two fixed transducers for data acquisition. These new methods have been applied to studies of ion-acoustic and plasma turbulence [18-21].

In one method developed by Harker and Ilić [18-19], the spatial Fourier transform is performed on the covariance of pressure signals measured by a movable probe at many sequential values of probe separation. In many cases, however, it is impractical to vary probe separation to obtain information over a sufficiently wide range of wavenumber. In order to avoid this difficulty, Iwama, Ohba, and Tsukishima [20] developed a cor-

relation method of measuring the first and second moments of the spectral density wavenumber space using fixed probe pairs based on the fact that

$$\frac{1}{i^n H(0, \omega)} \left(\frac{\partial^n H(\xi, \omega)}{\partial \xi^n} \right) \Big|_{\xi=0} = \int k^n s(k|\omega) dk,$$

where $H(\xi, \omega)$ is the cross-spectral density from the two transducers (separated by a distance ξ):

$$H(\xi, \omega) = \frac{1}{2\pi} \int S(k, \omega) e^{ik\xi} dk,$$

and $s(k|\omega)$ is the conditional wavenumber spectral density:

$$s(k|\omega) = \frac{S(k, \omega)}{S(\omega)}.$$

$S(\omega)$ is the auto spectral density defined by:

$$S(\omega) = H(0, \omega) = \int S(k, \omega) dk.$$

Introducing the concept of local wavenumber-frequency spectral density, Beall, Kim, and Powers [21] developed a new approach for estimating wavenumber-frequency spectra using fixed probe pairs. The local wavenumber is analogous to instantaneous frequency in the time domain. This local wavenumber method was used in the present investigation for estimating wavenumber-frequency spectra of the TBL pressure fluctuations from Demonstrator flight test data. The details of the theoretical approach to this method are given in Reference 21.

Most turbulence theories model the fluctuations in a turbulent medium as a homogeneous and stationary process [1-3]. Kraichnan's analysis of anisotropic homogeneous turbulence is cast mainly in terms of the Fourier coefficients of the velocity field. The turbulent field is supposed to be spatially periodic with very large period L , and the velocity may then be expressed as a Fourier series:

$$\mathbf{u}(\mathbf{x}, t) = \sum \mathbf{A}(\mathbf{k}, t) e^{i\mathbf{k} \cdot \mathbf{x}},$$

where the summation is over all the wavenumbers permitted by the cyclic boundary conditions. This analysis permits the representation of the fluctuations in a turbulent medium by a superposition of wave packets [21] or oscillations, which are approximately sinusoidal in both space and time with slowly varying amplitudes and wavenumbers. Under such conditions, Beall et al. showed that the local wavenumber-frequency spectral density is the same as the conventional wavenumber and frequency density [21].

In addition, a basic of property of wavefields that

$$k(x, \omega) = \frac{\partial \theta(x, \omega)}{\partial x},$$

just as in the time domain the circular frequency

$$\omega = \frac{\partial \theta(t, \omega)}{\partial t},$$

has been ingeniously used to obtain the local wavenumber.

The local wavenumber can be readily estimated from two fixed probe pairs at x_1 and x_2 :

$$k(x, \omega) \approx \frac{\theta(x_2, \omega) - \theta(x_1, \omega)}{x_2 - x_1},$$

where

$$x = \frac{x_1 + x_2}{2}.$$

The spectral densities $H(0, \omega)$, $H(\xi, \omega)$, and $S_l(k, \omega)$ may be estimated by using two probes at $x = x_1$ and x_2 separated by a distance $\xi = x_1 - x_2$. Here, $S_l(k, \omega)$ is the local wavenumber -frequency spectral density.

For a zero-mean, stationary, homogeneous random field $\phi(x, t)$, the Fourier transform relationship

$$\Phi(x, \omega) = \int \phi(x, t) e^{-i\omega t} dt,$$

can be represented by the following discrete Fourier series:

$$\Phi(x, \omega) = \frac{1}{N} \sum_{\ell=1}^N \phi(x, \ell \Delta t) e^{-i\omega \ell \Delta t}.$$

The sample cross spectrum is:

$$\begin{aligned} H^{(j)}(\xi, \omega) &= \Phi^{(j)*}(x_1, \omega) \Phi^{(j)}(x_2, \omega) \\ &= C^{(j)}(\omega) + iQ^{(j)}(\omega), \end{aligned}$$

where $C^{(j)}$ and $Q^{(j)}$ are, respectively, in-phase and quadrature components of the cross spectrum. The local wavenumber is given by:

$$k^{(j)}(\omega) = \frac{\theta^{(j)}(\omega)}{\xi},$$

where

$$\theta^{(j)} = \tan^{-1} \frac{Q^{(j)}(\omega)}{C^{(j)}(\omega)}.$$

The estimated wavenumbers are restricted to the interval $-\pi/\xi$ to π/ξ if indeterminacies of $\pm n2\pi/\xi$ are to be avoided.

The local wavenumber and frequency spectrum $S_\ell(k, \omega)$ is computed by summing the sample power values $S^{(j)}(\omega)$ at a fixed frequency from those records which have a sample local wavenumber in the range k to $k + \Delta k$, and dividing by M :

$$S_\ell(k, \omega) = \frac{1}{M} \sum_{j=1}^M I_{[0, \Delta k]}(k - k^{(j)}(\omega)) S^{(j)}(\omega).$$

The indicator function $I_{[0, h]}(x)$ is defined as

$$I_{[0, h]}(x) = \begin{cases} 1, & 0 \leq x < h \\ 0, & \text{otherwise} \end{cases}.$$

A.4 Flight Test Results

The wavenumber-frequency spectra for five flight conditions of the Demonstrator (see Table A-1) were estimated using the local wavenumber approach. The second flight condition is very similar to the first and was chosen to check the repeatability of the local wavenumber method. The locations of the probe microphones, exterior microphones 9 and 10, are shown in Figure 3-1 in the main report text. The spacing between these two microphones is 17.75 inches, which permits an estimation of the wavenumber spectra in the range of -2.1 to 2.1 ft^{-1} .

The sound pressure spectra with the two probe microphones for all flight conditions are shown in Figures A-2a through A-2e. It may be observed that the difference in overall sound pressure level between the two microphones for the first two flight conditions is about 5 to 6 dB, while for the other cases it is about 2 to 3 dB. The three-dimensional plots of the estimated wavenumber-frequency spectra for the TBL pressure fluctuations are correspondingly shown in Figures A-3a through A-3e, while Figures A-4a through A-4e show the contour plots of the pressure fluctuations. The variation of the TBL pressure spectra, and in particular the variation of the convective ridge peak with wavenumber and frequency, may be seen in these figures.

In order to compare the flight test data with the available wind tunnel or prediction models, the TBL pressure spectral density was normalized with respect to the following flow parameters: the free stream dynamic pressure (q_∞), the boundary layer displacement thickness (δ^*), and the free stream flow velocity (U_∞). The wavenumber k and the

circular frequency ω were non-dimensionalized as $k\delta^*$ and $\omega\delta^*/U_\infty$ (Strouhal Number), respectively. Wind tunnel measurements give convective velocity U_c typically in the range of 0.6 to $0.8U_\infty$, with the larger U_c corresponding to longer wavelength scales. Inflight measurements by Bhat [15] have shown U_c to approach an asymptotic value of $0.78U_\infty$ with increasing microphone separation. A value of $0.76U_\infty$ was chosen for U_c in our analysis.

Figures A-5a through A-5d show the variation of pressure spectral density in the wavenumber plane for fixed Strouhal numbers. These TBL pressure plots exhibit a pronounced peak occurring at or near the corresponding convective wavenumbers given by $k_c = \omega/U_c$. The location of the convective peak agrees well with that predicted by theoretical considerations. Since the acoustic and convective wavenumbers (k_a and k_c , respectively) are fairly close together, the TBL pressure spectrum between them is dominated by the convective ridge pressures. Above k_c , the TBL pressure decays rapidly.

The estimated TBL pressure wavenumber-frequency spectra were compared with three prediction models: Corcos' convective ridge, Laganelli's, and Witting's burst and sweep. The Corcos convective ridge model [4,13], based on similarity laws and slightly modified using Blake's cross-spectral density data [8], was used for comparison with the current flight test data. Figure A-6 shows a comparison of the estimated TBL pressure wavenumber spectra with those obtained from Corcos' model. The current TBL spectral levels are found to be much lower than those calculated from the convective ridge model. Martin and Leehy [13] have reasoned that due to the breakdown of similarity laws in the lower wavenumber region, the convective ridge model considerably overestimates the TBL spectral levels in this wavenumber range.

The estimated TBL spectral levels are compared in Figure A-7 with those obtained from Laganelli's model [6]. The figure shows that the flight test data for conditions 4 and 5 are in very good agreement with the values given by the prediction model, while data for conditions 1, 2, and 3 show a deviation of 4 to 7 dB. The reasons for this discrepancy with predictions are difficult to assess with the limited amount of data available. One possible explanation may be found in the location of the two-microphone probe, which was upstream from the modified pylon supporting the UHB engine. Flight test data has shown that there is a rapid acceleration of local airflow just upstream of this pylon. The turbulent boundary layer displacement thickness was found to be approximately 20% larger than that observed further upstream of the microphone probe. This may result in higher pressures at the microphone locations.

Figure A-8 shows a comparison of the normalized (convective ridge peak) wavenumber spectral density with the peak values of Witting's model spectra [5]. The normalization constant chosen for Witting's model is based on the convective velocity, U_c , and the overall sound pressure level. The estimated spectral levels are seen to be higher

(about 10 to 12 dB) than those obtained from Witting's model, particularly at very low wavenumbers. Several researchers in the past have observed that wavenumber spectral measurements in the low wavenumber range are very difficult to make and are subject to error. Further, there is considerable scatter among the various wind tunnel data in the low wavenumber region. It may also be mentioned that Witting's model is valid for incompressible flow velocities ($U_c \ll c_0$).

In summary, the wavenumber-frequency TBL pressure spectra estimated from flight test measurements were found to be on the high side when compared with Laganelli's and Witting's prediction models. Overall, the measured sound pressure levels, the normalized TBL pressure, and the wavenumber spectra are consistently higher than the predicted values, particularly in the very low wavenumber region, and might be an indication of the flight turbulent activity. The estimated wavenumber-frequency levels are in very good agreement with the predicted data in the mid-wavenumber and frequency range. The results presented in this appendix, therefore, show that the local wavenumber technique using a fixed probe can be used for estimating the wavenumber-frequency spectra of the TBL pressure fluctuations. This estimation method can be easily used to measure in situ TBL pressure wavenumber-frequency spectra during flight.

Further tests using the microphone array method should be conducted to examine the underlying assumption of homogeneity of the TBL pressure field. Additional measurements with smaller probe microphone spacing should also be undertaken, to expand the range of wavenumber spectra.

A.5 References

1. Kraichnan, R.H., "Pressure Field Within Homogeneous Anisotropic Turbulence," *J. Acoust. Soc. Am.*, 28(1), 64-72 (1956).
2. Kraichnan, R.H., "Noise Transmission from Boundary Layer Pressure Fluctuations," *J. Acoust. Soc. Am.*, 29(1), 65-80 (1957).
3. Phillips, O.M., "On the Aerodynamic Surface Sound from a Plane Turbulent Boundary Layer," *Proc. Royal Soc. Lond.*, A234, 327-335 (1956).
4. Corcos, G.M., "The Structure of the Turbulent Pressure Field in Boundary Layer Flows," *J. Fluid Mech.*, 18, 353-378 (1964).
5. Witting, J.M., "A Spectral Model of Pressure Fluctuations at a Rigid Wall Bounding an Incompressible Fluid, Based on Turbulent Structures in the Boundary Layer," *Noise Control Eng. Journal*, 26(1), 28-43 (1986).

6. Laganelli, A.L., Martellucci, A. and Shaw, L.L., "Wall Pressure Fluctuations in Attached Boundary-Layer Flow," *AIAA Journal*, 21(4), 495-502 (1983).
7. Bull, M.K., "Wall Pressure Fluctuations Associated with Subsonic Turbulent Boundary Layer Flow," *J. Fluid Mech.*, 28(4), 719-754 (1967).
8. Blake, W.K., "Turbulent Boundary Layer Wall Pressure Fluctuations on Smooth and Rough Walls," *J. Fluid Mech.*, 44(4), 637-660 (1970).
9. Willmarth, W.W. and Wooldridge, C.E., "Measurements of the Fluctuating Pressure at the Wall Beneath a Thick Turbulent Boundary Layer," *J. Fluid Mech.*, 14(2), 187-210 (1962).
10. Blake, W.K. and Chase, D.M., "Wavenumber-Frequency Spectra of Turbulent Boundary Layer Pressure Measured by Microphone Arrays," *J. Acoust. Soc. Am.*, 42(3), 862-877 (1971).
11. Farabee, T.M. and Geib, F.E., "Measurement of Boundary Layer Pressure Fields with an Array of Pressure Transducers in a Subsonic Flow," *David Taylor Naval Ship Res. and Dev. Ctr. Report No. 76-0031* (1976).
12. Martini, K., Leehy, P. and Moeller, M., "Comparison of Techniques to Measure the Low Wavenumber Spectrum of a Turbulent Boundary Layer," *Acoustics and Vibration Laboratory, MIT Report No. 92828-1* (1984).
13. Martin, N.C. and Leehy, P., "Low Wavenumber Wall Pressure Measurements Using a Rectangular Membrane as a Spatial Filter," *J. Sound Vib.*, 52(1), 95-120 (1977).
14. Jameson, P.W., "Measurements of the Low Wavenumber Component of Turbulent Boundary Layer Wall Pressure Spectrum," *Bolt Beranek and Newman Inc. Report No. 1937* (1970).
15. Bhat, W.V., "Flight Test Measurements of Exterior Turbulent Boundary Layer Pressure Fluctuations on Boeing Model 737 Airplane," *J. Sound Vib.*, 14(4), 439-457 (1971).
16. Maestrello, L., "Boundary Layer Pressure Fluctuations on the 707 Prototype Airplane," Paper presented at the 64th Meeting of the Acoustical Society of America, Seattle (1962).
17. Heron, H.K. and Webb, D.R.B., "Flight Measurements of Pressure Fluctuations in a Turbulent Subsonic Boundary Layer and the Relation with Wall Shear Stress," *R.A.E. Tech. Report No. 66338* (1966).

18. Harker, K.J. and Ilić, D.B., "Measurement of Plasma Wave Spectral Density from the Cross-Power Density Spectrum," *Rev. Sci. Instrum.*, 45(11), 1315-1324 (1974).
19. Ilić, D.B. and Harker, K.J., "Evaluation of Plasma Wave Spectral Density from Cross-Power Spectra," *Rev. Sci. Instrum.*, 46(9), 1197-1200, (1975).
20. Iwama, N., Ohba, Y. and Tsukishima, T., "Estimation of Wavenumber Spectrum Parameters from Fixed Probe Pair Data," *J. Appl. Phys.*, 50(5), 3197-3206 (1979).
21. Beall, J.M., Kim, Y.C. and Powers, E.J., "Estimation of Wavenumber and Frequency Spectra Using Fixed Probe Pairs," *J. Appl. Phys.*, 53(6), 3933-3940 (1982).
22. Corcos, G.M., "Resolution of Pressure in Turbulence," *J. Acoust. Soc. Am.*, 35(2), 192-199 (1963).

Table A-1. Flight Test Conditions and Parameters

Flt. Cond. No.	Flt/Point	Mach No.	Pressure Altitude (ft)	True Airspeed (knots)	Boundary Layer	
					Displacement Thickness δ^* , (inches)	Dynamic Pressure q_∞ , (Pa ²)
1	19530A02	0.76	35000	444	1.32	9660
2	19520A05	0.76	35000	445	1.32	9662
3	20330K04	0.77	22600	472	1.18	17203
4	19470002	0.57	22500	355	1.28	9575
5	19480004	0.81	34900	472	1.29	10966

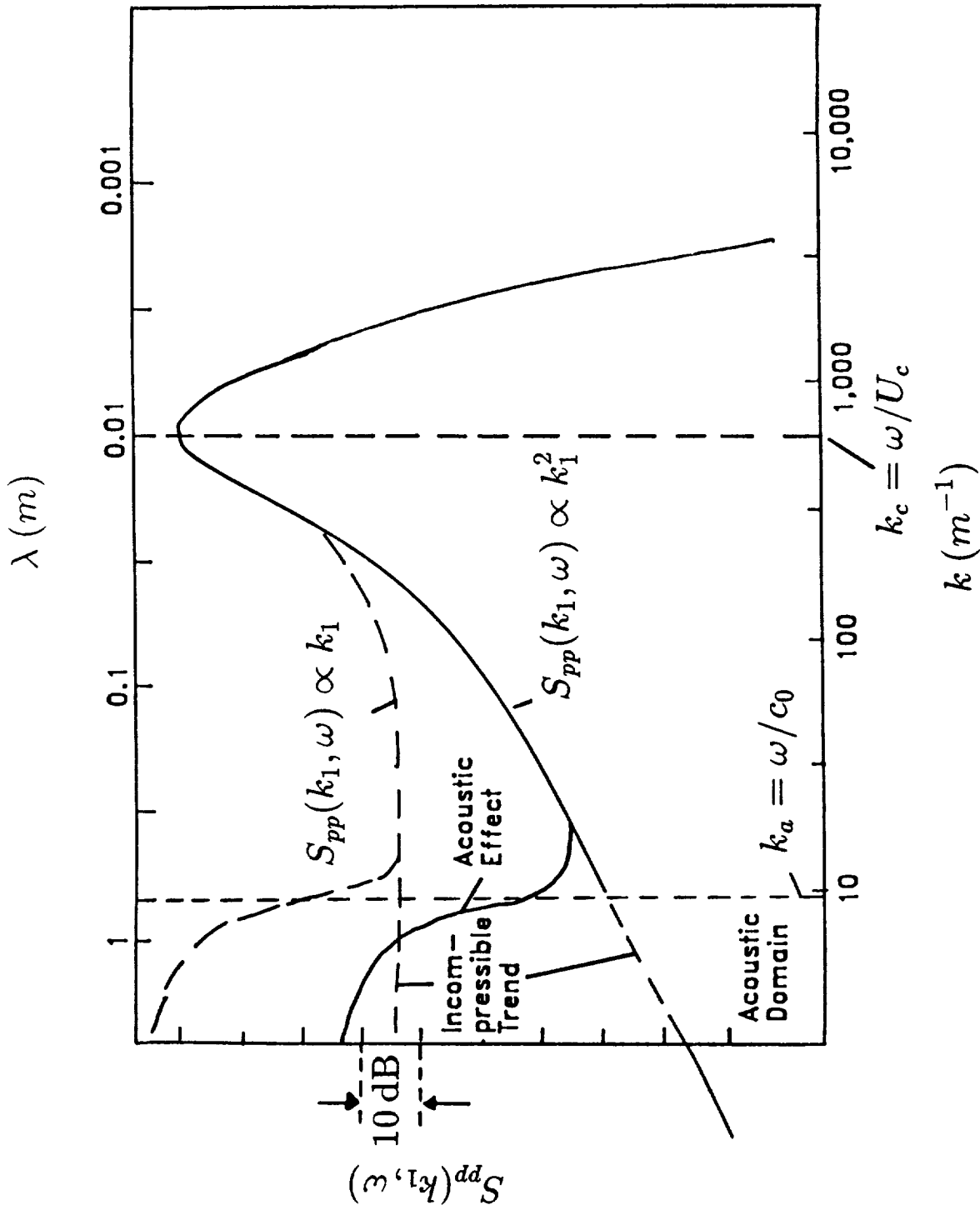


Figure A-1 Sketch of the Wavenumber-Frequency Spectrum

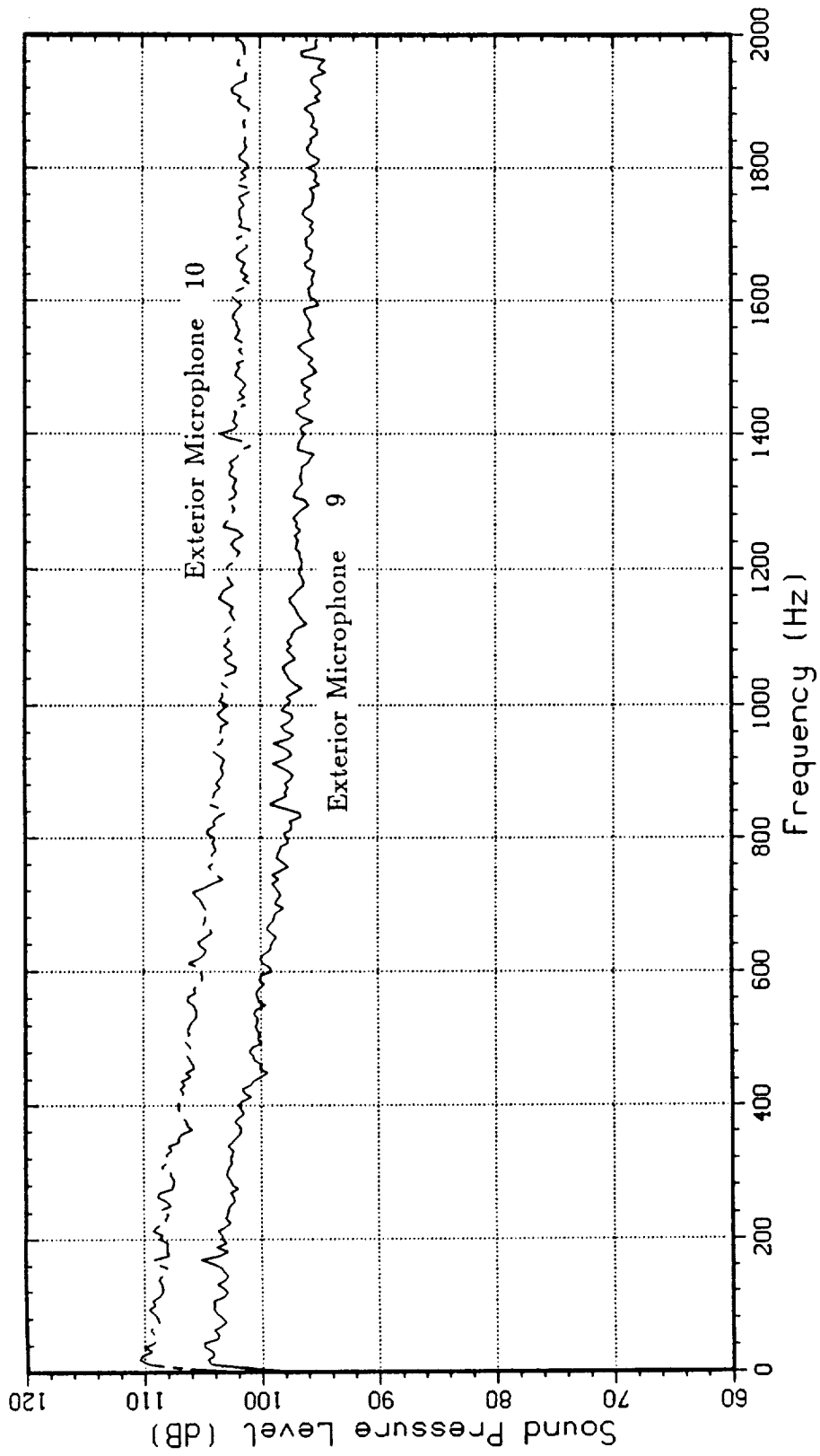


Figure A-2a. Sound Pressure Level Spectra for the Probe Microphones (Flight Condition 1)

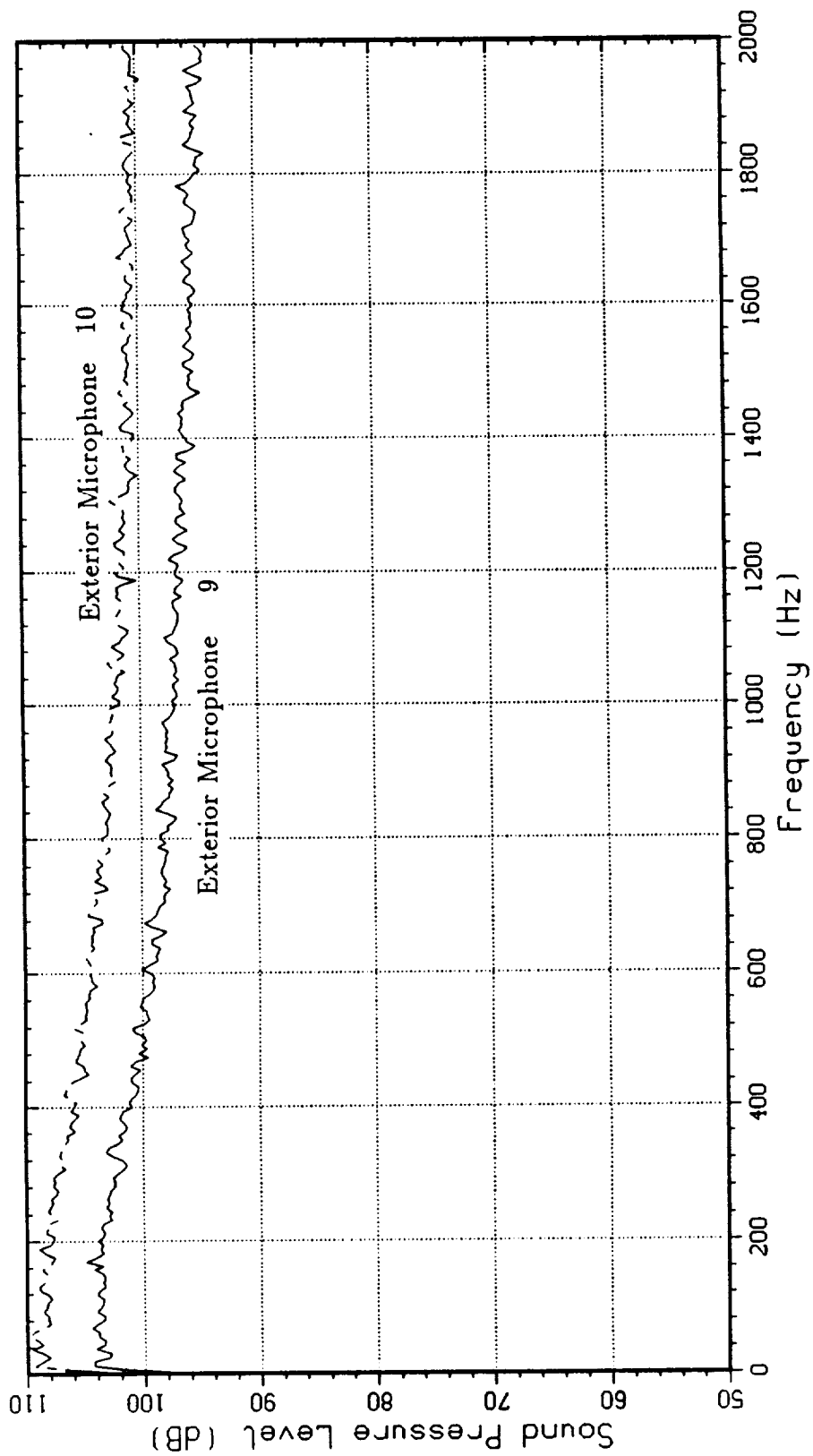


Figure A-2b. Sound Pressure Level Spectra for the Probe Microphones (Flight Condition 2)

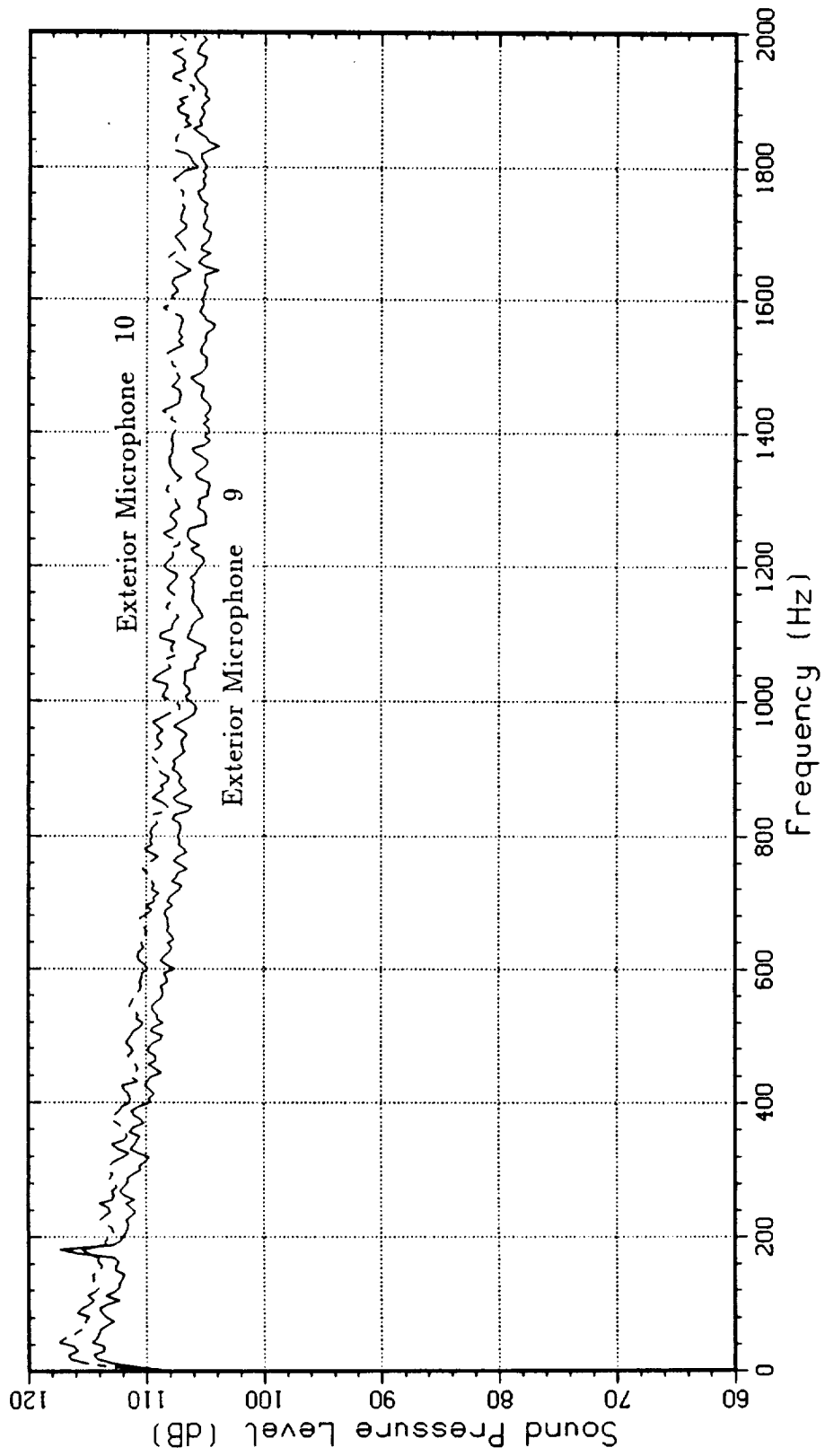


Figure A-2c. Sound Pressure Level Spectra for the Probe Microphones (Flight Condition 3)

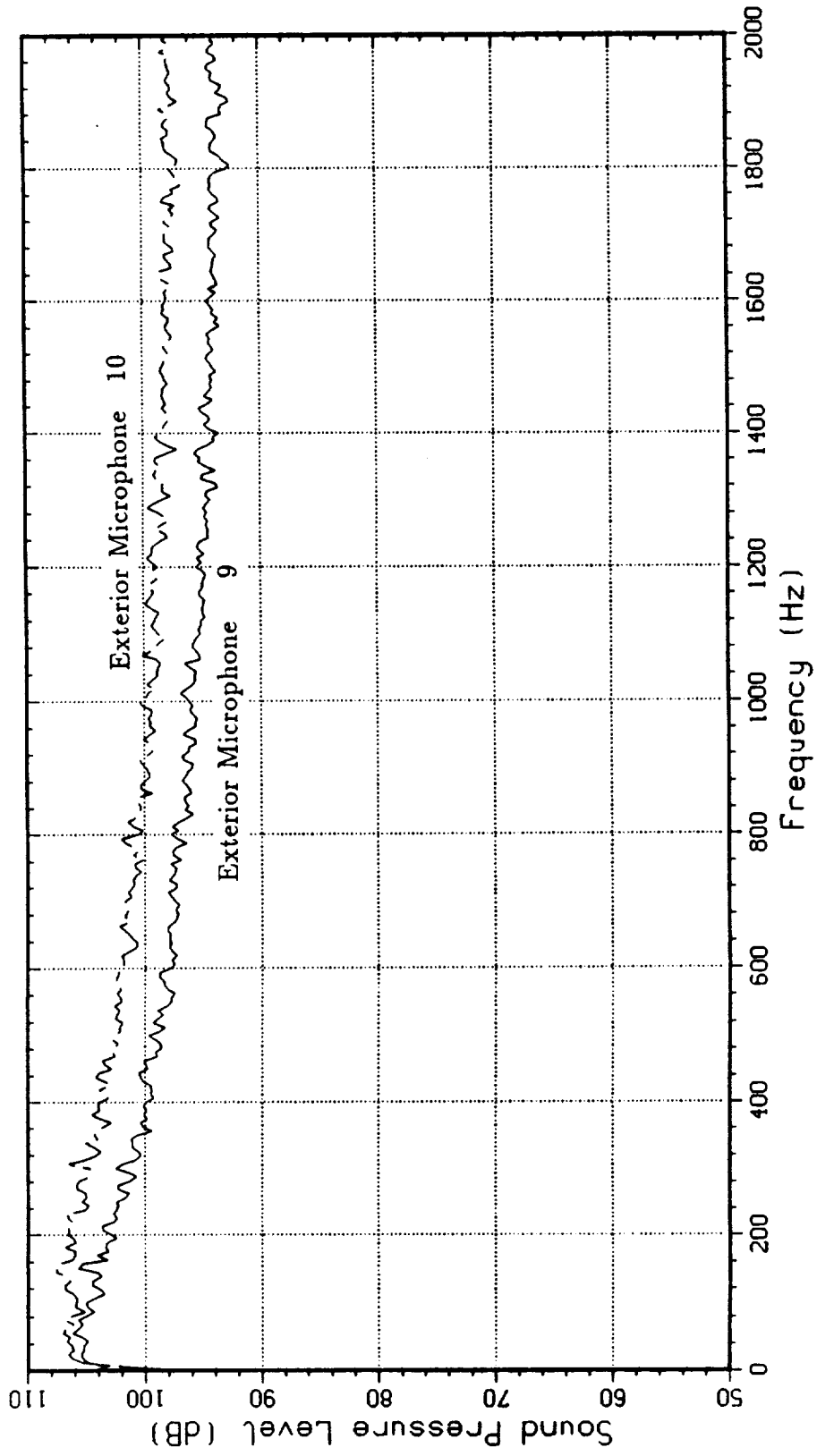


Figure A-2d. Sound Pressure Level Spectra for the Probe Microphones (Flight Condition 4)

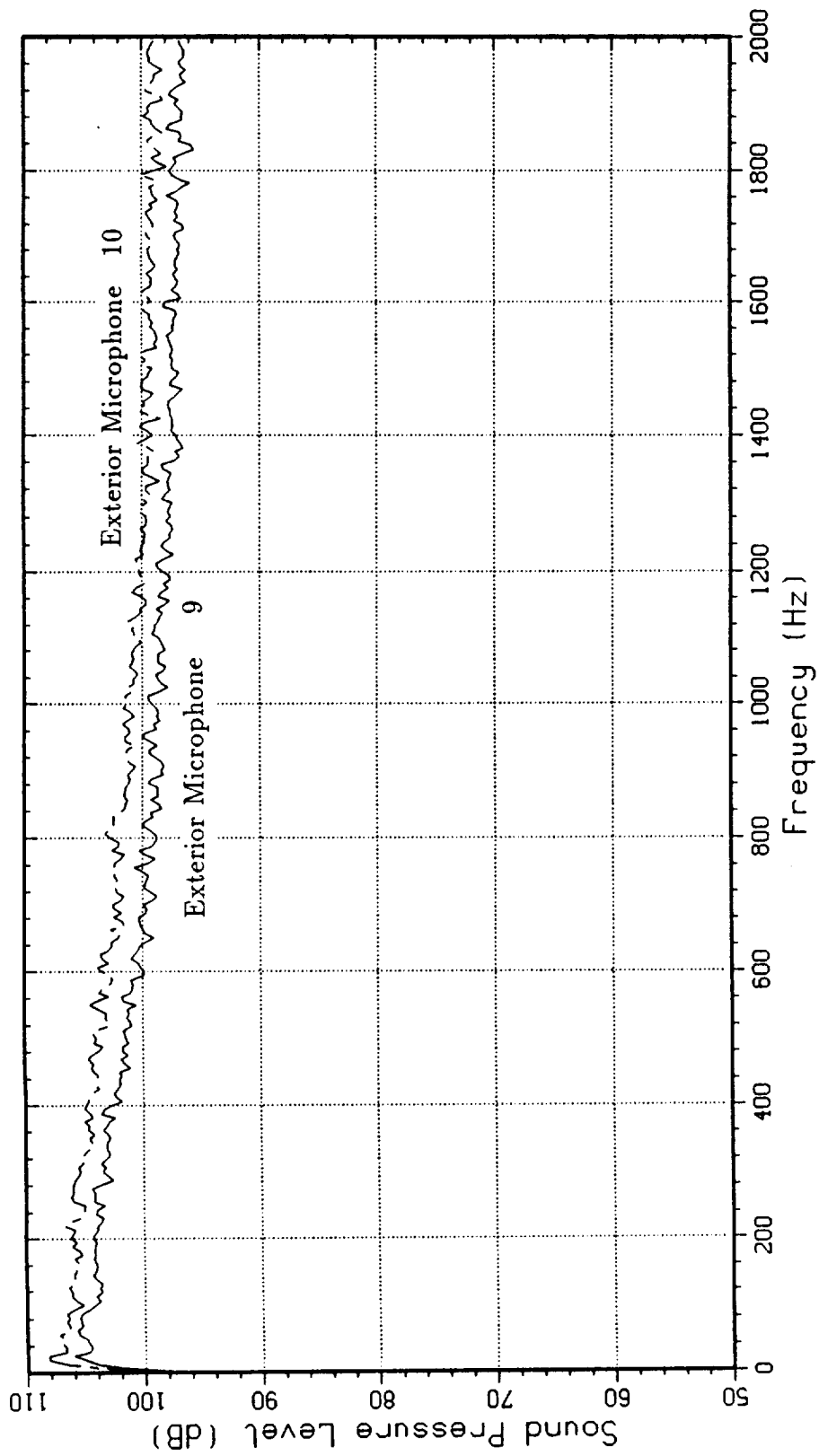


Figure A-2e. Sound Pressure Level Spectra for the Probe Microphones (Flight Condition 5)

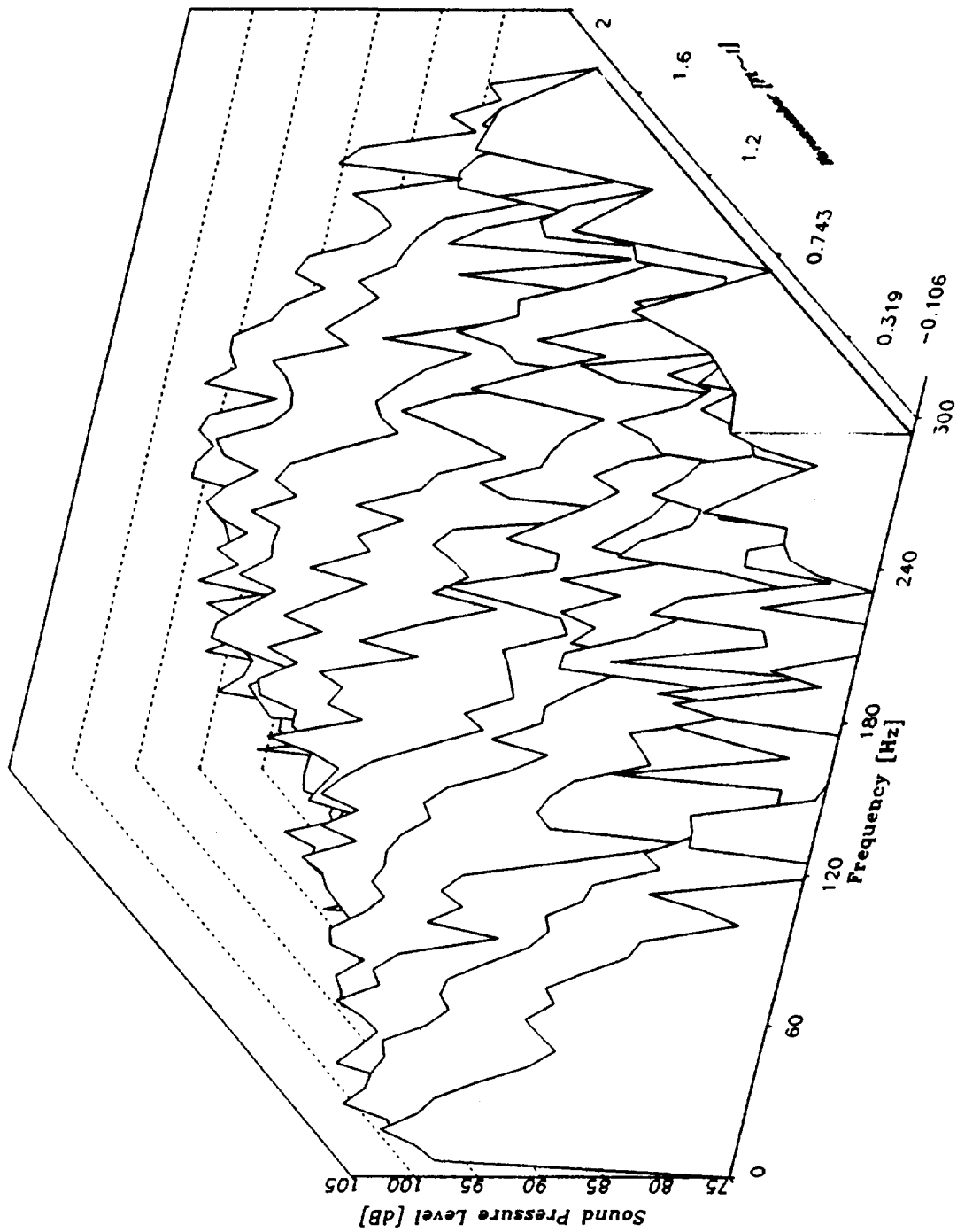


Figure A-3a. Estimated Wavenumber-Frequency Spectrum (Flight Condition 1)

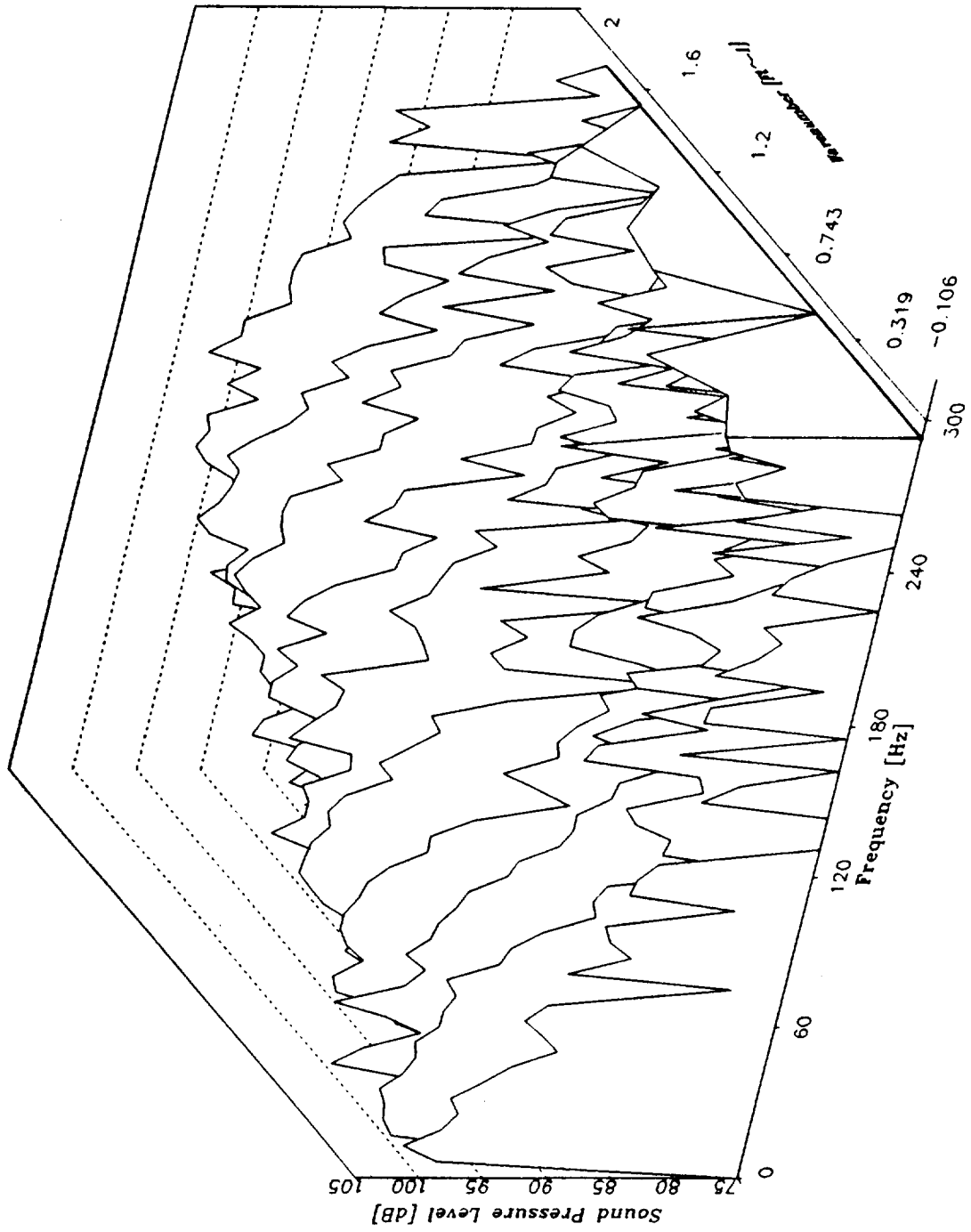


Figure A-3b. Estimated Wavenumber-Frequency Spectrum (Flight Condition 2)

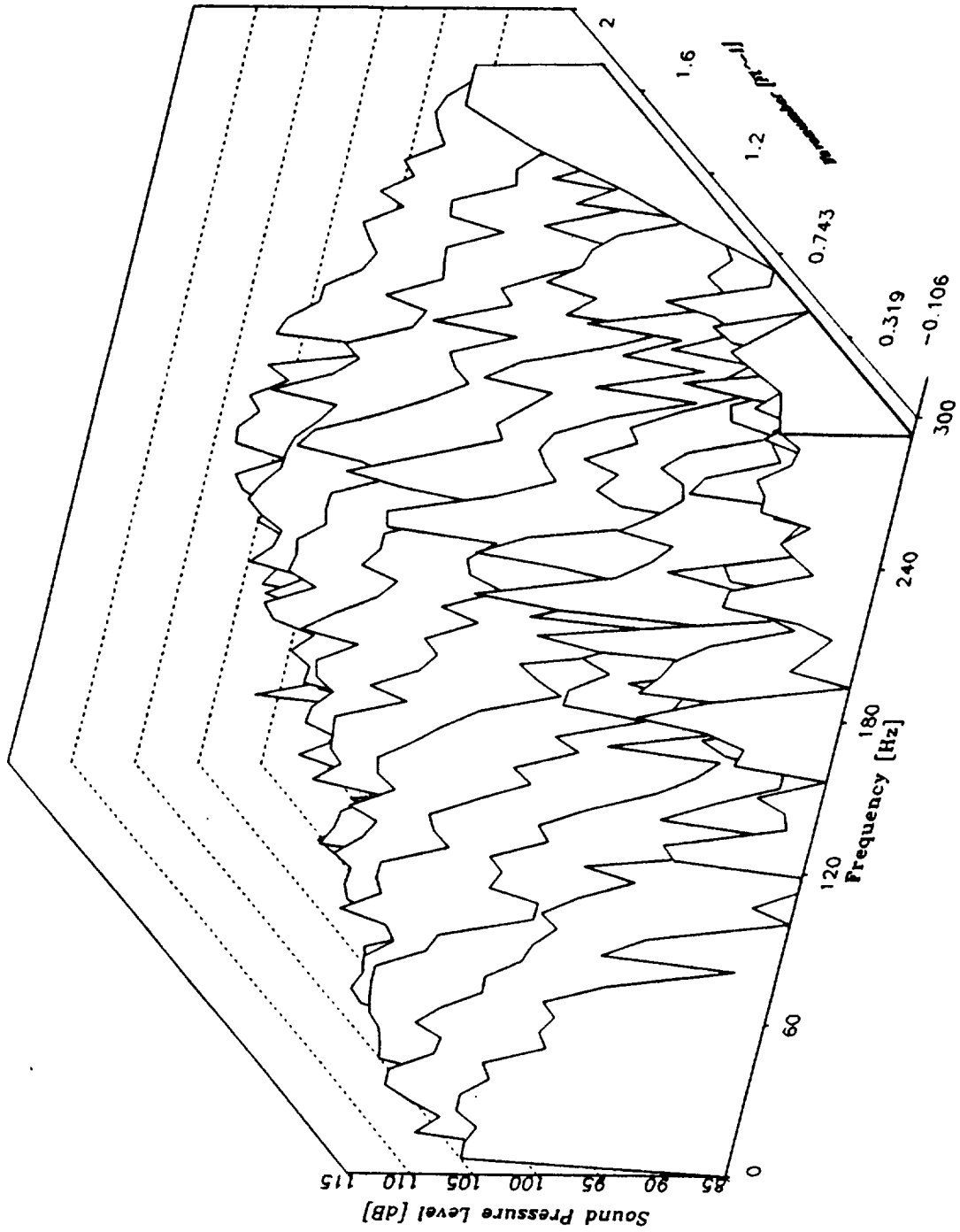


Figure A-3c. Estimated Wavenumber-Frequency Spectrum (Flight Condition 3)

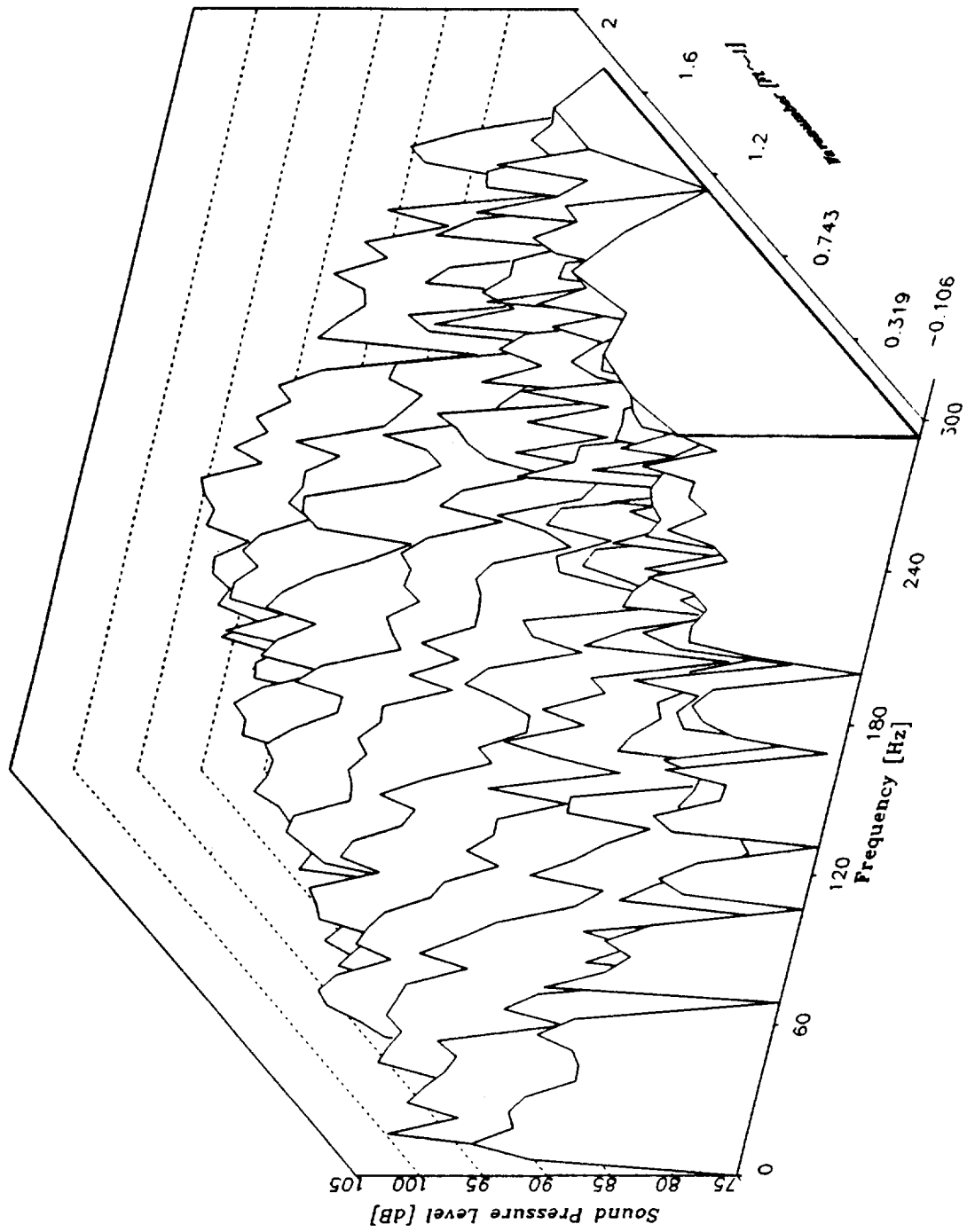


Figure A-3d. Estimated Wavenumber-Frequency Spectrum (Flight Condition 4)

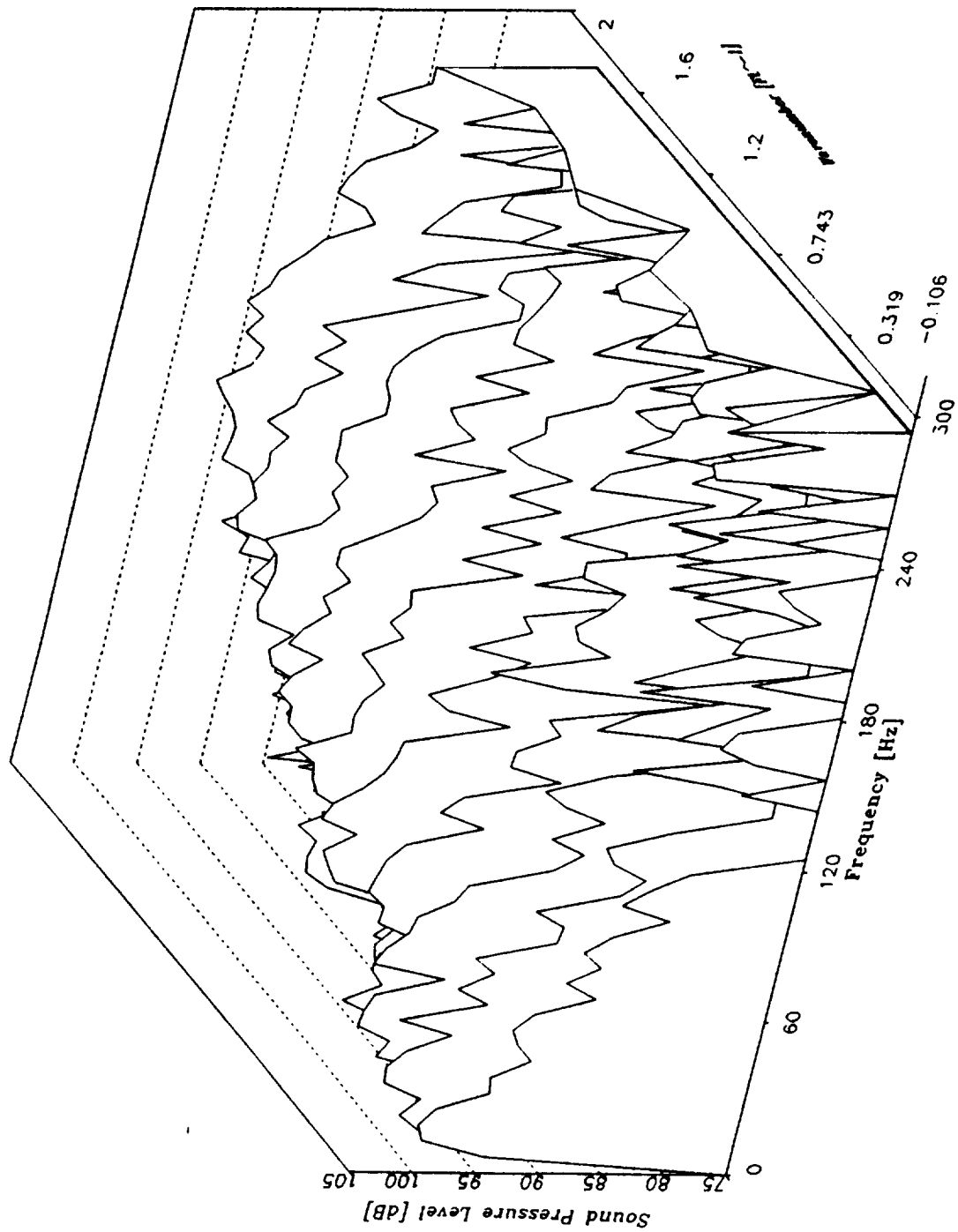


Figure A-3e. Estimated Wavenumber-Frequency Spectrum (Flight Condition 5)

Figure A-4a. Wavenumber-Frequency Contour Plot for TBL Pressure Spectrum (Flt. Cond. 1)

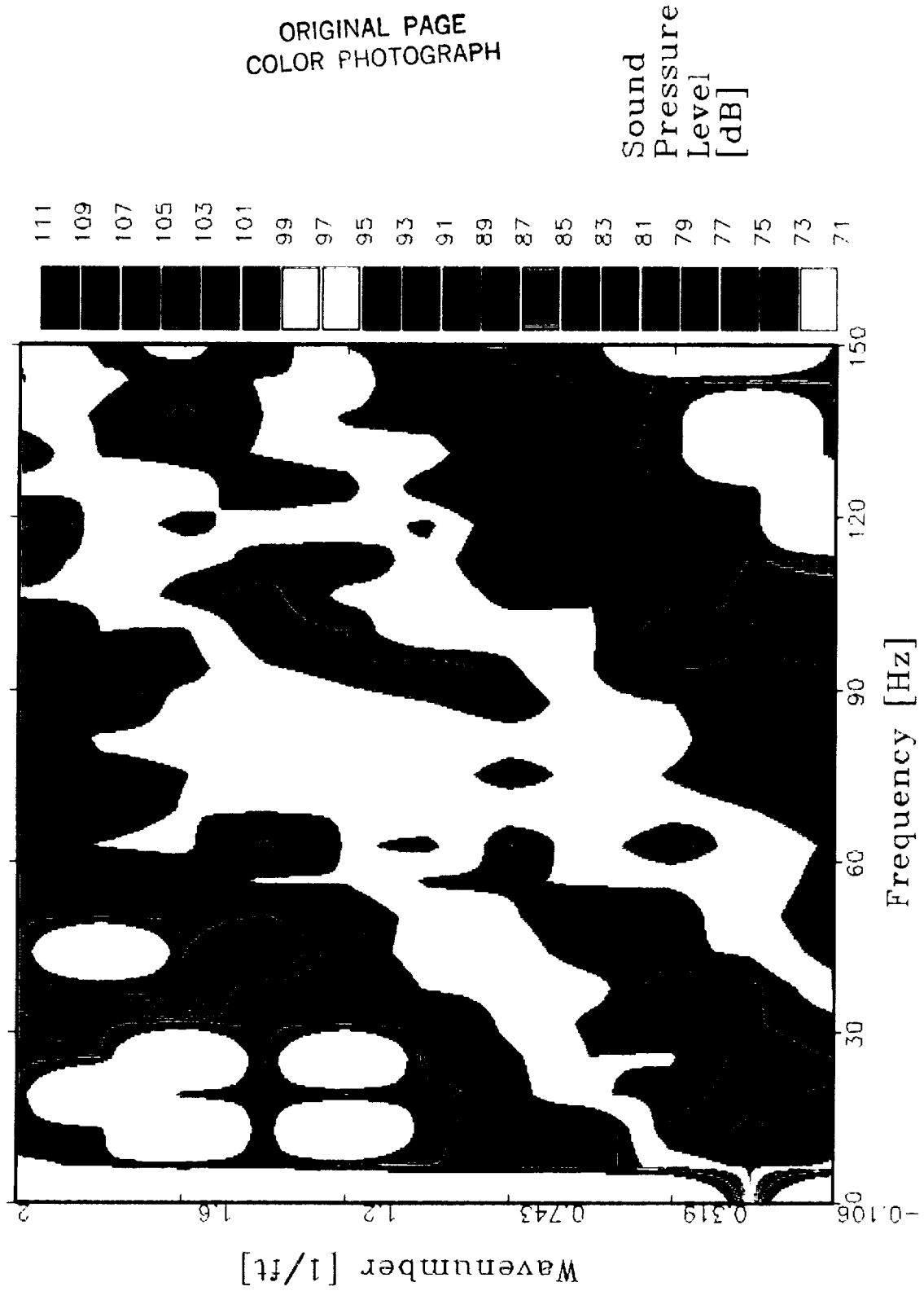


Figure A-4b. Wavenumber-Frequency Contour Plot for TBL Pressure Spectrum (Flt. Cond. 2)

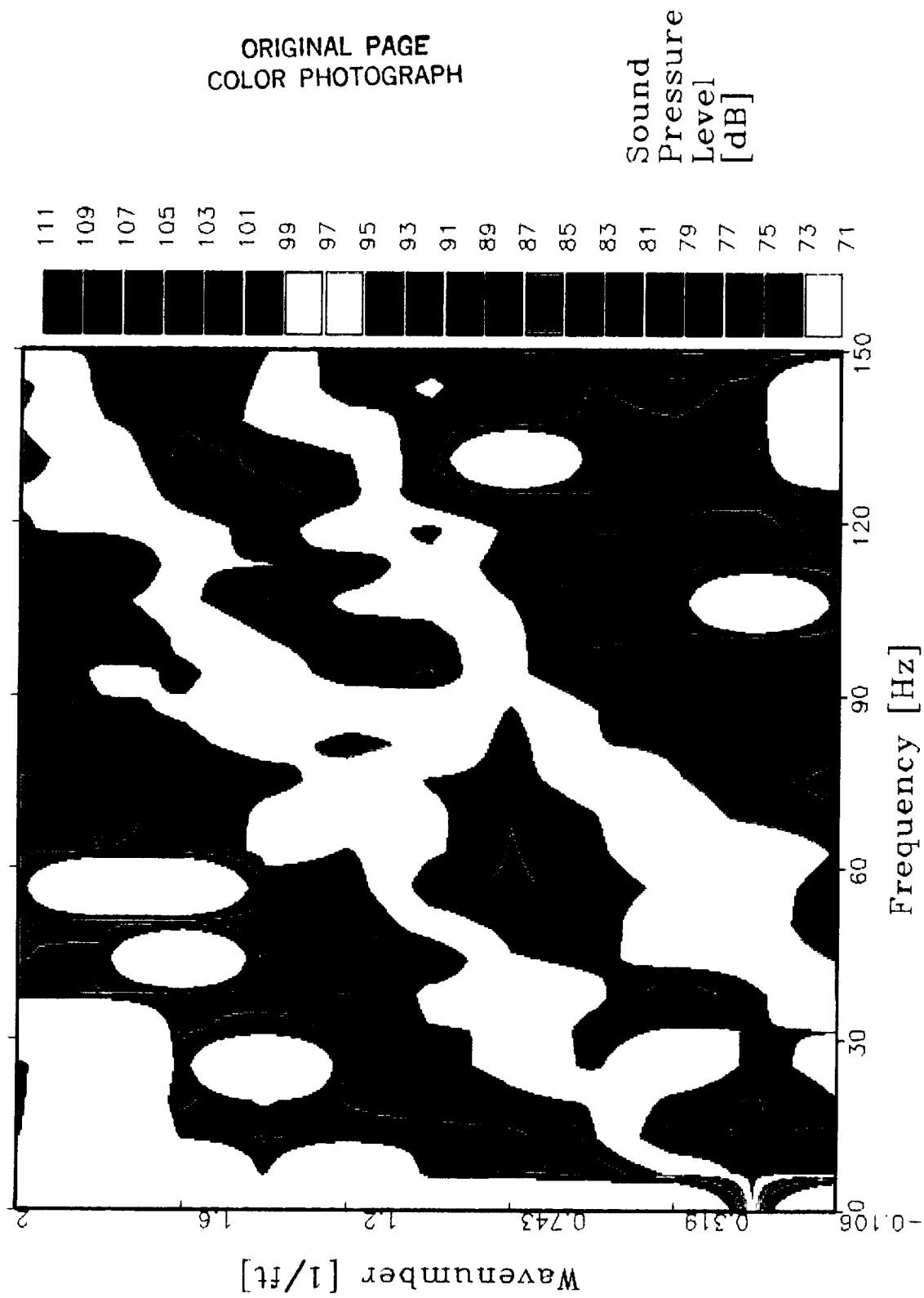


Figure A-4c. Wavenumber-Frequency Contour Plot for TBL Pressure Spectrum (Flt. Cond. 3)

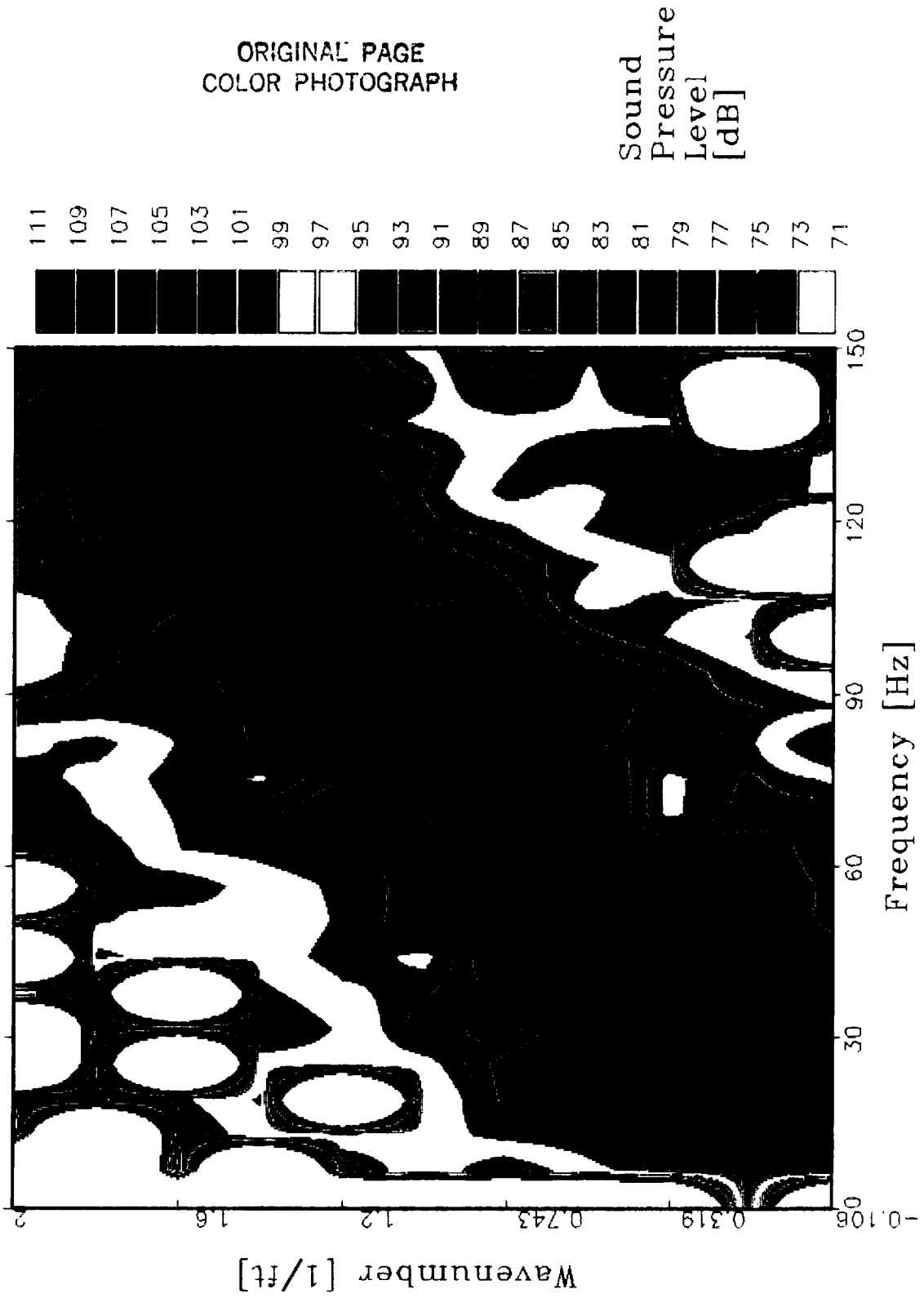


Figure A-4d. Wavenumber-Frequency Contour Plot for TBL Pressure Spectrum (Fit. Cond. 4)

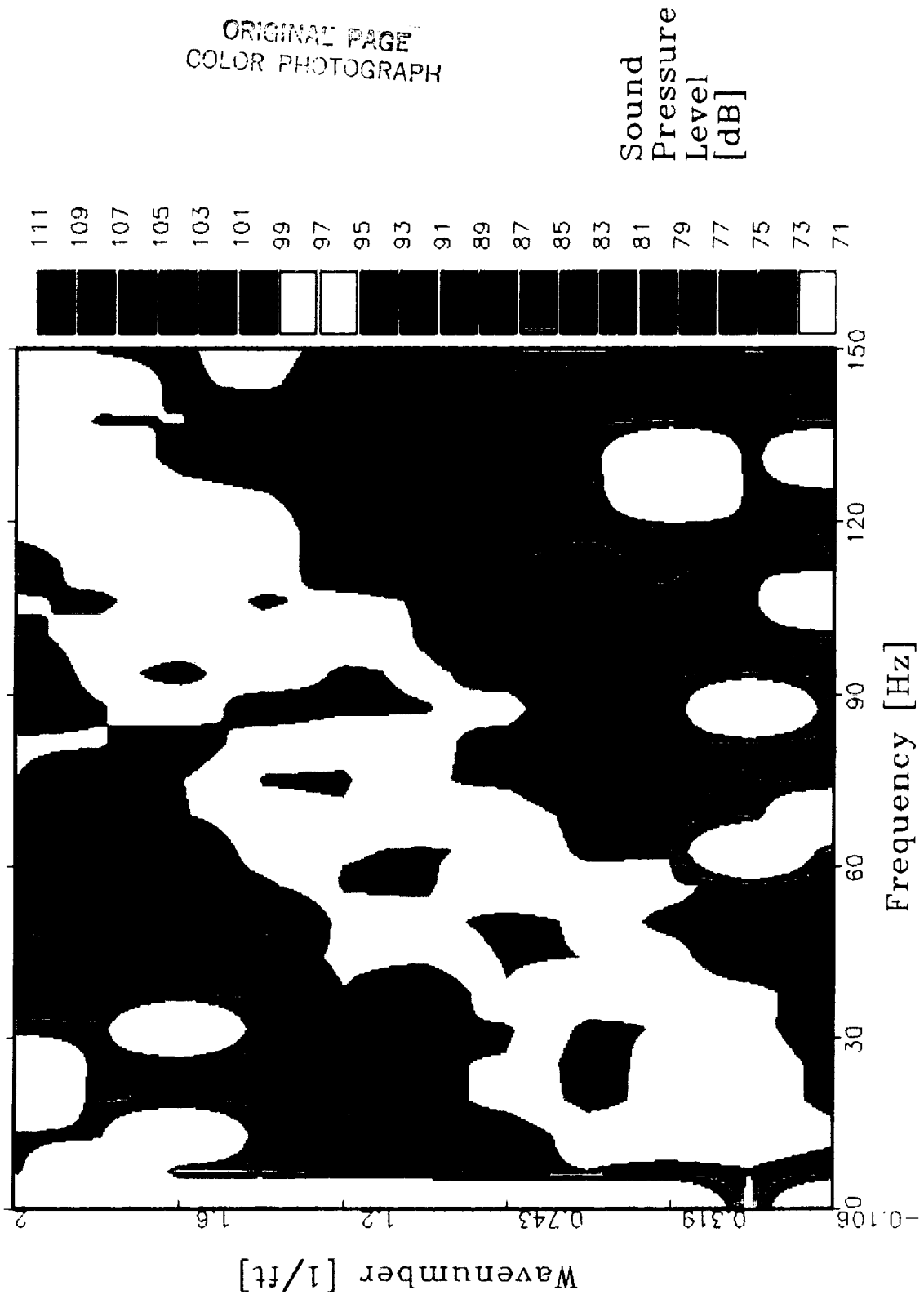
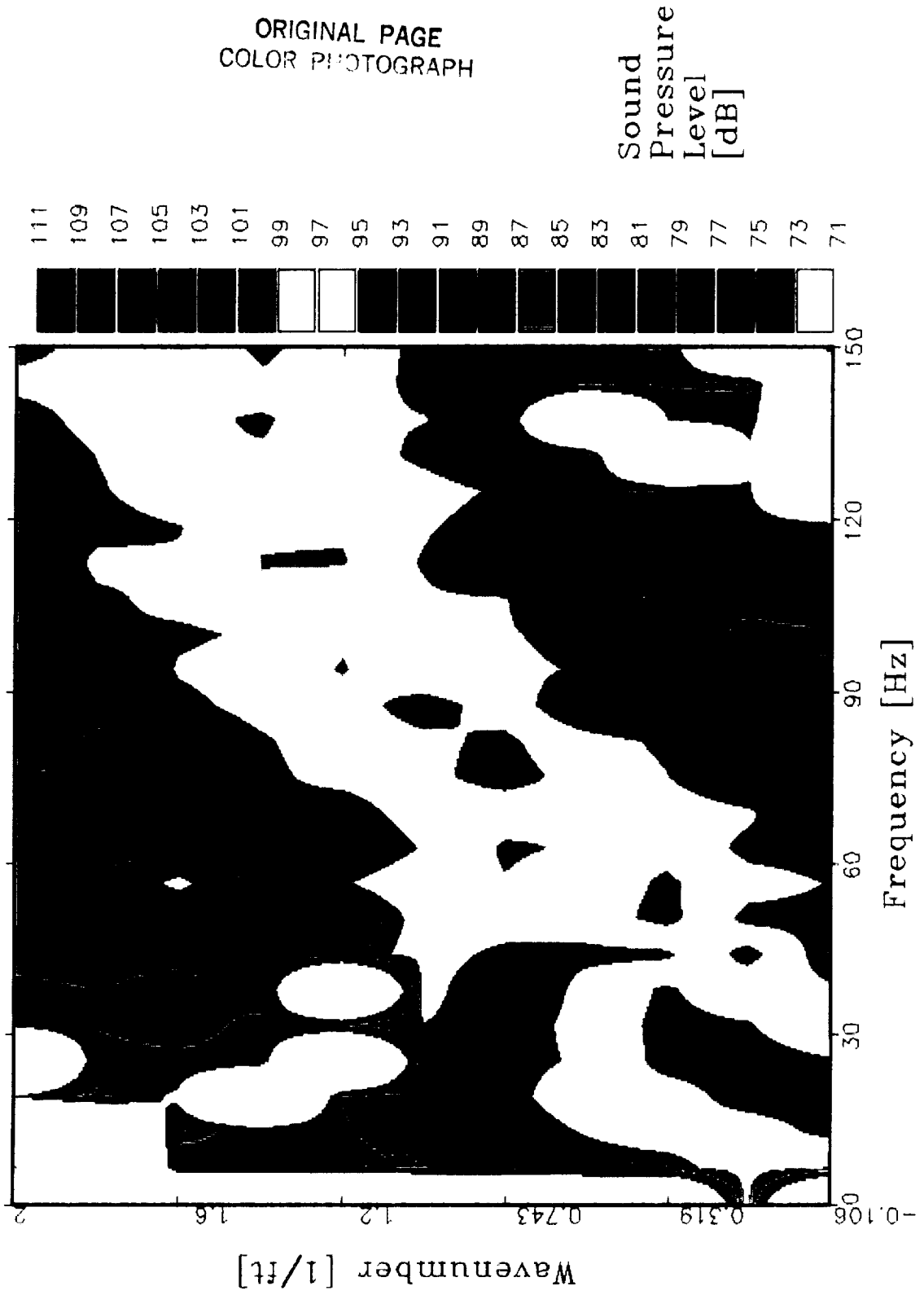


Figure A-4e. Wavenumber-Frequency Contour Plot for TBL Pressure Spectrum (Flt. Cond. 5)



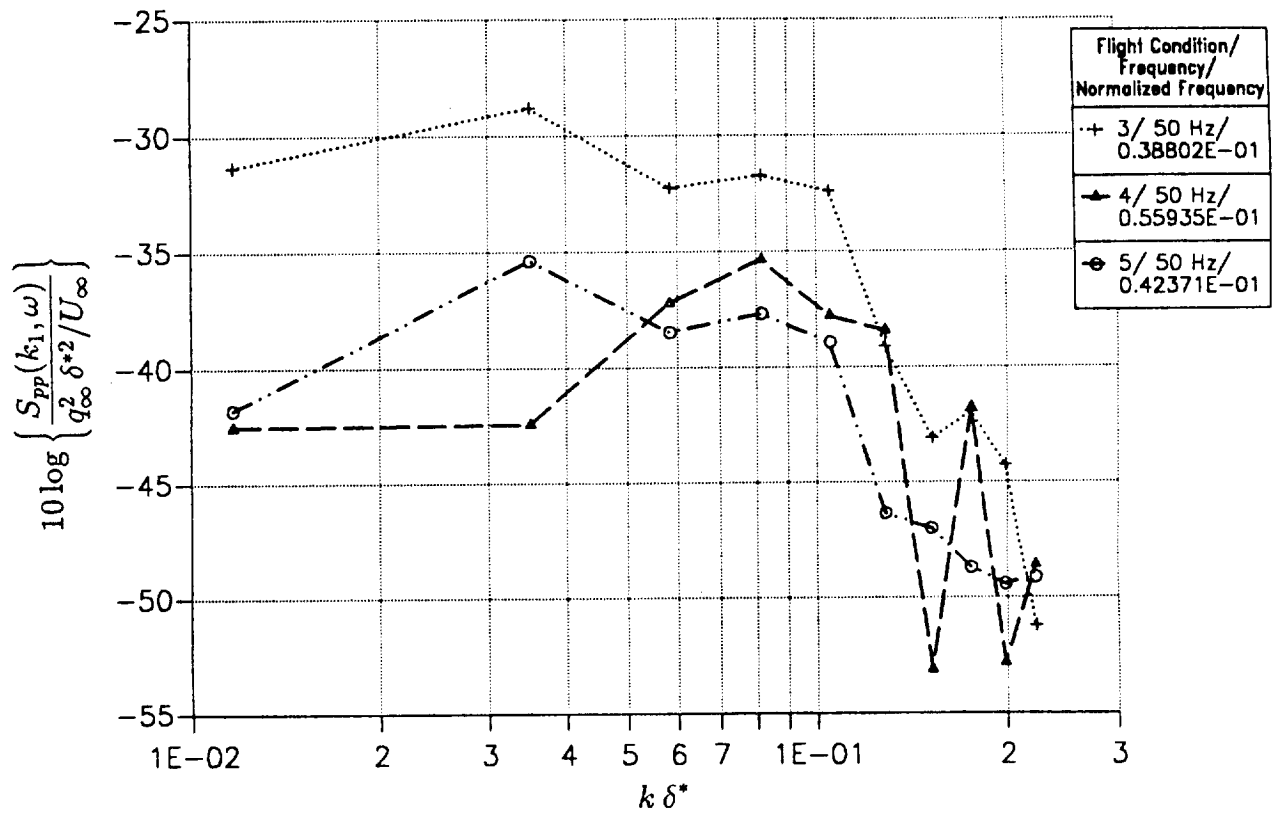
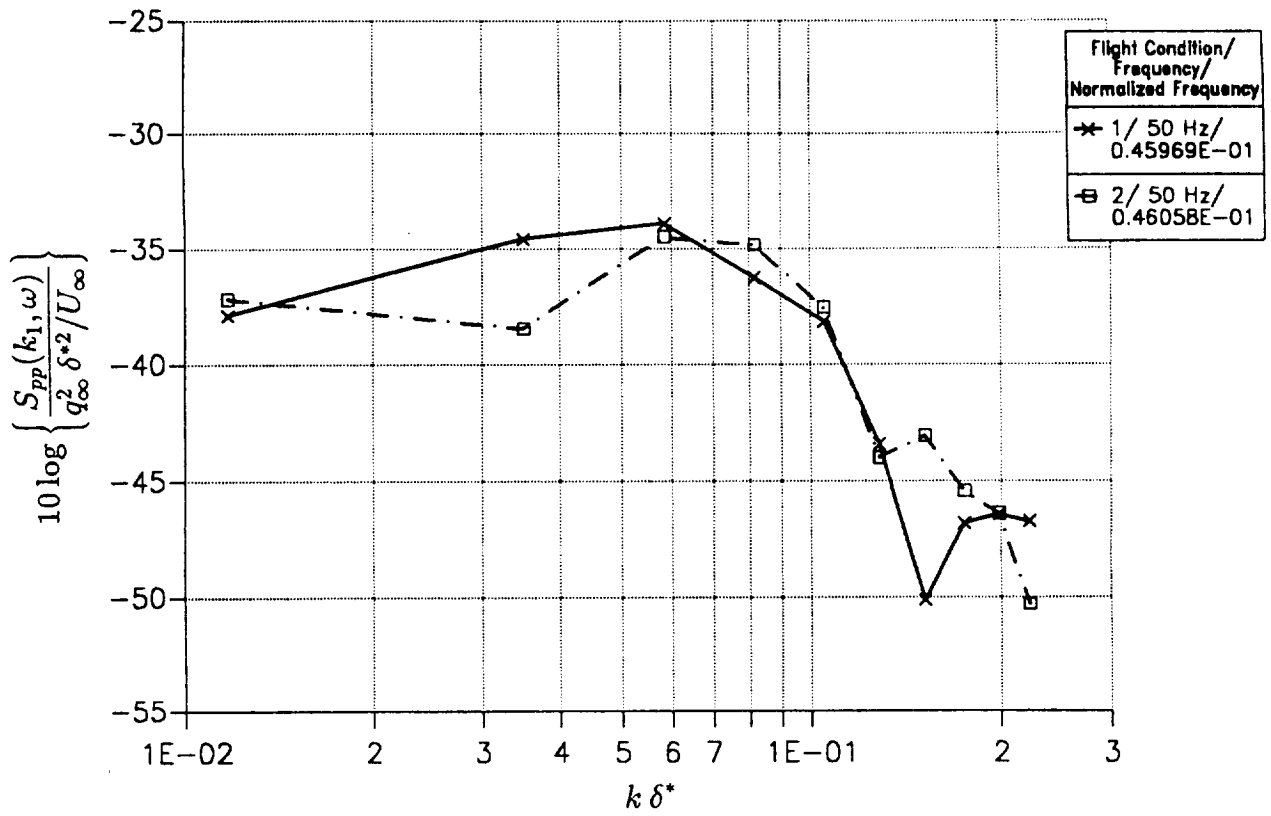


Figure A-5a. Wavenumber Variation of TBL Pressure Spectral Density ($F = 50$ Hz)

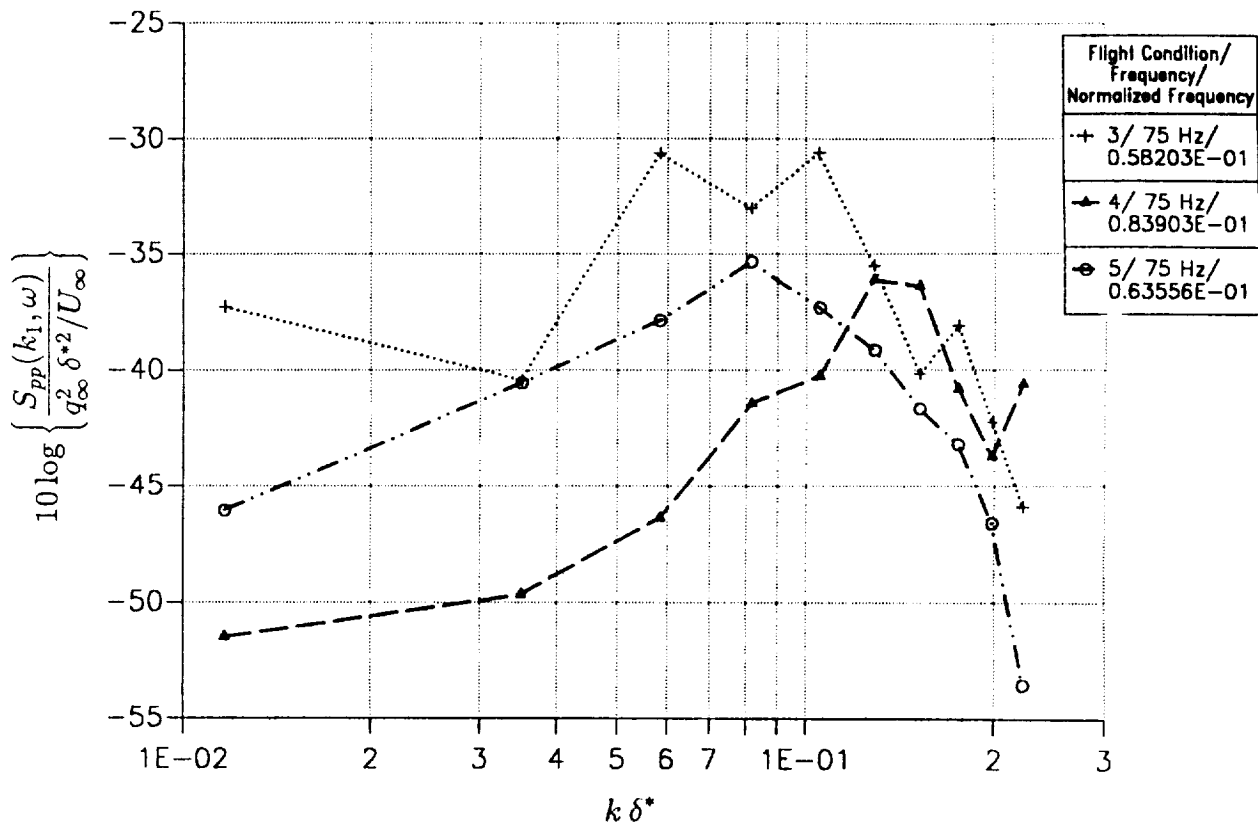
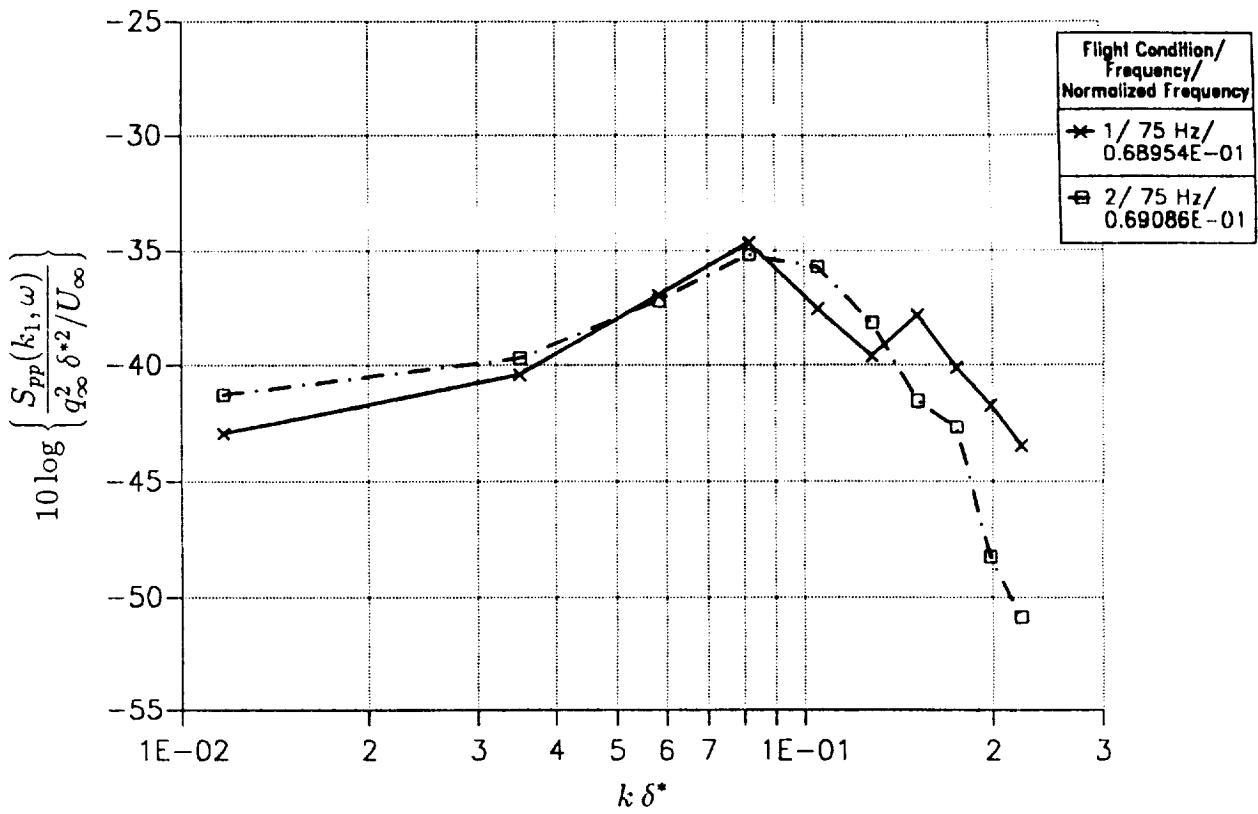


Figure A-5b. Wavenumber Variation of TBL Pressure Spectral Density (F = 75 Hz)

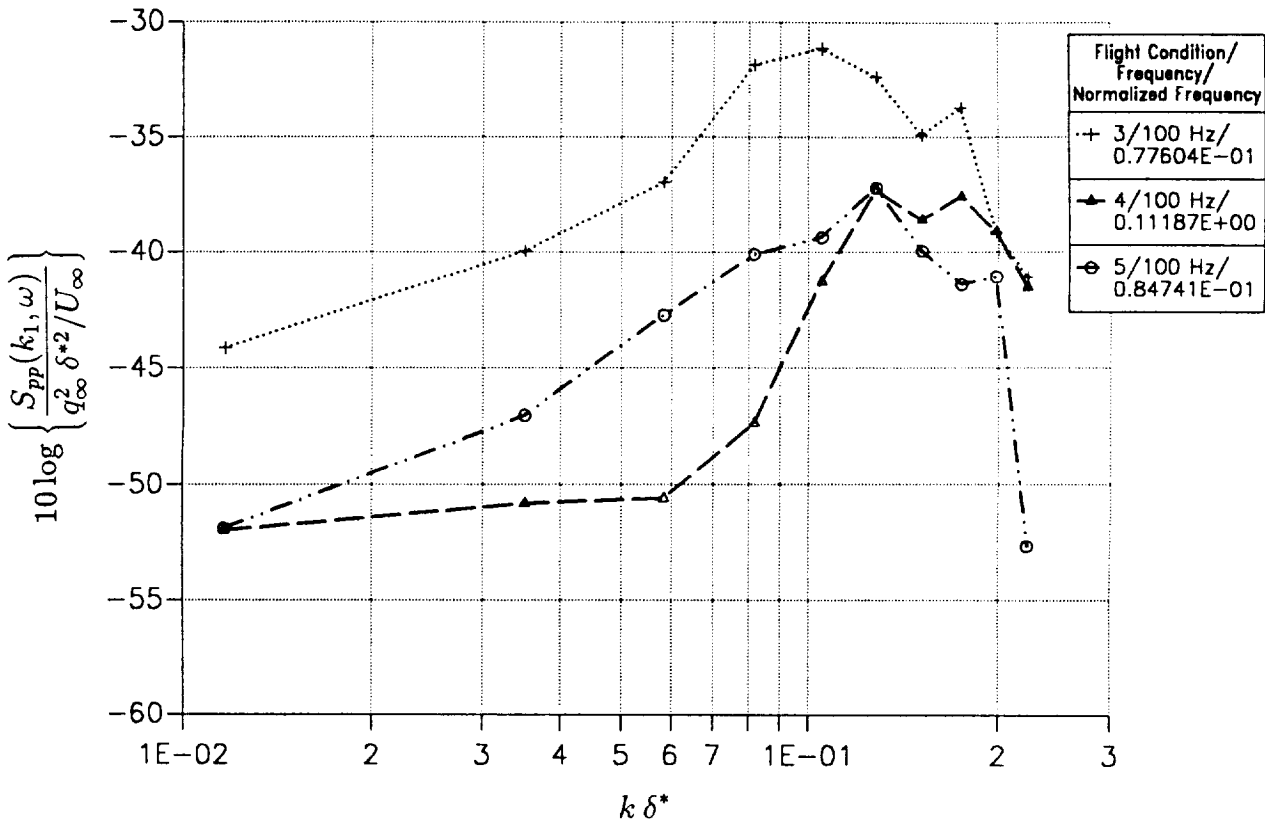
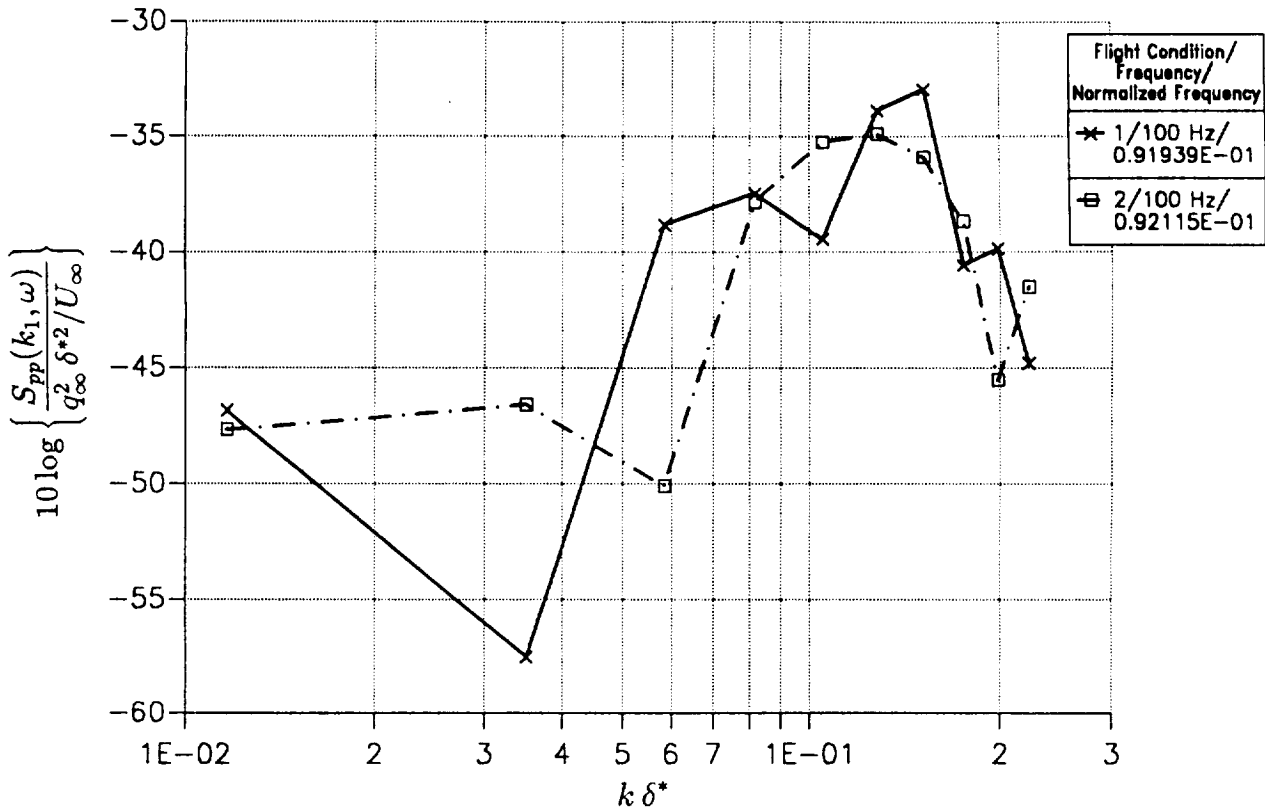


Figure A-5c. Wavenumber Variation of TBL Pressure Spectral Density (F = 100 Hz)

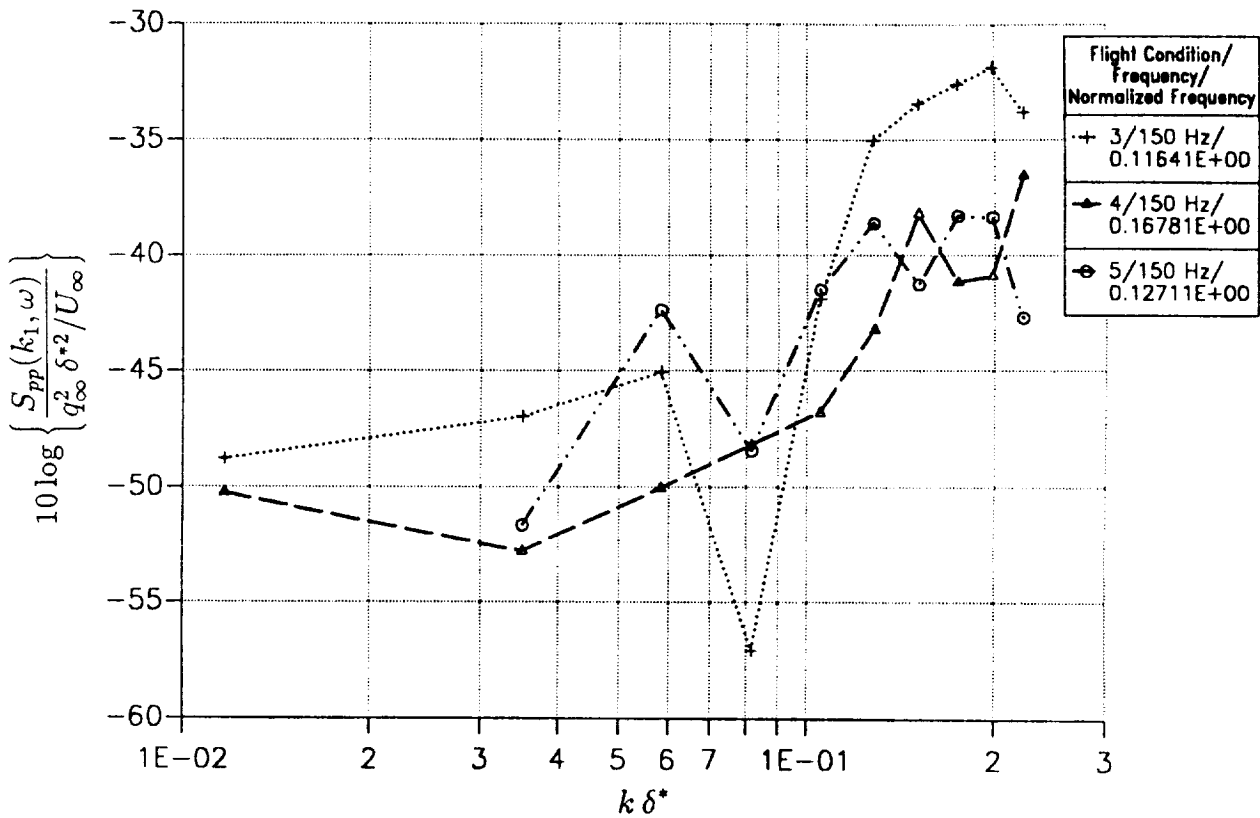
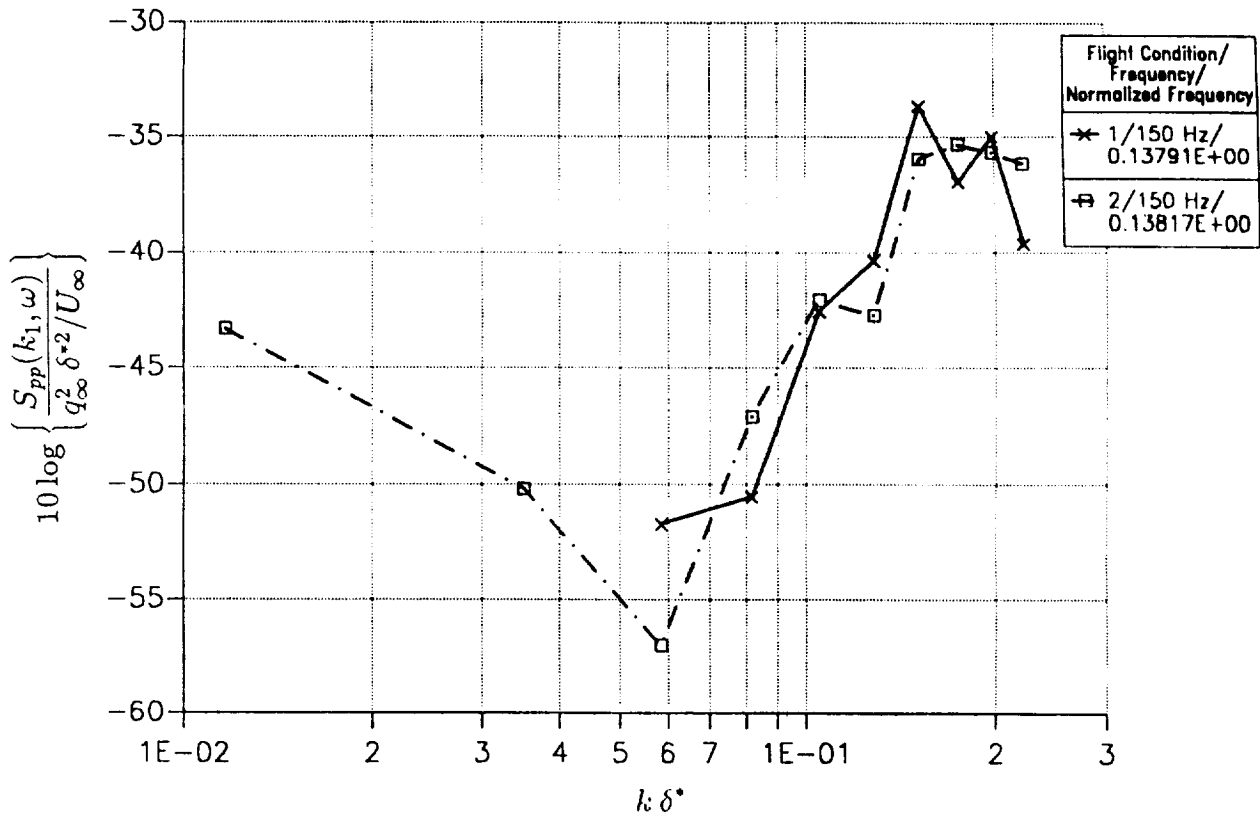


Figure A-5d. Wavenumber Variation of TBL Pressure Spectral Density (F = 150 Hz)

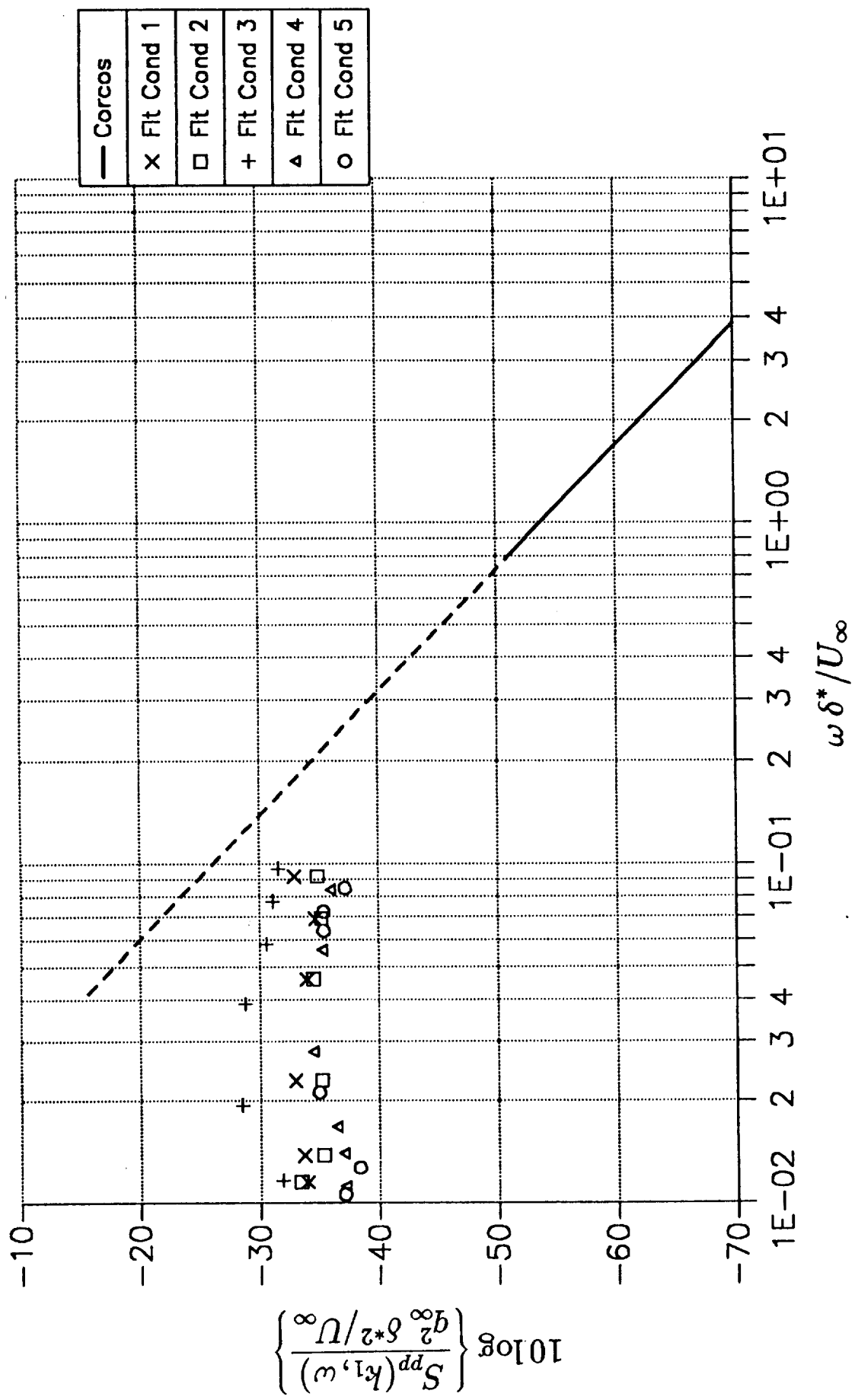


Figure A-6. Comparison of Flight Test TBL Pressure Data With Corcos' Model

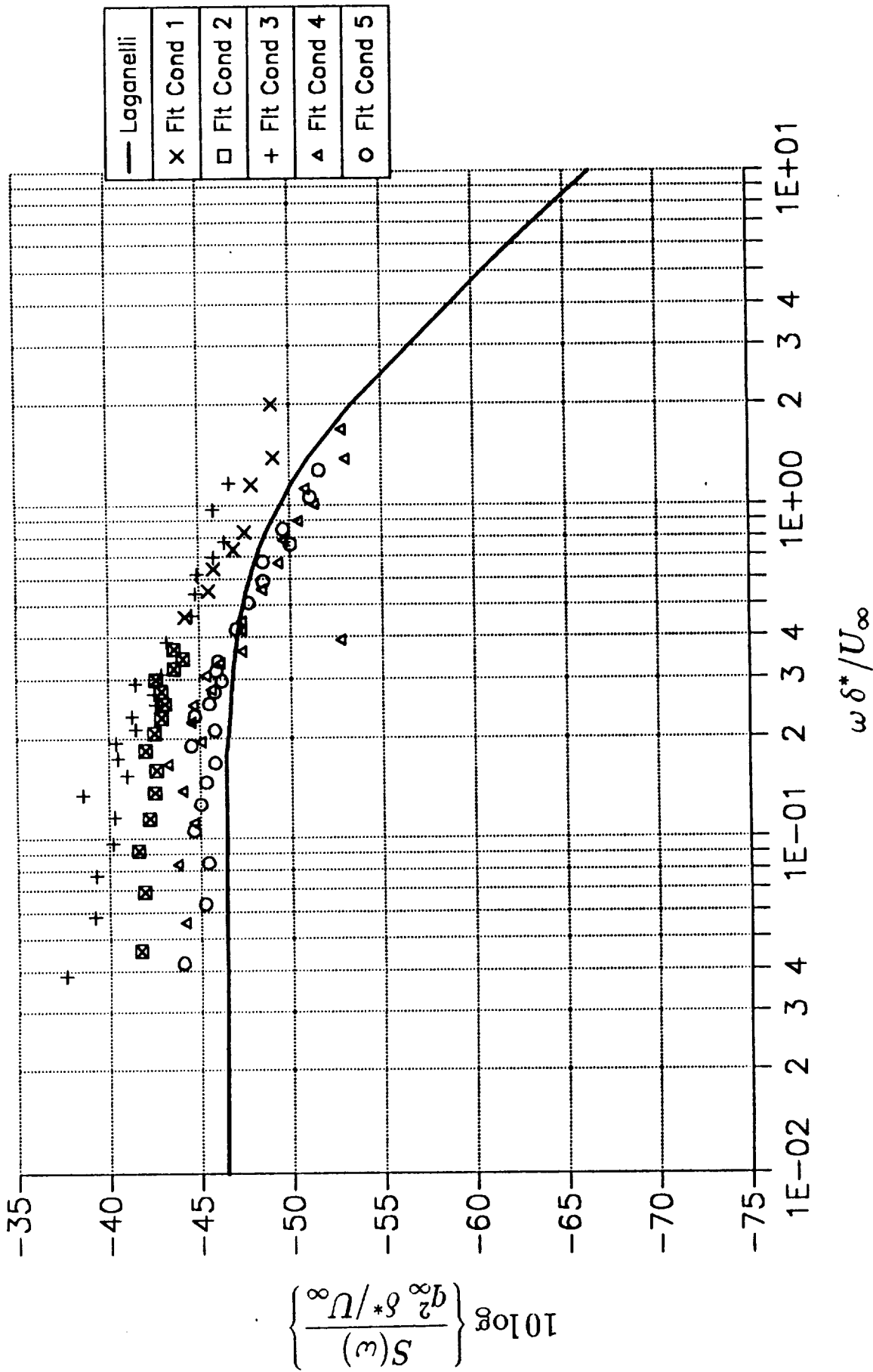


Figure A-7. Comparison of TBL Pressure Spectral Density With Laganelli's Model

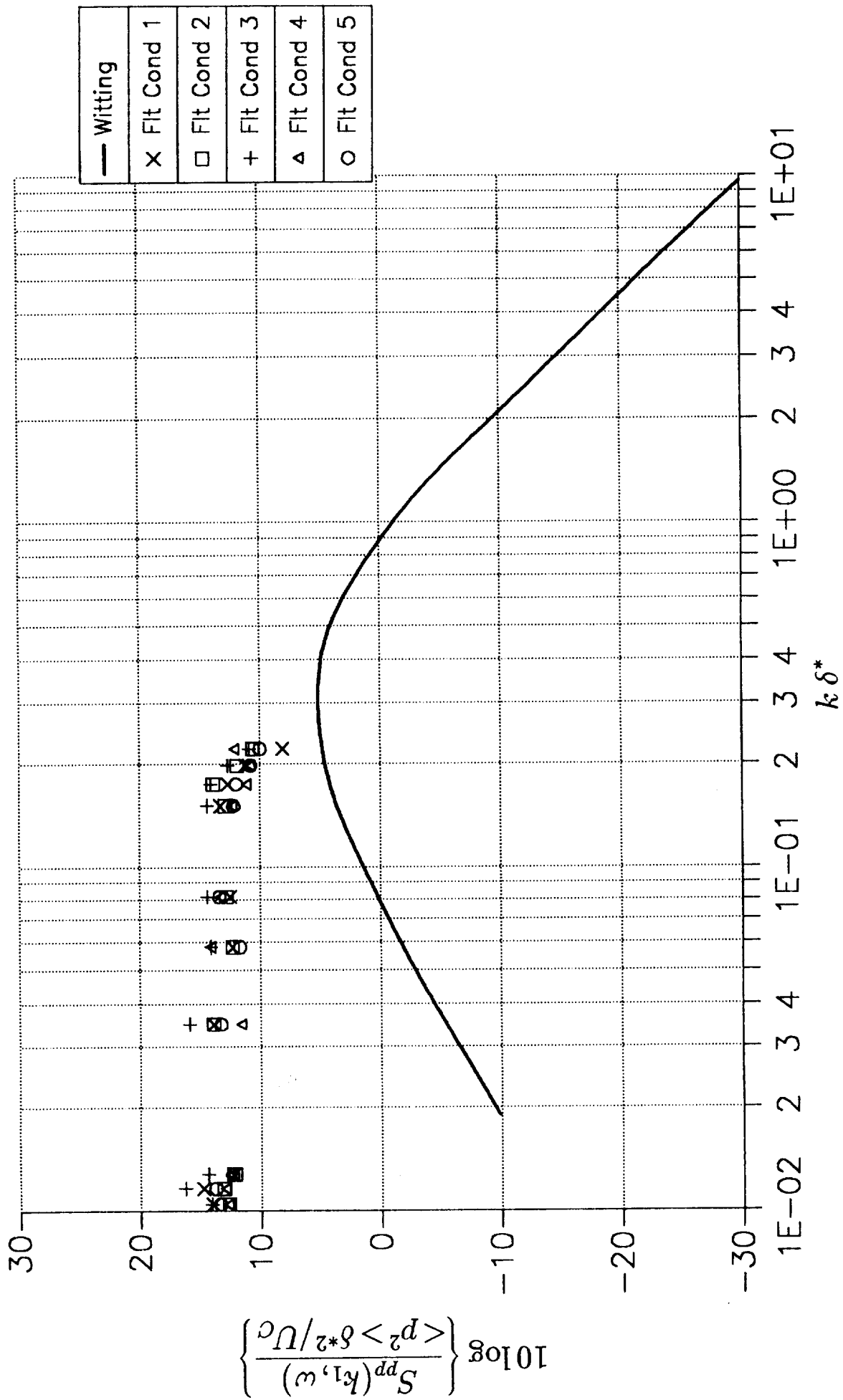


Figure A-8. Comparison of Flight Test TBL Pressure Data With Witting's model

B Partial Coherence Techniques

B.1 Mathematical Formulation

The noise at a specified cabin location can be modelled as a multiple-input, single output (MISO) system. The signals measured by microphones and accelerometers on the aircraft surfaces represent the inputs and the signal measured by an interior microphone represents the output. The physical measurements required to analyze a MISO system are the power spectra of all the inputs and the output, plus all the cross-spectra between them.

The basic frequency domain equation for a MISO system with q inputs is

$$Y(f) = \sum_{i=1}^q H_{iy}(f) X_i(f) + N(f) \quad (1)$$

where

$X_i(f)$ = Fourier transform of i^{th} input $x_i(t)$

$Y(f)$ = Fourier transform of output $y(t)$

$H_{iy}(f)$ = Transfer function between the i^{th} input x_i and the output y

$N(f)$ = Background Noise in the system

The auto- and cross-spectra of these time series data are calculated as

$$G_{yy}(f) = \lim_{T \rightarrow \infty} \frac{2}{T} \mathcal{E} [|Y(f)|^2] \quad (2)$$

$$G_{x_i x_j}(f) = G_{ij}(f) = \lim_{T \rightarrow \infty} \frac{2}{T} \mathcal{E} [X_i^*(f) X_j(f)] \quad (3)$$

$$G_{x_i y}(f) = G_{iy}(f) = \lim_{T \rightarrow \infty} \frac{2}{T} \mathcal{E} [X_i^*(f) Y(f)] \quad (4)$$

where

\mathcal{E} = Expectation operator

G_{ii} = Auto-spectrum of input $x_i(t)$

G_{yy} = Auto-spectrum of output $y(t)$

G_{ij} = Cross-spectrum between inputs $x_i(t)$ and $x_j(t)$

One very important concept in multiple input and output systems is the coherence function. It is a measure of the degree of relatedness of two signals; it is, however, not a cause and effect relationship.

Ordinary coherence function:

$$\gamma_{ij}^2 = \frac{|G_{ij}|^2}{G_{ii}G_{jj}} \quad (5)$$

Partial coherence function: The partial coherence function is a measure of the coherence between the i^{th} selected input with the effects of all r inputs preceding it in order removed and the j^{th} selected output with the effects of the same r inputs removed.

$$\gamma_{ij,r}^2 = \frac{|G_{ij,r}|^2}{G_{ii,r}G_{jj,r}} \quad (6)$$

Conditioned spectrum between the i^{th} and j^{th} inputs:

$$G_{ij,r} = G_{ij,(r-1)} - \frac{G_{rj,(r-1)}G_{ir,(r-1)}}{G_{rr,(r-1)}} \quad (7)$$

i^{th} conditioned output spectrum: The conditioned spectrum is the auto-spectrum of the i^{th} output with the effects of the selected r input and all inputs that precede it in order removed. The conditioned spectrum depends on the ordering of the inputs.

$$G_{ii,r} = G_{ii,(r-1)} - \frac{|G_{ir,(r-1)}|^2}{G_{rr,(r-1)}} \quad (8)$$

$$= G_{ii,(r-1)} \left(1 - \gamma_{ri,(r-1)}^2\right) \quad (9)$$

The equations above show the relationship between the present stage of the conditioned spectrum and the past stage of the conditioned spectrum. By induction, the following relation between the present conditioned spectrum and its entire past spectrum can be derived, in the form of partial coherence.

$$G_{ii,r} = G_{ii} \prod_{k=1}^r \left(1 - \gamma_{i(r-k+1),(r-k)}^2\right) \quad (10)$$

Multiple coherence function: The multiple coherence function is a measure of how much energy at the output is accounted for by the inputs.

$$\gamma_{yy,r}^2 = 1 - \prod_{i=1}^r \left(1 - \gamma_{iy,(i-1)}^2\right) \quad (11)$$

Eq. (7) is an iterative algorithm to compute the conditioned spectrum. It can also be written in terms of the partial coherence function as follows.

$$\gamma_{ij,r}^2 = \frac{\gamma_{ij,(r-1)}^2}{\left(1 - \gamma_{ri,(r-1)}^2\right) \left(1 - \gamma_{rj,(r-1)}^2\right)} \left| 1 - \frac{G_{rj,(r-1)}G_{ir,(r-1)}}{G_{rr,(r-1)}G_{ij,(r-1)}} \right|^2 \quad (12)$$

Rewriting eq. (10) in dB form yields

$$G_{ii:r}^{dB} = G_{ii}^{dB} + \Delta_{ii:r}^{dB} \quad (13)$$

where

$$G_{ii}^{dB} = 10 \log_{10} \left(\frac{G_{ii}}{G_{ref}} \right) \quad (14)$$

$$\Delta_{ii:r}^{dB} = 10 \sum_{k=1}^r \log_{10} \left(1 - \gamma_{(r-k+1)i \cdot (r-k)}^2 \right) \quad (15)$$

$$G_{ref} = 20 \times 10^{-6} \quad (16)$$

If $r \rightarrow \infty$, the auto-spectrum $G_{ii:r}^{dB}$, will approach the background noise level.

As an example, consider the case of two inputs, when the output is denoted as y .

For $r = 0$:

$$G_{ij:0!} = G_{ij} \quad (17)$$

$$G_{iy:0!} = G_{iy} \quad (18)$$

$$G_{yy:0!} = G_{yy} \quad (19)$$

For $r = 1$:

$$G_{ij:1!} = G_{ij:1} \quad (20)$$

$$= G_{ij} - \frac{G_{1j}G_{i1}}{G_{11}} \quad (21)$$

$$G_{iy:1!} = G_{iy:1} \quad (22)$$

$$= G_{iy} - \frac{G_{1y}G_{i1}}{G_{11}} \quad (23)$$

$$G_{yy:1!} = G_{yy:1} \quad (24)$$

$$= G_{yy} - \frac{G_{1y}G_{y1}}{G_{11}} \quad (25)$$

$$= G_{yy} - \frac{|G_{1y}|^2}{G_{11}} \quad (26)$$

$$= G_{yy} (1 - \gamma_{1y}^2) \quad (27)$$

For $r = 2$:

$$G_{iy:2!} = G_{iy:12} \quad (28)$$

$$= G_{iy:1!} - \frac{G_{1y:1!}G_{i1:1!}}{G_{22:1!}} \quad (29)$$

$$G_{yy \cdot 2!} = G_{yy \cdot 12} \quad (30)$$

$$= G_{yy \cdot 1} (1 - \gamma_{2y \cdot 1}^2) \quad (31)$$

$$= G_{yy} (1 - \gamma_{1y}^2) (1 - \gamma_{2y \cdot 1}^2) \quad (32)$$

$$= G_{yy} (1 - \gamma_{1y}^2) - \frac{\gamma_{12}^2}{G_{11} (1 - \gamma_{12}^2)} \left| G_{1y} - \frac{G_{2y} G_{11}}{G_{21}} \right|^2 \quad (33)$$

$$= G_{yy} \left(1 - \gamma_{1y}^2 \left(1 - \gamma_{12}^2 \left(1 - \left| 1 - \frac{G_{2y} G_{11}}{G_{1y} G_{21}} \right|^2 \right) \right) \right) \quad (34)$$

Note that $G_{yy \cdot 2!}$ is a function of combinations of input and output auto-spectra, cross-spectra and their respective coherence functions.

For general input $r > 2$, the conditioned output spectrum is given as

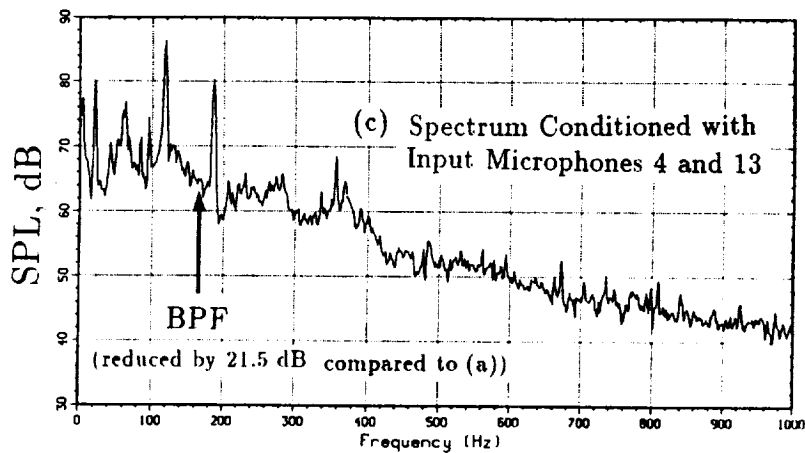
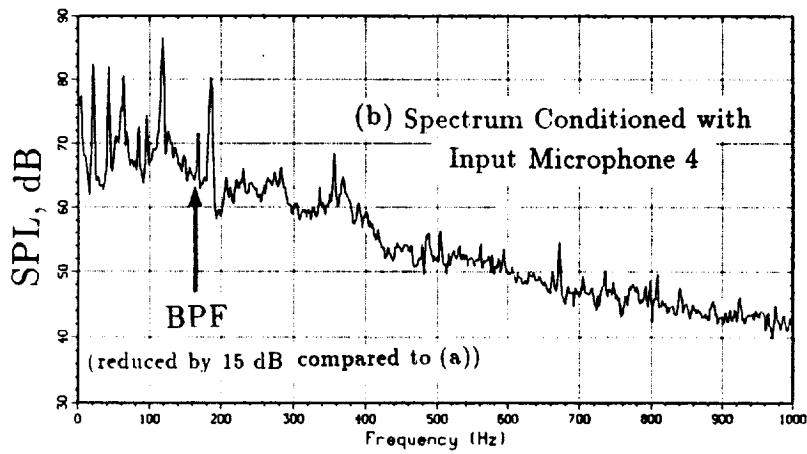
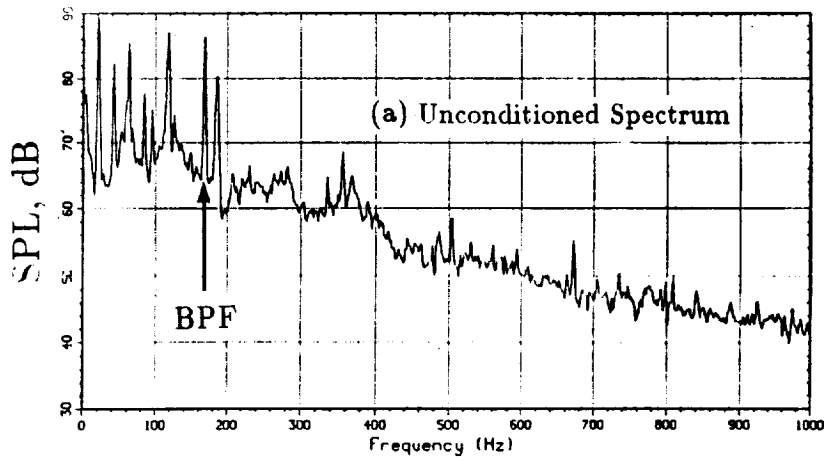
$$G_{yy \cdot r!} = G_{yy} \prod_{k=1}^r (1 - \gamma_{y(r-k+1) \cdot (r-k)!}^2) \quad (35)$$

It is obvious that $G_{yy \cdot r!}$ becomes rather complicated when r is large.

B.2 Flight Test Applications

An in-house computer program was used to calculate the ordinary and partial coherence values and the conditioned spectra using the iterative technique outlined in Bendat and Piersol's "Random Data - Analysis and Measurement Procedures," Chapter 7, 2nd Edition (Wiley Interscience, 1986). All the processing was performed with a resulting bandwidth of 1.5625 Hz, and yielded adequate spectral resolution without excessive computer storage requirements.

As an example of the results of the conditioning process, Figure B-1 shows an unconditioned output spectrum, and subsequent calculated spectra conditioned with selected inputs (the microphone locations are shown in Figure 8-7 in the main report text). The reduction in BPF level with each conditioning step can be seen in the figure.



See Figure 8-7 for microphone locations

FIGURE B-1.

Example of the Partial Coherence Conditioning
Process for Output Microphone 5,
8x8 Test Point 19550A03



Report Documentation Page

1. Report No. NASA CR-181897	2. Government Accession No.	3. Recipient's Catalog No.	
4. Title and Subtitle UHB Demonstrator Interior Noise Control Flight Tests and Analysis		5. Report Date October 1989	6. Performing Organization Code
		8. Performing Organization Report No.	
7. Author(s) M. A. Simpson, P. M. Druetz, A. J. Kimbrough, M. P. Brock, P. L. Burgé, G. P. Mathur, M. R. Cannon, and B. N. Tran		10. Work Unit No. 535-03-11-03	
		11. Contract or Grant No. NAS1-18037	
9. Performing Organization Name and Address Douglas Aircraft Company McDonnell Douglas Corporation Long Beach, CA 90846		13. Type of Report and Period Covered Contractor Report	
		14. Sponsoring Agency Code	
12. Sponsoring Agency Name and Address National Aeronautics and Space Administration Langley Research Center Hampton, VA 23665-5225			
15. Supplementary Notes Langley Technical Monitor: Kevin P. Shepherd Final Report - Task 4			
16. Abstract This report describes the measurement and analysis of MD-UHB Demonstrator noise and vibration flight test data related to passenger cabin noise. The objectives of these analyses were to investigate the interior noise characteristics of advanced turboprop aircraft with aft-mounted engines, and to study the effectiveness of selected noise control treatments in reducing passenger cabin noise. The UHB Demonstrator is an MD-80 test aircraft with the left JT8D engine replaced with a prototype UHB engine. For these tests, the UHB engine was a General Electric Unducted Fan, with either 8x8 or 10x8 counter-rotating propeller configurations. Interior noise level characteristics were studied for several altitudes and speeds, with emphasis on high altitude (35,000 ft), high speed (0.75 Mach) cruise conditions. The effectiveness of several noise control treatments was evaluated based on cabin noise measurements. The important airborne and structureborne transmission paths were identified for both tonal and broadband sources using the results of a sound intensity survey, exterior and interior noise and vibration data, and partial coherence analysis techniques. Estimates of the turbulent boundary layer pressure wavenumber-frequency spectrum were made, based on measured fuselage noise levels.			
17. Key Words (Suggested by Author(s)) Acoustics Advanced Turboprop Aircraft Flight Tests Interior Noise Control UHB Demonstrator		18. Distribution Statement Unclassified-Unlimited Subject Category - 71	
19. Security Classif. (of this report) Unclassified	20. Security Classif. (of this page) Unclassified	21. No. of pages 190	22. Price

